# Isomerism-Activity Relation in Molecular Electrocatalysis and Molecular Charge Storage

Thesis submitted to the Indian Institute of Science Education and Research in partial fulfilment of the requirements for the degree of

DOCTOR OF PHILOSOPHY


Submitted by

Alagar Raja K

Reg. No.: 20153382

Thesis Supervisor: Prof. Muhammed Musthafa O. T.

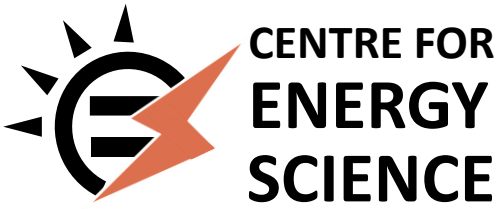



Indian Institute of Science Education and Research (IISER), Pune



January - 2021

भारतीय विज्ञान विक्षा एिं अनुसंधान संस्थान, पुणे

INDIAN INSTITUTE OF SCIENCE EDUCATION AND RESEARCH (IISER), PUNE

(An Autonomous Institution, Ministry of Human Resource Development, Govt. of India)

Dr. Homi Bhabha Road, Pune – 411 008.

Dr. Musthafa Muhammed O. T.

Associate Professor,

Department of Chemistry,

IISER Pune.

# CERTIFICATE

This is to certify that this thesis entitled "Isomerism-Activity Relation in Molecular Electrocatalysis and Molecular Charge Storage" towards the partial fulfilment of Ph.D. programme at the Indian Institute of Science Education and Research, Pune represents original research carried out by **Alagar Raja K** at Indian Institute of Science Education and Research, Pune under the supervision of **Prof. Muhammed Musthafa O. T.**, Associate Professor, Department of Chemistry and Centre for Energy Science, IISER Pune during the academic year 2015 - 2020 and that no part of it has been included in any other thesis submitted previously for the award of any degree.

Signature of the Thesis Supervisor

Date: 07th December, 2020

Dr. Muhammed Musthafa O. T.

Associate Professor,

Department of Chemistry and Centre for Energy Science,

IISER Pune.

भारतीय विज्ञान विक्षा एिं अनुसंधान संस्थान, पुणे
INDIAN INSTITUTE OF SCIENCE EDUCATION AND RESEARCH (IISER), PUNE
(An Autonomous Institution, Ministry of Human Resource Development, Govt. of India)
Dr. Homi Bhabha Road, Pune – 411 008

# DECLARATION

I hereby declare that the matter embodied in the thesis entitled "**Isomerism-Activity Relation in Molecular Electrocatalysis and Molecular Charge Storage**" are the results of the investigations carried out by me at the Department of Chemistry and Centre for Energy Science of the Indian Institute of Science Education and Research, under the supervision of **Prof. Muhammed Musthafa O. T.**, Associate Professor, Department of Chemistry and Centre for Energy Science, IISER Pune and that no part of this thesis has been included in any other thesis submitted previously for the award of any degree.

**Signature of the student** **Date:** 07th December, 2020

**Alagar Raja K**
**Reg. No: 20153382**
**IISER Pune.**

# ACKNOWLEDGEMENT

*First of all, I would like to express my deepest gratitude towards my supervisor Dr. Muhammed Musthafa O. T. for providing continuous support and guidance throughout my Ph.D. journey. He has provided me with an outstanding lab and an excellent working environment. He has given me full freedom to pursue various projects without any objection and has given many insightful discussions into each and every minute topic. I am utterly thankful to him for his scientific guidance and suggestions. Throughout my entire Ph.D. programme, his patience, enthusiasm, immense knowledge, constant motivation, and positive feedback has helped me to become an independent thinker. Amongst various other things, he has instilled in me the importance of always being technically sound and scientifically ethical. His teachings through regular one to one meetings and various informal chats during the morning and afternoon tea sessions were very valuable in building me as a researcher and as well as a good human being.*

*Also, I would want to express my deep gratitude and respect to my RAC members Prof. P. A. Joy from NCL Pune and Dr. Pramod Pillai from IISER Pune for their continuous support and extremely valuable scientific inputs during the last 4 years, especially during my RAC meetings.*

*Many thanks should go to my research collaborators Dr. M. N. K. Harish (Acharya Institute of Technology, Bangalore), Dr. C. P. Vinod (CSIR-NCL, Pune) and their students for their kind assistance and for allowing me to use their research facilities. Some of my experiments would never have been possible without their valuable contribution and technical support. I would like to make a special mention to Dr. Mohammed Azeezulla from CSIR-CECRI who performed the theoretical calculations for my projects, it was not possible to give my thesis its current shape without his help.*

*My deepest regards are also due to the former director, Prof. K.N Ganesh and the present director, Prof. Jayant Udgaonkar for providing me such a state-of-the-art institute, first-class research infrastructure and rich academic ambiance. The numerous invited talks by experts, symposia and conferences held at IISER Pune always brought rich insights to all of us. I am extremely thankful to the university grants commission (UGC) - India for providing me with*

*the Ph.D. fellowship for the last five years and for their travel support to attend various national/international conferences. My appreciations also extends to American Chemical Society (ACS), Royal Society of Chemistry (RSC), John Wiley & Sons, Elsevier Science Ltd., Springer, etc. for accepting and publishing my research articles and also their permission to reprint the materials under copyright.*

*I would like to convey my love and regards to all my past lab mates, Dr. Ravikumar T, Dr. Shahid P Shafi, Dr. Mruthyunjayachari, Dr. Chidananda, Shabbah, Dr. Shambulinga, Pramod, Swapnil, Dr. Mahesh, Fawaz, and Sarvojith as well as my present lab mates Manu, Neethu, Sanchayita, Abdul, Soumodip and Thamaraichelvan who have provided me a healthy lab atmosphere and their supportive and friendly nature made my journey a lot more enjoyable and exciting. A special acknowledgment to Zahid and Dr. Mruthyunjayachari who occupies a major part in my Ph.D. journey both professionally as well personally.*

*I would like to give my heartiest thanks and regards to all the academic and non-academic staff, especially Anil Prathamshetti, Suresh Kumar (IT), Sandeep Kanade, Nitin Dalvi, T.S. Yatish, Tushar Kurulkar, Mayuresh Kulkarni, Megha Paygude, Mahesh Jadhav, Ganesh Dimbre, Sayalee, Priyadarshini, Prabhas and Prabhakar for being extremely helpful throughout the last 5 years of my stay at IISER Pune. A special thanks to the housekeepers for keeping research laboratories and this institute clean and tidy all the time.*

*I am very much indebted to my friends Dr. Manoharan, Dr. Anandaraj, Bala, Dr. Vijayakanth, Dr. Veeresh, Sabari (IIT Bombay), Dr. Ravikumar, Thamarai, The Alchemist cricket team and IISER Pune friends. They have allowed me to keep a peaceful and refreshing mind throughout either by sports or by offering recreations during weekends.*

*Finally, words are not enough to give my heartiest and the deepest regards to my loving parents and brothers, family members without whom it would not have been possible to pursue my research career.*

*Though I may have missed to mention some friends and colleagues by name, I greatly appreciate all their support and help throughout my time at IISER Pune.*

*Alagar Raja K*

*Dedicated*

*to my beloved parents & brothers and all the mentors in life*

# Table of Contents


**Thesis synopsis** 1 - 10

**Chapter 1 Introduction**

1.1. $N_4$ macrocyclic metal complexes 11 - 16

1.1.1. Phthalocyanines (Pcs) 13 - 15

1.1.2. Properties of phthalocyanines 15 - 16

1.2. Metal phthalocyanines as electrocatalysts 16 - 21

1.3. Metal phthalocyanines as supercapacitors 21 - 23

1.4. Aim and scope of the thesis 23 - 27

1.5. References 28 - 42

**Chapter 2 Materials and Methods**

2.1. Materials 43

2.2. Material characterization 43 - 44

2.3. Electrochemical measurements 44 - 46

2.4. Synthesis of isomeric metal phthalocyanines and phthalocyanine anchored on carbon materials 46 - 48

2.4.1. Synthesis of 1,8,15,22-Tetranitrophthalocyanatocobalt (II) (α-TNCoPc), 2,9,16,23-Tetranitrophthalocyanatocobalt (II) (β-TNCoPc), 1,8,15,22-Tetranitrophthalocyanatozinc (II) (α-TNZnPc), 2,9,16,23-Tetranitrophthalocyanatozinc (II) (β-TNZnPc), and Phthalocyanatocobalt (II) (CoPc). 46 - 47

2.4.2. Preparation of 1,8,15,22 Tetraaminophthalocyanatocobalt (II) (α-TACoPc) and 2,9,16,23-Tetraaminophthalocyanatocibalt (II) (β-TACoPc) from corresponding 1,8,15,22-Tetranitrophthalocyanatocobalt (II) and 2,9,16,23-Tetranitrophthalocyanatocobalt (II) 47

2.4.3. Synthesis of α-TANiPc/β-TANiPc, α-TACuPc/β- 47

TACuPc, and α-TAZnPc/β-TAZnPc

2.4.4. Synthesis of CoPc, α-TNCoPc/ α-TACoPc and β-TNCoPc/ α-TACoPc anchored on carbon nanotubes (CNTs) 47 - 48

2.4.5. Synthesis of α-TACoPc and β-TACoPc anchored on YP-50F carbon 48

2.5. Self-assembly of α-TNMPc/α-TAMPc and β-TNMPc/β-TAMPc on glassy carbon (GC) and Au electrodes (Metal:- Co, Ni, Cu, Zn etc.) 48 - 49

2.6. Surface coverage calculations 49 - 50

2.6.1. Electrochemical methods 49

2.6.2. Amatore's model 49 - 50

2.6.3. Quartz crystal microbalance (QCM) study 50

2.7. Density functional theory (DFT) calculations 50 - 51

2.8. Calculation of the number of electron and catalytic rate constant (kcat) for arsenic (III) to arsenic (V) oxidation 51 - 52

2.9. Calculation of the number of electron and $H_2O_2$ % yield for ORR 52 - 53

2.10. $H_2$-$O_2$ fuel cell assembly 53 - 54

2.11. Specific capacity, energy density and power density calculations of molecular supercapacitor 54

2.12. Characteristic time constant ($\tau_0$), self-discharge current ($i_{sd}$) and leakage current ($i_{lk}$) measurements 55 - 56

2.13. References 56 - 59

**Chapter 3 Isomerism-Activity Relation in Oxidative Molecular Electrocatalysis**

3.1. Introduction 61 - 62

3.2. Results and discussion 62 - 81

3.2.1. Characterization of CoPc, α-TNCoPc and β-TNCoPc and their composites with carbon nanotube 62 - 67

| | | |
|---|---|---|
| 3.2.2. | Electrochemical analysis | 67 - 73 |
| 3.2.3. | X-ray photoelectron spectroscopy study | 73 - 75 |
| 3.2.4. | Density functional theory (DFT) calculations | 75 - 81 |
| 3.3. | Conclusions | 81 - 82 |
| 3.4. | References | 82– 87 |

**Chapter 4 Geometrical Isomerism Directed Electrochemical Sensing**

| | | |
|---|---|---|
| 4.1. | Introduction | 89 - 90 |
| 4.2. | Results and discussion | 90 - 104 |
| 4.2.1. | Electrochemical analysis | 91 - 96 |
| 4.2.2. | Investigation of number of electrons and catalytic rate constant (kcat) for the direct oxidation of arsenic (III) to arsenic (V) | 96 - 99 |
| 4.2.3. | X-ray photoelectron spectroscopy study | 97 - 101 |
| 4.2.4. | Analytical performance of the arsenic sensor | 101 - 104 |
| 4.3. | Conclusions | 104 |
| 4.4. | References | 104 - 112 |

**Chapter 5 Isomerism-Activity Relation in Reductive Molecular Electrocatalysis**

| | | |
|---|---|---|
| 5.1. | Introduction | 114 - 115 |
| 5.2. | Results and discussion | 115 - 140 |
| 5.2.1. | Characterization of α-TACoPc and β-TACoPc isomeric molecules | 115 - 117 |
| 5.2.2. | Electrochemical analysis | 117 - 119 |
| 5.2.3. | Orientation versus isomerism | 120 - 127 |
| 5.2.4. | Nuclear magnetic resonance (NMR) spectroscopy investigations | 127 - 131 |

| | | |
|---|---|---|
| 5.2.5. | Mechanism of ORR on α/β-TACoPc isomeric molecules | 131 - 133 |
| 5.2.6. | Density function theory (DFT) calculations | 133 - 138 |
| 5.2.7. | $H_2$-$O_2$ fuel cell study | 138 - 140 |
| 5.3. | Conclusions | 141 |
| 5.4. | References | 141-151 |
| **Chapter 6** | **Non-covalent Interaction Regulated Molecular Charge Storage** | |
| 6.1. | Introduction | 153 - 154 |
| 6.2. | Results and discussion | 154 - 177 |
| 6.2.1. | Characterization of α-TAMPc and β-TAMPc (M-Co, Ni, Cu and Zn)) | 154 - 157 |
| 6.2.2. | Electrochemical analysis | 157 - 160 |
| 6.2.3. | Density functional theory (DFT) calculation | 160 - 163 |
| 6.2.4. | Nuclear magnetic resonance (NMR) spectroscopy and X-ray photoelectron spectroscopic (XPS) investigations | 163 - 167 |
| 6.2.5. | Investigation of surface charge | 167 - 171 |
| 6.2.6. | Charge storage in composite electrodes | 171 - 177 |
| 6.3. | Conclusions | 177 - 178 |
| 6.4. | References | 178 - 185 |
| **Chapter 7** | **Conclusions** | 186 - 187 |

# Synopsis of the thesis entitled "Isomerism-Activity Relation in Molecular Electrocatalysis and Molecular Charge Storage"

Electrocatalysts play major roles in energy conversion/storage, electrochemical sensing, environmental remediation, green chemistry, etc.; which in turn are responsible for the exhaustive attempts in understanding their structure-activity relations.[1-4] Among the class of various electrocatalysts, the $N_4$ macrocycle based molecular electrocatalysts such as metal phthalocyanines and porphyrins stand out as potential non-precious electrocatalysts for an assortment of electrochemical applications due to their tunable optoelectronic properties and chemical and thermal stabilities.[5-8] While targeting the surface-to-volume ratio, exposing reactive crystal planes, interfacial modifications etc., are time-tested considerations for activating conventional electrocatalysts; the catalytic properties of molecular electrocatalysts are primarily tuned by the nature of the secondary sphere ($N_4$ macrocycle) functionality which in turn is known to modulate the electronic arrangement at the catalytic centre.[9-12] However, far too little attention has been paid to the fact that this electronic arrangement is not only a function of their chemical identity across the spectrochemical series but also can be a strong function of their isomerism. In the context of charge storage, since the energy density of supercapacitors scales-up linearly with surface-confined charge density, the pursuit towards high energy and high-power supercapacitors are conventionally accomplished in solid systems by maximizing their surface-to-volume ratio.[13-15] In molecular systems, a handful of reports suggest that the nature of the secondary sphere functionality can tune their supercapacitive charge storage, however, a clear knowledge gap exists in comprehending what controls their structure- charge storage relation.[16]

The primary aim of this thesis is to draw a distinction between a substituent's chemical identity and isomerism towards electrocatalysis and molecular charge storage when regioisomerism of electron-withdrawing/electron-donating substituents is conferred at the 'α' and 'β' positions of the $N_4$ macrocycle in metal-phthalocyanines (MPcs). The existing accounts fail to make any distinction between the chemical identity of groups and their isomerism in molecular electrocatalysis and charge storage, etc., and to the best of our knowledge no research has been found that surveyed and understood isomerism-catalytic

activity relation and isomerism-charge storage relation in molecular systems. Therefore, the major focus of this thesis is on studying how the geometric and electronic factors of substituents as a result of their isomerism at the secondary sphere influence molecular charge storage and molecular electrocatalysis of challenging electrochemical transformations. This study brings to light how the isomerism of secondary sphere functionality can be tapped to design efficient interfaces for energy conversion and electrochemical sensing and molecular platforms for charge storage devices. The thesis is subdivided in to six chapters.

**Chapter 1. Introduction:** This chapter explains the importance of $N_4$ macrocyclic complexes with particular emphasis on the electrochemical properties of metal phthalocyanines. Detailed discussions are provided for their important roles in various electrocatalytic transformations and supercapacitive charge storage. The role of the nature of the secondary sphere functionality in tuning molecular electrocatalysis and molecular charge storage is highlighted in the context of the reported literature. The knowledge gap existing in their structure-activity and structure charge storage relation is further highlighted towards the end of this chapter.

**Chapter 2. Materials and Methods:** This chapter explains the synthesis of $-NO_2$ and $-NH_2$ substituted isomeric phthalocyanine molecules and unsubstituted phthalocyanine molecules. The fabrication of carbon supported molecular platforms for applications ranging from electrocatalysis, electrochemical sensing and molecular charge storage are further elaborated. Various physico-chemical techniques used for the characterization of the synthesized compounds are provided.

**Chapter 3. Isomerism-Activity Relation in Oxidative Molecular Electrocatalysis:** This chapter elaborates how the isomerism of the substituents at the secondary sphere of MPcs can be tapped to tune the activity of catalytic metal center towards oxidative electrocatalytic reactions ranging from energy conversion to bio-sensing. When regioisomerism of electron withdrawing $-NO_2$ group substituent is conferred at the α and β positions on the $N_4$ macrocycle of cobalt phthalocyanine, an oxidative activation of the catalytic metal centre towards a variety of electrochemical oxidation reactions was distinctly evident in the 'β' isomer compared to the corresponding 'α' counterpart. Electrochemical investigation,

spectroscopic analyses and density functional theory (DFT) calculations suggested that isomerism of $–NO_2$ functionality at the $N_4$ macrocycle of MPc conjoin molecular planarity and catalytic activation through competing field effects and resonance effects. The proximity of $–NO_2$ group to the N atoms in the $N_4$ macrocycle in the α-TNCoPc isomer triggered repulsive field effects which in turn favored an out of plane configuration of $–NO_2$ group (dihedral angle is ~137.07°) with respect to the $N_4$ macrocycle leading to a vanishingly small electron withdrawing resonance effect (-R effect) between the former and the latter **(Figure 1)**. On the other hand, in the β-TNCoPc isomeric molecule field effect was negligible due to the spatial separation of the groups, leading to an in-plane configuration of the $-NO_2$ functionality (dihedral angle is ~179.99°) with respect to the $N_4$-macrocycle **(Figure 1)** that in turn activated the central metal ion noticeably via a cumulative influence of electron withdrawing resonance (-R effect) effect and electron withdrawing inductive effects (-I effect). This combined influence of -R and –I effects in β-TNCoPc isomeric molecule significantly enhanced the kinetics of various electrochemical oxidation reactions **(Figure 1)**. This study brings to light a crucial factor that is often overlooked in electrocatalysis that isomerism of substituents can redefine the electronic arrangement in the catalytic center and make an additional contribution to electrocatalysis over its chemical identity.

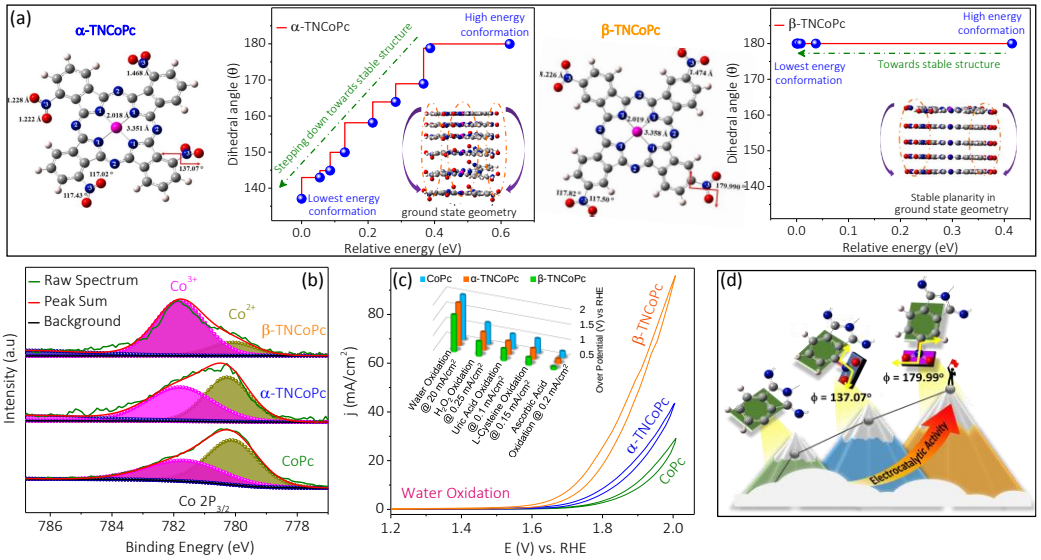


**Figure 1:** (a) Stable geometry for α-TNCoPc isomer and β-TNCoPc isomer from DFT calculations along with plot of dihedral angle vs. relative energy for α-TNCoPc isomer and β-TNCoPc isomer. In the insets of Figure 1a, the orange colored curvature depict the cascading of oxygen atoms of $-NO_2$ group towards non-planar geometry for α-TNCoPc

isomer and planar geometry for β-TNCoPc isomer. (b) X-ray photoelectron spectroscopy (XPS) of isomeric molecules. (c) Catalytic performance of α and β-TNCoPc isomers in comparison to unsubstituted CoPc for electrochemical water oxidation reaction. Inset: the corresponding performance metrics for various electrochemical transformations. d) Schematic representation of isomerism-activity relation in molecular electrocatalysis.

**Chapter 4. Isomerism Directed Electrochemical Sensing:** This chapter explains how the isomerism-activity relation in molecular electrocatalysis can be exploited for designing a non-precious sensing platforms for the detection of As (III) via its direct oxidation pathway which is a potentially important electrochemical pathway for water remediation and arsenic detection. The employment more active β-TNCoPc isomer for catalyzing the multi-electron oxidation of As (III) to As (V) leads to the development of an arsenic detection platform with experimental detection limit close to WHO guidelines, **Figure 2**. Therefore, this methodology of isomerism induced activation of catalytic metal centre opens-up an unusual approach in analytical chemistry for developing various sensing platforms for challenging electrochemical transformations.

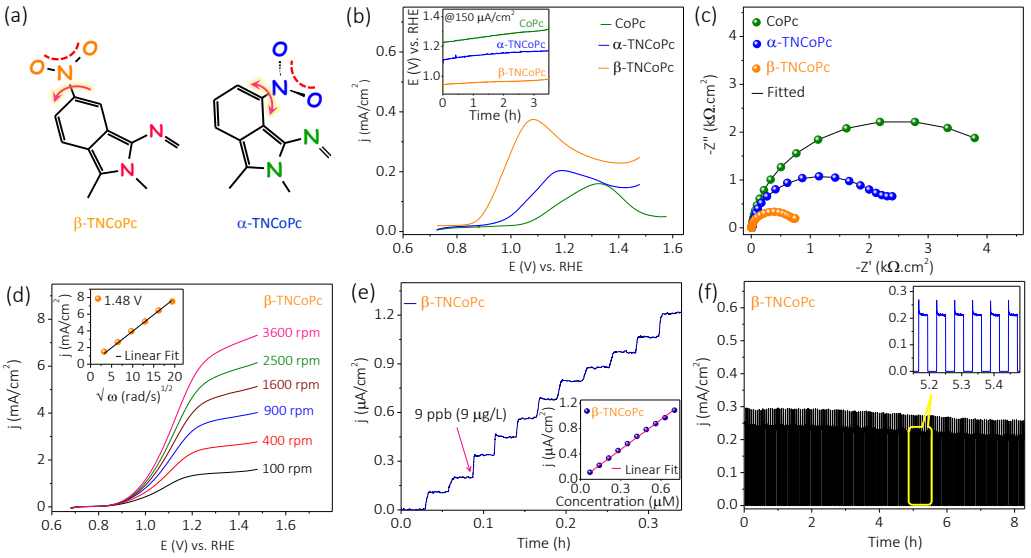


**Figure 2:** (a) Scheme depicting the relative configuration of -$NO_2$ plane with respect to $N_4$ macrocycle plane in α-TNCoPc and β-TNCoPc isomers. Electrochemical studies of unsubstituted CoPc, α and β-TNCoPc isomers toward direct As (III) oxidation: (b) Voltammograms recorded at a scan rate of 10 mV/s (inset: chronopotentiometry traces at 150 μA/cm$^2$), (c) impendence spectroscopy (Nyquist plots) and (d) rotating disk electrode (RDE) measurements (inset: corresponding Levich plot at 1.48 V vs. RHE) in the presence

of 5 mM of arsenite in phosphate buffer of pH = 8. (e) Chronoamperometry traces (background subtracted currents are plotted) at 1.1 V vs. RHE during successive increment in the concentration of arsenite in phosphate buffer of pH = 8. Inset: the corresponding calibration plot. (f) Cyclic stability of β-$NO_2$ isomer catalyst at 1.0 V vs. RHE in phosphate buffer of pH = 8 containing 1 mM arsenite.

**Chapter 5. Isomerism-Activity Relation in Reductive Molecular Electrocatalysis:** Robust and durable molecular electrocatalysts based on earth-abundant metals are essential for the interconversion of electrical energy and fuels to address the growing mismatch between the availability of renewable energy and its demand. In this context, development of efficient electrocatalysts for oxygen reduction reaction (ORR); the limiting half-cell reactions in fuel cells and metal-air batteries assume great significance. This chapter discusses how the regioisomerism of electron-donating -$NH_2$ substituent at the $N_4$ macrocycle of cobalt phthalocyanine alters the activity of catalytic Co centre to such an extent that ORR mechanism changes from a 4 electron pathway to a 2 electron pathway when regioisomerism of the functionality is shifted from α to β position. Various physicochemical analyses reveal that isomerism of secondary sphere functionality influences the reaction kinetics as well as reaction mechanism of ORR which in turn highlights that isomerism-activity relationship is well applicable in reductive electrocatalysis as well. This type of regioisomerism induced activation of the catalytic centre is explained in the literature as a consequence of the difference in the orientation of central metal ion with respect to the anchoring substrate. However, electrochemical studies, spectroscopic analyses and DFT calculations invalidate the theory of orientation as a reason for this electrochemical activation but point to non-covalent interaction (H bonding) as the responsible factor. Intramolecular H-bonding existing in the α-TACoPc isomeric molecule activated the central cobalt ion towards ORR and changed its mechanistic pathway to a 4 electron pathway by preferential side-on binding to molecular oxygen. On the other hand, in the corresponding β-TACoPc isomeric molecule ORR mechanism followed a 2 electron pathway (**Figure 3**) by favouring end-on interactions with $O_2$. Therefore, isomerism induced activation induce selectivity in molecular electrocatalysis which in turn provides a new approach in the design of efficient non-precious electrocatalysts for energy conversion (4 electron process) and peroxide production (2 electron process),

**Figure 3.** Therefore, the uncovering of isomerism-activity relation in $N_4$-macrocyclic molecules is expected to fill the inadequacies and knowledge gap in their structure-activity relations which is expected to immensely contribute to the development of next generation electrodes for energy storage and energy conversion devices.

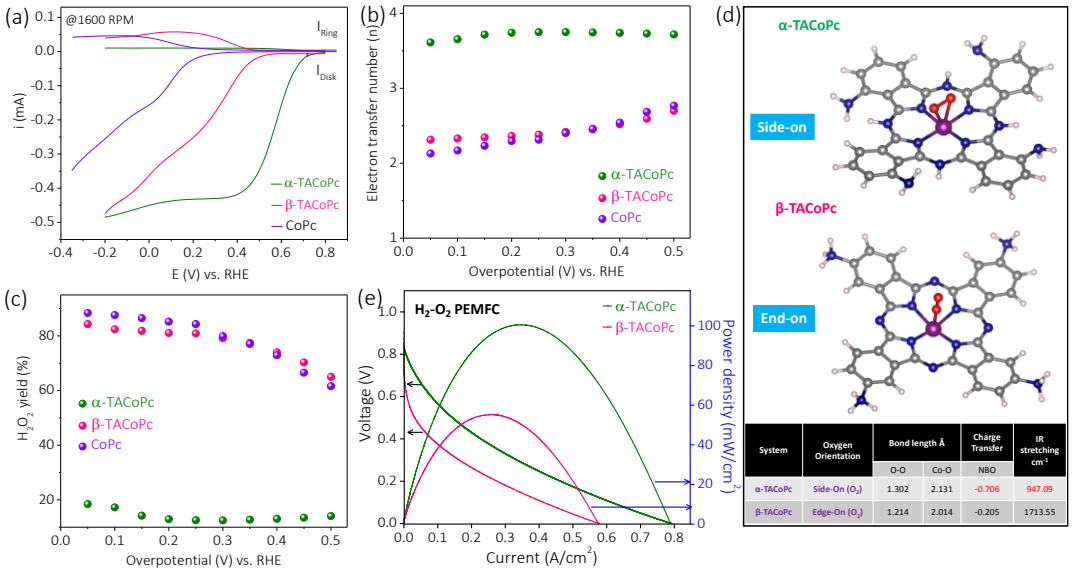


| System | Oxygen Orientation | Bond length Å | | Charge Transfer | IR stretching $cm^{-1}$ |
|---|---|---|---|---|---|
| | | O-O | Co-O | NBO | |
| α-TACoPc | Side-On ($O_2$) | 1.302 | 2.131 | -0.706 | 947.09 |
| β-TACoPc | Edge-On ($O_2$) | 1.214 | 2.014 | -0.205 | 1713.55 |

**Figure 3:** (a) Rotating ring-disk electrode (RRDE) measurements (at 1600 rpm) with unsubstituted CoPc and α and β-TACoPc isomers for ORR at a scan rate of 10 mV/s in oxygen saturated 0.5 M $H_2SO_4$. (b) The calculated electron transfer numbers and (c) the peroxide production percentage during the ORR process. (d) The stable geometry for α-TACoPc isomer and β-TACoPc isomer from DFT calculations in the presence of oxygen. (e) Room temperature (25° C) $H_2$-$O_2$ fuel cell polarization curves with α-TACoPc isomer (1.0 mg/cm$^2$) and β-TACoPc isomer (1.0 mg/cm$^2$) as ORR cathode catalysts. Anode Pt/C catalysts loading was 0.5 mg/cm$^2$ and the flow rate of $H_2$/$O_2$ was 100 mL/min.

**Chapter 6. Non-covalent Interaction Regulated Molecular Charge Storage:** This chapter shows how the molecular charge storage is interconnected with the nature as well as isomerism of secondary sphere functionality via non-covalent interactions. Since the energy density of supercapacitors scales-up linearly with surface-confined charge density, the pursuit towards high energy and high-power supercapacitors are conventionally accomplished in solid systems by maximizing their surface-to-volume ratio. With regard to molecular systems, despite a few reports on improving their surface charge density by secondary-sphere functionalization, a lack of in-depth understanding exists in defining what controls their structure-charge storage relationship. This chapter demonstrates an unusual molecular

structure-charge storage relation; where solvent dependent non-covalent interactions in the molecule strongly interconnected their charge storage with the nature as well as the isomerism of the secondary sphere functionality. Electrochemical, spectroscopic and DFT calculations suggest that isomerism of amino functionality triggered attractive field-effect via intramolecular hydrogen-bonding in the α-TACoPc isomeric molecule that in turn suppressed the extent of protonation and consequently their electrochemical capacity **(Figure 4)**. When attractive field effect is inhibited by spatially separating the H-bonding groups via geometrical isomerism (in the β-TACoPc isomeric molecule), electrochemical capacity is significantly enhanced. Interestingly, repulsive field effect in isomeric nitro molecules leads only to a geometric rotation of the $-NO_2$ functionality which did not contribute to a disparity in their molecular charge storage. Unveiling the subtle role of non-covalent interactions in conjoining the molecular charge storage with nature as well as isomerism of the functionality opens up an alternative pathway in the design of molecular supercapacitors to target their energy density without compromising the power capability.

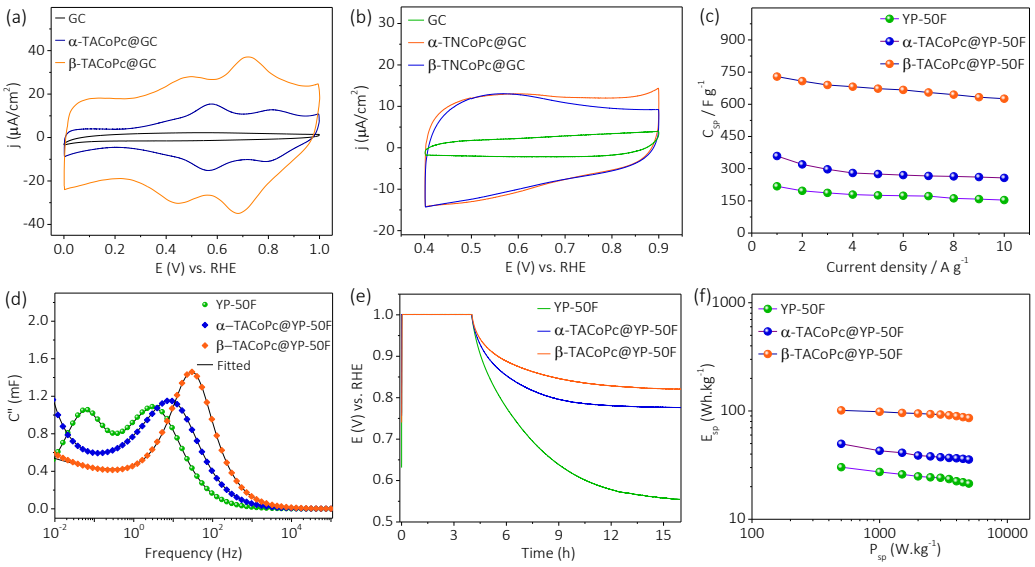


**Figure 4:** (a and b) Cyclic voltammograms (CVs) of isomeric -$NH_2$ molecules and isomeric -$NO_2$ molecules at a scan rate of 20 mV/s in $N_2$ saturated 0.5 M $H_2SO_4$ when they are incorporated as a monolayer on a glassy carbon electrode. Charge-discharge characteristics of α and β-TACoPc isomeric molecules modified YP-50F composite electrodes. (c) Comparative rate profiles obtained from galvanostatic charge-discharge, (d) comparative plot of the imaginary part of capacitance (C") vs. frequency, (e) self-discharge profiles and (f) Ragone plot for the isomeric -$NH_2$ molecules.

In essence the work outlined in this thesis uncovers an isomerism-catalytic activity relation and an isomerism-charge storage relation in molecular systems (Scheme 1). Specifically, while the nature of the substituent plays a central part in tuning the electrocatalysis and charge storage, its isomerism-induced contribution undeniably offers a unique pathway for utilizing the maximum potential of the molecule for challenging electrochemical transformations and charge storage applications. Further, the structure-activity relations of molecules will be incomplete if one neglects this isomerism induced contribution because as demonstrated they are too significant to be neglected. It is to be noted that the effect cannot be generalized across the spectrochemical series as this relation is substituent specific. This indeed demands insightful studies about each substituent at a molecular level to understand their substituent specific isomerism–catalytic activity/charge storage relation. This is mainly because, often non-covalent interactions interconnects the electrochemical properties of the molecule with the nature of the functionality as well as its isomerism, and such interactions are often substituent specific which offers a plethora of opportunities for researchers working in the domain of molecular electrocatalysis and molecular charge storage. The uncovering of isomerism-activity relation in $N_4$-macrocyclic molecules is expected to fill the inadequacies and knowledge gap in their structure-activity relations which will immensely contribute to the development of next generation electrodes for electrocatalysis, bio-sensing, and energy storage.

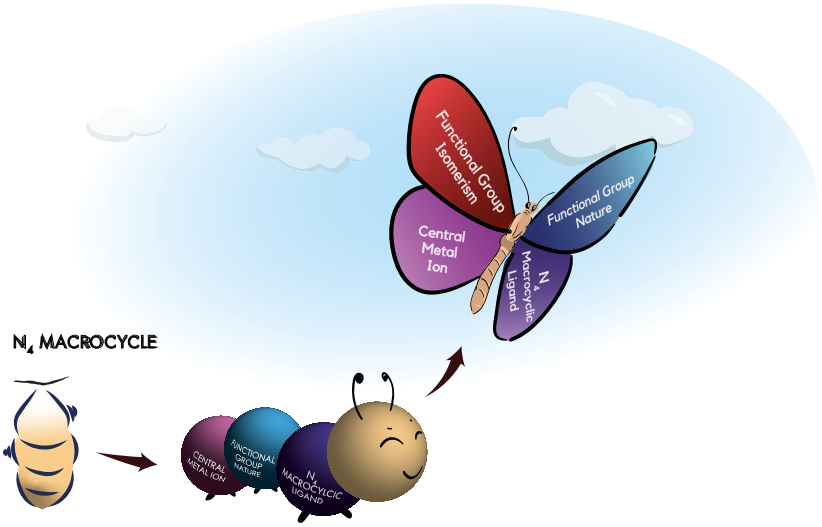


**Scheme 1:** A bird's eye view of isomerism-activity relation in molecular electrocatalysis and molecular charge storage.

## References


[1] Liang, Y.; McLaughlin, D.; Csoklich, C.; Schneider, O.; Bandarenka, A. S. The Nature of Active Centers Catalyzing Oxygen Electro-Reduction at Platinum Surfaces in Alkaline Media. *Energy Environ. Sci.* **2019**, *12* (1), 351–357.

[2] Costentin, C.; Savéant, J. M. Towards an Intelligent Design of Molecular Electrocatalysts. *Nat. Rev. Chem.* **2017**, *1* (11), 1–8.

[3] Löffler, T.; Meyer, H.; Savan, A.; Wilde, P.; Garzón Manjón, A.; Chen, Y. T.; Ventosa, E.; Scheu, C.; Ludwig, A.; Schuhmann, W. Discovery of a Multinary Noble Metal–Free Oxygen Reduction Catalyst. *Adv. Energy Mater.* **2018**, *1802269*, 1–7.

[4] Vaddypally, S.; Tomlinson, W.; O'Sullivan, O. T.; Ding, R.; Van Vliet, M. M.; Wayland, B. B.; Hooper, J. P.; Zdilla, M. J. Activation of C-H, N-H, and O-H Bonds via Proton-Coupled Electron Transfer to a Mn(III) Complex of Redox-Noninnocent Octaazacyclotetradecadiene, a Catenated-Nitrogen Macrocyclic Ligand. *J.Am.Chem.Soc.* **2019**, *141* (14), 5699–5709.

[5] Wan, X.; Liu, X.; Li, Y.; Yu, R.; Zheng, L.; Yan, W.; Wang, H.; Xu, M.; Shui, J. Fe–N–C Electrocatalyst with Dense Active Sites and Efficient Mass Transport for High-Performance Proton Exchange Membrane Fuel Cells. *Nat. Catal.* **2019**, *2* (3), 259–268.

[6] Zagal, J.H.; Bedioui, F.; Dodelet, J. P. *$N_4$-macrocyclic metal complexes.* Springer, New York. **2006.**

[7] Sorokin, A. B. Phthalocyanine Metal Complexes in Catalysis. *Chem. Rev.* **2013**, *113* (10), 8152–8191.

[8] Bottari, G.; de la Torre, G.; Guldi, D. M.; Torres, T. Covalent and Noncovalent Phthalocyanine–Carbon Nanostructure Systems: Synthesis, Photoinduced Electron Transfer, and Application to Molecular Photovoltaics. *Chem. Rev.* **2010**, *110* (11), 6768–6816.

[9] Li, R.; Zhang, X.; Zhu, P.; Ng, D. K. P.; Kobayashi, N.; Jiang, J. Electron-Donating or -Withdrawing Nature of Substituents Revealed by the Electrochemistry of Metal-Free Phthalocyanines. *Inorg. Chem.* **2006**, *45* (5), 2327–2334.

[10] Wang, J.; Huang, X.; Xi, S.; Lee, J.-M.; Wang, C.; Du, Y.; Wang, X. Linkage Effect in the Heterogenization of Cobalt Complexes by Doped Graphene for Electrocatalytic $CO_2$ Reduction. *Angew. Chemie Int. Ed.* **2019**, 58 (38), 13532–13539.

[11] Zagal, J. H.; Koper, M. T. M. Reactivity Descriptors for the Activity of Molecular $MN_4$ Catalysts for the Oxygen Reduction Reaction. *Angew. Chemie - Int. Ed.* **2016**, *55* (47), 14510–14521.

[12] Raja, R.; Ratnasamy, P. Selective Oxidation of Phenols Using Copper Complexes Encapsulated in Zeolites. *Applied Catalysis A: General* **1996**, *143*, 145–158.

[13] Wang, F.; Wu, X.; Yuan, X.; Liu, Z.; Zhang, Y.; Fu, L.; Zhu, Y.; Zhou, Q.; Wu, Y.; Huang, W. Latest Advances in Supercapacitors: From New Electrode Materials to Novel Device Designs. *Chem. Soc. Rev.* **2017**, *46* (22), 6816–6854.

[14] Wu, Z.; Li, L.; Yan, J. M.; Zhang, X. B. Materials Design and System Construction for Conventional and New-Concept Supercapacitors. *Adv. Sci.* **2017**, *4* (6), 1600382.

[15] Cavaliere, S.; Subianto, S.; Savych, I.; Jones, D. J.; Rozière, J. Electrospinning: Designed Architectures for Energy Conversion and Storage Devices. *Energy Environ. Sci.* **2011**, *4* (12), 4761–4785.

[16] Chidembo, A. T.; Ozoemena, K. I.; Agboola, B. O.; Gupta, V.; Wildgoose, G. G.; Compton, R. G. Nickel (II) Tetra-Aminophthalocyanine Modified MWCNTs as Potential Nanocomposite Materials for the Development of Supercapacitors. *Energy Environ. Sci.* **2010**, *3* (2), 228–236.

# Chapter 1

# Introduction

Electrocatalytic phenomena play central roles in energy conversion and storage, sensing clinically and biologically relevant substrates, environmental sector, electroorganic synthesis etc.; which are primarily responsible for the intensive efforts in understanding their structure-activity relations. Among the class of various electrocatalysts, $N_4$ macrocyclic systems such as phthalocyanines and porphyrins have been extensively explored as potential non-precious molecular catalysts for a wide variety of electrochemical applications because of their tunable optoelectronic properties and high thermal and chemical stabilities. They have been utilized as promising molecular electrocatalysts in fuel cells, batteries and electroorganic synthesis, as sensitizers in photocatalysis and solar cells, as electrical transducers in sensors and biosensors, and as molecular charge storage platforms in energy storage devices.[1-6] Given the fundamental and technological relevance of such molecular architectures, comprehending their structure-activity relations are of particular importance. This chapter provides an overview on $N_4$ macrocyclic systems with a special emphasis on their electrochemical aspects such as electrocatalysis and charge storage and highlights the inadequacies and knowledge gap existing in their structure-activity relations. Our approach based on electrochemical and spectroscopic analyses and density functional theory calculations has led to the uncovering of an isomerism-activity relation in molecular electrocatalysis and molecular charge storage which in turn deepen the understanding of their structure-activity relationships.

## 1.1. $N_4$ macrocyclic metal complexes

Metalloporphyrins (MPs) and metallophthalocyanines (MPcs) (Figure 1.1) are important molecules belonging to a class of transition metal complexes known as $N_4$ macrocyclic metal complexes ($MN_4$).[1,7,8] The unique physical, chemical, and spectral properties of this class of compounds along with the diversity in their structural features are significant factors governing their importance and utility in an impressive list of potential applications. They are 18 $\pi$-electron aromatic macrocycles exhibiting rich optical, photochemical, coordination, catalytic, and electrochemical properties.[7] The rich and

reversible redox chemistry of $N_4$ metal macrocyclic complexes allied to the several strategies for immobilizing them on the surfaces of different types of electrode surfaces have opened up innumerable possibilities of using these molecules as potential candidates in various electrochemical applications. Phthalocyanines [1,7] (Figure 1.1) have also been proposed as convenient molecular models for the study of the physicochemical properties of naturally occurring tetrapyrrolic macrocycles due to their structural similarities. For these reasons, there have been great interests in both artificial and naturally occurring $MN_4$ complexes in various fields, including electrochemistry.[7]

The basic porphyrine ring is formed by the cyclization of four pyrrole rings through methine (=CH–) bridges, whereas the phthalocyanine ring has imine (=N–) bridges and a benzene ring fused to the 3, 4 - positions of the pyrrole rings.[7] In both porphyrins and phthalocyanines, the pyrrole nitrogen atoms are turned inward generating a square planar coordination site with four-fold axial symmetry which provide them the capability to chelate with ions of various elements.[7,9,10] These strong equatorial bonds favor the delocalization of metal electronic density throughout the macrocyclic π-system imparting large effects on the axial ligands for e.g., the reacting species binding to the central metal ion, thereby activating them for both catalytic and electrocatalytic processes.[7,10, 11] Indeed, the strong equatorial bonding weakens the axial ligands making them more labile which in turn enhances the turnover number. The presence of more electronegative nitrogen atoms at the meso-positions and the expanded π- aromatic system of phthalocyanines diminish the basicity of inner nitrogen atom lone pairs, which is also known to impart distinct electronic, charge transfer, and redox properties to the metallated phthalocyanines.[7,11]

The basic structure of $N_4$ macrocyclic systems can be modified by incorporating substituents to the ring periphery as shown in Figure 1.1. Phthalocyanines can be substituted at the fused benzene ring carbon atoms (secondary sphere) whereas porphyrin presents two possibilities as shown in Figure 1.1., i.e. (a) substitution at the meso- and or (b) substitution at the beta pyrrolic positions. The substituents can be tailored in order to impart additional specific physicochemical properties, for controlling the interactions and the behavior of those macrocyclic derivatives.[7,10] In fact, biological systems are the best examples of how their structures should be engineered and organized in more complex systems in order to generate functional molecular machines.[7]

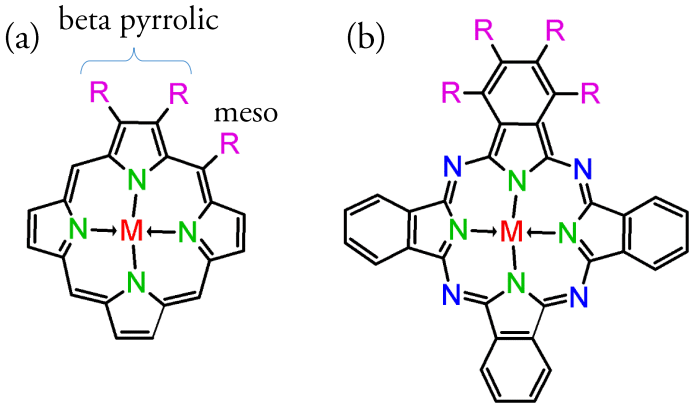


**Figure 1.1:** The molecular structures of (a) metalloporphyrin (MP) and (b) metallophthalocyanine (MPc) complexes. Basic structures showing the square planar site available for coordination with a metal ion "M" and the ring substitution positions in the porphyrine (meso and beta-pyrrolic) and phthalocyanine rings.

The metallophthalocyanines are purely synthetic molecules that show strong structural resemblance with the metalloporphyrins.[7] They display a low flexibility of the macrocycle ring caused by the extensive unsaturation, as shown in Figure 1.1 and also an enhanced electron delocalization in the molecular structure. Owing to the increased thermal stability and solubility, improved electronic conductivity and architectural flexibility, phthalocyanines are able to function as efficient electron transfer mediators which in turn make them as one of the highly studied macrocyclic and coordination compounds.[1,7,8] For aforementioned reasons, phthalocyanines have emerged as attractive molecular platforms for energy conversion, green synthesis and electrochemical sensing, as promising sensitizers for photocatalysis and solar cells, and as excellent electrode materials for electrochromic applications.[3,12–15]

### 1.1.1. Phthalocyanines (Pcs)

Phthalocyanines [8,16-18] were discovered in 1928, and from that point on, these engineered analogues of the naturally occurring porphyrins/phthalocyanines have been the subject of extensive investigation in numerous distinctive research fields.[19, 20] Pcs are planar aromatic macrocycles consisting of four isoindole sub-units showing an delocalised 18 π electron aromatic cloud over an arrangement of alternated nitrogen and carbon atoms. Various metal Pcs substituted by tetra, octa and 16 were synthesized by replacing the

peripheral hydrogen atoms at the secondary sphere of the phthalocyanine molecules by functional groups like $NH_2$, $NO_2$, $Cl^-$, $Br^-$, $F^-$, COOH, $SO_3H$, $CH_3$, etc.[21-26] The central metal ions (Co, Fe, Ni, Cu, etc.,) in unsubstituted and substituted metal phthalocyanines are bonded with nitrogen atoms of the isoindole units as shown in Figure 1.2.

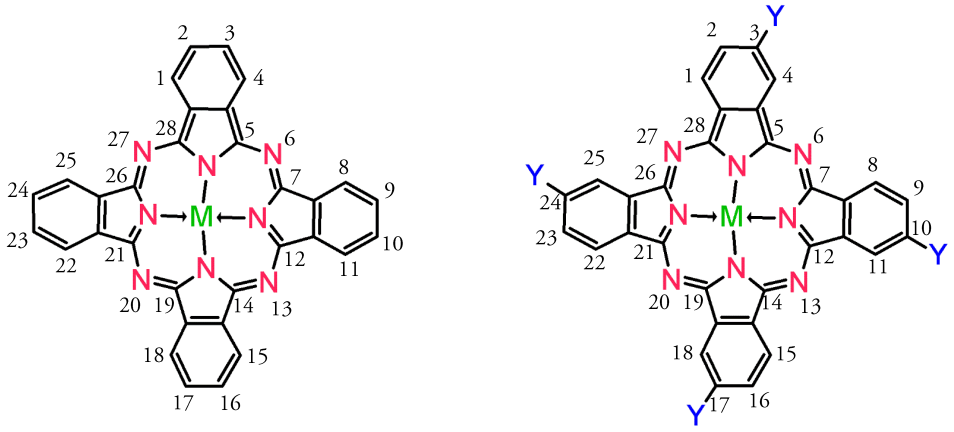

Unsubstituted metal phthalocyanine  Substituted metal phthalocyanine

M = Co, Fe, Ni etc.,
Y = $NO_2$, $NH_2$, SH, COOH, OR etc.,

**Figure 1.2:** The molecular structure of the unsubstituted and substituted metal phthalocyanine with numbering of constituent atoms.

While the structure of Pcs appears to be very complex, it was primarily synthesized from their corresponding ligands in a single-step reaction.[1,8,16] Unlike metalloporphyrins, phthalocyanine complexes are seldom obtained from an available phthalocyanine ligand. More often, the complex is formed from precursors via a metal-templated cyclotetramerization reaction.[7] It is well known that the addition of substituents to the secondary sphere of phthalocyanines in order to improve their properties is easier to achieve using appropriately substituted starting materials rather than adding them to a pre-existing macrocycle.[7,8,11,15-18] The mechanism of this condensation reaction has been examined which probably involves a stepwise polymerization of phthalocyanine precursors or reactive intermediates followed by coordination of the central metal ion and ring closure to the macrocycle.[7,17,27,28] Ring closure is driven by the template effect of the central metal ion, the inherent stabilization this type of coordination achieves and also added aromaticity involved in the formation of the phthalocyanine macrocycles.[7] The aromatic character of the phthalocyanine system is clearly demonstrated by its magnetic anisotropy, which is 15 times larger than that of benzene.[7,29] Unsubstituted and substituted phthalocyanines as

shown in Figure 1.2 can be prepared from aromatic ortho-dicarboxylic acid derivatives, phthalonitriles, phthalic anhydrides, phthalimides, diiminoisoindolines and 2-cyanobenzamides etc., Scheme 1.1.[30-36]

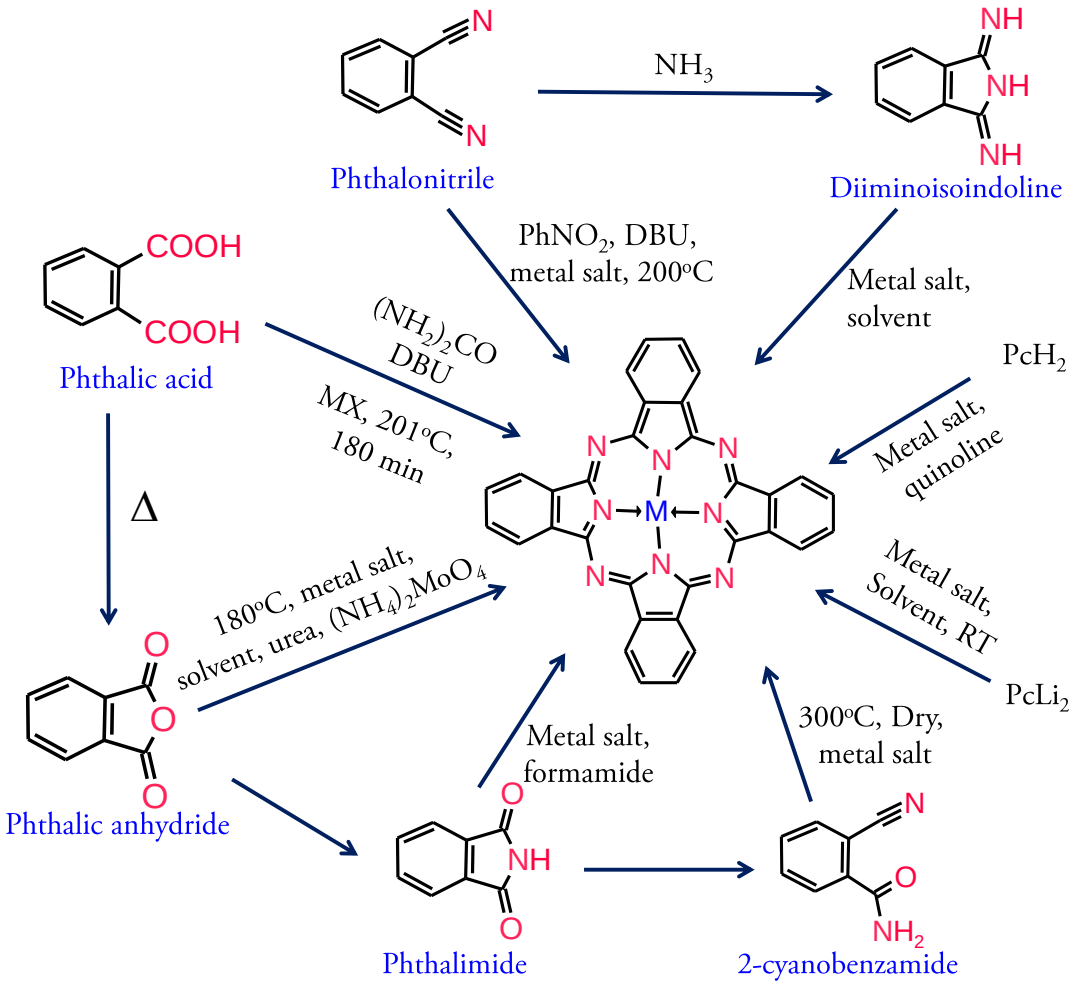


**Scheme 1.1.** Various routes for the synthesis of metal phthalocyanines. $PcH_2$ and $PcLi_2$ are non metallated phthalocyanine and dilithium phthalocyanine.

### 1.1.2. Properties of phthalocyanines

In the context of coordination chemistry the phthalocyanine (Pcs) molecules are one of the prominent ligand. One of the distinctive properties of Pcs is their rich redox behaviour, which is primarily due to the extended network of conjugated electrons (eighteen of which are aromatic) which are delocalized over four isoindoline units bridged by eight azamethines in the Pc macrocycle (Figure 1.2).[7] With such a stable electronic conformation, the Pc macrocycle cannot undergo many reactions other than redox or substitution reactions in which electrons or hydrogen atoms are exchanged respectively by suitable oxidizing/reducing agents[7,15] or electrophilic/nucleophilic reactants.[7,37] Additions and ring opening are

very rare reactions for the Pc ring because they would require drastic conditions which lead mostly to a disruption of the Pc skeleton.[38-40] On the other hand, reactions which do not alter the aromatic character of Pc's, e.g. acid-base reactions[41-43] or transformations of the central metal ion,[44-46] are more commonly encountered.

In the field of electrochemical applications what makes Pcs outstanding are their interesting electrical properties, thermal and chemical stabilities and tunable optoelectronic properties.[4,6,47,48] Their redox processes are often very fast involving minimal reorganizational energies and they can function as redox mediators in electron transfer processes involving a great variety of substrates.[15,49,50] Another notable feature is their flexibility; more than 70-80 metals can be transferred from the two hydrogen atoms of the central cavity and various alternatives can be combined in the secondary sphere positions of the $N_4$ macrocycle, thus allowing their electronic properties to be fine-tuned. These versatility in their structural modifications transform them as potential candidates for the development of non-precious molecular platforms especially in the field of energy conversion/storage, green chemistry, electrochromic windows and sensing applications.[1-3,5] The rich electrochemistry of Pcs also broadens the applicability of this sort of $N_4$-macrocycles in electrochemical capacitors for charge storage applications[51-55] which can be tuned through the linkage with appropriate functional units. It is to be noted that the relation between electrocatalysis and the nature of the secondary sphere ($N_4$ macrocycle) functionality is reasonably understood well. For example, electron withdrawing or electron donating nature of the secondary sphere substituents at the $N_4$ macrocyclic ligand is known to tune the activity of the central metal ion towards electrochemical reactions by modulating the electronic arrangement in the molecule.[1-3,5,50-58]

## 1.2. Metal phthalocyanines as electrocatalysts

The utilization of fossil fuels such as coal, petroleum and common gas regardless of the severe energy crisis and environmental pollution postures incredible challenges to the planet.[59-62] Hence, the development of environmental-friendly and powerful next-generation clean energy systems for the modern world becomes a dominant target. Electrochemical energy conversion/storage systems such as fuel cells, metal-air batteries, water splitting devices, and $CO_2$ reduction technology into electricity, should be considered

as a pledge by candidates to address these challenges. Figure 1.3 shows possible sustainable pathways for the production of essential fuels and chemicals, including hydrogen, hydrocarbons, oxygenates, and ammonia can be modified or worked in conjunction with a conventional energy sequence, producing sustainable paths.[60] If electrocatalysts with the required properties can be developed, universal ingredients of water, carbon dioxide, and nitrogen from the earth's atmospheres could potentially be converted into the aforementioned substances by the combination of electrochemical processes with renewable vigorous.[60] Due to the multi electron transfer nature of many these reaction pathways, the reaction chemistry often suffer from sluggish kinetics and catalyst poisoning. Therefore, high efficiency and low-cost electrocatalyst capable for activating the electrochemical transformations at lower overpotential (driving force) with advanced selectivity are required per hour. Therefore, the electrocatalysts have a vital role to play in renewable energy landscape.[61,62]

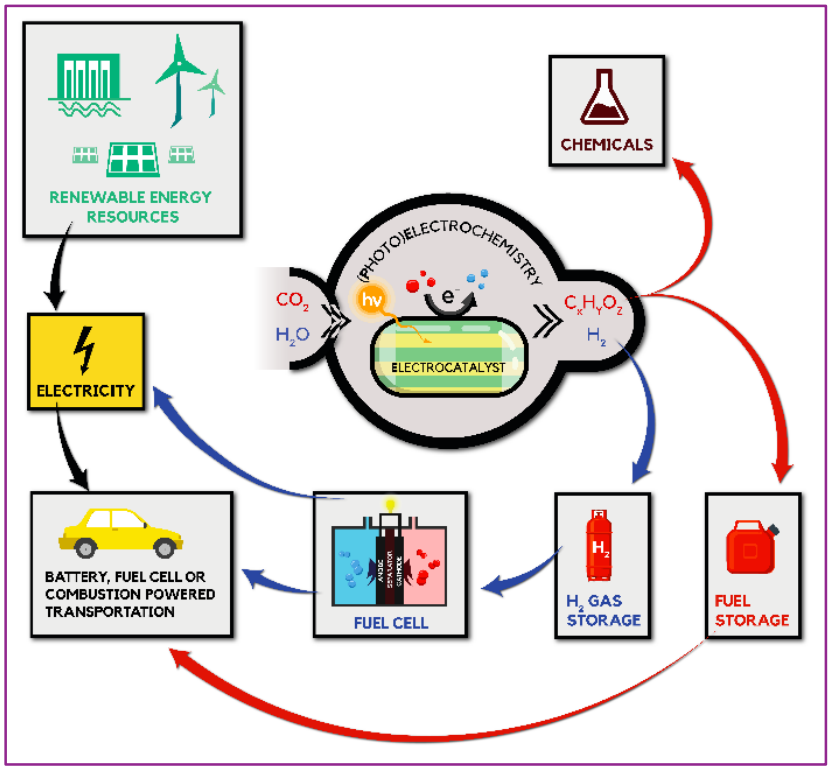


**Figure 1.3:** Schematics of a sustainable energy landscape routed via electrocatalysis.

Electrochemical reactions often require a substantial overpotential [63] to proceed at an appreciable rate. This is particularly true when the reaction does not consist of an outer-sphere electron transfer without significant bond rearrangements but consists of a path with

bond breaking and bond formation, involving several reactants and products, which may trigger the uptake/release of additional electrons, as sketched in Scheme 1.2.

$$aA + bB + \ldots. \pm ne^- \rightleftharpoons cC + dD + \ldots.$$

For example:

$$O_2 + 4e^- + 4H^+ \rightleftharpoons 4H_2O$$

$$H_2 + 2e^- \rightleftharpoons 2H^+$$

**Scheme 1.2:** General electrochemical reaction pathway involving uptake or release of additional electrons. Oxygen reduction reaction pathway and hydrogen oxidation pathway are shown as representative examples for multielectron electrochemical pathways.

In such situations, catalysis of the electrochemical reaction is sought to increase the reaction current, at a potential as close as possible to the equilibrium potential.[64] The term electrocatalysis is traditionally used for reactions involving metals which are chemically involved in the catalytic process.[64,65] Although the chemical properties of the electrode material play an important role in governing the catalytic efficiency, geometric and crystallographic features and nature and number of defects, are also known to influence electrocatalysis.[64-66] The catalysis and electrochemistry communities have created volcano plots based on thermodynamic properties, for the rapid analysis of large data sets intending to comprehend many aspects of the electrocatalysis. The volcano plot for exchange current density ($j_0$) as a function of Gibb's free energy change in adsorption/desorption step (eg. $\Delta G_{H^+}/\Delta G_{OOH+}$) for most of the electrochemical transformations suggests that platinum based electrocatalysts are the benchmark electrocatalyst.[67-69]

There are various types of electrocatalysts available like metal surface or metal nanoparticles,[70-72] coordination complexes (molecular), enzymes etc.[2,5,47,73] Noble-metal-based materials are identified as state-of-the-art electrocatalysts for a variety of electrochemical reactions,[71] for example, platinum (Pt) based materials are utilized as potential electrocatalysts toward oxygen reduction reaction (ORR),[74-76] hydrogen evolution reaction (HER) and hydrogen oxidation reaction (HOR).[77-79] Further, ruthenium (Ru)/iridium (Ir) oxide is known as the benchmark catalyst toward oxygen evolution reaction (OER).[80-83] Similarly gold (Au) and silver (Ag) have been utilized to catalyze $CO_2$ reduction reaction ($CO_2RR$).[84-86] However, the metal-based electrocatalysts

have disadvantages such as limited reserves in the earth, low selectivity, insufficient durability and high-price during the operation which greatly limit their broad-scale penetration in renewable energy technologies. Therefore, the development of cost-effective earth-abundant electrocatalysts with high activity and durability is a key step for the practical use of clean energy technologies.[71,87-89]

Recent studies have demonstrated that in noble metal based electrocatalysts, an increased number of catalytically active sites and more exposed active surface areas can be engineered by diminishing the size of catalyst particles.[71] It is also reported that the catalysis can be enhanced through interfacial modifications and exposing highly reactive crystal planes.[90-93] Downsizing the catalyst particles to the level possible (e.g. near to the atomic level) offers an effective way to realize maximum utilization efficiency of the metal and improve the intrinsic catalytic activity of the electrocatalyst.[71,94] In order to reduce or replace the dependence of renewable energy landscapes on the use of noble metal-based electrocatalysts, such molecular electrocatalysts have been the subject of tremendous efforts over the past decades to develop non-noble transition metal-based electrocatalysts [95] The challenges in harvesting and storing renewable energy provide strong motivation for the exploitation of non-precious molecular electrocatalysts, for effecting the transformations of substrates such as $H_2O$, $H_2$, $O_2$, $H^+$ and $CO_2$.[96-100] As of now, these transformations are mediated by an ever-growing number of molecular catalysts, and primary attention has been invested to understand their structure-activity relations, which is considered important for the design of improved molecular electrocatalysts.[7,47,60,73,74,101,102]

The family of molecular electrocatalysts such as MPcs ($N_4$ macrocyclic framework) and MPcs supported on carbon and other graphitic structures have been widely investigated as viable non-precious molecular electrocatalysts for a wide range of electrochemical reactions ranging from energy conversion to biosensing.[103-105] For example, these electrocatalysts are capable of catalyzing the electrooxidation of carbon monoxide, glucose, and nitrogen monoxide; as well as the electro reduction reactions of molecular oxygen, hydrogen peroxide, molecular nitrogen and nitrate.[7,106-111] In addition to their technological relevance, these metal-based phthalocyanines prove to be good examples to reveal the relation between their electrochemical properties and structure.[7,50]

In the context of contemporary energy challenges, important signs of progress have

been made in recent years in understanding structure-activity relations of molecular electrocatalysts.[71] This has led to the development of tools for catalyst benchmarking which has opened the way for the intelligent design of new molecular electrocatalysts.[71] In its molecular form (Figure 1.2), the MPc molecules contain a central metal ion and surrounding N-containing ligand groups.[7] The central metal ion is linked to the ligands through metal-nitrogen bond formation so that its electronic structure can be modulated by the ligand groups.[7] Therefore, the electrocatalytic activity of the MPcs could be tuned by varying the central transition metal ion and modifying the secondary sphere ligands as highlighted previously.[7,24,112,113] Large amounts of studies have been devoted to tuning the nature of substituents on the secondary sphere of MPcs to enhance their electrocatalytic performance.[56-58,114-116] For faradaic electrochemical transformations, the metal centre is the active site whose activity can be controlled by the electronic effect of secondary sphere substituent (electron-donating/electron withdrawing). It is known that the nature of the substituent tunes the electron density at the active metal centre by activating the catalyst towards reduction/oxidation reactions. For example, Chuan Li et.al demonstrated that the electron-withdrawing sulfonic functionality activates the molecule as an effective bifunctional electrocatalyst for oxygen reduction reaction (ORR) as well as oxygen evolution reaction (OER).[117] Valentin Rodionov et al., demonstrated that immobilized perfluorinated cobalt phthalocyanine (CoFPc) acts as an efficient molecular heterogeneous catalyst for water oxidation in phosphate buffer at neutral pH.[118] Tetra-substituted 4-(2-mercaptoquinoline phthalocyaninato) Co(II) (CoPcSHQn) and 4-(2-phenoxy-4-trifluoromethylpyridine phthalocyaninato) Co(II) (CoPcOHPy) were explored for the electrochemical oxidation of L-cysteine,[119] and self-assembled monolayer of tetracarboxylic acid-functionalized cobalt (II) phthalocyanine were demonstrated as a biosensor for glucose detection in presence of cysteine, uric acid and oxalic acid.[120] Philani Mashazi and Tebello Nyokong reported that cobalt/manganese tetra amino phthalocyanine complexes catalyze the 2 electron reduction of $H_2O_2$ under physiological conditions.[121] Min Wang et.al reported that by substitution with a positively charged trimethyl ammonium group and three tert-butyl groups on a cobalt phthalocyanine macrocycle, an efficient electrocatalyst for the selective reduction of $CO_2$ to CO in water can be obtained.[122] Xing Zhang et.al showed the ability of electron-withdrawing cyano substituted cobalt phthalocyanine towards $CO_2$ reduction in aqueous

solutions.[123] Elif Turker Acar et.al demonstrated that mono (pyridine-4-oxy)-tri(tert-butyl) phthalocyaninato Co (II) and mono (pyridine-4-oxy)-hexa(hexyl)phthalocyaninato Co (II) as efficient electrocatalysts for ORR[124] İbrahim Özçeşmeci et.al reported an electrocatalytic hydrogen evolution reaction catalyst with a cobalt (II) phthalocyanine system bearing four cobaloxime moieties.[125] Li Cui, Ying Liu and Xingquan He showed the interesting application of amino-functionalized iron (II) phthalocyanine in direct methanol fuel cells.[126] In particular, deciphering the relationship between substituent's electronic effects within a family of molecular catalysts towards their electrochemical properties have been one of the important achievements.[71,117-126]

Furthermore, it has been found that heat treatment processes of a mixture of metal macrocyclic molecules and carbon materials can improve both the activity and durability of the attained MPc/C composites.[71] For example, Jahnke et al.[7,127] showed that heat treatment had a significant effect on the catalytic activity of carbon-supported CoTAA (colbalt-dihydrodibenotetraazaannulene) for ORR. They found that all the heat-treated CoTAA samples had better catalytic performance than untreated ones for ORR. Moreover, Chu et al. prepared their catalysts by heat-treating a series of single transition metalloporphyrins (metals: V, Mn, Fe, Co, Ni, Cu, and Zn) and a combination of two transition metalloporphyrins (systems: V/Fe, Co/Fe, Ni/De, and Cu/Fe). They found that the heat-treated FeTPP/CoTPP was the best catalyst for ORR which was also methanol-tolerant.[7,128] Also, functional carbon nanostructures (such as reduced graphene oxide and carbon nanotubes (CNT)) have been used as the substrates for $MN_4$ macrocyclic complexes to improve their catalytic performance. In particular, different graphene/MWCNT macrocyclic complex composites assembled via π–π interaction were characterized and evaluated for their electrocatalytic properties.[7,129-131]

Taken together, the foregoing discussion highlights that the electrocatalytic properties of metal phthalocyanines/porphyrins molecules toward a variety of electrochemical transformation can be tuned by the nature of the secondary sphere functionality as well as by the nature of the support material.

## 1.3. Metal phthalocyanines as supercapacitors

In a different direction, researchers have widely investigated metallophthalocyanine

(MPc) complexes ($N_4$- macrocyclic metal compounds) as electrode materials for designing molecular supercapacitors.[52-54,132-140] A supercapacitor differs from a capacitor in terms of the amount of energy that can be stored. A supercapacitor has a capacity value higher than conventional parallel plate capacitors, so a high-capacity capacitor bridges the gap between conventional capacitors and rechargeable batteries.[141-144] It can, in general, store 10 to 100 times more energy per unit volume or mass than capacitors and can be utilized for loading and delivering much faster than batteries, and can withstand many more charge and discharge cycles than rechargeable batteries.[145,146] A supercapacitor typically employs porous carbon material as electrodes and electrostatically stores the charge. Supercapacitors are employed in applications where instant power is required. They are further classified into two types depending upon the charge storage mechanisms, 1) Electrochemical Double Layer Capacitors (EDLCs) and 2) Pseudocapacitors.

It should be noted that the charge storage is primarily surface-confined in electrochemical capacitors as opposed to the bulk charge storage in batteries. This is directly responsible for the well-known energy deficiency of high power supercapacitors and moderate power capability of high energy batteries and high energy and high power supercapacitors are future generation electrochemical devices.[147-154] Since there exists a direct relationship between energy density and surface charge density in electrochemical capacitors, next generation supercapacitors with high energy density are conventionally targeted in solid systems by maximizing their surface to volume ratio.[147-150] In molecular systems such as $N_4$ macrocyclic complexes, there have been a few demonstrations on improving their charge storage capability by the nature of the secondary sphere functionality. Also, functional carbon nanostructures such as graphene and CNTs have been used as the surfaces for anchoring $MN_4$ macrocyclic complexes to improve their overall charge storage properties.[52-54, 132-140]

For example, Chidembo et al., reported that the nickel (II) tetra-aminophthalocyanine (NiTAPc) modified multi-walled carbon nanotubes (MWCNTs) as potential nanocomposite materials for the development of supercapacitors in 1 M $H_2SO_4$ and a maximum specific capacitance of 981 ± 57 $F.g^{-1}$ (200 ± 12 $mF.cm^{-1}$), a maximum power density of 700 ± 1 $W.kg^{-1}$, and a maximum specific energy of 134 ± 8 $Wh.kg^{-1}$ were obtained for the composite electrodes. When compared to MWCNTs modified with

unsubstituted nickel(II) phthalocyanine (MWCNT-NiPc) or nickel(II) tetratert-butyl phthalocyanine (MWCNT-tBuNiPc), MWCNT-NiTAPc exhibited superior supercapacitive behaviour, possibly due to the influence of nitrogen-containing groups on the phthalocyanine rings.[52] Chidembo and Ozoemena, also reported the supercapacitive properties of the electropolymeric nickel tetraaminophthalocyanine (poly-NiTAPc) supported on MWCNTs which demonstrated repetitive charge discharge cycles of over 1000 without detectable deterioration in the stability.[132] Composites of cobalt based phthalocyanines with MWCNTs and nickel based phthalocyanines with graphene based electrodes were reported to demonstrate superior charge storage capability.[133,134] Ultrahigh specific capacitance was demonstrated with an electrode architecture prepared by covalently and homogenously functionalized graphene with iron tetraaminophthalocyanine.[135] The superior performance was attributed to facile charge and ionic transport due to the structural and functional synergy of the covalently bound components, giving rise to a zwitterionic surface with extensive π–π stacking. Recently, outstanding cycling stability and a high areal capacitance were observed with copper phthalocyanine based 2D metal-organic framework nanosheets.[136] In similar lines, researchers have explored the charge storage in various metallophthalocyanine complexes and these demonstrations undeniably signal their potential to excel as electrodes for supercapacitive charge storage.[53,54,138-140]

In summary, to date, MPcs have been successfully incorporated as active components for electrochemical applications such as electrocatalysis and charge storage. The foregoing discussion highlights that the electrochemical properties of phthalocyanine molecules depend on the type of the central metal ion and the structure of the ligand. The discussion provided here serve as only demonstrative examples in the vast electrochemistry literature of metal phthalocyanines with the conclusion that their electrocatalytic activities and charge storage capabilities can be tuned by the nature of the secondary sphere functionality as well as by the nature of the support material.

## 1.4. Aim and scope of the thesis

As discussed, MPc molecules have been utilized as electrodes for catalyzing various electrochemical transformations and charge storage applications.[53,54,138-140] The

electrocatalytic and supercapacitive properties of phthalocyanine molecules depend on the metal and the complex ligand framework, which in turn provide an extra handle to tune their activity via nature of the functionality at the secondary sphere of phthalocyanine molecules.[24,112,113] It has been well established that nature of functionalities at the $N_4$ macrocycle affects the electronic arrangement and consequently; its electrocatalytic activity.[117-126] However, in the context of electrocatalysis far too little attention has been paid to the fact that this electronic arrangement is not only a function of their chemical identity across the spectrochemical series, but also can be a function of their isomerism. The existing accounts fail to make any distinction between the chemical identity of groups and their isomerism in molecular electrocatalysis and to the best our knowledge, no research has been found that surveyed and understood isomerism-electrocatalytic activity relation with respect to MPc molecules. In the context of charge storage by MPc molecules, as highlighted previously a few reports suggest that the nature of secondary sphere functionality improves their charge storage capability.[52] Also, supercapacitive charge storage by MPc molecules were noticeably improved when carbon materials such as graphene and CNTs were used as anchoring substrates.[133,134] With regard to molecular systems, though the nature of the functionality in the secondary sphere of MPcs provides an extra handle to control their supercapacitive performance, a lack of in-depth understanding exists in defining what controls their structure-charge storage relationship. Therefore, the primary aim of this thesis is to draw a distinction between the nature of groups and their isomerism in molecular electrocatalysis and molecular charge storage and fill the knowledge gap in their structure-activity relation. The molecular structures of the isomeric molecules of metal phthalocyanines used in this investigation to comprehend the isomerism-activity relationship are shown in Figure 1.4. This thesis is specific to regioisomers of substituted metal phthalocyanines (MPcs) when substituents are effect at the $\alpha$ and $\beta$ positions on the $N_4$ macrocycle of the molecule (Figure 1.4). The primary focus of this investigation is to understand how the geometric and electronic factors of substituents at the $N_4$ macrocycle of molecular architecture as a results of functionality's isomerism affect charge storage and electrocatalysis of challenging electrochemical transformations.

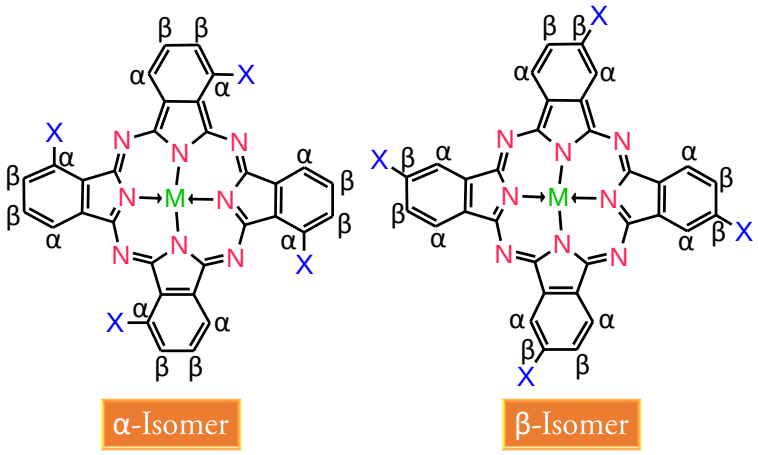


X = $NO_2$, $NH_2$, SH, COOH, OR etc.,
M = Co, Fe, Ni, Cu, Zn etc.,

**Figure 1.4:** Molecular structure of tetra-substituted regioisomers of metal phthalocyanines. α and β positions are labelled on the $N_4$ macrocycle.

Towards this direction, regioisomers of metal phthalocyanine molecules bearing various secondary sphere functionality are synthesized and characterized. In the working chapters to follow, the independent role of isomerism over its chemical identity in tuning molecular electrocatalysis and molecular charge storage via non-covalent interactions like hydrogen bonding, repulsive and attractive field-effect, etc., are explained.

Chapter wise details are provided below.

**Chapter 1** provides a general introduction about the $N_4$ macrocyclic complexes with particular emphasis on their electrochemical properties. Detailed discussions are provided for their important roles in various electrocatalytic reactions and supercapacitive charge storage applications. The role of the nature of the secondary sphere functionality in tuning the molecular electrocatalysis and molecular charge storage is highlighted in the context of published literature. At the end of Chapter 1, the aim and objective of the present research work is explained.

**Chapter 2** explains the synthesis of $–NO_2$ and $–NH_2$ substituted isomeric phthalocyanine molecules and unsubstituted phthalocyanine molecules. The fabrication of carbon supported molecular platforms for applications ranging from electrocatalysis, electrochemical sensing and molecular charge storage are further elaborated. Further, the electrochemical and other physico-chemical techniques used for the characterization of the synthesized compounds are provided.

**Chapter 3** shows how the isomerism of electron withdrawing $–NO_2$ substituent at the secondary sphere of MPc molecule tunes the catalytic metal center towards oxidative electrocatalytic reactions of immense technological and environmental significance. Towards this direction, the role of isomerism of electron withdrawing $–NO_2$ functionality on a cobalt phthalocyanine molecular electrocatalyst (CoPc) is investigated for various electrochemical transformations ranging from energy conversion to biosensing. Detailed discussion based on electrochemical analyses, spectroscopic investigation and theoretical calculations are provided on how the catalytic activation of the metal center is achieved when regioisomerism of the $–NO_2$ substituent is conferred at the α and β positions on the $N_4$ macrocycle. These studies demonstrate that substituent's isomerism in CoPc molecular catalyst conjoins molecular planarity and catalytic activation through competing field effects and resonance effects.

**Chapter 4** discusses how this isomerism-activity relation in oxidative electrocatalysis, can be exploited to design a non-precious sensing platform for the detection of arsenic via the direct oxidation of arsenic (III) to arsenic (V). In plane conformation of the $–NO_2$ functionality with respect to the $N_4$-macrocycle in the β-$NO_2$ CoPc isomeric molecule (Figure 1.4) activated the central cobalt ion noticeably via a cumulative influence of resonance and inductive effects, which in turn enhanced the kinetics of direct oxidation of As (III) to As (V). This isomerism induced activation of catalytic metal centre is utilized to design a non-precious electrochemical sensing architecture for arsenic sensing with experimental detection limit close to WHO guidelines.

**Chapter 5** discusses how the regioisomerism of electron-donating $-NH_2$ substituent on the $N_4$ macrocyclic phthalocyanine ligand influences reductive electrocatalysis. This investigation proves that intramolecular H bonding in the α-$NH_2$ CoPc isomeric molecule activated the central cobalt ion towards oxygen reduction reaction (ORR) and changed its mechanistic pathway via a 4 electron route with respect to the corresponding β-$NH_2$ CoPc isomeric molecule where it primarily followed a 2 electron ORR route. Therefore, isomerism induced activation induce selectivity in molecular electrocatalysis which in turn provides a new approach in the design of efficient non-precious electrocatalysts for energy conversion (4 electron process) and peroxide production (2 electron process). These studies bring to light a crucial factor that is often overlooked in electrocatalysis that isomerism of substituents can

redefine the electronic arrangement in the catalytic center and make an additional contribution to electrocatalysis over its chemical identity.

**Chapter 6** deals with the molecular charge storage and discusses a molecular strategy for amplifying the density of charge storage pockets in electroactive metal macrocycles. Electrochemical, spectroscopic and theoretical investigations demonstrate that isomerism of amino functionality triggered attractive field-effect via intramolecular hydrogen-bonding which in turn suppressed the extent of protonation and consequently the electrochemical capacity of MPc molecule. When attractive field effect is inhibited by spatially separating the H-bonding groups via geometrical isomerism, electrochemical capacity of MPc molecule is significantly enhanced. Interestingly, repulsive field effect in nitro substitute isomeric MPc molecules leads only to a geometric rotation of the $-NO_2$ functionality which did not contribute to a disparity in their charge storage capability. Unveiling the subtle role of short-range interactions in conjoining the molecular charge storage with the nature as well as the isomerism of the functionality opens up an alternative pathway in the design of molecular supercapacitors to target their energy density without compromising the power capability.

**Chapter 7** concludes the current work and provides a future outlook.

Overall, the approach based on electrochemical and spectroscopic analyses and density functional theory calculations uncover an isomerism induced contribution in molecular electrocatalysis and molecular charge storage via non-covalent interactions such as H bonding interaction and attractive and repulsive field effects. This study makes major contributions to the research in molecular electrocatalysis and charge storage by establishing,

1) that isomerism of substituents makes an additional contribution to electrocatalysis and charge storage over its chemical identity

2) that this isomerism-activity relation varies across the spectrochemical series making this dependence strongly substituent specific. Often, non-covalent interactions interlink the electrochemical activation with the nature of substituents as well as its isomerism leading to interesting events in electrocatalysis and energy storage.

3) that prime considerations should be given to isomerism to make the maximum potential of the molecule available for electrocatalysis and charge storage.

## 1.5. References


[1] Zagal, J.H.; Bedioui, F.; Dodelet, J. P. *$N_4$-macrocyclic metal complexes.* Springer, New York. **2006**; volume 1; Energy.

[2] Wan, X.; Liu, X.; Li, Y.; Yu, R.; Zheng, L.; Yan, W.; Wang, H.; Xu, M.; Shui, J. Fe–N–C Electrocatalyst with Dense Active Sites and Efficient Mass Transport for High-Performance Proton Exchange Membrane Fuel Cells. *Nat. Catal.* **2019**, *2* (3), 259–268.

[3] Sorokin, A. B. Phthalocyanine Metal Complexes in Catalysis. *Chem. Rev.* **2013**, *113* (10), 8152–8191.

[4] Sobbi, A. K.; Wöhrle, D.; Schlettwein, D. Photochemical Stability of Various Porphyrins in Solution and as Thin Film Electrodes. *J. Chem. Soc., Perkin Trans. 2* **1993**, (3), 481–488.

[5] Rigsby, M. L.; Wasylenko, D. J.; Pegis, M. L.; Mayer, J. M. Medium Effects Are as Important as Catalyst Design for Selectivity in Electrocatalytic Oxygen Reduction by Iron-Porphyrin Complexes. *J. Am. Chem. Soc.* **2015**, *137* (13), 4296–4299.

[6] Bottari, G.; de la Torre, G.; Guldi, D. M.; Torres, T. Covalent and Noncovalent Phthalocyanine–Carbon Nanostructure Systems: Synthesis, Photoinduced Electron Transfer, and Application to Molecular Photovoltaics. *Chem. Rev.* **2010**, *110* (11), 6768–6816.

[7] Zagal, J.H.; Bedioui, F. (eds) *Electrochemistry of $N_4$-macrocyclic metal complexes.* Springer, New York. **2006**; volume 1-2.

[8] McKeown, N. B. *Phthalocyanine materials: synthesis, structure, and function*. Cambridge University Press, Cambridge. **1998**.

[9] Ishihara S, Labuta J, Van Rossom W, Ishikawa D, Minami K, Hill JP, Ariga K Porphyrin-based sensor nanoarchitectonics in diverse physical detection modes. *Phys Chem Chem Phys.* **2014**, *16* (21), 9713–9746.

[10] De La Torre, G.; Bottari, G.; Sekita, M.; Hausmann, A.; Guldi, D. M.; Torres, T. A Voyage into the Synthesis and Photophysics of Homo- and Heterobinuclear Ensembles of Phthalocyanines and Porphyrins. *Chem. Soc. Rev.* **2013**, *42* (20), 8049–8105.

[11] Leznoff CC, Lever ABP *Phthalocyanines, properties and applications*, Wiley, New York. **1997**; volume 4.

[12] De La Torre, G.; Claessens, C. G.; Torres, T. Phthalocyanines: Old Dyes, New Materials. Putting Color in Nanotechnology. *Chem. Commun.* **2007**, (20), 2000–2015.

[13] Kobayashi, N.; Konami, H.; Leznoff, C. C.; Lever, A. B. P. *Phthalocyanines: properties and applications*, VCH, New York. **1996,** volume 4.

[14] Milaeva, E. R.; Speier, G.; Lever, A. B. P. *The redox chemistry of metallophthalocyanines in solution.* Wiley, New York, **1992**, *pp 162–227*

[15] Leznoff, C. C.; Lever, A. B. P. *Phthalocyanines: properties and applications*, VCH Publishers, Cambridge. (**1989, 1993, 1996**), volume 1–4.

[16] Kadish K. M.; Smith K. M.; Guilard R. *The porphyrin handbook,* Academic, San Diego. **2003,** volume 16–20.

[17] Berezin, B. D. *Coordination Compounds of Porphyrins and Phthalocyanines.* John Wiley and Sons Ltd.: New York, **1981.**

[18] De la Torre, G.; Nicolau M.; Torres T. *Supramolecular photosensitive and electroactive materials.* In: Nalwa H. (ed) Academic, New York, **2001,** *pp 1-111.*

[19] De la Torre, G.; Vázquez, P.; Agulló-López, F.; Torres, T. Role of Structural Factors in the Nonlinear Optical Properties of Phthalocyanines and Related Compounds. *Chem. Rev.* **2004**, *104* (9), 3723–3750.

[20] Jiang, J.; Dennis, K. P. N. G. A Decade Journey in the Chemistry of Sandwich-Type Tetrapyrrolato-Rare Earth Complexes. *Acc. Chem. Res.* **2009**, *42* (1), 79–88.

[21] Kropf, H. Katalyse durch phthalocyanine - V autoxydation von cumol in gegenwart von vanadyl-phthalocyanin, *Tetrahedron Letters*, **1962**, *3(13)*, 577.

[22] Francisco Silva, J.; Griveau, S.; Richard, C.; Zagal, J. H.; Bedioui, F. Glassy Carbon Electrodes Modified with Single Walled Carbon Nanotubes and Cobalt Phthalocyanine and Nickel Tetrasulfonated Phthalocyanine: Highly Stable New Hybrids with Enhanced Electrocatalytic Performances. *Electrochem. commun.* **2007**, *9* (7), 1629–1634.

[23] Hirabaru, O.; Nakase, T.; Hanabusa, K.; Shirai, H.; Hojo, N.; Takemoto, K. Functional Metal-Porphyrazine Derivatives and Their Polymers. Part 1I.tSecondary

Fuel Cells based on Oxygen Reduction at a Platinum Electrode modified by Metal-2,9,16,23-Tet racarboxyphthalocyanine covalently bound to Poly(2-vinylpyridine-styrene) *J. Chem. Soc., Dalton Trans.* **1984**, (8), 1485-1489.

[24] Masa, J.; Ozoemena, K.; Schuhmann, W.; Zagal, J. H. Oxygen Reduction Reaction Using N4-Metallomacrocyclic Catalysts: Fundamentals on Rational Catalyst Design. *J. Porphyr. Phthalocyanines* **2012**, *16* (7–8), 761–784.

[25] Vasudevan, P.; Phougat, N.; Shukla, A. K. Metal Phthalocyanines as Electrocatalysts for Redox Reactions. *Appl. Organomet. Chem.* **1996**, *10* (8), 591–604.

[26] Preethi, N.; Shinohara, H.; Nishide, H. Reversible Oxygen-Binding and Facilitated Oxygen Transport in Membranes of Polyvinylimidazole Complexed with Cobalt-Phthalocyanine. *React. Funct. Polym.* **2006**, *66 (8)*, 851–855.

[27] Robinson, M. A.; Trotz, S. I.; Hurley, T. J. Complexes Derived from 1,3-Diiminoisoindolinecontaining Ligands. I. Deprotonation of 1,3-Bis(2-Pyridylimino)Isoindoline Complexes. *Inorg. Chem.* **1967**, *6* (2), 392–394.

[28] Gaspard, S.; Maillard, P. Structure of tetra tert-butylated phthalocyanines: mechanism of synthesis *Tetrahedron* **1987**, *43*(6), 1083-1090.

[29] Lonsdale, K.; Magnetic Anisotropy and Electronic Structure of Aromatic Molecules. *Proc. R. Soc. London. Ser. A - Math. Phys. Sci.* **1937**, *159* (896), 149–161.

[30] Byrne, T.; Linstead, R. P.; Lowe, A. R.; Phthalocyanines. Part II. The preparation of phthalocyanine and some metallic derivatives from o-cyanobenzamide and phthalimide. *J. Chem. Soc.*, **1934**, (0), 1017-1022.

[31] Dent, C. E.; Linstead, R. P. Phthalocyanines. Part IV. Copper phthalocyanines. *J. Chem. Soc.*, **1934**, (0), 1027-1031.

[32] Linstead, R. P. Phthalocyanines. Part I. A new type of synthetic colouring matters. *J. Chem. Soc.*, **1934**, (0), 1016-1017.

[33] Linstead, R. P.; Lowe, A. R. Phthalocyanines. Part V. The molecular weight of magnesium phthalocyanine. *J. Chem. Soc.*, **1934**, (0), 1031-1033.

[34] Barrett, P. A.; Frye, D.; Linstead, R. P. Phthalocyanines and associated compounds. Part XIV. Further investigations of metallic derivatives. *J. Chem. Soc.*, **1938**, (0), 1157-1163.

[35] Moser, F. H.; Thomas, A. L. Phthalocyanine Compounds. *J. Chem. Educ.* **1964**, *41*

(5), 245–249.

[36] Liu, J. N.; Chen, Z. R.; Yuan, S. F. Study on the Prediction of Visible Absorption Maxima of Azobenzene Compounds. *J. Zhejiang Univ. Sci.* **2005**, *6B* (6), 584–589.

[37] Hanack, M.; Lang, M. Conducting Stacked Metallophthalocyanines and Related Compounds *Advanced Materials,* **1994**, 6(11), 819-833.

[38] Nath, A.; Prushan, M. J.; Gilbert, J. G. Can super-excited molecules survive fragmentation? J. *Radioanal. Nucl. Chem.* **2001**, 247, 589.

[39] Lalande, G.; Côté, R.; Tamizhmani, G.; Guay, D.; Dodelet, J. P.; Dignard-Bailey, L.; Weng, L. T.; Bertrand, P. Physical, Chemical and Electrochemical Characterization of Heat-Treated Tetracarboxylic Cobalt Phthalocyanine Adsorbed on Carbon Black as Electrocatalyst for Oxygen Reduction in Polymer Electrolyte Fuel Cells. *Electrochim. Acta* **1995**, *40* (16), 2635–2646.

[40] Eley, D. D.; Hazeldine, D. J.; Palmer, T. F. Mass spectra, ionization potentials and related properties of metal-free and transition metal phthalocyanines *J. Chem. Soc., Faraday Trans.* 2 **1973**, *69*, 1808.

[41] Weitman, H.; Schatz, S.; Gottlieb, H. E.; Kobayashi, N.; Ehrenberg, B. Spectroscopic Probing of the Acid-Base Properties and Photosensitization of a Fluorinated Phthalocyanine in Organic Solutions and Liposomes. *Photochem. Photobiol.* **2007**, *73* (5), 473–481.

[42] Nagao, K.; Kayo, A.; Tetsuo, O. Some Spectroscopic, Electrochemical and Spectroelectrochemical Properties of Tetrapyrazinoporphyrazine and Its Iron and Cobalt Complexes. *Anal. Sci.* **1990**, *6 (3)*, 449–453.

[43] Gaspard, S.; Viovy, R. Protonation of phthalocyanines. III-Case of free phthalocyanine: $H_2Pc$ *J. Chim. Phys.,* **1981**, *78*, 851-853.

[44] Schneider, T.; Heckmann, H.; .Barthel, M.; Hanack, M. Synthesis and Characterization of Soluble Chloro- and Aryl(naphthalocyaninato)indium(III) Complexes and Their Precursors. *Eur. J. Org. Chem.* **2001**, *2001*(16), 3055-3065.

[45] Cook, M. J.; Dunn, A. J.; Howe, S. D.; Thomson, A. J.; Harrison, K. J. Octa-alkoxy phthalocyanine and naphthalocyanine derivatives: dyes with Q-band absorption in the far red or near infrared. *J. Chem. Soc. Perkin Trans. 1* **1988**, (8), 2453-2458.

[46] Barthel, M.; Hanack, M. Axially substituted titanium(IV) phthalocyanines. *J.*

*Porphyrins Phthalocyanines* **2000**, *4* (7), 635-638.

[47] Costentin, C.; Savéant, J. M. Towards an Intelligent Design of Molecular Electrocatalysts. *Nat. Rev. Chem.* **2017**, *1* (11), 1–8

[48] González-Rodríguez, D.; Bottari, G. Phthalocyanines, Subphthalocyanines and Porphyrins for Energy and Electron Transfer Applications. *J. Porphyr. Phthalocyanines* **2009**, *13* (4–5), 624–636.

[49] Manassen, J. Metal Complexes of Porphyrinlike Compounds As Heterogeneous Catalysts *Catal. Rev. Sci. Eng.* **1974**, *9*, 223.

[50] Zagal, J. H.; Griveau, S.; Silva, J. F.; Nyokong, T.; Bedioui, F. Metallophthalocyanine-Based Molecular Materials as Catalysts for Electrochemical Reactions. *Coord. Chem. Rev.* **2010**, *254* (23–24), 2755–2791.

[51] Kotz, R.; Carlen, M. Principles and applications of electrochemical capacitors, *Electrochim. Acta* **2000**, *45*, 2483–2498.

[52] Chidembo, A. T.; Ozoemena, K. I.; Agboola, B. O.; Gupta, V.; Wildgoose, G. G.; Compton, R. G. Nickel(Ii) Tetra-Aminophthalocyanine Modified MWCNTs as Potential Nanocomposite Materials for the Development of Supercapacitors. *Energy Environ. Sci.* **2010**, *3* (2), 228–236.

[53] Agboola, B. O.; Ozoemena, K. I. Synergistic Enhancement of Supercapacitance upon Integration of Nickel (II) Octa [(3,5-Biscarboxylate)-Phenoxy] Phthalocyanine with SWCNT-Phenylamine. *J. Power Sources* **2010**, *195* (12), 3841–3848.

[54] Mu, J.; Shao, C.; Guo, Z.; Zhang, M.; Zhang, Z.; Zhang, P.; Chen, B.; Liu, Y. Solvothermal Synthesis and Electrochemical Properties of 3D Flower-like Iron Phthalocyanine Hierarchical Nanostructure. *Nanoscale* **2011**, *3* (12), 5126–5131.

[55] Sakthivel K, Munichadraiah N and Scanlon LG. *J. Electrochem Soc.* **2005**, *152*, C756–C763.

[56] Li, R.; Zhang, X.; Zhu, P.; Ng, D. K. P.; Kobayashi, N.; Jiang, J. Electron-Donating or -Withdrawing Nature of Substituents Revealed by the Electrochemistry of Metal-Free Phthalocyanines. *Inorg. Chem.* **2006**, *45* (5), 2327–2334.

[57] Silva, N.; Calderón, S.; Páez, M. A.; Oyarzún, M. P.; Koper, M. T. M.; Zagal, J. H. Probing the Fen +/Fe(n – 1)+ Redox Potential of Fe Phthalocyanines and Fe Porphyrins as a Reactivity Descriptor in the Electrochemical Oxidation of Cysteamine.

*J. Electroanal. Chem.* **2018**, *819*, 502–510.

[58] Rajić, N. Z.; Stojaković, D. R. Synthesis and Characterization of Some Nitro-Substituted Phthalocyanines of Nickel(II), Cobalt(II) and Copper(II). *J. Coord. Chem.* **2009**, *19 (4)*, 295–301.

[59] Chen, X.; Paul, R.; Dai, L. Carbon-Based Supercapacitors for Efficient Energy Storage. *Natl. Sci. Rev.* **2017**, *4* (3), 453–489.

[60] She, Z. W.; Kibsgaard, J.; Dickens, C. F.; Chorkendorff, I.; Nørskov, J. K.; Jaramillo, T. F. Combining Theory and Experiment in Electrocatalysis: Insights into Materials Design. *Science* **2017**, *355*, 6321.

[61] Wang, Z. L.; Xu, D.; Xu, J. J.; Zhang, X. B. Oxygen Electrocatalysts in Metal-Air Batteries: From Aqueous to Nonaqueous Electrolytes. *Chem. Soc. Rev.* **2014**, *43* (22), 7746–7786.

[62] Dai, L.; Xue, Y.; Qu, L.; Choi, H. J.; Baek, J. B. Metal-Free Catalysts for Oxygen Reduction Reaction. *Chem. Rev.* **2015**, *115* (11), 4823–4892.

[63] Pingarrón, J. M.; Labuda, J.; Barek, J.; Brett, C. M. A.; Camões, M. F.; Fojta, M.; Hibbert, D. B. Terminology of Electrochemical Methods of Analysis (IUPAC Recommendations 2019). *Pure Appl. Chem.* **2020**, *92 (4)*, 641–694.

[64] Costentin, C.; Robert, M.; Savéant, J. M. Molecular Catalysis of Electrochemical Reactions. *Curr. Opin. Electrochem.* **2017**, *2 (1)*, 26–31.

[65] Savéant, J. M. Molecular Catalysis of Electrochemical Reactions. Mechanistic Aspects. *Chem. Rev.* **2008**, *108*, 2348–2378.

[66] Guerrini, E.; Trasatti, S. Recent Developments in Understanding Factors of Electrocatalysis. *Russ. J. Electrochem.* **2006**, *42* (10), 1017–1025.

[67] Quaino, P.; Juarez, F.; Santos, E.; Schmickler, W. Volcano Plots in Hydrogen Electrocatalysis-Uses and Abuses. *Beilstein J. Nanotechnol.* **2014**, *5* (1), 846–854.

[68] Toulhoat, H.; Raybaud, P. Prediction of Optimal Catalysts for a given Chemical Reaction. *Catal. Sci. Technol.* **2020**, *10 (7)*, 2069–2081.

[69] Jiao, Y.; Zheng, Y.; Jaroniec, M.; Qiao, S. Z. Design of Electrocatalysts for Oxygen- and Hydrogen-Involving Energy Conversion Reactions. *Chem. Soc. Rev.* **2015**, *44* (8), 2060–2086.

[70] Ali, A.; Shen, P. K. Recent Advances in Graphene-Based Platinum and Palladium

Electrocatalysts for the Methanol Oxidation Reaction. *J. Mater. Chem. A* **2019**, *7* (39), 22189–22217.

[71] Sun, T.; Xu, L.; Wang, D.; Li, Y. Metal Organic Frameworks Derived Single Atom Catalysts for Electrocatalytic Energy Conversion. *Nano Res.* **2019**, *12 (9)*, 2067–2080.

[72] Sunarso, J.; Glushenkov, A. M.; Torriero, A. A. J.; Howlett, P. C.; Chen, Y.; MacFarlane, D. R.; Forsyth, M. Bi-Functional Water/ Oxygen Electrocatalyst Based on PdO-RuO2 Composites. *J. Electrochem. Soc.* **2013**, *160* (1), H74–H79.

[73] Chen, H.; Cai, R.; Patel, J.; Dong, F.; Chen, H.; Minteer, S. D. Upgraded Bioelectrocatalytic $N_2$ Fixation: From $N_2$ to Chiral Amine Intermediates. *J. Am. Chem. Soc.* **2019**, *141* (12), 4963–4971.

[74] Bezerra, C. W. B.; Zhang, L.; Lee, K.; Liu, H.; Marques, A. L. B.; Marques, E. P.; Wang, H.; Zhang, J. A Review of Fe-N/C and Co-N/C Catalysts for the Oxygen Reduction Reaction. *Electrochim. Acta* **2008**, *53* (15), 4937–4951.

[75] Lin, L.; Zhu, Q.; Xu, A. W. Noble-Metal-Free Fe-N/C Catalyst for Highly Efficient Oxygen Reduction Reaction under both Alkaline and Acidic Conditions. *J. Am. Chem. Soc.* **2014**, *136* (31), 11027–11033.

[76] Yin, P.; Yao, T.; Wu, Y.; Zheng, L.; Lin, Y.; Liu, W.; Ju, H.; Zhu, J.; Hong, X.; Deng, Z.; Zhou, G.; Wei, S.; Li, Y. Single Cobalt Atoms with Precise N-Coordination as Superior Oxygen Reduction Reaction Catalysts. *Angew. Chemie - Int. Ed.* **2016**, *55* (36), 10800–10805.

[77] Wu, J.; Yang, H. Platinum-Based Oxygen Reduction Electrocatalysts. *Acc. Chem. Res.* **2013**, *46* (8), 1848–1857.

[78] Esposito, D. V.; Hunt, S. T.; Stottlemyer, A. L.; Dobson, K. D.; McCandless, B. E.; Birkmire, R. W.; Chen, J. G. Low-Cost Hydrogen-Evolution Catalysts Based on Monolayer Platinum on Tungsten Monocarbide Substrates. *Angew. Chemie - Int. Ed.* **2010**, *49* (51), 9859–9862.

[79] Morales-Guio, C. G.; Hu, X. Amorphous Molybdenum Sulfides as Hydrogen Evolution Catalysts. *Acc. Chem. Res.* **2014**, *47* (8), 2671–2681.

[80] Antolini, E. Iridium as Catalyst and Co-catalyst for Oxygen Evolution/Reduction in Acidic Polymer Electrolyte Membrane Electrolyzers and Fuel Cells. *ACS Catal.* **2014**, *4* (5), 1426–1440.

[81] Ma, T. Y.; Dai, S.; Jaroniec, M.; Qiao, S. Z. Metal-Organic Framework Derived Hybrid Co3O4-Carbon Porous Nanowire Arrays as Reversible Oxygen Evolution Electrodes. *J. Am. Chem. Soc.* **2014**, *136* (39), 13925–13931.

[82] Huang, J.; Chen, J.; Yao, T.; He, J.; Jiang, S.; Sun, Z.; Liu, Q.; Cheng, W.; Hu, F.; Jiang, Y.; Pan, Z.; Wei, S. CoOOH Nanosheets with High Mass Activity for Water Oxidation. *Angew. Chemie - Int. Ed.* **2015**, *54* (30), 8722–8727.

[83] Wang, Y.; Xie, C.; Zhang, Z.; Liu, D.; Chen, R.; Wang, S. In Situ Exfoliated, N-Doped, and Edge-Rich Ultrathin Layered Double Hydroxides Nanosheets for Oxygen Evolution Reaction. *Adv. Funct. Mater.* **2018**, *28* (4), 1–6.

[84] Trindell, J. A.; Clausmeyer, J.; Crooks, R. M. Size Stability and H2/CO Selectivity for Au Nanoparticles during Electrocatalytic CO2 Reduction. *J. Am. Chem. Soc.* **2017**, *139* (45), 16161–16167.

[85] Weng, Z.; Jiang, J.; Wu, Y.; Wu, Z.; Guo, X.; Materna, K. L.; Liu, W.; Batista, V. S.; Brudvig, G. W.; Wang, H. Electrochemical $CO_2$ Reduction to Hydrocarbons on a Heterogeneous Molecular Cu Catalyst in Aqueous Solution. *J. Am. Chem. Soc.* **2016**, *138* (26), 8076–8079.

[86] Weng, Z.; Zhang, X.; Wu, Y.; Huo, S.; Jiang, J.; Liu, W.; He, G.; Liang, Y.; Wang, H. Self-Cleaning Catalyst Electrodes for Stabilized $CO_2$ Reduction to Hydrocarbons. *Angew. Chemie - Int. Ed.* **2017**, *56* (42), 13135–13139.

[87] Lu, C.; Tranca, D.; Zhang, J.; Rodríguez Hernández, F.; Su, Y.; Zhuang, X.; Zhang, F.; Seifert, G.; Feng, X. Molybdenum Carbide-Embedded Nitrogen-Doped Porous Carbon Nanosheets as Electrocatalysts for Water Splitting in Alkaline Media. *ACS Nano* **2017**, *11* (4), 3933–3942.

[88] Wu, Y.; Liu, X.; Han, D.; Song, X.; Shi, L.; Song, Y.; Niu, S.; Xie, Y.; Cai, J.; Wu, S.; Kang, J.; Zhou, J.; Chen, Z.; Zheng, X.; Xiao, X.; Wang, G. Electron Density Modulation of NiCo2S4 Nanowires by Nitrogen Incorporation for Highly Efficient Hydrogen Evolution Catalysis. *Nat. Commun.* **2018**, *9*, 1425.

[89] Sun, T.; Xu, L.; Li, S.; Chai, W.; Huang, Y.; Yan, Y.; Chen, J. Cobalt-Nitrogen-Doped Ordered Macro-/Mesoporous Carbon for Highly Efficient Oxygen Reduction Reaction. *Appl. Catal. B Environ.* **2016**, *193*, 1–8.

[90] Liu, J.; Jiao, M.; Lu, L.; Barkholtz, H. M.; Li, Y.; Jiang, L.; Wu, Z.; Liu, D. J.; Zhuang, L.; Ma, C.; Zeng, J.; Zhang, B.; Su, D.; Song, P.; Xing, W.; Xu, W.; Wang, Y.; Jiang, Z.; Sun, G. High Performance Platinum Single Atom Electrocatalyst for Oxygen Reduction Reaction. *Nat. Commun.* **2017**, *8*, 15938.

[91] Sun, T.; Xu, L.; Yan, Y.; Zakhidov, A. A.; Baughman, R. H.; Chen, J. Ordered Mesoporous Nickel Sphere Arrays for Highly Efficient Electrocatalytic Water Oxidation. *ACS Catal.* **2016**, *6* (3), 1446–1450.

[92] Tang, T.; Jiang, W. J.; Niu, S.; Liu, N.; Luo, H.; Chen, Y. Y.; Jin, S. F.; Gao, F.; Wan, L. J.; Hu, J. S. Electronic and Morphological Dual Modulation of Cobalt Carbonate Hydroxides by Mn Doping toward Highly Efficient and Stable Bifunctional Electrocatalysts for Overall Water Splitting. *J. Am. Chem. Soc.* **2017**, *139* (24), 8320–8328.

[93] Panda, C.; Menezes, P. W.; Walter, C.; Yao, S.; Miehlich, M. E.; Gutkin, V.; Meyer, K.; Driess, M. From a Molecular 2Fe-2Se Precursor to a Highly Efficient Iron Diselenide Electrocatalyst for Overall Water Splitting. *Angew. Chemie* **2017**, *129* (35), 10642–10646.

[94] Long, B.; Tang, Y.; Li, J. New Mechanistic Pathways for CO Oxidation Catalyzed by Single-Atom Catalysts: Supported and Doped Au1/ThO2. *Nano Res.* **2016**, *9* (12), 3868–3880.

[95] Chen, D.; Chen, C.; Baiyee, Z. M.; Shao, Z.; Ciucci, F. Nonstoichiometric Oxides as Low-Cost and Highly-Efficient Oxygen Reduction/Evolution Catalysts for Low-Temperature Electrochemical Devices. *Chem. Rev.* **2015**, *115* (18), 9869–9921.

[96] Hoffert, M. I.; Caldeira, K.; Jain, A. K.; Haites, E. F.; Harvey, L. D. D.; Potter, S. D.; Schlesinger, M. E.; Schneider, S. H.; Watts, R. G.; Wigley, T. M. L.; Wuebbles, D. J. Energy Implications of Future Stabilization of Atmospheric CO2 Content. *Nature* **1998**, *395* (6705), 881–884.

[97] Lewis, N. S.; Nocera, D. G. Powering the Planet: Chemical Challenges in Solar Energy Utilization (Proceedings of the National Academy of Science of the United States of America (2006) 103, 43, (15729-15735) DOI:10.1073/Pnas.0603395103). *Proc. Natl. Acad. Sci. U. S. A.* **2007**, *104* (50), 20142.

[98] Gray, H. B. Powering the Planet with Solar Fuel. *Nat. Chem.* **2009**, *1*, 7.

[99] Chu, S.; Majumdar, A. Opportunities and Challenges for a Sustainable Energy Future. *Nature* **2012**, *488* (7411), 294–303.

[100] Artero, V.; Fontecave, M. Solar Fuels Generation and Molecular Systems: Is It Homogeneous or Heterogeneous Catalysis? *Chem. Soc. Rev.* **2013**, *42* (6), 2338–2356.

[101] Bligaard, T.; Bullock, R. M.; Campbell, C. T.; Chen, J. G.; Gates, B. C.; Gorte, R. J.; Jones, C. W.; Jones, W. D.; Kitchin, J. R.; Scott, S. L. Toward Benchmarking in Catalysis Science: Best Practices, Challenges, and Opportunities. *ACS Catal.* **2016**, *6* (4), 2590–2602.

[102] Costentin, C.; Drouet, S.; Robert, M.; Savéant, J. M. Turnover Numbers, Turnover Frequencies, and Overpotential in Molecular Catalysis of Electrochemical Reactions. Cyclic Voltammetry and Preparative-Scale Electrolysis. *J. Am. Chem. Soc.* **2012**, *134* (27), 11235–11242.

[103] Wiesener, K.; Ohms, D.; Neumann, V.; Franke, R. N4 Macrocycles as Electrocatalysts for the Cathodic Reduction of Oxygen. *Mater. Chem. Phys.* **1989**, *22* (3–4), 457–475.

[104] Nguyen, T. Q.; Escaño, M. C. S.; Kasai, H. Nitric Oxide Adsorption Effects on Metal Phthalocyanines. *J. Phys. Chem. B* **2010**, *114* (31), 10017–10021.

[105] Medina, W. S. G.; Santos, N. A. G. dos; Curti, C.; Tedesco, A. C.; Santos, A. C. dos. Effects of Zinc Phthalocyanine Tetrasulfonate-Based Photodynamic Therapy on Rat Brain Isolated Mitochondria. *Chem. Biol. Interact.* **2009**, *179* (2–3), 402–406.

[106] van Baar, J. F.; van Veen, J. A. R.; de Wit, N. Selective Electro-Oxidation of Carbon Monoxide with Carbon-Supported Rh- and Ir-Porphyrins at Low Potentials in Acid Electrolyte. *Electrochim. Acta* **1982**, *27* (1), 57–59.

[107] Villagra, E.; Bedioui, F.; Nyokong, T.; Canales, J. C.; Sancy, M.; Páez, M. A.; Costamagna, J.; Zagal, J. H. Tuning the Redox Properties of Co-N4 Macrocyclic Complexes for the Catalytic Electrooxidation of Glucose. *Electrochim. Acta* **2008**, *53* (14), 4883–4888.

[108] Vilakazi, S. L.; Nyokong, T. Voltammetric Determination of Nitric Oxide on Cobalt Phthalocyanine Modified Microelectrodes. *J. Electroanal. Chem.* **2001**, *512* (1–2), 56–63.

[109] Jiang, R.; Dong, S. Study on the Electrocatalytic Reduction of $H_2O_2$ at Iron Protoporphyrin Modified Electrode with a Rapid Rotation-Scan Method. *Electrochim. Acta* **1990**, *35* (8), 1227–1232.

[110] Furuya, N.; Yoshiba, H. Electroreduction of Nitrogen to Ammonia on Gas-Diffusion Electrodes Loaded with Inorganic Catalyst. *J. Electroanal. Chem.* **1990**, *291* (1–2), 269–272.

[111] Shibata, M.; Furuya, N. Simultaneous Reduction of Carbon Dioxide and Nitrate Ions at Gas-Diffusion Electrodes with Various Metallophthalocyanine Catalysts. *Electrochim. Acta* **2003**, *48* (25–26), 3953–3958.

[112] Richards, G.; Swavey, S. Electrooxidation of Fe, Co, Ni and Cu Metalloporphyrins on Edge-Plane Pyrolytic Graphite Electrodes and Their Electrocatalytic Ability towards the Reduction of Molecular Oxygen in Acidic Media. *Eur. J. Inorg. Chem.* **2009**, *2009* (35), 5367–5376.

[113] Yuasa, M.; Nishihara, R.; Shi, C.; Anson, F. C. A Comparison of Several Meso-Tetraalkyl Cobalt Porphyrins as Catalyst for the Electroreduction of Dioxygen. *Polym. Adv. Technol.* **2001**, *12* (3–4), 266–270.

[114] Wang, J.; Huang, X.; Xi, S.; Lee, J. M.; Wang, C.; Du, Y.; Wang, X. Linkage Effect in the Heterogenization of Cobalt Complexes by Doped Graphene for Electrocatalytic CO2 Reduction. *Angew. Chemie - Int. Ed.* **2019**, *58* (38), 13532–13539.

[115] Zagal, J. H.; Koper, M. T. M. Reactivity Descriptors for the Activity of Molecular $MN_4$ Catalysts for the Oxygen Reduction Reaction. *Angew. Chemie - Int. Ed.* **2016**, *55* (47), 14510–14521.

[116] Raja, R.; Ratnasamy, P. Selective Oxidation of Phenols Using Copper Complexes Encapsulated in Zeolites. *Appl. Catal. A Gen.* **1996**, *143* (1), 145–158.

[117] Li, C.; Huang, T.; Huang, Z.; Sun, J.; Zong, C.; Yang, J.; Deng, W.; Dai, F. A Sulfonated Cobalt Phthalocyanine/Carbon Nanotube Hybrid as a Bifunctional Oxygen Electrocatalyst. *Dalt. Trans.* **2019**, *48* (46), 17258–17265.

[118] Morlanés, N.; Takanabe, K.; Rodionov, V. Simultaneous Reduction of $CO_2$ and Splitting of $H_2O$ by a Single Immobilized Cobalt Phthalocyanine Electrocatalyst. *ACS Catal.* **2016**, *6* (5), 3092–3095.

[119] Erdomu, A.; Booysen, I. N.; Nyokong, T. Synthesis and Electrochemical Properties of New Tetra Substituted Cobalt Phthalocyanine Complexes, and Their Application in Electrode Modification for the Electrocatalysis of l-Cysteine. *Synth. Met.* **2011**, *161* (3–4), 241–250.

[120] Mashazi, P. N.; Ozoemena, K. I.; Nyokong, T. Tetracarboxylic Acid Cobalt Phthalocyanine SAM on Gold: Potential Applications as Amperometric Sensor for $H_2O_2$ and Fabrication of Glucose Biosensor. *Electrochim. Acta* **2006**, *52* (1), 177–186.

[121] Mashazi, P.; Nyokong, T. Electrocatalytic Studies of Covalently Immobilized Metal Tetra-Amino Phthalocyanines onto Derivatized Screen-Printed Gold Electrodes. *Microchim. Acta* **2010**, *171* (3), 321–332.

[122] Wang, M.; Torbensen, K.; Salvatore, D.; Ren, S.; Joulié, D.; Dumoulin, F.; Mendoza, D.; Lassalle-Kaiser, B.; Işci, U.; Berlinguette, C. P.; Robert, M. $CO_2$ Electrochemical Catalytic Reduction with a Highly Active Cobalt Phthalocyanine. *Nat. Commun.* **2019**, *10*, 3602.

[123] Zhang, X.; Wu, Z.; Zhang, X.; Li, L.; Li, Y.; Xu, H.; Li, X.; Yu, X.; Zhang, Z.; Liang, Y.; Wang, H. Highly Selective and Active $CO_2$ Reduction Electrocatalysts Based on Cobalt Phthalocyanine/Carbon Nanotube Hybrid Structures. *Nat. Commun.* **2017**, *8*, 14675.

[124] Acar, E. T.; Tabakoglu, T. A.; Atilla, D.; Yuksel, F.; Atun, G. Synthesis, Electrochemistry and Electrocatalytic Activity of Cobalt Phthalocyanine Complexes – Effects of Substituents for Oxygen Reduction Reaction. *Polyhedron* **2018**, *152*, 114–124.

[125] Özçeşmeci, İ.; Demir, A.; Akyüz, D.; Koca, A.; Gül, A. Electrocatalytic Hydrogen Evolution Reaction with a Supramolecular Cobalt(II)Phthalocyanine Carrying Four Cobaloxime Moieties. *Inorganica Chim. Acta* **2017**, *466*, 591–598.

[126] Cui, L.; Liu, Y.; He, X. Iron(II) Tetraaminophthalocyanine Functionalized Graphene: Synthesis, Characterization and Their Application in Direct Methanol Fuel Cell. *J. Electroanal. Chem.* **2014**, *727*, 91–98.

[127] Jahnke, H.; Schönborn, M.; Zimmermann, G. Organic Dyestuffs as Catalysts for Fuel Cells. *Top. Curr. Chem.* **1976**, *61*, 133–181.

[128] Khotseng, L. Electrocatalysts for Direct Methanol Fuel Cells. *Direct Methanol Fuel Cells Appl. Perform. Technol.* **2017**, *148*, 1–49.

[129] Jiang, Y.; Lu, Y.; Lv, X.; Han, D.; Zhang, Q.; Niu, L.; Chen, W. Enhanced Catalytic Performance of Pt-Free Iron Phthalocyanine by Graphene Support for Efficient Oxygen Reduction Reaction. *ACS Catal.* **2013**, *3* (6), 1263–1271.

[130] Li, T.; Peng, Y.; Li, K.; Zhang, R.; Zheng, L.; Xia, D.; Zuo, X. Enhanced Activity and Stability of Binuclear Iron (III) Phthalocyanine on Graphene Nanosheets for Electrocatalytic Oxygen Reduction in Acid. *J. Power Sources* **2015**, *293*, 511–518.

[131] Chidembo, A. T.; Ozoemena, K. I.; Agboola, B. O.; Gupta, V.; Wildgoose, G. G.; Compton, R. G. Nickel(II) Tetra-Aminophthalocyanine Modified MWCNTs as Potential Nanocomposite Materials for the Development of Supercapacitors. *Energy Environ. Sci.* **2010**, *3* (2), 228–236.

[132] Chidembo, A. T.; Ozoemena, K. I. Electrochemical Capacitive Behaviour of Multiwalled Carbon Nanotubes Modified with Electropolymeric Films of Nickel Tetraaminophthalocyanine. *Electroanalysis* **2010**, *22* (21), 2529–2535.

[133] Makgopa, K.; Ejikeme, P. M.; Ozoemena, K. I. Graphene Oxide-Modified Nickel (II) Tetra-Aminophthalocyanine Nanocomposites for High-Power Symmetric Pseudocapacitor. *Electrochim. Acta* **2016**, *212*, 876–882.

[134] Xu, Z.; Li, Z.; Holt, C. M. B.; Tan, X.; Wang, H.; Amirkhiz, B. S.; Stephenson, T.; Mitlin, D. Electrochemical Supercapacitor Electrodes from Sponge-like Graphene Nanoarchitectures with Ultrahigh Power Density. *J. Phys. Chem. Lett.* **2012**, *3* (20), 2928–2933.

[135] Bakandritsos, A.; Chronopoulos, D. D.; Jakubec, P.; Pykal, M.; Čépe, K.; Steriotis, T.; Kalytchuk, S.; Petr, M.; Zbořil, R.; Otyepka, M. High-Performance Supercapacitors Based on a Zwitterionic Network of Covalently Functionalized Graphene with Iron Tetraaminophthalocyanine. *Adv. Funct. Mater.* **2018**, *28* (29), 1–9.

[136] Wang, M.; Shi, H.; Zhang, P.; Liao, Z.; Wang, M.; Zhong, H.; Schwotzer, F.; Nia, A. S.; Zschech, E.; Zhou, S.; Kaskel, S.; Dong, R.; Feng, X. Phthalocyanine-Based 2D Conjugated Metal-Organic Framework Nanosheets for High-Performance Micro-Supercapacitors. *Adv. Funct. Mater.* **2020**, *30* (30).

[137] Madhuri, K. P.; John, N. S. Supercapacitor Application of Nickel Phthalocyanine Nanofibres and Its Composite with Reduced Graphene Oxide. *Appl. Surf. Sci.* **2018**, *449*, 528–536.

[138] Lu, Y.; Zheng, Q.; Wu, J.; Yu, Y. Enhanced Electrochemical Charge Storage Performance by Doping of Copper Phthalocyanine-3,4′,4″,4‴-Tetrasulfonic Acid Tetrasodium Salt into Polypyrrole/Multi-Walled Carbon Nanotubes 3D-Nanostructured Electrodes. *Electrochim. Acta* **2018**, *265*, 594–600.

[139] Ramachandran, R.; Hu, Q.; Wang, F.; Xu, Z. X. Synthesis of N-$CuMe_2Pc$ Nanorods/Graphene Oxide Nanocomposite for Symmetric Supercapacitor Electrode with Excellent Cyclic Stability. *Electrochim. Acta* **2019**, *298*, 770–777.

[140] Taşaltln, N.; Taşaltln, C.; Aydln, H.; Şahintürk, U.; Gürek, A. G. Hexylsulfanyl-Substituted CoPc and GO-CoPc on Ni Foam as Electroactive Material for Supercapacitors. *J. Porphyr. Phthalocyanines* **2019**, *23* (11–12), 1616–1621.

[141] Frackowiak, E.; Fic, K.; Meller, M.; Lota, G. Electrochemistry Serving People and Nature: High-Energy Ecocapacitors Based on Redox-Active Electrolytes. *ChemSusChem* **2012**, *5* (7), 1181–1185.

[142] Akinwolemiwa, B.; Peng, C.; Chen, G. Z. Redox Electrolytes in Supercapacitors. *J. Electrochem. Soc.* **2015**, *162* (5), A5054–A5059.

[143] Jost, K.; Dion, G.; Gogotsi, Y. Textile Energy Storage in Perspective. *J. Mater. Chem. A* **2014**, *2* (28), 10776–10787.

[144] Zhang, S. W.; Chen, G. Z. Manganese Oxide Based Materials for Supercapacitors. *Energy Mater. Mater. Sci. Eng. Energy Syst.* **2008**, *3* (3), 186–200.

[145] Guan, L.; Yu, L.; Chen, G. Z. Capacitive and Non-Capacitive Faradaic Charge Storage. *Electrochim. Acta* **2016**, *206*, 464–478.

[146] Huang, J.; Sumpter, B. G.; Meunier, V. A Universal Model for Nanoporous Carbon Supercapacitors Applicable to Diverse Pore Regimes, Carbon Materials, and Electrolytes. *Chem. - A Eur. J.* **2008**, *14* (22), 6614–6626.

[147] Gogotsi, Y. What Nano Can Do for Energy Storage. *ACS Nano* **2014**, *8* (6), 5369–5371.

[148] Ke, Q.; Wang, J. Graphene-Based Materials for Supercapacitor Electrodes – A Review. *J. Mater.* **2016**, *2* (1), 37–54.

[149] Lukatskaya, M. R.; Dunn, B.; Gogotsi, Y. Multidimensional Materials and Device Architectures for Future Hybrid Energy Storage. *Nat. Commun.* **2016**, *7*, 1–13.

[150] Wang, F.; Wu, X.; Yuan, X.; Liu, Z.; Zhang, Y.; Fu, L.; Zhu, Y.; Zhou, Q.; Wu, Y.; Huang, W. Latest Advances in Supercapacitors: From New Electrode Materials to Novel Device Designs. *Chem. Soc. Rev.* **2017**, *46* (22), 6816–6854.

[151] Tehrani, Z.; Thomas, D. J.; Korochkina, T.; Phillips, C. O.; Lupo, D.; Lehtimäki, S.; O'Mahony, J.; Gethin, D. T. Large-Area Printed Supercapacitor Technology for Low-Cost Domestic Green Energy Storage. *Energy* **2017**, *118*, 1313–1321.

[152] Dubal, D. P.; Chodankar, N. R.; Kim, D. H.; Gomez-Romero, P. Towards Flexible Solid-State Supercapacitors for Smart and Wearable Electronics. *Chem. Soc. Rev.* **2018**, *47* (6), 2065–2129.

[153] Mourad, E.; Coustan, L.; Lannelongue, P.; Zigah, D.; Mehdi, A.; Vioux, A.; Freunberger, S. A.; Favier, F.; Fontaine, O. Biredox Ionic Liquids with Solid-like Redox Density in the Liquid State for High-Energy Supercapacitors. *Nat. Mater.* **2017**, *16* (4), 446–454.

[154] Simon, P.; Gogotsi, Y. Materials for Electrochemical Capacitors. *Nat. Mater.* **2008**, 7, 845–854.

# Chapter-2

# Materials and Methods

## 2.1. Materials

The chemicals such as N,N dimethylformamide (DMF) (99%), hexane (95%), isopropyl alcohol (99%), isopropyl alcohol (99%), cobalt (II) chloride hexahydrate (≥98%), nickel (II) chloride hexahydrate (≥98%), copper (II) chloride dehydrate (≥98%), zinc (II) chloride hydrate (99.99%) ($ZnCl_2$), ammonium molybdate (99.99%), 4-nitrophthalimide (98%), 3-nitrophthalimide (98%), sodium sulfide nonahydrate (≥98%), ammonium chloride (≥98%), toluene (99.5%), methanol (99%), ethanol (95%), sulfuric acid (96%), potassium phosphate dibasic ($K_2HPO_4$) (98%), potassium phosphate monobasic ($KH_2PO_4$) (99%), L-ascorbic acid (99%) and nitrobenzene (99%) were procured from Alfa Aesar, India. Dimethyl sulfoxide-$d_6$ (DMSO-$d_6$) (99.9 atom % D), sodium acetate (≥99%), sodium arsenite (≥90%), uric acid (≥99%), L-cysteine (≥98%), sodium hydroxide (≥99%), hydrogen peroxide (30%), hydrochloric acid (37.0%) and Nafion solutions (5 wt%) were procured from Sigma-Aldrich, India. The carbon nanotubes (CNTs) were purchased from C-Nano (FT 9000). The YP-50F carbon was purchased from Kuraray chemicals, India.

## 2.2. Material characterization

UV-Visible measurements of CoPc, α-TNCoPc, β-TNCoPc and α- and β-TAMPc (M- Co, Ni, Cu, Zn etc.,) were carried out in a quartz cuvette using a Perkin Elmer Lambda 950 instrument. FTIR spectra of CoPc, α-TNCoPc/α-TACoPc, β-TNCoPc/α-TACoPc and the molecules anchored on CNT and YP-50F were obtained using a Bruker Alpha ATR-FTIR spectrometer. Scanning electron microscopy (SEM) with energy dispersive X-ray (EDS) spectrum (Zeiss Ultraplus-4095) was used for morphological characterization and elemental analysis. Raman spectra were recorded using a Raman microscope (LabRAM HR, Horbia Jobin Yvon). Nuclear magnetic resonance (NMR) spectra of α-TNZnPc/α-TAZnPc and β-TNZnPc/β-TAZnPc were recorded using Bruker 400 MHz spectrometer.

Quartz crystal microbalance (QCM) measurements were carried out using EG&G QCM922A with carbon coated and Au coated quartz crystals. X-ray photo electron

spectroscopy (XPS) was carried out using Thermo Scientific Kalpha+ spectrometer. The measurements were carried out using a monochomated Al Kα (1486.6 eV) X-ray source with 72 W power. The spot size of the X-rays were 400 μm. For electron energy analysis a $180^0$ double focusing hemispherical analyzer with 128 channel detector was used. An ultra-low energy co-axial electron beam and $Ar^+$ ion beam was used for charge compensation and the charge compensation gun was switched on during the spectral acquisition. The final spectra were cross verified for charge accumulation with C1s standard value at 284.6 eV. The base pressure of the spectrometer was always better than ~$5x10^{-9}$ mbar (gun vacuum) and ~$1x10^{-7}$ mbar (system vacuum) during data acquisition with flood gun on. The survey scan was collected at 200 eV pass energy and individual core-levels at 50 eV. Peak fitting was carried out using Avantage software with a smart background. The relative percentage of $2p_{3/2}$ and $2p_{1/2}$ in Co 2p during peak fitting was maintained at a ratio of 2:1.

## 2.3. Electrochemical measurements

The electrochemical experiments were carried out using Biologic VMP 300 potentiostat. A double jacketed three-electrode cell (10 ml volume) configuration with a 3 mm diameter glassy carbon disk (or 2 mm Au disk electrode) as the working electrode and a platinum wire as the counter electrode was employed for electrochemical measurements. Ag/AgCl (3 M KCl) electrode was used for neutral pH, $Hg/Hg_2SO_4/SO_4^{2-}$ electrode was used for acidic pH and $Hg/HgO/OH^-$ electrode was used for alkaline pH as the reference electrodes. All the potentials were finally converted to reversible hydrogen scale (RHE scale) based on the redox potentials for hydrogen redox reactions in respective electrolytes obtained on a Pt disc working electrode. All solutions were prepared using Millipore water (resistivity value is 18.2 MΩ.cm and TOC value below 5 ppb) and the cell temperature was maintained at 25˚C using a water bath fitted with a temperature controller. The electrode surface was cleaned by 0.05 μm of alumina powder by polishing. Each time before the measurement, electrochemical cycling was carried out in the respective electrolytes for electrochemically cleaning the surface. For establishing the isomerism-activity relation in molecular electrocatalysis with respect to nitro substituted molecular electrocatalysts (1,8,15,22-Tetranitrophthalocyanatocobalt (II) (α-TNCoPc), 2,9,16,23-Tetranitrophthalocyanatocobalt (II) (β-TNCoPc) and unsubstituted phthalocyanine

cobalt(II) (CoPc)), electrochemical investigations were performed for water oxidation reaction in pH 14 (1 M KOH) alkaline solution at a rotation rate of 1600 rpm with CoPc, α-TNCoPc isomer and β-TNCoPc isomer modified glassy carbon electrodes (Discussed in Chapter 3). Ascorbic acid oxidation was carried out in acetate buffer (pH-2) solutions (unstirred solution), uric acid oxidation and L-cysteine oxidation) were carried out in acetate buffer (pH-4) solutions (unstirred solution) with CoPc, α-TNCoPc isomer and β-TNCoPc isomer modified glassy carbon electrodes. Hydrogen peroxide oxidation was carried out in phosphate buffer (pH-7) solutions (unstirred solution) and arsenite (III) oxidation was performed in phosphate buffer (pH-8) solutions (unstirred solution) with CoPc, α-TNCoPc isomer and β-TNCoPc isomer modified glassy carbon electrodes (Discussed in Chapter 3). The working electrodes were prepared by drop casting the catalysts (composites with carbon nanotube) on the glassy carbon electrode. The catalyst ink was prepared by dispersing a known amount of catalyst in isopropyl alcohol with 5 wt% Nafion as the binder and all the experiments were conducted in $N_2$ saturated solution unless and otherwise specified. During the experiments the surface of the solution was maintained under a $N_2$ blanket. The electrochemical experiments were repeated by forming a monolayer of CoPc, α-TNCoPc isomer and β-TNCoPc isomer molecules on glassy carbon electrodes to show that the effects are the intrinsic characteristics of the molecules. The monolayers were formed from a solution of CoPc, α-TNCoPc isomer and β-TNCoPc isomer molecules (2 mM) in distilled DMF solvent. The electrodes were incubated in respective solutions for nearly 6 hours. The electrodes were then washed with distilled DMF solvent to remove any physisorbed molecules.

For oxygen reduction reactions (ORR), the electrochemical experiments were carried out in 0.5 M $H_2SO_4$ and 0.5 M NaOH solutions with amino substituted isomers (1,8,15,22 Tetraaminophthalocyanatocobalt (II) (α-TACoPc) and 2,9,16,23-Tetraaminophthalocyanatocibalt (II) (β-TACoPc)) modified glassy carbon (or Au disk electrode) as working electrodes. Each time the glassy carbon/Au electrode was cleaned by polishing with 0.05 micron alumina powder followed by electrochemical cycling in the respective supporting electrolytes. The TACoPc@YP-50F (composite with activated carbon YP-50F) modified glassy carbon electrodes were prepared by the drop-casting method. A homogeneous dispersion was prepared by sonicating a known amount of catalysts (α-

TACoPc isomer, and β-TACoPc isomer composite with activated carbon YP-50F) in isopropyl alcohol (IPA) with 5 wt% Nafion as the binder to prepare the catalyst ink. All the experiments were carried out in $O_2$ saturated solutions unless and otherwise specified. During the experiments the surface of the solution was maintained under an $O_2$ blanket. The electrochemical experiments were repeated by forming a monolayer of α-TACoPc isomer and β-TACoPc isomer on glassy carbon electrodes and Au electrodes to show that the effects are the intrinsic characteristics of the molecules. The monolayers were formed from a solution of α-TACoPc isomer and β-TACoPc isomer molecules (2 mM) in distilled DMF solvent. For achieving the monolayer formation, the electrodes were incubated in respective solutions for ~6 hours. The electrodes were then was washed with distilled DMF solvent to remove any physisorbed molecules.

## 2.4. Synthesis of isomeric metal phthalocyanines and phthalocyanine anchored on carbon materials

### 2.4.1. Synthesis of 1,8,15,22-Tetranitrophthalocyanatocobalt (II) (α-TNCoPc), 2,9,16,23-Tetranitrophthalocyanatocobalt (II) (β-TNCoPc), 1,8,15,22-Tetranitrophthalocyanatozinc (II) (α-TNZnPc), 2,9,16,23-Tetranitrophthalocyanatozinc (II) (β-TNZnPc), and Phthalocyanatocobalt (II) (CoPc)

Synthesis of 2,9,16,23-Tetranitro Cobalt Phthalocyanine/1,8,15,22-Tetranitro Cobalt Phthalocyanine were carried out according to the literature.[1-3] A 250 ml round bottomed flask was charged with finely grounded mixture of 4-nitro phthalimide/3-nitro phthalimide (3.86 g), urea (6.0 g), ammonium molybdate (0.05 g), ammonium chloride (0.5 g) and 30 ml of nitrobenzene. The reaction mixture was stirred for 10 minutes to get a homogeneous mixture and then added cobalt (II) chloride hexahydrate (1.2 g) followed by subsequent vigorous stirring at 100°C for about 30 minutes. Then the temperature was increased to 180°C at a ramping rate of 10°C/30 minutes followed by refluxing the reaction mixture at 180°C for about 4 hours. The mixture was then diluted with toluene (50 ml) and the resulting precipitate was filtered, washed thoroughly with hot water and methanol and finally washed with hexane and then dried in an oven at 80°C. For the synthesis of CoPc, the same protocol was employed with phthalimide as the precursor. For the synthesis of α and

β-TNZnPc, the same procedure was adopted with zinc chloride ($ZnCl_2$) as the metal salt.

### 2.4.2. Preparation of 1,8,15,22 Tetraaminophthalocyanatocobalt (II) (α-TACoPc) and 2,9,16,23-Tetraaminophthalocyanatocibalt (II) (β-TACoPc) from corresponding 1,8,15,22-Tetranitrophthalocyanatocobalt (II) and 2,9,16,23-Tetranitrophthalocyanatocobalt (II)

The synthesis of α-TACoPc/β-TACoPc from α-TNCoPc/β-TNCoPc were carried out as per the reported literature.[1-3]. A 250 ml round-bottomed flask was charged with tetra nitro cobalt phthalocyanine (0.75 g), sodium sulfide nonahydrate (3.0 g) and 30 ml of N, N, dimethylformamide. The reaction mixture was heated to 80°C for about 2 hours. It was then cooled to room temperature and diluted with ice water (200 ml), and the resulting precipitate was filtered off and thoroughly washed with hot water followed by methanol and finally with hexane. The obtained precipitate was dried in an oven to obtain 1,8,15,22-tetraamino cobalt phthalocyanine (α-TACoPc)/2,9,16,23-tetraamino cobalt phthalocyanine (β-TACoPc).

### 2.4.3. Synthesis of α-TANiPc/β-TANiPc, α-TACuPc/β-TACuPc, and α-TAZnPc/β-TAZnPc

The above same synthetic protocol [1-3] was followed for the synthesis of α-TANiPc/β-TANiPc, α-TACuPc/β-TACuPc and α-TAZnPc/β-TAZnPc with nickel (II) chloride, copper (II) chloride and zinc chloride ($ZnCl_2$) as the metal salts respectively.

### 2.4.4. Synthesis of CoPc, α-TNCoPc/ α-TACoPc and β-TNCoPc/ α-TACoPc anchored on carbon nanotubes (CNTs)

The CNTs were purified according to the procedure reported in the literature,[4] by being immersed in concentrated HCl solution for 5 days and then refluxed for 5 h, followed by thoroughly washing with water and acetone. The purified CNTs was dried overnight at 80°C in vacuum oven for stock. CoPc and TNCoPc/TACoPc isomers were anchored on CNT by mixing known amounts of CNT and TNCoPc/TACoPc in the stoichiometric ratio of 2:1 (w/w) in DMF and sonicated for about 30 minutes to obtain a well-mixed suspension.[4,5] The suspension was further stirred at room temperature for 24 h.

Subsequently, the mixture was centrifuged and the precipitate was washed with DMF and ethanol. Finally, the precipitate was lyophilized to yield the final product.

### 2.4.5. Synthesis of α-TACoPc and β-TACoPc anchored on YP-50F carbon

The TACoPc@YP-50F hybrid catalyst was prepared by mixing TACoPc with activated carbon YP-50F in DMF with the assistance of sonication and magnetic stirring. The YP-50F was purchased from Kuraray chemicals. To form hybrid catalysts systems of TACoPc@YP-50F, a known stoichiometric ratio of YP-50F and TACoPc (2:1 w/w) was dissolved in DMF followed by 30 min of sonication to obtain a well-mixed suspension.[4,5] The suspension was further stirred at 80°C temperature for 24 h. Subsequently, the mixture was centrifuged and the precipitate was washed with DMF followed by ethanol several times. Finally, the precipitate was lyophilized to yield the final product.

## 2.5. Self-assembly of α-TNMPc/α-TAMPc and β-TNMPc/β-TAMPc on glassy carbon (GC) and Au electrodes (Metal:- Co, Ni, Cu, Zn etc.)

In order to understand the pristine behaviour of the $–NO_2$ and $–NH_2$ substituted isomeric molecules, the electrochemical experiments were also carried out by forming self-assembled monolayers of CoPc, α-TNMPc/α-TAMPc (where M stands for Co, Ni, Cu and Zn) isomer and β-TNMPc/β-TAMPc isomer on glassy carbon/Au electrodes. Self-assembly of α and β-TAMPc/α and β-TNMPc molecules were achieved as follows. 2 mM solutions of isomeric molecules were prepared in dimethylformamide (DMF) by ultrasonication. GC/Au electrodes were first polished by alumina polishing powder and then cleaned electrochemically. The polished GC electrode was electrochemically cleaned between the potential 0.2 to 1.3 V vs. RHE in 0.5 M $H_2SO_4$ using potentiodynamic cycling until reproducible voltammograms were obtained. The polished Au electrode was electrochemically cleaned between the potential 0.2 V to 1.8 V vs. RHE in 0.5 M $H_2SO_4$ using potentiodynamic cycling until reproducible voltammograms were obtained. The electrodes were washed with a copious amount of distilled water and finally with DMF and then the electrode were incubated in respective phthalocyanine solution for ~6 hours. The modified electrodes were washed with fresh DMF to remove physisorbed molecules and

finally washed with distilled water. α and β-TNMPc molecules were mainly adsorbed on glassy carbon electrodes as monolayers to investigate their electrochemical properties.

## 2.6. Surface coverage calculations

### 2.6.1. Electrochemical methods

The molecular surface coverage ($\Gamma_{MPc}$ in mol/cm$^2$) of the redox active film on the electrode surface was estimated by integrating the area of $Co^{III}/Co^{II}$ couple in the cyclic voltammograms.[6-8, 6-823,24] The surface coverage of the redox active film from a plot of the background corrected peak current versus scan rate according to eq 2.1.[23,24]

$$I_p = \frac{n^2F^2\Gamma_{MPc}A\nu}{4RT} \ldots\ldots (2.1)$$

where $I_P$ is background corrected current (A), n is the number of moles of electrons transferred, F is the Faraday constant (96485 C mol$^{-1}$), $\Gamma_{MPc}$ is the surface coverage (mol cm$^{-2}$), A is the area of the electrode (cm$^2$), ν is the scan rate (V s$^{-1}$), R is the gas constant (8.314 J K$^{-1}$ mol$^{-1}$), and T is the temperature (K).

### 2.6.2. Amatore's model

The fractional surface coverage (θ) was estimated for modified α-TACoPc and β-TACoPc electrodes using Amatore's model based on the Nyquist plots of bare and modified electrodes and the plot of real part of impedance, (Z') vs. $1/(\omega)^{1/2}$, where ω is the angular frequency in radian/s. A ferrocyanide/ferricyanide redox couple was employed to study the blocking behavior of monolayer electrodes.[9,10] Using the equations 2.2 and 2.3, θ values were estimated and the values were found to be ~0.96 reflecting a monolayer coverage.

$$\theta_{IS}^{R} = 1 - \left(\frac{R_{ct}^{Bare}}{R_{ct}^{SAM}}\right) \ldots\ldots (2.2)$$

$$\theta_{IS}^{P} = 1 - \left(\frac{\sigma_W}{m-\sigma_W}\right) \ldots\ldots (2.3)$$

where, $R_{ct}^{Bare}$ is the charge-transfer resistance measured at the bare electrode, and $R_{ct}^{SAM}$ the charge-transfer resistance under the same conditions at the monolayer-covered electrode.

From equation (2.2) coverage can be estimated based on $R_{ct}$. Using equation 2.3, the coverage can be estimated by using a model that is based on the pinhole size, where $\sigma_W$ is the Warburg coefficient calculated from the characterization of the pretreated bare GC and Au, and m is the slope of the linear interval observed in the high frequency region of the Z' vs. $1/(\omega)^{1/2}$ function obtained at the modified electrode.

### 2.6.3. Quartz crystal microbalance (QCM) study

As explained above, to understand the pristine behaviour of the $-NO_2$ and $-NH_2$ substituted isomeric molecules, the electrochemical experiments were also carried out by forming monolayers of CoPc, α-TNCoPc/α-TACoPc isomer and β-TNCoPc/β-TACoPc isomer on glassy carbon/Au electrodes. The formation and surface coverage of monolayer were confirmed by QCM studies which were carried out in flow cell mode using carbon (9.12 MHz) or Au (8.93 MHz) coated quartz resonator as the base crystal. A 0.2 mM solution of molecules in DMF was circulated at a flow rate of 1 ml/min to the QCM cell. Initially fresh DMF solution was circulated for 2 hours to get a stable background signal. This was followed by passing the solution of the molecule for nearly 7 hours to allow the formation of monolayer on the electrode surface. Finally, the fresh DMF solution was again passed to remove any weakly adsorbed molecule.

The Sauerbrey equation was then used to find the mass of adsorbed molecules on the crystal by correlating the frequency shift (Δf) to mass change (Δm) as in equation 2.4.[11,12]

$$\Delta m = -c\left(\frac{\Delta f}{n}\right) \ldots\ldots (2.4)$$

where, Δf is the net resonance frequency shift due to adsorption of molecules and n is the overtone number (QCM analysis were measured at the third overtone (n=3)). The sensitivity (c) of the QCM crystal was 5.608 ng $cm^{-2}$ $Hz^{-1}$.

The surface coverage (Γ, $mol.cm^{-2}$) was calculated using equation 2.5,

$$\Gamma = \frac{\Delta m}{Molecular\ mass} \ldots\ldots (2.5)$$

## 2.7. Density functional theory (DFT) calculations

All the density functional theory (DFT) calculations were performed by employing a hybrid CAM-B3LYP (Coulomb-Attenuating Method, Becke, three-parameter, Lee-Yang-Parr)[13] exchange-correlation functional in Gaussian 09 (Revision C.01) suite of packages.[14] Double zeta valence polarization (dg-DZVP) basis sets have been used for all the atoms, viz., H, C, N and O. However, for cobalt atoms Stuttgart-Dresden (SDD) effective core potentials have been used in all the calculations. Unrestricted Kohn-Sham formalism has been utilized for the ground state (GS) optimizations of all the structures under study. Default convergence criterion with Berny algorithm and extra quadratically convergent (XQC) self-consistent field (SCF) method is used for all the GS geometry optimizations and are confirmed as the local minima with all positive vibrational frequencies. The empirical dispersion (iop (3/124=30), Grimme D3, DFT-D3)[15,16] term is included for all the calculations as well for the relative energy. Relative energies ($E_{R.E}$) is calculated using the equation 2.6,

$$E_{R.E} = E_{GS} - E_{HES} \ldots\ldots (2.6)$$

where, $E_{GS}$ and $E_{HES}$, respectively are the total corrected energies (free energy) of the ground state (GS) and high energy state (HES). Natural atomic orbital and natural bond orbital analysis (NBO) program of Gaussian NBO Version 3.1[17] were used for charge density calculations. In addition, Mulliken and Hirshfeld charge population schemes also have been used for the electronic spin densities and charge densities calculations. All the images were plotted from Gauss View 5.0 and VESTA 3.4.4.[18]

## 2.8. Calculation of the number of electron and catalytic rate constant ($k_{cat}$) for arsenic (III) to arsenic (V) oxidation

Rotating disk electrode (RDE) measurements were carried out with PINE instruments integrated with a PARSTAT MC (AMETEK) potentiostat. α-TNCoPc and β-TNCoPc isomer modified glassy carbon electrodes (area = 0.196 $cm^2$) were used as the working electrodes, Ag/AgCl/(3 M KCl) was used as the reference electrode, and platinum mesh was used as the counter electrode. The measurements were carried out in nitrogen purged solutions containing 5 mM arsenite in pH 8 phosphate buffer at a scan rate of 5 mV/s at different rotations per minute (100, 400, 900, 1600, 2500, and 3600). The experimental

data were analyzed with the help of the Koutecky–Levich equation (eq 2.7),[19,20] and the number of electrons were calculated from the limiting current (1.48 V vs. RHE) using the Levich equation (eq 2.8).

The Koutecky–Levich (K–L) plots were linear straight lines obeying the equation:

$$1/i_{lim} = 1/i_{Lev} + 1/i_{k,E} \quad \ldots\ldots (2.7)$$

where $i_{Lev}$ is the Levich current (limiting current) and $i_{k,E}$ is the kinetic current at the potential E.

$$i_{lev} = 0.62nFAD_{AS(III)}^{2/3} v^{-\frac{1}{6}} C_{As(III)} \omega^{1/2} \quad \ldots\ldots (2.8)$$

where $i_{Lev}$ is limiting current, n is number of electrons, F is Faraday constant (96485 C $mol^{-1}$), A is area of the electrode ($cm^2$), D is diffusion coefficient ($cm^2$ $s^{-1}$), υ is kinematic viscosity ($cm^2$ $s^{-1}$), C is concentration (mol $cm^{-3}$), and ω is rotational speed (rad $s^{-1}$). The y-intercept of the K–L plot at different potentials gives the reciprocal of the kinetic current ($i_{k,E}$). The x-intercept of the plot of overpotential (η) vs. logarithm of kinetic current density was used to calculate the exchange current density.[19,20]

The catalytic rate constant ($k_{cat}$) was estimated by eq 2.9.[21,22]

$$i_{K,E} = nFAk_{cat} C_{As(III)} \Gamma_{MPc} \quad \ldots\ldots (2.9)$$

where $\Gamma_{MPc}$ is the surface coverage of redox active film in mol/$cm^2$, which was estimated by using equation 2.1 (section 2.6.1.).

## 2.9. Calculation of the number of electron and $H_2O_2$ % yield for ORR

Rotating ring disk electrode (RRDE) experiments carried out with PINE instruments integrated with a PARSTAT MC (AMETEK) potentiostat. The experiments were performed by using a glassy carbon (GC) disk electrode (area = 0.196 $cm^2$) and a platinum (Pt) ring (area = 0.11 $cm^2$) electrode. The electrode cleaning was carried out by soaking in dilute sulfuric acid and hydrogen peroxide solution. They were then rinsed repeatedly in boiling water and the electrode was electrochemically cleaned in 0.5 M $H_2SO_4$ solution in the potential range of 0.2 to 1.3 V vs. RHE. The disk electrode was then modified by drop

casting with α-TACoPc and β-TACoPc isomeric molecules.

All the RRDE electrochemical measurements were collected in oxygen saturated 0.5 M $H_2SO_4$ solution at a scan rate 10 mV/s in a three-electrode system containing α-TACoPc and β-TACoPc isomer modified glassy carbon electrodes as the working electrode. The disk electrode was scanned cathodically between 0.8 to -0.2 V vs. RHE at a scan rate 5 mV/s, keeping the ring potential constant at 1.0 V vs RHE. The disk and ring currents were acquired for various rotation rates (100, 400, 900, 1600, 2500 and 3600 rpm). The % of $H_2O_2$ and the electron transfer number (n) were determined using equation 2.10 and 2.11.[23]

$$\% H_2O_2 = 200\left[\left(\frac{I_r}{N}\right)/\left(I_d + \left(\frac{I_r}{N}\right)\right)\right] \ldots\ldots (2.10)$$

$$n = 4\left[(I_d)/\left(I_d + \left(\frac{I_r}{N}\right)\right)\right] \ldots\ldots (2.11)$$

where $I_d$ is the disc current, Ir is the ring current and N is the collection efficiency of gold ring.

Collection efficiency N was determined using α-TACoPc and β-TACoPc isomer modified glassy carbon electrodes as working electrode, Ag/AgCl (3 M KCl)) as the reference electrode and platinum as the counter electrode, in $N_2$ saturated 10 mM potassium ferricyanide solution. The disk electrode was scanned cathodically between 0.7 to -0.1 V vs RHE at a scan rate 5 mV/s, keeping the ring potential at 0.5 V vs RHE at various rotation rates (100, 400, 900, 1600, 2500 and 3600 rpm).[23]

## 2.10. $H_2$-$O_2$ fuel cell assembly

The $H_2$-$O_2$ fuel cell was assembled using Pt/C (40 wt% Pt), as the anode hydrogen oxidation electrocatalyst and α and β-TACoPc isomers supported on CNT (TACoPc/CNT) as the cathode ORR electrocatalyst. The anode Pt/C loading was 0.5 mg/cm$^2$ and the cathode TACoPc/CNT loading was 1 mg/cm$^2$. Nafion 117 membrane was pre-treated as follows. A Nafion 117 membrane was treated with $H_2O_2$ and water solution (1:3 ratio) and the solution was heated at 80°C for ~30 minutes. After washing with distilled water, Nafion membrane was again heated at 80°C for ~30 minutes in $H_2SO_4$ solution to make it proton conducting.

The pretreated Nafion membrane was placed between the anode and cathode gas diffusion layers and pressed under 1 ton pressure for 3 minutes at 125°C to fabricate the membrane electrode assembly. It was then kept between gold plated stainless steel endplates. Fuel cell experiments were carried out at 25°C with a $H_2$-$O_2$ flow rate of 100 mL/min.

## 2.11. Specific capacity, energy density and power density calculations of molecular supercapacitor

The specific capacitance ($C_{sp}$) or capacitance/gram was calculated from cyclic voltammetry (CV) curves (in three electrode configurations) at various scan rates using the following equation 2.12.[24-26]

$$C_{sp} = \frac{\int i.dV}{2*m*\nu*\Delta V} \ldots\ldots (2.12)$$

where, $C_{sp}$ is specific capacitance ($F.g^{-1}$), $\int i.dV$ is the integrated area in the cyclic voltammogram, m is mass of the active material (g), $\nu$ is the scan rate ($mVs^{-1}$), and $\Delta V$ is the potential window (V).

The $C_{sp}$ from the galvanostatic charge-discharge (GCD) measurements (in three electrode configurations) was calculated using the equation (2.13)

$$C_{sp} = \frac{I*\Delta t}{m*\Delta V} \ldots\ldots (2.13)$$

where $C_{sp}$ is specific capacitance ($F.g^{-1}$), I is applied current (A), $\Delta V$ represents the potential window (V), $\Delta t$ signifies discharge time (s), and m is the mass of the active material (g). The energy density and power density of the device were obtained from equations 2.14 and 2.15:[26]

$$E = \frac{1}{2}CV^2 \ldots\ldots (2.14)$$

$$P = \frac{E}{\Delta t} \ldots\ldots (2.15)$$

where E is the energy density (in Wh $g^{-1}$), P is the power density (in W $g^{-1}$) and $\Delta t$ is the total discharge time (in hrs).

## 2.12. Characteristic time constant ($\tau_0$), self-discharge current ($i_{sd}$) and leakage current ($i_{lk}$) measurements

The characteristic time constant ($\tau_0$) (also known as the relaxation time) reflects the minimum time required to discharge the capacitor fully [27-29] and it was estimated from the equation, 2.16.

$$\tau_0 = 1/f_o \quad \text{.....(2.16)}$$

The characteristic frequency known as "knee" or "onset" frequency ($f_o$) which reflects the power capability of a supercapacitor, was calculated by plotting imaginary part of capacitance (C") as a function of frequency. The C" is associated with the energy loss and the real part (C') reflects the deliverable capacitance and these can be calculated according to the following equations 2.17 and 2.18. [28, 30]

$$C''(\omega) = \frac{Z'(\omega)}{\omega |Z(\omega)|^2} \quad \text{..... (2.17)}$$

$$C'(\omega) = \frac{-Z''(\omega)}{\omega |Z(\omega)|^2} \quad \text{..... (2.18)}$$

where $|Z(\omega)|$ is the impedance modulus and C"(ω) and C'(ω) is imaginary and real parts of capacitance.

Self-discharge experiments were performed by measuring the time within which the voltage dropped from the completely charged state to the potential equal to mean of charged state and the open circuit voltage (OCV). Leakage current was calculated by holding the potential at full charge and the current required to maintain the fully charged state was measured over time.[31-33] Before self-discharge and leakage current measurements, initially, the system was charged with a rate of 1 $mA \cdot g^{-1}$ to 1.0 V and then held at this voltage for 4 hours. After a full charge, the system was allowed to undergo self-discharge for ~15 hrs while monitoring the open circuit voltage decay. The self-discharge currents were estimated from the equation 2.19.[32]

$$i_{sd} = C * \frac{(V_1 - V_2)}{\Delta t} \quad \text{..... (2.19)}$$

$V_1$- potential of charged state, $V_2$- mean potential between charged state and the open circuit voltage and Δt-time (in sec) taken to reach $V_2$.

## 2.13. References


[1] Al-lami, A. K. a; Majeed, N. N.; Al-mowali, A. H. Synthesis, Mesomorphic and Molar Conductivity Studies of Some Macrocyclic Phthalocyanine Palladium (II). *Chemistry and Materials Research*. **2013**, *3* (4), 59–68.

[2] Lukyanets, E. A.; Nemykin, V. N. The Key Role of Peripheral Substituents in the Chemistry of Phthalocyanines and Their Analogs. *J. Porphyr. Phthalocyanines* **2010**, *14* (1), 1–40.

[3] Kottaichamy, A. R.; Makri Nimbegondi Kotresh, H.; Devendrachari, M. C.; Thimmappa, R.; Paswan, B.; Tiwari, O.; Chanda, V.; Gaikwad, P.; Thotiyl, M. O. Effects of Electrochemical Tailoring of Monolayers on a Catalytic Redox Entity: An ON-OFF Phenomenon Regulated by the Surrounding Medium. *J. Phys. Chem. C* **2015**, *119* (51), 28276–28284.

[4] Cao, R.; Thapa, R.; Kim, H.; Xu, X.; Gyu Kim, M.; Li, Q.; Park, N.; Liu, M.; Cho, J. Promotion of Oxygen Reduction by a Bio-Inspired Tethered Iron Phthalocyanine Carbon Nanotube-Based Catalyst. *Nat. Commun.* **2013**, *4* , 2076.

[5] Zhu, M.; Chen, J.; Guo, R.; Xu, J.; Fang, X.; Han, Y. F. Cobalt Phthalocyanine Coordinated to Pyridine-Functionalized Carbon Nanotubes with Enhanced CO2 Electroreduction. *Appl. Catal. B Environ.* **2019**, *251*, 112–118.

[6] Revell, D. J.; Chambrier, I.; Cook, M. J.; Russell, D. A. Formation and Spectroscopic Characterisation of Self-Assembled Phthalocyanine Monolayers. *J. Mater. Chem.* **2000**, *10 (1)*, 31–37.

[7] Kalyuzhny, G.; Vaskevich, A.; Ashkenasy, G.; Shanzer, A.; Rubinstein, I. UV/Vis Spectroscopy of Metalloporphyrin and Metallophthalocyanine Monolayers Self-Assembled on Ultrathin Gold Films. *J. Phys. Chem. B* **2002**, *104 (34)*, 8238–8244.

[8] Foster, C. W.; Pillay, J.; Metters, J. P.; Banks, C. E. Cobalt Phthalocyanine Modified Electrodes Utilised in Electroanalysis: Nano-Structured Modified Electrodes vs. Bulk Modified Screen-Printed Electrodes. *Sensors (Basel).* **2014**, *14* (11), 21905–21922.

[9] Wallen, R.; Gokarn, N.; Bercea, P.; Grzincic, E.; Bandyopadhyay, K. Mediated Electron Transfer at Vertically Aligned Single-Walled Carbon Nanotube Electrodes during Detection of DNA Hybridization. *Nanoscale Res. Lett.* **2015**, *10* (1), 268.

[10] Campuzano, S.; Pedrero, M.; Montemayor, C.; Fatás, E.; Pingarrón, J. M. Characterization of Alkanethiol-Self-Assembled Monolayers-Modified Gold Electrodes by Electrochemical Impedance Spectroscopy. *J. Electroanal. Chem.* **2006**, *586*, 112–121.

[11] Vogt B. D.; Lin E. K.; Wu W.; White C. C. Effect of Film Thickness on the Validity of the Sauerbrey Equation for Hydrated Polyelectrolyte Films. *J. Phys. Chem. B,* **2004**, *108*, 12685–12690.

[12] Mokrani C.; Fatisson J.; Guérente L.; Labbé P. Structural Characterization of (3-Mercaptopropyl)sulfonate Monolayer on Gold Surfaces. *Langmuir,* **2005**, *21(10)*, 4400– 4409.

[13] Yanai, T.; Tew, D. P.; Handy, N. C. A New Hybrid Exchange-Correlation Functional Using the Coulomb-Attenuating Method (CAM-B3LYP). *Chem. Phys. Lett.* **2004**, *393 (1–3)*, 51–57.

[14] Frisch, M.J.; Trucks, G.W.; Schlegel, H.B.; Scuseria., G.E.; Robb, M.A.; Cheeseman, J.R.; Scalmani, G.; Barone, V.; Mennucci, B.; Petersson, G.A.; Nakatsuji, H.; Caricato, M.; Li, X.; Hratchian, H.P.; Izmaylov, A.F.; Bloino, J.; Zheng, G.; Sonnenberg, J.L.; Hada, M.; Ehara, M.; Toyota, K.; Fukuda, R.; Hasegawa, J.; Ishida, M.; Nakajima, T.; Honda, Y.; Kitao, O.; Nakai, H.; Vreven, T.; Montgomery, J.A.; Peralta, J.J.E.; Ogliaro, F.; Bearpark, M.; Heyd, J.J.; Brothers, E.; Kudin, K.N.; Staroverov, V.N.; Keith, T.; Kobayashi, R.; Normand, J.; Raghavachari, K.; Rendell, A.; Burant, J.C.; Iyengar, S.S.; Tomasi, J.; Cossi, M.; Rega, N.; Millam, J.M.; Klene, M.; Knox, J.E.; Cross, J.B.; Bakken, V.; Adamo, C.; Jaramillo, J.; Gomperts, R.; Stratmann, R.E.; Yazyev, O.; Austin, A.J.; Cammi, R.; Pomelli, C.; Ochterski, J.W.; Martin, R.L.; Morokuma, K.; Zakrzewski, V.G.; Voth, G.A.; Salvador, P.; Dannenberg, J.J.; Dapprich, S.; Daniels, A.D.; Farkas, O.; Foresman, J.B.; V Ortiz, J.; Cioslowski, D.J.; and Fox, I.; Gaussian Wallingford CT.; *Gaussian 09, Revis. C.01.* **2010**.

[15] Grimme, S.; Antony, J.; Ehrlich, S.; Krieg, H. A Consistent and Accurate Ab Initio Parametrization of Density Functional Dispersion Correction (DFT-D) for the 94 Elements H-Pu. *J. Chem. Phys.* **2010**, *132* (15).

[16] Stefan, G.; Stephan, E.; Lars, G. Effect of the damping function in dispersion corrected density functional theory *J. Comput. Chem.* **2011**, *32*, 1456–1465.

[17] Glendening, F.; Reed, E. D.; Carpenter, A. E.; Weinhold J, E. *NBO Version 3.0,* **2003.**

[18] Momma, K.; Izumi, F. VESTA 3 for three-dimensional visualization of crystal, volumetric and morphology data *J. Appl. Crystallogr.* **2011**, *44*, 1272–1276.

[19] Devendrachari, M. C.; Thimmappa, R.; Bhat, Z. M.; Shafi, S. P.; Nimbegondi Kotresh, H. M.; Kottaichamy, A. R.; Venugopala Reddy, K. R.; Thotiyl, M. O. A Vitamin C Fuel Cell With A Non-Bonded Cathodic Interface. *Sustain. Energy Fuels* **2018**, *2 (8)*, 1813–1819.

[20] Bhat, Z. M.; Thimmappa, R.; Devendrachari, M. C.; Shafi, S. P.; Aralekallu, S.; Kottaichamy, A. R.; Gautam, M.; Thotiyl, M. O. A Direct Alcohol Fuel Cell Driven By An Outer Sphere Positive Electrode. *J. Phys. Chem. Lett.* **2017**, *8 (15)*, 3523–3529.

[21] Nellaiappan, S.; Pillai, K. C.; Kumar, A. S. Flow-Injection Analysis Coupled with Electrochemical Detection of Poisonous Inorganic arsenic(III) Species Using a Gold Nanoparticle/carbon Nanofiber/chitosan Chemically Modified Carbon Screen Printed Electrode in Neutral pH Solution. *Anal. Methods* **2018**, *10* (7), 799–808.

[22] Salimi, A.; Mamkhezri, H.; Hallaj, R.; Soltanian, S. Electrochemical Detection of Trace Amount of Arsenic (III) at Glassy Carbon Electrode Modified with Cobalt Oxide Nanoparticles. *Sensors Actuators, B Chem.* **2008**, *129*, 246–254.

[23] R. Zhou, Y. Zheng, M. Jaroniec, S.-Z. Qiao, Determination of the Electron Transfer Number for the Oxygen Reduction Reaction: From Theory to Experiment *ACS Catal.* **2016**, *6*, 4720–4728.

[24] Bae, J.; Song, M. K.; Park, Y. J.; Kim, J. M.; Liu, M.; Wang, Z. L. Fiber Supercapacitors Made of Nanowire-Fiber Hybrid Structures for Wearable/Flexible Energy Storage. *Angew. Chemie* **2011**, *123* (7), 1721–1725.

[25] Wang, Q.; Wang, X.; Xu, J.; Ouyang, X.; Hou, X.; Chen, D.; Wang, R.; Shen, G. Flexible Coaxial-Type Fiber Supercapacitor Based on $NiCo_2O_4$ Nanosheets Electrodes. *Nano Energy* **2014**, *8*, 44–51.

[26] Wu, H.; Lou, Z.; Yang, H.; Shen, G. A Flexible Spiral-Type Supercapacitor Based on $ZnCo_2O_4$ Nanorod Electrodes. *Nanoscale*, **2015**, *7* (60), 1921–1926.

[27] Yang, K.; Cho, K.; Kim, S. Effect of Carbon Black Addition on Thermal Stability and Capacitive Performances of Supercapacitors. *Sci. Rep.* **2018**, *8* (1), 1–7.

[28] Taberna, P. L.; Simon, P.; Fauvarque, J. F. Electrochemical Characteristics and Impedance Spectroscopy Studies of Carbon-Carbon Supercapacitors. *J. Electrochem. Soc.* **2003**, *150* (3), A292.

[29] Yoo, Y.; Kim, M. S.; Kim, J. K.; Kim, Y. S.; Kim, W. Fast-Response Supercapacitors with Graphitic Ordered Mesoporous Carbons and Carbon Nanotubes for AC Line Filtering. *J. Mater. Chem. A* **2016**, *4* (14), 5062–5068.

[30] Rodrigues, A. C.; Da Silva, E. L.; Quirino, S. F.; Cuña, A.; Marcuzzo, J. S.; Matsushima, J. T.; Gonçalves, E. S.; Baldan, M. R. Ag@activated Carbon Felt Composite as Electrode for Supercapacitors and a Study of Three Different Aqueous Electrolytes. *Mater. Res.* **2018**, *22* (1), 1–9.

[31] Wang, X.; Song, T. Buckypaper Templating Ni – Co Hydroxide Ultrathin and Flexible Supercapacitors. *New J. Chem.,* **2016**, *40*, 8006–8011.

[32] Mourad, E.; Coustan, L.; Lannelongue, P.; Zigah, D.; Mehdi, A.; Vioux, A.; Freunberger, S. A.; Favier, F.; Fontaine, O. Biredox Ionic Liquids with Solid-like Redox Density in the Liquid State for High-Energy Supercapacitors. *Nat. Mater.* **2017**, *16* (4), 446–454.

[33] El-kady, M. F.; Kaner, R. B. Scalable fabrication of high-power graphene micro-supercapacitors for flexible and on-chip energy storage *Nat. Commun.* **2013**, *4*, 1475–1479.

# Chapter-3

## Isomerism-Activity Relation in Oxidative Molecular Electrocatalysis

**Abstract**: The role of electrocatalysts in energy storage/conversion, biomedical and environmental sectors, green chemistry, and much more has generated enormous interest in comprehending their structure–activity relations. While targeting the surface-to-volume ratio, exposing reactive crystal planes and interfacial modifications are time-tested considerations for activating metallic catalysts; it is primarily by substitution in molecular electrocatalysts. This chapter draws a distinction between a substituent's chemical identity and isomerism in oxidative electrocatalysis, when regioisomerism of the $-NO_2$ substituent is conferred at the "α" and "β" positions on the macrocycle of cobalt phthalocyanines. Spectroscopic analysis and theoretical calculations establish that the β isomer accumulates catalytically active intermediates via a cumulative influence of inductive and resonance effects. However, the field effect in the α isomer restricts this activation due to a vanishing resonance effect. The demonstration of the distinct role of isomerism in substituted molecular electrocatalysts for reactions ranging from energy conversion to biosensing highlights that isomerism of the substituents makes an additional contribution to oxidative electrocatalysis over its chemical identity.

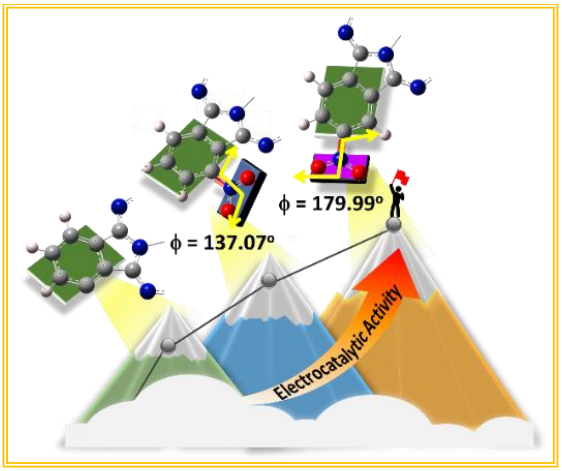


This work has been published in the following journal.

Alagar Raja K. et al., *J. Phys. Chem. Lett.* **2020**, *11*, 263–271. Copyright American Chemical Society.

## 3.1. Introduction

Electrocatalytic phenomena play central roles in energy conversion/storage, electrochemical sensing, environmental remediation, green chemistry, etc., which in turn has generated enormous interest in understanding structure–activity relations of electrocatalysts.[1-6] Among the class of various electrocatalysts, $N_4$ macrocyclic systems such as phthalocyanines (Pcs) and porphyrins have been extensively explored as potential nonprecious molecular catalysts for a variety of electrochemical applications because of their tunable optoelectronic properties and high thermal and chemical stabilities.[7–12] It has been well established that the nature of functionalities at the $N_4$ macrocycle affects the electronic arrangement and electrocatalytic activity.[12-18] However, in the context of electrocatalysis, far too little attention has been paid to the fact that this electronic arrangement is not only a function of their chemical identity across the spectrochemical series but also a strong function of their isomerism. The existing accounts fail to make any distinction between the chemical identity of groups and their isomerism in molecular electrocatalysis, and to the best our knowledge no research has been found that surveyed and understood the isomerism–activity relation at a molecular level. The aim of this study is to draw a distinction between the nature of groups and their isomerism in molecular electrocatalysis pertaining to electrochemical oxidation reactions and fill the knowledge gap in their structure–activity relation through an examination of the isomerism-induced electrocatalysis in $-NO_2$ substituted metal Pcs. This investigation reveals that the isomerism of $-NO_2$ groups at the $N_4$ macrocycle of cobalt Pcs can tune the catalytic metal center with the β isomer highly favoring oxidative electrocatalysis compared to the corresponding α isomer and unsubstituted CoPc (Figure 3.1). This investigation contributes to the growing area of electrocatalytic research by demonstrating that isomerism of substituents can induce an additional contribution to electrocatalysis over its chemical identity, which can be tapped to make the maximum potential of the molecule available for electrocatalysis. In addition, it provides an important opportunity to advance the understanding of molecular electrocatalysis by establishing a strongly substituent specific isomerism-electrochemical activity relation, which opens up an elegant approach for reinvigorating the catalytic center for reactions ranging from energy conversion to biosensing.

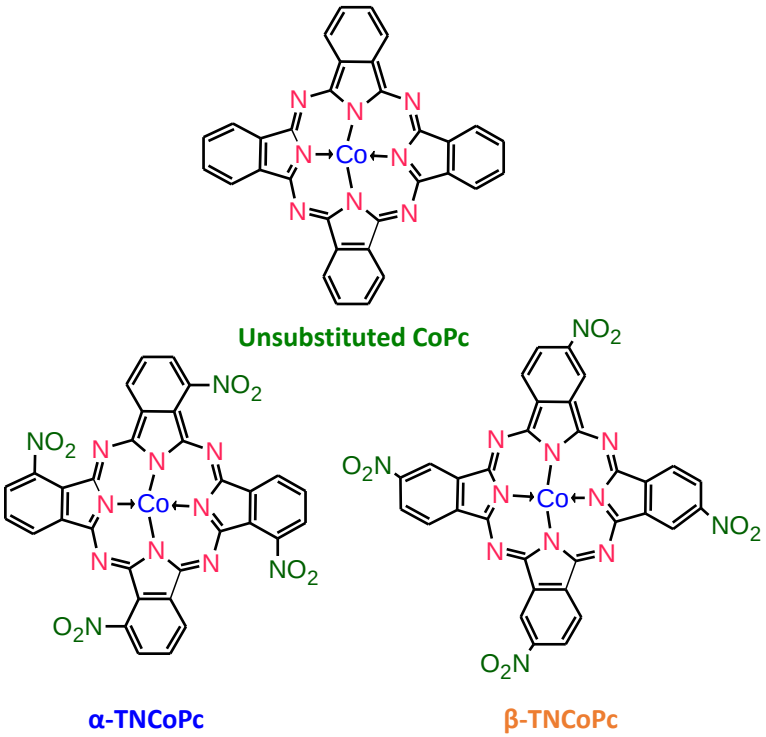


**Figure 3.1:** Molecular structure of unsubstituted CoPc and regioisomers of tetra-nitro cobalt phthalocyanines (α-TNCoPc and β-TNCoPc).

## 3.2. Results and discussion

### 3.2.1. Characterization of CoPc, α-TNCoPc and β-TNCoPc and their composites with carbon nanotube

It is well-known that electron-withdrawing substituents at the $N_4$ macrocycle of metal Pcs can activate the catalytic central metal ion toward electrochemical oxidation reactions.[16-18] However, it is not yet understood how the isomerism of the same functionality influences the electrocatalytic pathways. In order to shed light on this in the context of electron-withdrawing substituents, regioisomers of tetra-nitro cobalt Pc (TNCoPc) were synthesized as per the literature [19-21] (for synthetic procedure please refer to chapter 2, section 2.4.1, pages 46-47) by shifting the position of the $-NO_2$ group from the alpha (α- TNCoPc) to beta (β-TNCoPc) position, Figure 3.1. Matrix-assisted laser desorption ionization time-of-flight mass spectrometry (MALDI-TOF) confirms the formation of TNCoPcs ($C_{32}H_{12}CoN_{12}O_8$, MW = 751.45 g/mol) and unsubstituted CoPc ($C_{32}H_{16}CoN_8$, MW = 571.45 g/mol), Figure 3.2a-c. UV–vis spectra (Figure 3.2d) indicate the presence of a B-band and Q-band in the ranges of 300–400 and 550–750 nm,

respectively, which are characteristics of a phthalocyanine (Pc) ring.[22,23] The Q-band is well known to have more ligand characteristics; therefore, the regioisomerism of the $-NO_2$ group should primarily influence the Q-band.[22-24] A broader Q-band for β-TNCoPc compared to α-TNCoPc and unsubstituted CoPc (Figure 3.2d) demonstrates that the β isomer experiences comparatively extensive electronic delocalization than the corresponding α isomer. Fourier-transform infrared spectroscopy (FTIR) of isomeric molecules demonstrates vibrations at ~1635, ~1369, ~1246, and ~1137 $cm^{-1}$, signaling C=C macrocycle ring vibration, C–N stretching vibrations, C–C stretching vibrations and C–H stretching vibrations respectively. Vibrations at ~1515 $cm^{-1}$ indicate the presence of $-NO_2$ functionality. Pc skeletal vibrations are observed at ~1025, ~935, ~875, and ~750 $cm^{-1}$ (Figure 3.2e).[25,26] The Raman shift between 400 and 600 $cm^{-1}$ corresponds to C–C–C in-plane bending, and bands at ~764 $cm^{-1}$ represent the macrocyclic stretching vibration.[27,28] The Raman spectral bands in the range of 800–1200 $cm^{-1}$ correspond to C–N stretching, C–C stretching, and C–H bending vibrations. The spectral band at ~1237 $cm^{-1}$ represents the C–H in-plane deformation in the macrocyclic ring.[27,28] The Raman shift at ~1456 $cm^{-1}$ corresponds to stretching vibration of the isoindole ring unit, and the bands at ~1404 and ~1678 $cm^{-1}$ represent the C–N in-plane stretching vibration[27,28] (Figure 3.2f).

For structural elucidation of isomeric molecules, $^1H$ nuclear magnetic resonance (NMR) spectroscopic analysis of α and β–$NO_2$ isomers were carried out. Because cobalt-based α-TNCoPc and β-TNCoPc isomers (Figure 3.1) are paramagnetic in nature, the corresponding Zn-based diamagnetic nitro Pcs (α-TNZnPc and β-TNZnPc)[29,30] were synthesized (for more details please refer to chapter 2, section 2.4.1, pages 46-47) for NMR studies, and the results were then correlated to corresponding Co-based Pcs. In the NMR spectra of α and β isomers of TNZnPc (Figure 3.3a,b), three aromatic protons with distinct chemical shift values (labeled as $H_A$, $H_B$, and $H_C$ in Figure 3.3a,b) indicate distinctly different chemical environments surrounding these protons. As per the structures given in the insets of Figure 3.3a,b for the arrangement of protons around the aromatic ring of the $N_4$ macrocycle, the regioisomerism of the $-NO_2$ group should affect the chemical shift values of aromatic protons quite differently in the two isomers. To elucidate this unambiguously, we carried out 2D $^1H$ NMR analysis (COSY) (Figure 3.3c,d). In the case of α isomer, the $H_B$

proton couples with $H_A$-type as well as $H_C$-type protons (COSY spectrum, Figure 3.3c). On the other hand, in β-TNZnPc, the $H_B$ proton could couple only with the $H_A$ proton and not with the $H_C$ proton (COSY spectrum, Figure 3.3d). All of these evidences the formation of regioisomers as per the molecular structure in Figure 3.1.

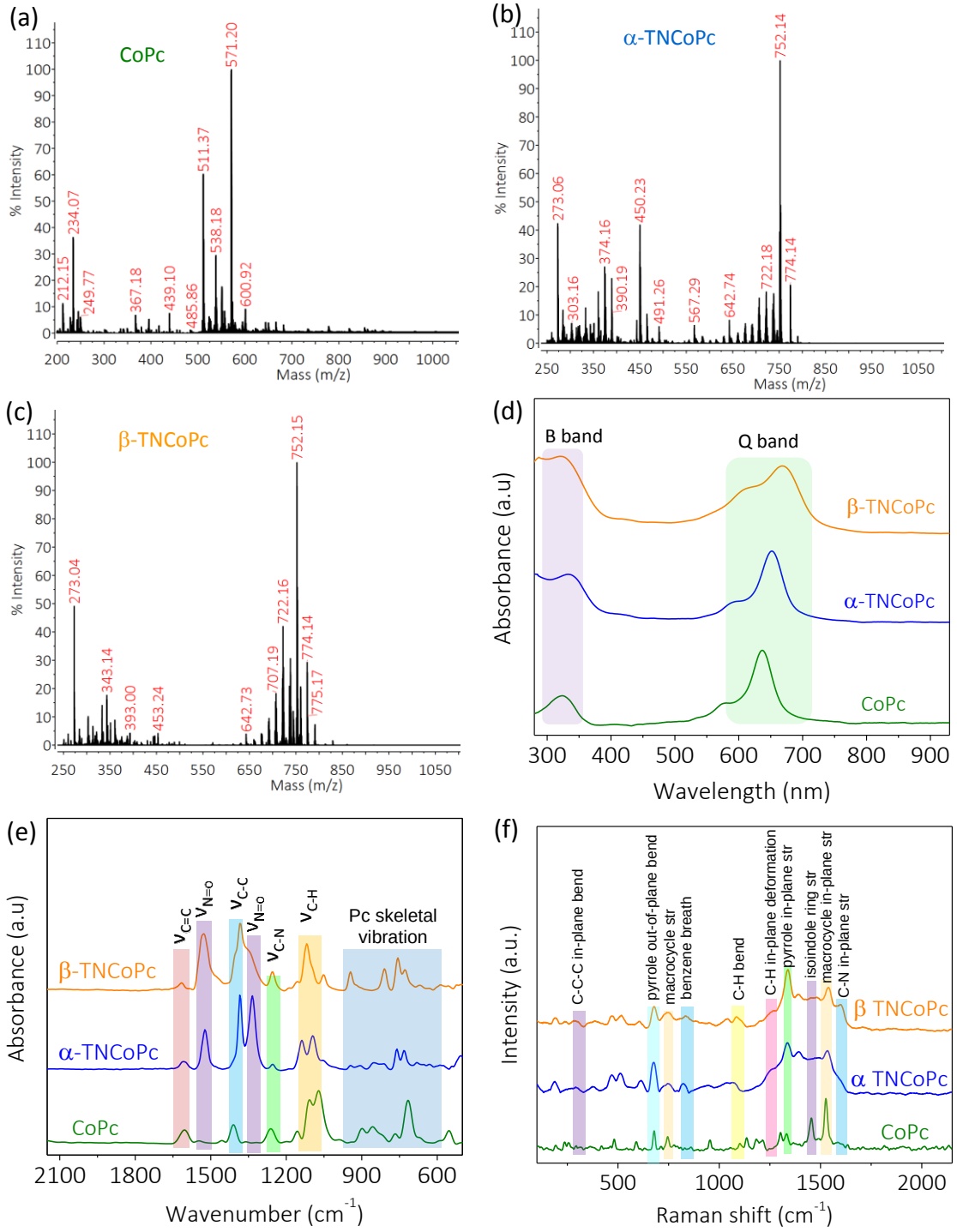


**Figure 3.2:** Matrix-assisted laser desorption ionization time-of-flight mass spectrometry (MALDI-TOF) of (a) unsubstituted CoPc, (b) α-TNCoPc isomer and (c) β-TNCoPc isomer. (d) UV-Visible spectroscopy, (e) Fourier transform infrared (FTIR) spectroscopy and

(f) Raman spectroscopy of unsubstituted CoPc, α-TNCoPc and β-TNCoPc isomers.

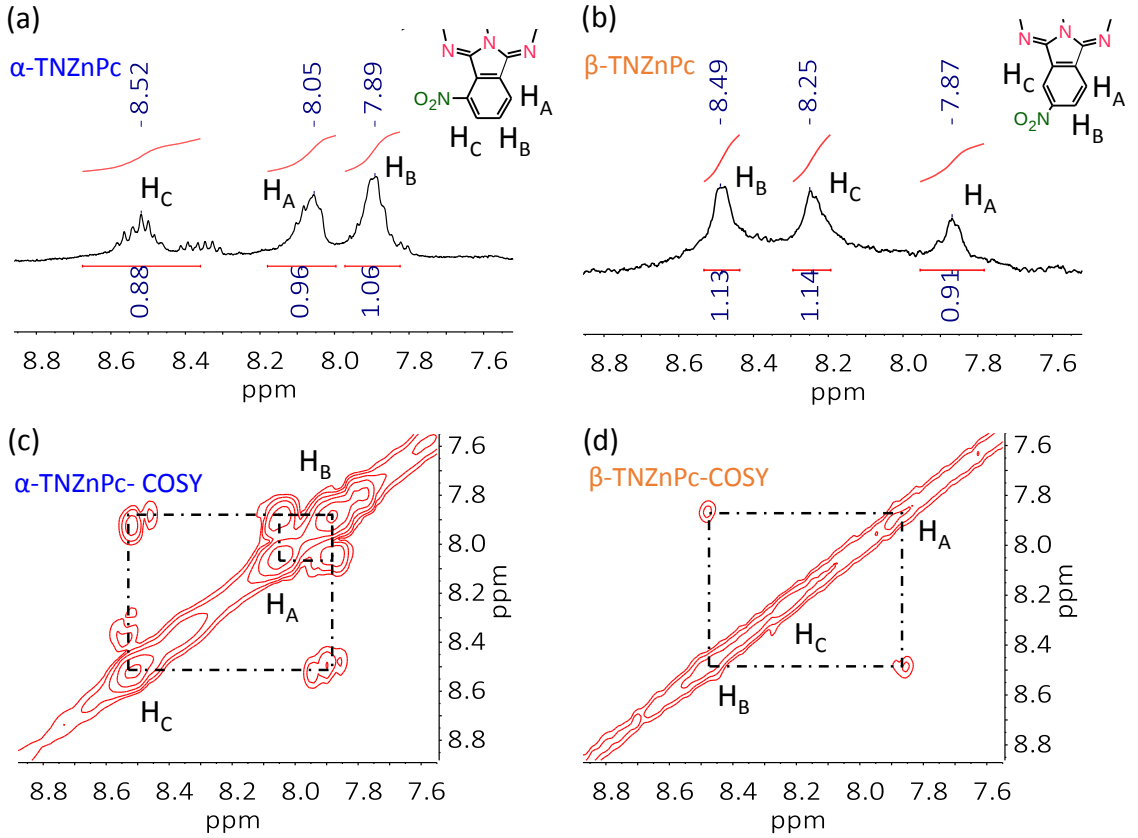


**Figure 3.3:** $^{1}$H Nuclear magnetic resonance (NMR) spectra of (a) α-TNZnPc and (b) β-TNZnPc isomers. 2D $^{1}$H NMR (COSY) spectra of (c) α-TNZnPc and (d) β-TNZnPc isomers. Insets of Figures 3.3a and 3.3b show the expected arrangements of protons around the aromatic ring.

To investigate their activity toward oxidation reactions, synthesized molecular catalysts were anchored on carbon nanotube (CNT) by π–π interaction (see chapter 2, section 2.4.4 for more details, pages 47-48).[31,32] CNT is known to facilitate electron transfer to and from the catalytic entity, explaining the reason behind its choice to fabricate the electrocatalytic platform.[31,33] α- and β-TNCoPcs and unsubstituted CoPc anchored on CNT (α-TNCoPc/CNT and β-TNCoPc/CNT) were characterized by FTIR, Raman spectroscopy, and UV–visible spectroscopy (Figure 3.4). FTIR indicates the features of the CNT in the TNCoPc/CNT catalytic system along with the corresponding Pc features (Figure 3.4a). UV–visible spectroscopy of the composite catalytic system (Figure 3.4b) signals the presence of B and Q-bands, reflecting successful incorporation of Pcs on CNT. Raman spectra show the presence of characteristic defect and graphitic bands in the CNT as well as the composite, (Figure 3.4c); however, the Pc features were almost masked (due to their low

concentration) by the intense defect and graphitic bands of CNTs. Nevertheless, the $I_D/I_G$ (intensity of defect band/intensity of graphitic band) ratio in the CNT demonstrates a noticeable increase upon anchoring it with TNCoPcs (Figure 3.4c,d), in line with the literature,[34,35] suggesting their successful incorporation. Scanning electron microscopy (SEM) with energy-dispersive X-ray spectroscopy (EDS) (Figures 3.5 and 3.6) indicate the characteristic nanotubular morphology of the CNT along with the presence of Co, N, C, and O (EDS pattern), further reinforcing the successful incorporation of TNCoPcs on the CNT. For comparative purposes the data of unsubstituted cobalt phthalocyanines (CoPc) were also provided in Figures 3.4–3.6. Taken together, all of the characterization techniques adopted evidence the presence of CNT and TNCoPcs isomers as a part of the electrocatalytic architecture.

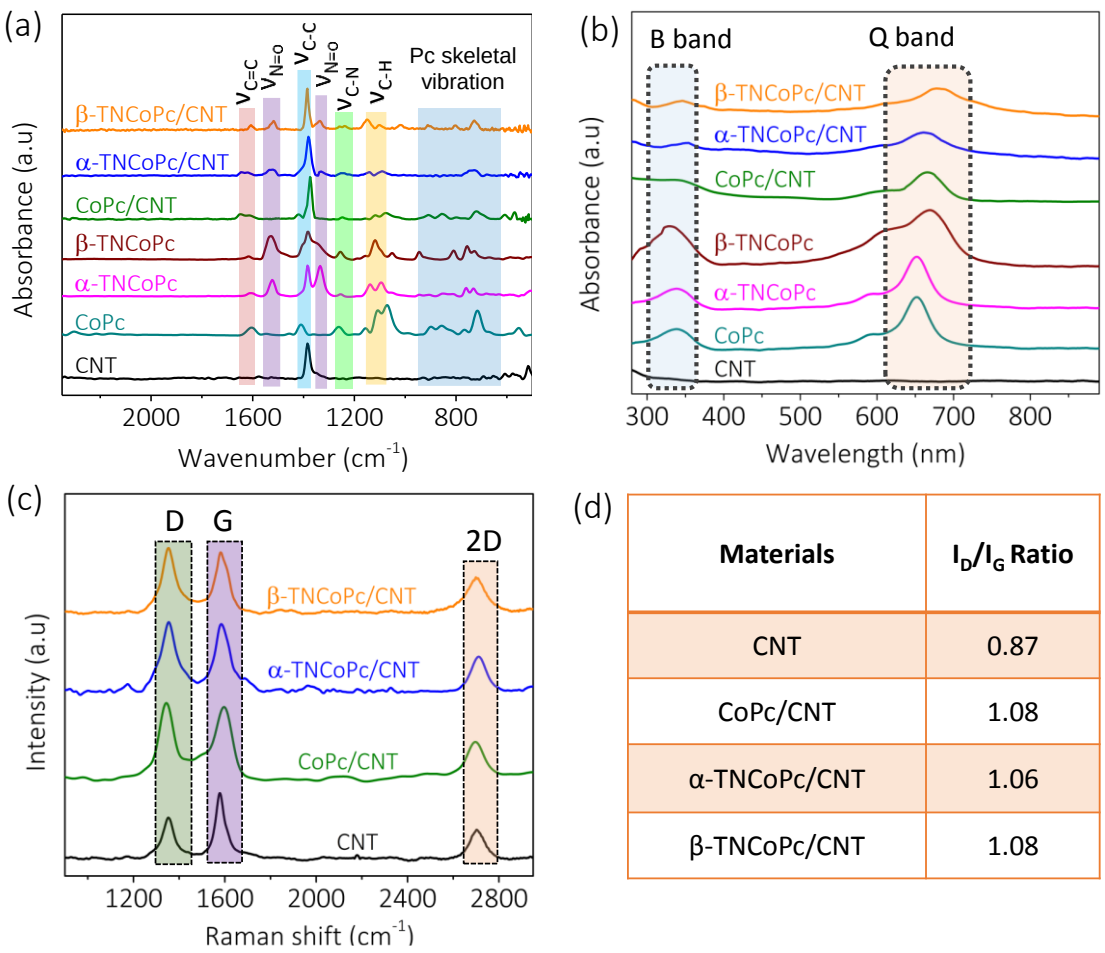


| Materials | $I_D/I_G$ Ratio |
|---|---|
| CNT | 0.87 |
| CoPc/CNT | 1.08 |
| α-TNCoPc/CNT | 1.06 |
| β-TNCoPc/CNT | 1.08 |

**Figure 3.4:** (a) FTIR spectra, (b) UV-Visible spectra, (c) Raman spectra and (d) $I_D/I_G$ ratios of CoPc/CNT, α-TNCoPc/CNT and β-TNCoPc/CNT.

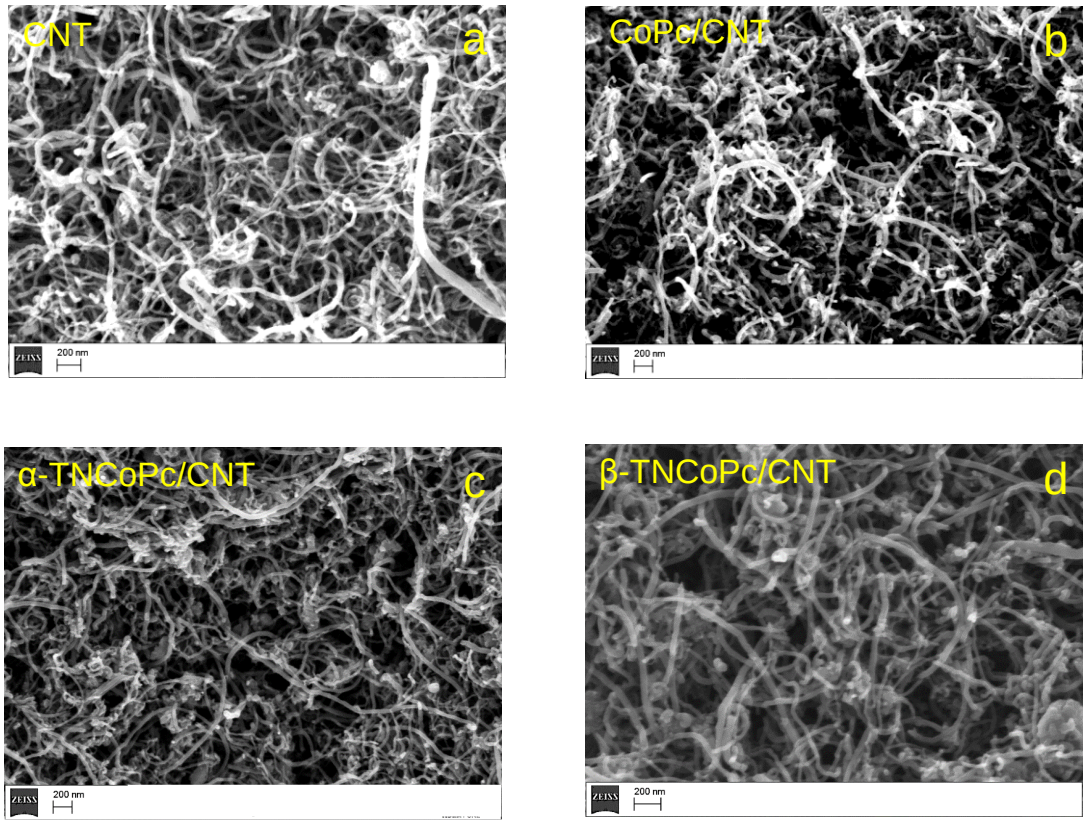


**Figure 3.5:** FE-SEM images of (a) CNT, (b) CoPc/CNT, (c) α-TNCoPc/CNT and (d) β-TNCoPc/CNT.

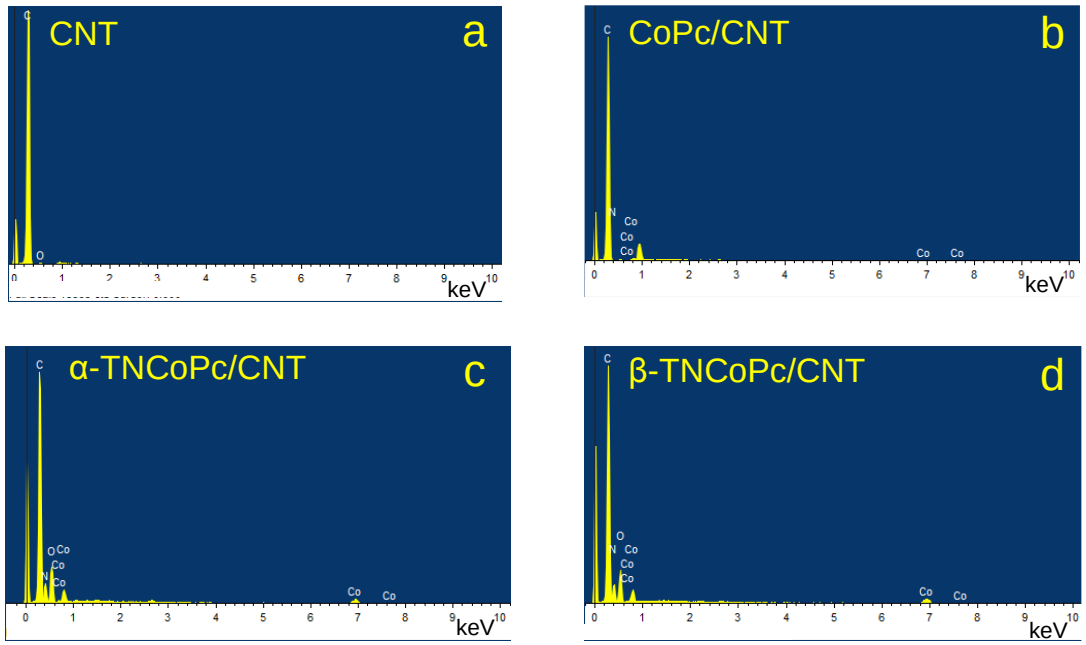


**Figure 3.6:** EDS pattern of (a) CNT, (b) CoPc/CNT, (c) α-TNCoPc/CNT and (d) β-TNCoPc/CNT.

### 3.2.2. Electrochemical analysis

Subsequently, α-TNCoPc/CNT and β-TNCoPc/CNT are investigated for their electrochemical activity toward various electrochemical oxidation reactions, such as the water splitting reaction, As (III) oxidation, ascorbic acid oxidation, uric acid oxidation, hydrogen peroxide oxidation, and cysteine oxidation (Figure 3.7). These were chosen as signature reactions to demonstrate the isomeric effects on electrocatalysis because of their well-known relevance in energy conversion and biological and environmental sectors.[8-10,36,37] Voltammograms (Figure 3.7) suggest that the β-TNCoPc isomer outperforms the corresponding α-TNCoPc isomer in terms of onset potential and the driving force (potential) required for achieving a particular current density (Table 3.1). To understand their long-term stability, durability and the driving force required to achieve a particular reaction rate (current density), chronopotentiometry (potential vs. time) analysis were carried out. The results shown in Figure 3.8 confirm an active and a durable β isomer compared to α isomer and unsubstituted CoPc (Figure 3.8). It is to be noted that the activity toward oxidation reactions upon substitution by an electron-withdrawing $-NO_2$ group has substantially improved, comparative voltammetry and chronopotentiometry with unsubstituted CoPc; however, the effect of regioisomerism is distinct in all the substrates with an active β isomer compared to the corresponding α isomer (Table 3.1, Figure 3.7 and 3.8).

In order to prove that this isomerism-dependent electrochemical activation is the pristine behavior of molecular electrocatalysts, these molecules were adsorbed as a monolayer on a glassy carbon (GC) electrode (see in chapter 2, section 2.6.3 and page 50). The adsorption step was monitored by the in-situ quartz crystal microbalance (QCM) technique (Figure 3.9), which indicated surface coverage values in the order of $10^{-11}$ mol/cm$^2$ (inset of Figure 3.9). This confirms that isomeric α and β-TNCoPc molecular catalysts were adsorbed as a monolayer with nearly a flat orientation on the GC electrode surface.[38,39] When these modified electrodes were used for the above-mentioned electrooxidation reactions, a similar trend with respect to the overpotential was observed (Figure 3.10) as that in Figure 3.7, which confirms that this oxidative activation is intrinsic to the molecules. In order to understand the chemical stability and integrity of molecular electrocatalysts in the long run, chronopotentiometric analysis were carried out for the water oxidation reaction for nearly 8 h with post electrochemical characterization of the electrodes (Figures 3.11a). The long term durability tests outlined in Figure 3.11 evidence the maintenance of higher activity by the β-

TNCoPc isomer over the α-TNCoPc and post electrochemical characterizations indicate stability of molecular catalysts on the electrode surface.

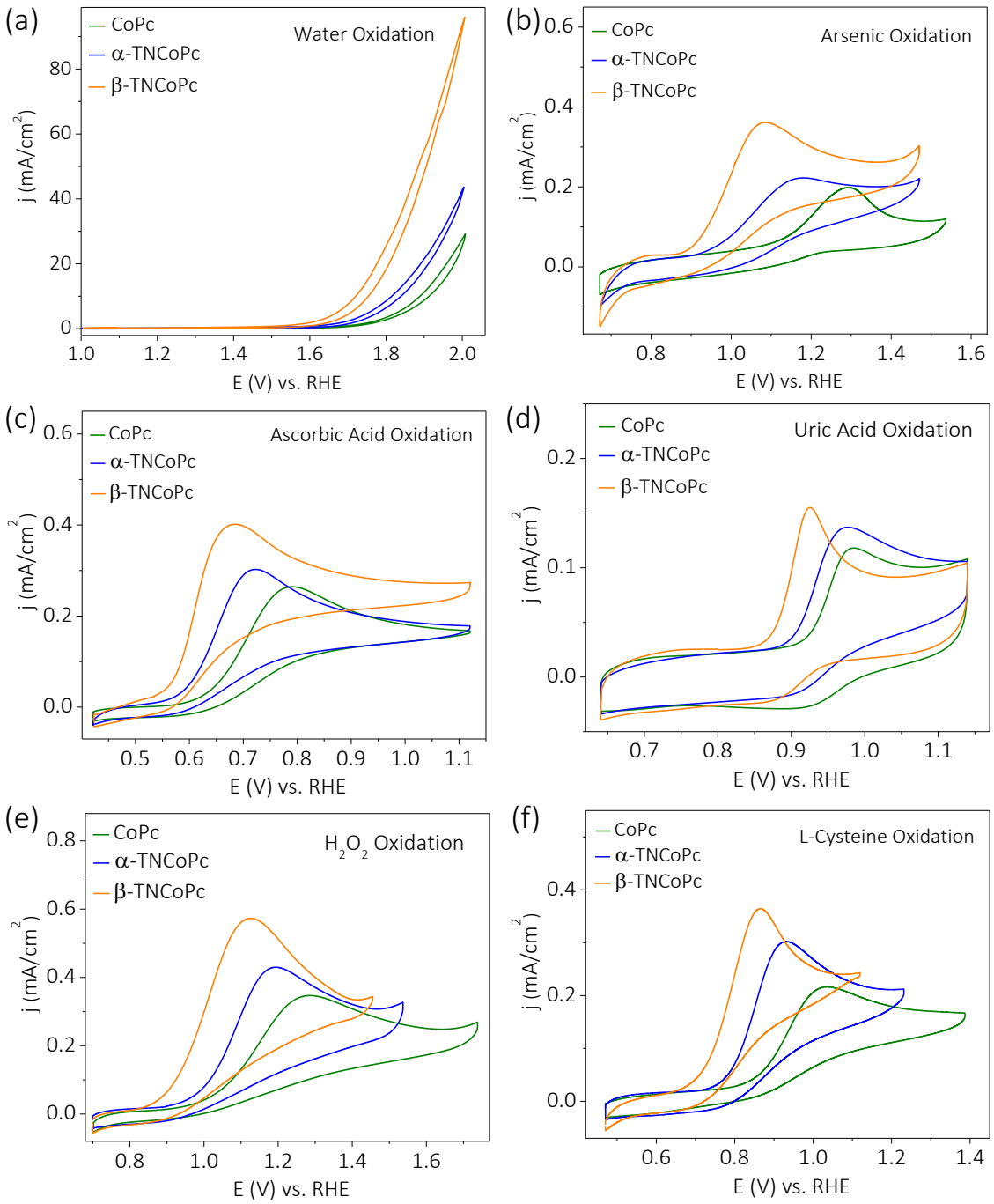


**Figure 3.7.** (a) Cyclic voltammograms recorded with unsubstituted CoPc and α and β-TNCoPc isomers anchored on CNT at a scan rate of 5 mV/s for the water oxidation reaction (pH = 14) at a rotation rate of 1600 RPM. Cyclic voltammograms recorded with unsubstituted CoPc and α and β-TNCoPc isomers at a scan rate of 10 mV/s in the presence of 1 mM concentrations of (b) arsenite (As(III)) in phosphate buffer (pH-8), (c) ascorbic acid in acetate buffer (pH-2), (d) uric acid in acetate buffer (pH = 4), (e) hydrogen peroxide in

phosphate buffer (pH-7), and (f) L-cysteine in acetate buffer (pH-4).

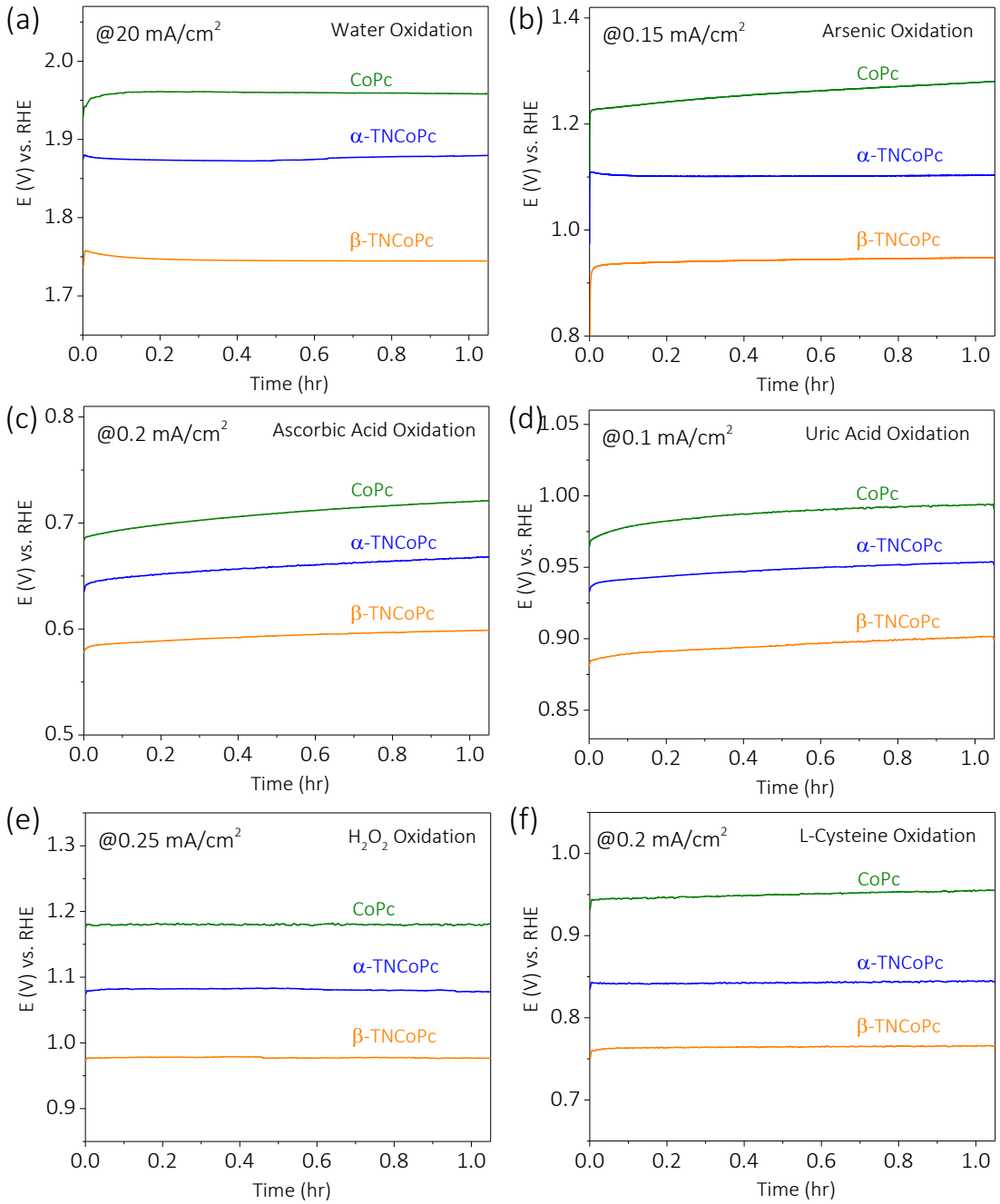


**Figure 3.8.** (a) Chronopotentiometric traces recorded with unsubstituted CoPc and α and β-TNCoPc isomers anchored on CNT for water oxidation reaction (pH=14). Chronopotentiometric traces recorded with unsubstituted CoPc and α and β-TNCoPc isomers in the presence of 1 mM concentrations of (b) As (III) in phosphate buffer (pH-8), (c) ascorbic acid in acetate buffer (pH-2), (d) uric acid in acetate buffer (pH=4), (e) hydrogen peroxide in phosphate buffer (pH-7) and (f) L-cysteine in acetate buffer (pH-4).

Table 3.1: Electrochemical parameters extracted from Figure 3.7 and 3.8.

| Electrodes | | CoPc | α-TNCoPc | β-TNCoPc |
|---|---|---|---|---|
| **Water Oxidation** | Onset Potential (V) vs. RHE | 1.76 ± 5*10 $^{-3}$ | 1.72 ± 3*10$^{-3}$ | 1.65 ± 6*10$^{-3}$ |
| | Potential (V) @ 20 mA/cm$^2$ | 1.97 ± 5*10$^{-3}$ | 1.91 ± 7*10$^{-3}$ | 1.72 ± 5*10$^{-3}$ |
| **Arsenic Oxidation** | Onset Potential (V) vs. RHE | 1.08 ± 5*10$^{-3}$ | 0.98 ± 5*10$^{-3}$ | 0.86 ± 4*10$^{-3}$ |
| | Potential (V) @ 0.15 mA/cm$^2$ | 1.25 ± 5*10-3 | 1.12 ± 7*10$^{-3}$ | 0.95 ± 4*10$^{-3}$ |
| **Ascorbic Acid Oxidation** | Onset Potential (V) vs. RHE | 0.62 ± 3*10$^{-3}$ | 0.59 ± 3*10$^{-3}$ | 0.55 ± 2*10$^{-3}$ |
| | Potential (V) @ 0.2 mA/cm$^2$ | 0.70 ± 6*10$^{-3}$ | 0.66 ± 2*10$^{-3}$ | 0.60 ± 3*10$^{-3}$ |
| **Uric Acid Oxidation** | Onset Potential (V) vs. RHE | 0.92 ± 3*10$^{-3}$ | 0.89 ± 3*10$^{-3}$ | 0.86 ± 2*10$^{-3}$ |
| | Potential (V) @ 0.1 mA/cm$^2$ | 0.97 ± 4*10$^{-3}$ | 0.94 ± 2*10$^{-3}$ | 0.90 ± 3*10$^{-3}$ |
| **$H_2O_2$ Oxidation** | Onset Potential (V) vs. RHE | 1.03 ± 4*10$^{-3}$ | 0.96 ± 2*10$^{-3}$ | 0.86 ± 3*10$^{-3}$ |
| | Potential (V) @ 0.25 mA/cm$^2$ | 1.20 ± 7*10$^{-3}$ | 1.09 ± 3*10$^{-3}$ | 0.99 ± 5*10$^{-3}$ |
| **L-Cysteine Oxidation** | Onset Potential (V) vs. RHE | 0.83 ± 5*10$^{-3}$ | 0.76 ± 5*10$^{-3}$ | 0.69 ± 3*10$^{-3}$ |
| | Potential (V) @ 0.15 mA/cm$^2$ | 0.97 ± 6*10$^{-3}$ | 0.85 ± 6*10$^{-3}$ | 0.76 ± 5*10$^{-3}$ |

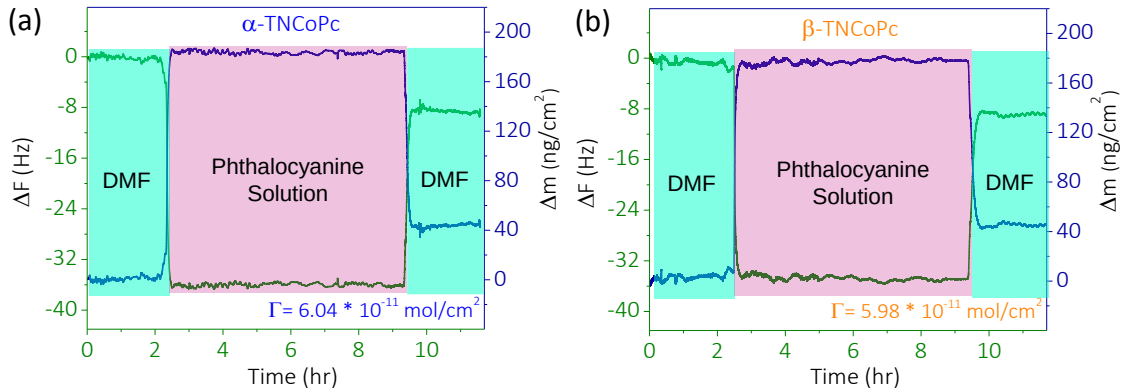


Figure 3.9: Quartz crystal microbalance (QCM) response during the adsorption of isomeric molecules from a 0.2 mM solution of (a) α-TNCoPc and (b) β-TNCoPc in dimethyl formamide (DMF). Green trace shows the frequency change during adsorption and the blue trance shows the mass change calculated using Saurbrey equation. Surface coverage (Γ) values of molecular catalysts extracted from QCM experiments are provided in respective images.

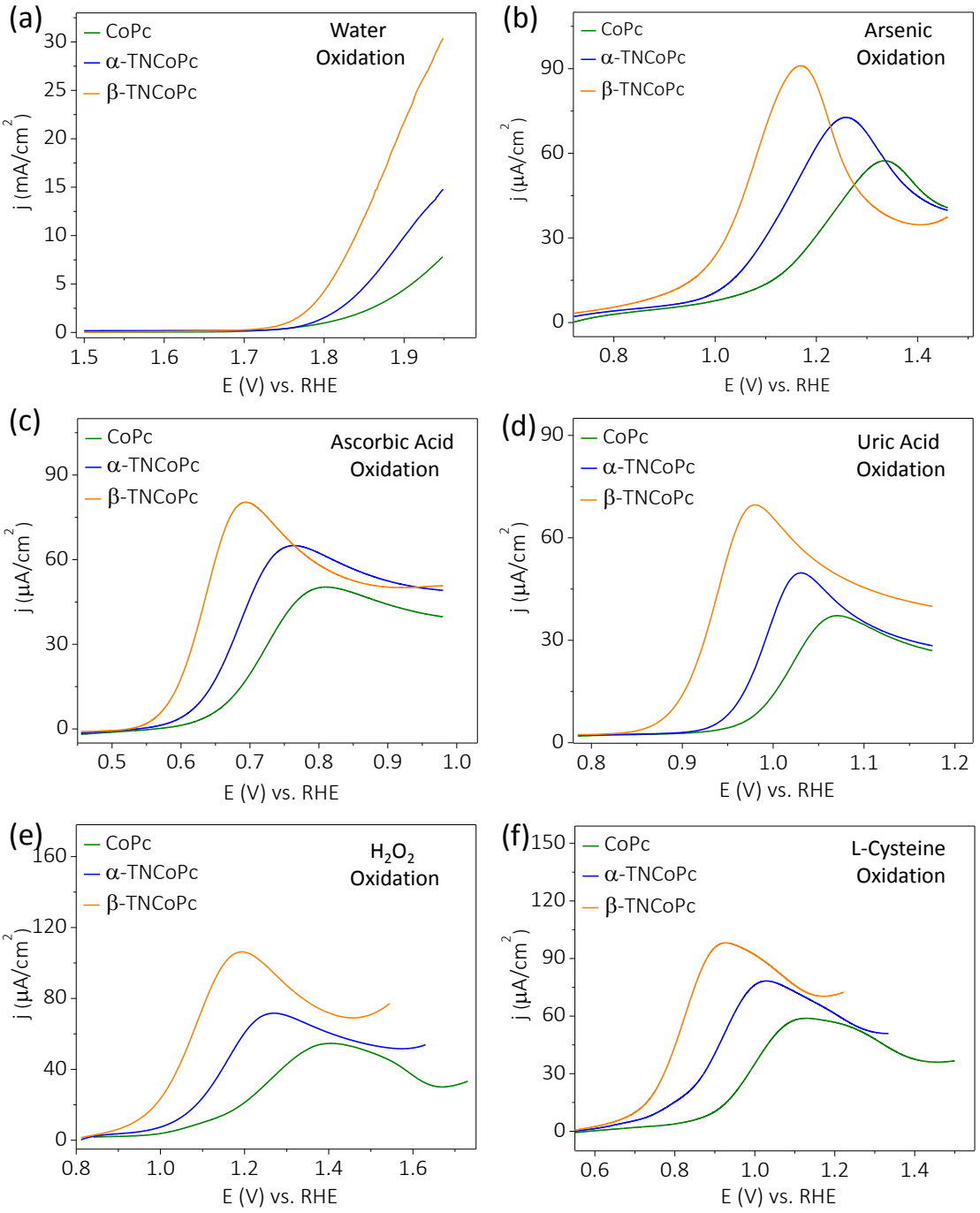


**Figure 3.10:** Voltammograms recorded with unsubstituted CoPc and α and β-TNCoPc isomers when they were adsorbed as a monolayer on a glassy carbon electrode surface. (a) Voltammograms recorded at 5 mV/s for the monolayer electrodes for water oxidation reaction in pH=14 alkaline solution at a rotation rate of 1600 RPM. Voltammograms recorded with monolayer of molecular catalysts at a scan rate of 10 mV/s in the presence of 1 mM concentrations of (b) arsenite in phosphate buffer (pH-8), (c) ascorbic acid in acetate buffer (pH-2), (d) uric acid in acetate buffer (pH=4), (e) hydrogen peroxide in phosphate buffer (pH-7) and (f) L-cysteine in acetate buffer (pH-4).

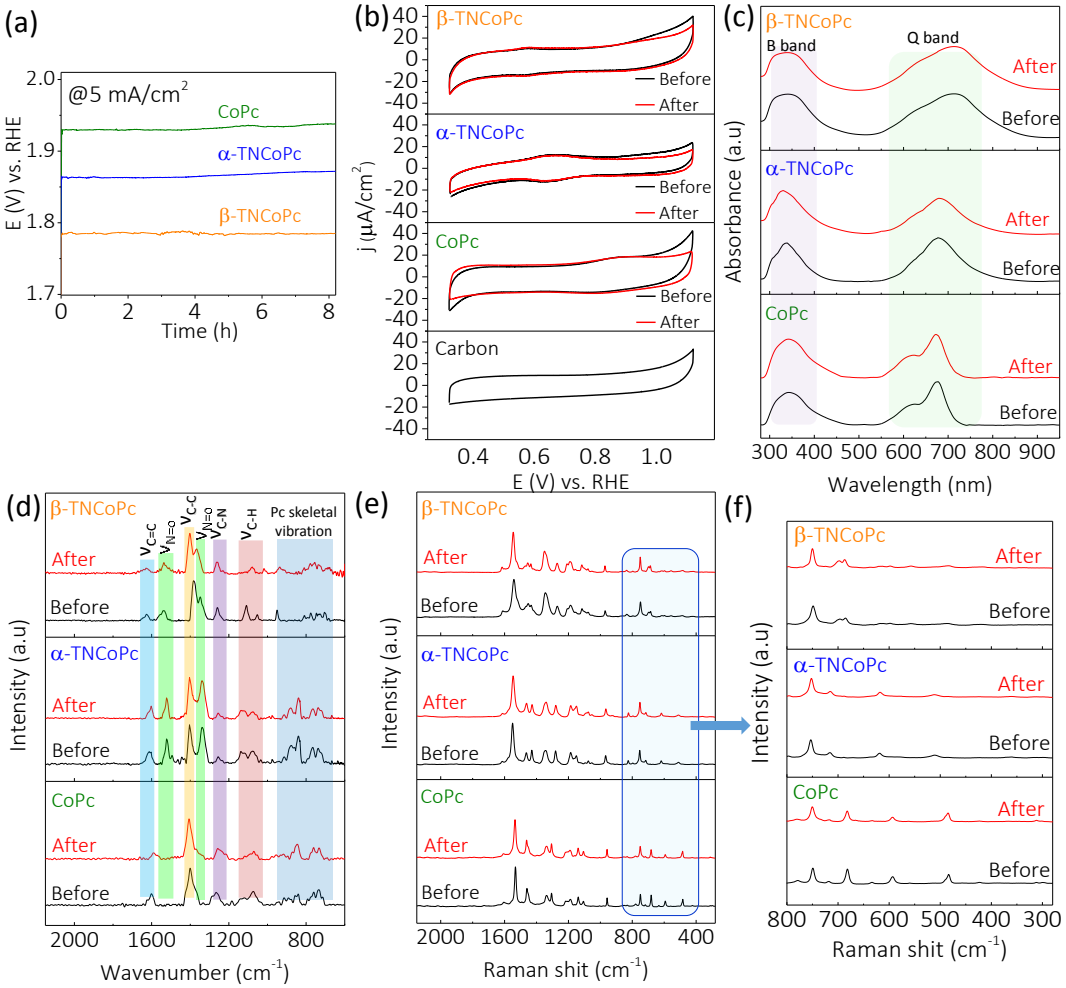


**Figure 3.11:** (a) Chronopotentiometric traces at 5 mA/cm² with unsubstituted CoPc and α and β-TNCoPc isomers when they are adsorbed as a monolayer on a glassy carbon electrode for water oxidation reaction (pH=14) at a rotation rate of 1600 RPM. (b) Cyclic voltammograms of CoPc and α and β-TNCoPc isomer at a scan rate of 10 mV/s in acetate buffer (pH-2) before and after prolonged water oxidation (at 5 mA/cm²) for 8 hours. For comparison, cyclic voltammetry of bare GC electrode is provided. (c) UV-Visible spectra, (d) FTIR spectra and (e) Raman spectra of CoPc and α and β-TNCoPc isomer molecules before and after prolonged water oxidation for 8 hours. (f) Represents the zoomed view of Figure 3.11e in the range of 800 to 280 $cm^{-1}$.

### 3.2.3. X-ray photoelectron spectroscopy study

In order to understand the origin of this activation, the catalytic system was examined by X-ray photoelectron spectroscopy (XPS). XPS analysis of unsubstituted CoPc (Figure 3.12a) demonstrated two deconvoluted peaks at binding energies of ~780.1 and ~781.6 eV corresponding to $Co^{2+}$ ($2p_{3/2}$) and $Co^{3+}$ ($2p_{3/2}$) species, respectively, along with a satellite

feature at ~789.2 eV, which is a distinguishing feature of $Co^{2+}$.[40-43] Similarly, α- and β-TNCoPc isomers exhibited peaks at similar binding energies; however, the relative contributions of $Co^{2+}$ (2p3/2) and $Co^{3+}$ (2p3/2) species were distinctly different with a higher $Co^{3+}/Co^{2+}$ ratio in favor of the β isomer (Figure 3.12a). The binding energy assignments are based on the available literature and on the clear peak broadening and asymmetry of the observed peaks in the Co 2p region.[42,43] It is to be noted that it is the partial charge on the cobalt that is changing while going from CoPc to the β isomer through the α isomer; however, this cannot be quantified precisely by XPS. Therefore, this is explained it in terms of an increase in the $Co^{3+}$ state by deconvolution of the raw spectra. Moreover, even the raw XPS data clearly show the increase in the positive nature of the central metal ion in the molecular catalyst in the order CoPc < α-TNCoPc < β-TNCoPc, which is evident from the peak shift of $2p_{3/2}$ from 780.2 (CoPc) to 781.8 eV (β- TNCoPc), Figure 3.12b. Further, the $Co^{3+}/Co^{2+}$ area ratio (Figure 3.12c) followed the order β-TNCoPc > α-TNCoPc > CoPc, which can be very well followed by the presence of a satellite feature at 789.2 eV (indicated by arrows), which more or less vanishes when the composition of $Co^{2+}$ in the catalyst decreases below 50% as compared to $Co^{3+}$ species. Taken together, XPS analysis suggests that regioisomerism of the $-NO_2$ group has a profound influence on the electron density experienced by the catalytic metal center. The XPS data suggest that, compared to the α position, the substitution of $-NO_2$ group at the β position contributes to electron withdrawal from the metal center to a greater extent (Figure 3.12), leading to a higher positive charge associated with the central metal ion. Therefore, the central Co metal ion experiences a greater electron-withdrawing environment in the β isomer compared to the α isomer, and this should activate the central metal ion towards electrochemical oxidation reactions (Figures 3.7, 3.8 and 3.10). This is because, on these types of molecular catalysts the electrochemical oxidation of various substrates (Figures 3.7, 3.8 and 3.10) proceeds in a pathway mediated by Co (III), as given in eqs 3.1 and 3.2.[44-46] Accordingly, the Co (II) center in the molecular catalyst gets electrochemically oxidized to Co (III) which in turn activates the substrate. However, we note that the exact fate of eq 3.1 and 3.2 depends heavily on the type of substrate as some of these reactions are highly mechanistically complicated and cannot be described by the reaction scheme shown in eq 3.1 and eq 3.2. The primary aim of this investigation is to establish an isomerism–activity relation in molecular electrocatalysis, and

an in-depth investigation of individual reaction mechanisms is therefore beyond the scope of the present chapter. It is known that during electrocatalytic oxidation of various substrates by unsubstituted CoPc, $Co^{3+}$ is the active species [47,48] and XPS data (Figure 3.12) signaled that its contribution is significantly enriched in the β isomer, Figure 3.12. Therefore, distinctly higher contribution of active catalytic species in the β isomer may accelerate the kinetics of the reaction, thereby enhancing the oxidative electrocatalysis of various substrates. Thus, the order of positive charge on the central metal ion and the order of their electrochemical activities are in coherence (Figures 3.7, 3.8, 3.10 and 3.12).

$$Co\ (II) \rightarrow Co\ (III) + e^{-} \ldots\ldots (3.1)$$

$$Co\ (III) + Substrates \rightarrow Co\ (II) + Products \ldots\ldots (3.2)$$

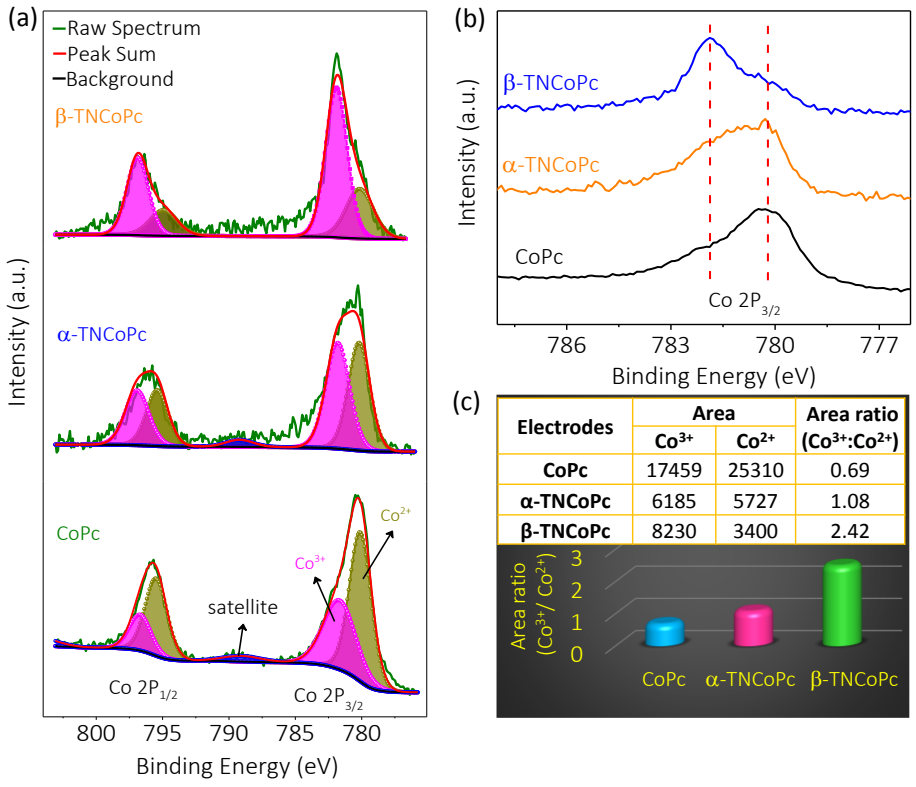


| Electrodes | Area | | Area ratio |
|---|---|---|---|
| | $Co^{3+}$ | $Co^{2+}$ | ($Co^{3+}$:$Co^{2+}$) |
| CoPc | 17459 | 25310 | 0.69 |
| α-TNCoPc | 6185 | 5727 | 1.08 |
| β-TNCoPc | 8230 | 3400 | 2.42 |

**Figure 3.12:** (a) X-ray photoelectron spectroscopy (XPS) of unsubstituted CoPc and α and β-TNCoPc isomers, (b) raw XPS spectra of molecular catalysts demonstrating a shift of Co $2P_{3/2}$ peak towards higher binding energies on moving from CoPc to β-TNCoPc through α-TNCoPc and (c) $Co^{3+}/Co^{2+}$ area ratio extracted from Co $2P_{3/2}$ region in Figure 3.12a.

### 3.2.4. Density functional theory (DFT) calculations

In order to answer the obvious question as to why the isomerism of the $–NO_2$ group

in the secondary sphere of the Pc leads to an oxidative activation of the catalytic metal centre, density functional theory calculations were performed (please refer to chapter 2, section 2.7 for more details, pages 50-51). It is to be noted that the $-NO_2$ group as the electron-withdrawing group at the $N_4$ macrocycle possesses both an electron-withdrawing inductive effect (-I) and electron-withdrawing resonance effect (-R). In the case of the β isomer, free rotation of the $-NO_2$ group along the axial bond is possible (Scheme 3.1). However, the preferable configuration of the $-NO_2$ group with respect to the $N_4$ macrocycle should be parallel because of the stability incurred from the cumulative influence of -I and -R effects (Scheme 3.1). In this configuration, the $N_4$ macrocycle should experience extensive electron delocalization toward the $-NO_2$ group (away from the central metal ion), as evidenced by UV–vis spectroscopy (Figure 3.2d), leading to oxidative activation of the catalytic center (XPS analysis, Figure 3.12). In the case of α isomer, a parallel configuration of the $-NO_2$ plane and $N_4$ macrocycle plane should lead to a dominant field effect due to repulsive electronic interactions between the O atom of $-NO_2$ group and the imine nitrogen of the Pc ring, making it a least stable configuration, Scheme 3.1. Therefore, in the most stable configuration, the $-NO_2$ group should be out of plane to the conjugative plane of the $N_4$ macrocycle (Scheme 3.1). Therefore, the field effect should restrict the rotation of the $-NO_2$ group in the α isomer, leading to a vanishing resonance effect between the $-NO_2$ plane and $N_4$ macrocycle plane (UV–vis spectra, Figure 3.2d). Consequently, the field effect should limit the oxidative activation of the catalytic metal center in the α isomer (XPS analysis, Figure 3.12). Hence, it can be argued that combined -R and -I effects in the β isomer make the electrocatalytic center experiencing a more electron-withdrawing environment compared to the α isomer, which has a vanishing -R effect. In order to strengthen these arguments, density functional theory (DFT) calculation on α and β isomers (Figures 3.13, 3.14 and Table 3.2) were performed. Upon comparison of the most stable structures of isomeric molecules, it was observed that the dihedral angle between the $N_4$ macrocycle plane and $-NO_2$ plane is 137.07° in the α isomer (Figure 3.13a; the path of the dihedral angle is highlighted with a red line). It indicates that the $-NO_2$ group (labeled as 3 in Figure 3.13a) is not in plane with the $N_4$ macrocycle plane, leading to a vanishing -R effect between them. On the other hand, in the most stable conformation of the β isomer, the dihedral angle between the $N_4$ macrocycle plane and $-NO_2$ plane is 179.99° (Figure 3.13b), which indicates

that the $-NO_2$ group and $N_4$ macrocycle are in plane. This allows the β isomer to experience the -R effect via electronic delocalization between the $N_4$ macrocyclic plane and $-NO_2$ plane. In the β isomer, this is reflected by a comparative decrease in energy gap (from 4.11 eV in the α-TNCoPc isomer to 3.73 eV in the β-TNCoPc isomer) between the highest occupied molecular orbital (HOMO) and lowest unoccupied molecular orbital (LUMO) (Figures 3.13, 3.14a and Table 3.2). It is reported in the literature that activity is directly correlated to chemical softness/hardness of the electrocatalysts.[49-51] Therefore, the oxidizability of cobalt species (Figure 3.12) and its higher electrochemical activity towards oxidation reactions in the β isomer compared to the α isomer (Figure 3.7, 3.8 and 3.10) can be correlated to its higher chemical softness and lower chemical hardness (Table 3.2). This higher chemical softness of the β isomer is reflected in their lower HOMO–LUMO gap (Figure 3.13, Figure 3.14a and Table 3.2).[50,51]

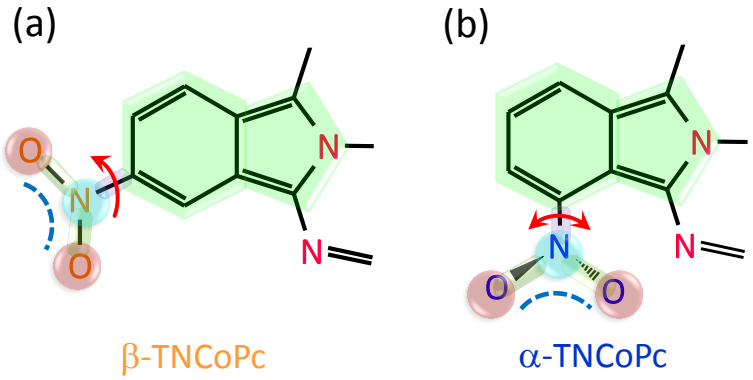


**Scheme 3.1:** Scheme depicting the relative configuration of $-NO_2$ plane with respect to $N_4$ macrocycle plane in α and β-TNCoPc isomers.

Geometrically, both the α and β-TNCoPc isomers in their most stable conformation (Figure 3.13) differ fundamentally by their point group symmetry; the former belongs to the $S_4$ point group and the latter to $C_4h$. Inherently, the most notable geometric property responsible for this change is the dihedral angle of the $-NO_2$ group in these isomers. Figure 3.14b,c depicts the variation of the dihedral angle with respect to the relative energy of isomeric molecules. For the α-TNCoPc isomer, a decrease in the dihedral angle from 179.99 to 137.07° when the relative energy of the molecule approaches zero suggests the cascading of oxygen atoms of the nitro group out of plane with respect to the $N_4$ macrocycle (Figure 3.14b). The reason for the α-TNCoPc isomer to be non-planar stems from the repulsion between valence shell lone-pair orbitals of iminic nitrogen (labeled as 2 in Figure 3.13a) and

the valence shell lone-pair orbitals of oxygen atoms of the $-NO_2$ groups (field effect, as noted earlier) due to their spatial proximity. This is substantiated by the increase in distance between the iminic nitrogen atoms (of the macrocycle) to the oxygen atoms of $-NO_2$ groups from 2.615 Å in the initial geometry to 2.878 Å in the ground-state geometry (Figure 3.14d). Therefore, in the most stable conformation of the α-TNCoPc isomer, the molecule possesses a nonplanar geometry with $S_4$ point group symmetry. However, in the β-TNCoPc isomer, because the field effect is less dominant as the $-NO_2$ group is farther away from iminic nitrogen, it stays in plane to the $N_4$ macrocycle plane as the molecule approaches the local minima on the potential energy surface (Figure 3.14c). This makes the β-TNCoPc isomer planar with $C_4h$ point group symmetry. Further, electronegativity (χ) analysis of the isomers (Table 3.2) reflects a higher χ value for the β-TNCoPc isomer (5.285) than the α-$NO_2$ isomer (4.677), indicating that in the former both -I and -R effects are active due to its planar geometry and in the latter the field effect and consequently its non-planar geometry eventually lead to a vanishing -R effect.

Charge population analysis were carried out by three methods, natural bond orbital analysis (NBO) and Mulliken and Hirshfeld charge population schemes (Table 3.2), to further support this argument. Despite the difference in the numerical values of charges on cobalt (due to different population analysis), they nevertheless carry a mutual trend. From NBO analysis, the positive charge density on the cobalt was higher (ca. NBO charge is 0.753) in the β isomer than that in the α isomer (NBO charge is 0.516), and the 3d orbital occupancies (from NBO) in α and β-TNCoPc isomers were found to be 7.87 and 7.60, respectively, suggesting that due to the combined -I and -R effect the d- orbital occupancy of the Co atom in the β-TNCoPc isomer is less than that of the α-TNCoPc isomer. It should be noted that the catalytically active species in all of the reactions probed in Figure 3.7, 3.8 and 3.10 are $Co^{3+}$, and consequently, the positive charge density of the catalytic metal centre should define the activity of the molecular electrocatalysts. Taken together, the DFT calculations support the argument that the β isomer is under the cumulative influence of -R and -I effects due to its planar geometry and the α isomer experiences dominantly a -I effect and a vanishing -R effect due to the $-NO_2$ group's out-of-plane geometry. These eventually lead to a comparatively higher oxidative activation of the catalytic metal centre in the β-TNCoPc isomer compared to the α-TNCoPc isomer.

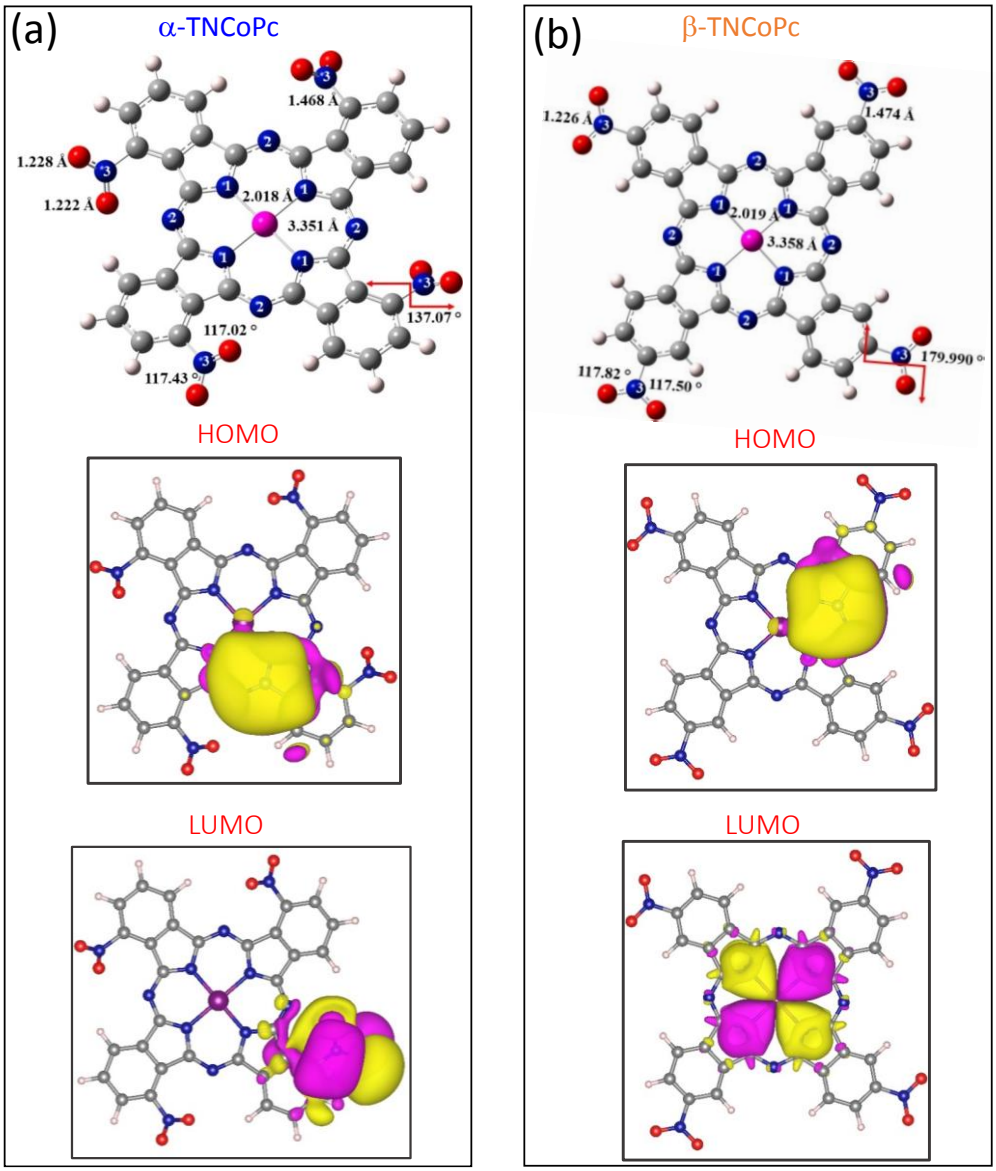


**Figure 3.13:** Stable geometry of (a) α-TNCoPc isomer and (b) β-TNCoPc isomer from DFT calculations along with the electronic properties of HOMO and LUMO. Nitrogen atoms are labelled in their stable geometry: N1: pyrrole-nitrogen atoms, N2: iminic-nitrogen atoms and N3: nitrogen atom of $NO_2$ groups. Yellow and pink colors indicate the positive and negative lobes of the orbital surfaces.

As discussed earlier, $Co^{3+}$ is the active species during the electrochemical oxidation of various substrates on these molecular catalysts, and spectroscopic analysis (Figures 3.2d and 3.12) and theoretical calculations (Figure 3.13 and 3.14) reflect that its contribution is distinctly higher on the β isomer due to combined -R and -I effects as a result of its planar geometry. On the other hand, the nonplanar geometry of the α isomer restricts the accumulation of active species in the catalytic center due to a vanishing -R effect. Therefore,

isomerism of $-NO_2$ groups at the $N_4$ macrocycle redefines the electronic arrangement in the entire molecule via geometrical factors, which in turn leads to oxidative activation of the catalytic metal center. The research in molecular electrocatalysis to date has tended to focus only on how the chemical identity of substituents affects the electronic arrangement and electrocatalysis, with far too little attention paid to their isomerism-dependent electronic perturbations. This study unambiguously reveals that isomerism of substituents offers an additional contribution to electrocatalysis over its chemical identity and provides a clear distinction between the nature of groups and their isomerism in molecular electrocatalysis.

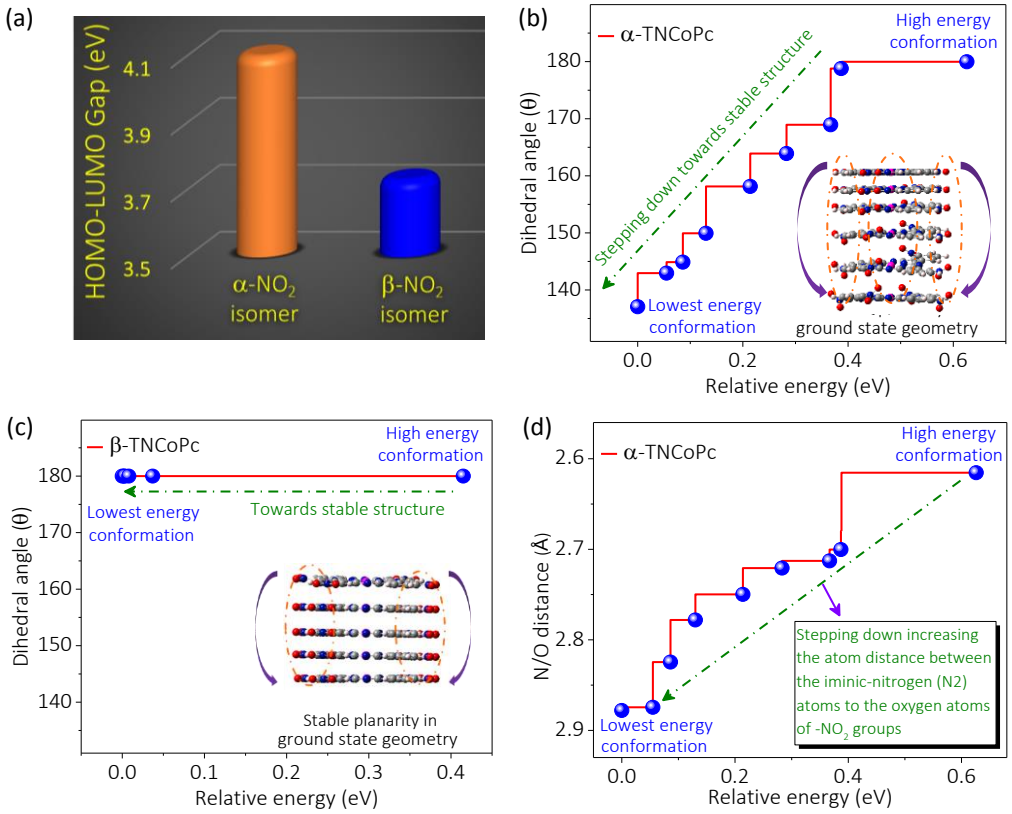


**Figure 3.14:** (a) HOMO–LUMO gap of α-TNCoPc isomer and β-TNCoPc isomer in their most stable conformation. The plot of dihedral angle vs. relative energy for (b) α-TNCoPc isomer and (c) β-TNCoPc isomer. Insets of Figure 3.14b and 3.14c: The orange colored curvature depict the cascading of oxygen atoms of -$NO_2$ group towards non-planar geometry for α-TNCoPc isomer and planar geometry for β-TNCoPc isomer. (d) The plot of N/O distance between the iminic-nitrogen atoms (N2 in Figure 3.13) and the oxygen atoms of -$NO_2$ groups (N3 in Figure 3.13) vs. relative energy for α-TNCoPc isomer.

**Table 3.2:** The data derived from DFT calculations. The parameters are extracted from Figure 3.13.

| System | | α-TNCoPc | β-TNCoPc |
|---|---|---|---|
| HOMO-LUMO Gap (eV) | | 4.110 | 3.730 |
| Chemical Hardness, η (eV) | | 2.055 | 1.865 |
| Chemical Softness, 1/η (eV) | | 0.486 | 0.536 |
| Electronegativity, χ | | 4.677 | 5.285 |
| Chemical Potential, μ | | -4.677 | -5.285 |
| Global Electrophilicity Index, ω | | 5.322 | 7.490 |
| Dihedral angle | | 137.07° | 179.990° |
| Charge on Cobalt | Hirshfeld | 0.100 | 0.220 |
| | Mulliken | 0.495 | 0.590 |
| | NBO | 0.516 | 0.753 |
| 3d-orbital occupancy | | 7.87 | 7.60 |

## 3.3. Conclusions

In this Chapter, the central role of isomerism of secondary sphere functionality for electrocatalytic reactions ranging from energy conversion to biosensing was investigated when regioisomerism of the $-NO_2$ substituent is conferred at the α and β positions on the $N_4$ macrocycle of molecular electrocatalysts. Electrochemical and spectroscopic analyses and theoretical calculations established that the regioisomerism of the $-NO_2$ substituent at the β position of the $N_4$ macrocycle forces the entire molecule to be planar, which facilitates oxidative activation of the catalytic center via a cumulative influence of inductive and resonance effects. On the other hand, the field effect in the α isomer favors the $-NO_2$ plane to cascade away from the $N_4$ macrocycle plane, which in turn restricts this oxidative activation due to a vanishing resonance effect. This study brings to light a crucial factor that is often overlooked in electrocatalysis that isomerism of substituents can redefine the electronic arrangement in the catalytic center and make an additional contribution to electrocatalysis

over its chemical identity. This investigation unambiguously proves that, while the nature of the substituent is fundamental for enhancing the electrocatalysis, its isomerism-induced contribution offers an elegant approach for reinvigorating the catalytic center for various reactions ranging from energy conversion to biosensing. We note that across the spectrochemical series this isomerism–activity relation is strongly substituent-specific, which demands insightful studies with respect to a specific substituent itself to understand the origin of its isomerism-induced activation. For example, it has been observed that non-covalent interactions often interlink the chemical identity of substituents and their isomerism with electrochemical activation, leading to unprecedented events in electrocatalysis and energy storage which will be discussed in subsequent chapters.

## 3.4. References

[1] Löffler, T.; Meyer, H.; Savan, A.; Wilde, P.; Garzón Manjón, A.; Chen, Y. T.; Ventosa, E.; Scheu, C.; Ludwig, A.; Schuhmann, W. Discovery of a Multinary Noble Metal–Free Oxygen Reduction Catalyst. *Adv. Energy Mater.* **2018**, *1802269*, 1–7.

[2] Liang, Y.; McLaughlin, D.; Csoklich, C.; Schneider, O.; Bandarenka, A. S. The Nature of Active Centers Catalyzing Oxygen Electro-Reduction at Platinum Surfaces in Alkaline Media. *Energy Environ. Sci.* **2019**, *12* (1), 351–357.

[3] Costentin, C.; Savéant, J. M. Towards an Intelligent Design of Molecular Electrocatalysts. *Nat. Rev. Chem.* **2017**, *1* (11), 1–8.

[4] Vaddypally, S.; Tomlinson, W.; O'Sullivan, O. T.; Ding, R.; Van Vliet, M. M.; Wayland, B. B.; Hooper, J. P.; Zdilla, M. J. Activation of C-H, N-H, and O-H Bonds via Proton-Coupled Electron Transfer to a Mn (III) Complex of Redox-Noninnocent Octaazacyclotetradecadiene, a Catenated-Nitrogen Macrocyclic Ligand. *J.Am.Chem.Soc.* **2019**, *141* (14), 5699–5709.

[5] Chen, H.; Cai, R.; Patel, J.; Dong, F.; Chen, H.; Minteer, S. D. Upgraded Bioelectrocatalytic $N_2$ Fixation: From N2 to Chiral Amine Intermediates. *J. Am. Chem. Soc.* 2019, 141 (12), 4963–4971.

[6] Sunarso, J.; Glushenkov, A. M.; Torriero, A. A. J.; Howlett, P. C.; Chen, Y.; MacFarlane, D. R.; Forsyth, M. Bi-Functional Water/Oxygen Electrocatalyst Based on PdO-$RuO_2$ Composites . *J. Electrochem. Soc.* **2013**, *160* (1), H74–H79.

[7] Zagal, J.H.; Bedioui, F.; Dodelet, J. P. *$N_4$-macrocyclic metal complexes.* Springer, New York. **2006.**

[8] Wan, X.; Liu, X.; Li, Y.; Yu, R.; Zheng, L.; Yan, W.; Wang, H.; Xu, M.; Shui, J. Fe–N–C Electrocatalyst with Dense Active Sites and Efficient Mass Transport for High-Performance Proton Exchange Membrane Fuel Cells. *Nat. Catal.* **2019**, *2* (3), 259–268.

[9] Sorokin, A. B. Phthalocyanine Metal Complexes in Catalysis. *Chem. Rev.* **2013**, *113* (10), 8152–8191.

[10] Sobbi, A. K.; Wöhrle, D.; Schlettwein, D. Photochemical Stability of Various Porphyrins in Solution and as Thin Film Electrodes. *J. Chem. Soc., Perkin Trans. 2* **1993**, No. 3, 481–488.

[11] Rigsby, M. L.; Wasylenko, D. J.; Pegis, M. L.; Mayer, J. M. Medium Effects Are as Important as Catalyst Design for Selectivity in Electrocatalytic Oxygen Reduction by Iron-Porphyrin Complexes. *J. Am. Chem. Soc.* **2015**, *137* (13), 4296–4299.

[12] Bottari, G.; de la Torre, G.; Guldi, D. M.; Torres, T. Covalent and Noncovalent Phthalocyanine–Carbon Nanostructure Systems: Synthesis, Photoinduced Electron Transfer, and Application to Molecular Photovoltaics. *Chem. Rev.* **2010**, *110* (11), 6768–6816.

[13] Wang, J.; Huang, X.; Xi, S.; Lee, J.-M.; Wang, C.; Du, Y.; Wang, X. Linkage Effect in the Heterogenization of Cobalt Complexes by Doped Graphene for Electrocatalytic $CO_2$ Reduction. *Angew. Chemie Int. Ed.* **2019**, 58 (38), 13532–13539.

[14] Li, R.; Zhang, X.; Zhu, P.; Ng, D. K. P.; Kobayashi, N.; Jiang, J. Electron-Donating or -Withdrawing Nature of Substituents Revealed by the Electrochemistry of Metal-Free Phthalocyanines. *Inorg. Chem.* **2006**, *45* (5), 2327–2334.

[15] Zagal, J. H.; Koper, M. T. M. Reactivity Descriptors for the Activity of Molecular MN4 Catalysts for the Oxygen Reduction Reaction. *Angew. Chemie - Int. Ed.* **2016**, *55* (47), 14510–14521.

[16] Silva, N.; Calderón, S.; Páez, M. A.; Oyarzún, M. P.; Koper, M. T. M.; Zagal, J. H. Probing the Fe N + /Fe (N −1)+ Redox Potential of Fe Phthalocyanines and Fe Porphyrins as a Reactivity Descriptor in the Electrochemical Oxidation of Cysteamine. *J. Electroanal. Chem.* **2018**, *819* (August 2017), 502–510.

[17] Rajić, N. Z.; Stojaković, D. R. Synthesis and Characterization of Some Nitro-Substituted Phthalocyanines of Nickel(II), Cobalt(II) and Copper(II). *J. Coord. Chem.* **2009**, *19* (4), 295–301.

[18] Raja, R.; Ratnasamy, P. Selective Oxidation of Phenols Using Copper Complexes Encapsulated in Zeolites. *Applied Catalysis A: General,* **1996**, *143*, 145–158.

[19] Al-lami, A. K. a; Majeed, N. N.; Al-mowali, A. H. Synthesis, Mesomorphic and Molar Conductivity Studies of Some Macrocyclic Phthalocyanine Palladium (II). *Chemistry and Materials Research*. **2013**, *3* (4), 59–68.

[20] Lukyanets, E. A.; Nemykin, V. N. The Key Role of Peripheral Substituents in the Chemistry of Phthalocyanines and Their Analogs. *J. Porphyr. Phthalocyanines* **2010**, *14* (1), 1–40.

[21] Kottaichamy, A. R.; Makri Nimbegondi Kotresh, H.; Devendrachari, M. C.; Thimmappa, R.; Paswan, B.; Tiwari, O.; Chanda, V.; Gaikwad, P.; Thotiyl, M. O. Effects of Electrochemical Tailoring of Monolayers on a Catalytic Redox Entity: An ON-OFF Phenomenon Regulated by the Surrounding Medium. *J. Phys. Chem. C* **2015**, *119* (51), 28276–28284.

[22] Panwar, V.; Kumar, P.; Ray, S. S.; Jain, S. L. Organic Inorganic Hybrid Cobalt Phthalocyanine / Polyaniline as Efficient Catalyst for Aerobic Oxidation of Alcohols in Liquid Phase. *Tetrahedron Lett.* **2015**, *56* (25), 3948–3953.

[23] Kobayashi, N.; Miwa, H.; Nemykin, V. N. Adjacent versus Opposite Type Di-Aromatic Ring-Fused Phthalocyanine Derivatives: Synthesis, Spectroscopy, Electrochemistry, and Molecular Orbital Calculations. *J. Am. Chem. Soc.* **2002**, *124* (27), 8007–8020.

[24] Chauhan, D.; Kumar, P.; Joshi, C.; Labhsetwar, N.; Ganguly, S. K.; Jain, S. L. Photo-Assisted Oxidation of Thiols to Disulfides Using cobalt “Nanorust” under Visible Light. *New J. Chem.* **2015**, *39* (8), 6193–6200.

[25] Zhu, L.; Jing, X.; Song, L.; Liu, B.; Zhou, Y.; Xiang, Y. Solid-Phase Synthesis and Catalytic Sweetening Performance of Sulfonated Cobalt Phthalocyanine from Sulfonated Phthalic Anhydride Mixture. *New J. Chem.* **2014**, 663–668.

[26] Burcu, B.; Gündüz, G.; Mavis, B.; Çolak, Ü. Dyes and Pigments Synthesis and Characterization of Copper Phthalocyanine and Tetracarboxamide Copper Phthalocyanine Deposited Mica-Titania Pigments. *Dye. Pigment.* **2013**, *96* (1), 31–37.

[27] Georgescu, R.; Boscornea, C.; Calinescu, I.; State, R. Raman, IR and UV-Vis Spectroscopic Investigations of Some Substituted Phthalocyanines. *Rev. Chim.* **2016**, *10*, 1554-1557.

[28] Lokesh, K. S.; Adriaens, A. Dyes and Pigments Synthesis and Characterization of Tetra-Substituted Palladium Phthalocyanine Complexes. *Dye. Pigment.* **2013**, *96* (1), 269–277.

[29] Cong, F.; Ning, B.; Du, X.; Ma, C.; Yu, H.; Chen, B. Facile Synthesis , Characterization and Property Comparisons of Tetraaminometallophthylocyanines with and without Intramolecular Hydrogen Bonds. *Dye. Pigment.* **2005**, *66*, 1–6.

[30] Zhang, X.; Li, X.; Niu, L.; Sun, L.; Liu, L. Charge Transfer Photophysics of Tetra (α - Amino) Zinc Phthalocyanine Charge Transfer Photophysics of Tetra (α -Amino) Zinc. *J Fluoresc*, **2009**, *19*, 947-954.

[31] Abbaspour, A.; Mirahmadi, E. Electrocatalytic Activity of Iron and Nickel Phthalocyanines Supported on Multi-Walled Carbon Nanotubes towards Oxygen Evolution Reaction. *Electrochim. Acta* **2013**, *105*, 92–98.

[32] Chidembo, A. T.; Ozoemena, K. I.; Agboola, B. O.; Gupta, V.; Wildgoose, G.; Compton, R. G. Nickel (II) Tetra-Aminophthalocyanine Modified MWCNTs as Potential Nanocomposite Materials for the Development of Supercapacitors *Energy Environ. Sci.,* **2010**, 228–236.

[33] Zhang, M.; Gorski, W. Electrochemical Sensing Platform Based on the Carbon Nanotubes / Redox Mediators-Biopolymer System. *J. Am. Chem. Soc.* **2005**, *127*, 2058–2059.

[34] Zhang, X.; Wu, Z.; Zhang, X.; Li, L.; Li, Y.; Xu, H.; Li, X.; Yu, X.; Zhang, Z.; Liang, Y.; et al. Highly Selective and Active CO2 Reduction Electrocatalysts Based on Cobalt Phthalocyanine/carbon Nanotube Hybrid Structures. *Nat. Commun.* **2017**, *8* , 14675.

[35] Zhu, J.; Li, Y.; Chen, Y.; Wang, J.; Zhang, B.; Zhang, J.; Blau, W. J. Graphene Oxide Covalently Functionalized with Zinc Phthalocyanine for Broadband Optical Limiting. *Carbon N. Y.* **2011**, *49* (6), 1900–1905.

[36] Yuan, B.; Wang, H.; Cai, J.; Peng, Y.; Niu, Y.; Chen, H.; Bai, L.; Zhang, S.; Jin, J.; Liu, L.; et al. A Novel Oxidation-Reduction Method for Highly Selective Detection of Cysteine over Reduced Glutathione Based on Synergistic Effect of Fully Fluorinated Cobalt Phthalocyanine and Ordered Mesoporous Carbon. *Sensors Actuators, B Chem.* **2019**, *288*, 180–187.

[37] Lim, C. S.; Chua, C. K.; Pumera, M. Detection of Biomarkers with Graphene Nanoplatelets and Nanoribbons. *Analyst* **2014**, *139* (5), 1072–1080.

[38] Somashekarappa, M. P.; Keshavayya, J.; Sampath, S. Self-Assembled Molecular Films of Tetraamino Metal (Co, Cu, Fe) Phthalocyanines on Gold and Silver. Electrochemical and Spectroscopic Characterization. *Pure Appl. Chem.* **2002**, *74* (9), 1609–1620.

[39] Makinde, Z. O.; Louzada, M.; Mashazi, P.; Nyokong, T.; Khene, S. Electrocatalytic Behaviour of Surface Confined Pentanethio Cobalt (II) Binuclear Phthalocyanines towards the Oxidation of 4-Chlorophenol. *Appl. Surf. Sci.* **2017**, *425*, 702–712.

[40] Arechederra, R. L.; Artyushkova, K.; Atanassov, P.; Minteer, S. D. Growth of Phthalocyanine Doped and Undoped Nanotubes Using Mild Synthesis Conditions for Development of Novel Oxygen Reduction Catalysts. *ACS Appl. Mater. Interfaces* **2010**, *2* (11), 3295–3302.

[41] Gu, W.; Hu, L.; Hong, W.; Jia, X.; Li, J.; Wang, E. Noble-Metal-Free Co3S4-S/G Porous Hybrids as an Efficient Electrocatalyst for Oxygen Reduction Reaction. *Chem. Sci.* **2016**, *7* (7), 4167–4173.

[42] Venegas, R.; Recio, F. J.; Zuñiga, C.; Viera, M.; Oyarzún, M. P.; Silva, N.; Neira, K.; Marco, J. F.; Zagal, J. H.; Tasca, F. Comparison of the Catalytic Activity for $O_2$ Reduction of Fe and Co MN4 Adsorbed on Graphite Electrodes and on Carbon Nanotubes. *Phys. Chem. Chem. Phys.* **2017**, *19* (31), 20441–20450.

[43] Li, C.; Huang, T.; Huang, Z.; Sun, J.; Zong, C.; Yang, J.; Deng, W.; Dai, F. A sulfonated cobalt phthalocyanine/carbon nanotube hybrid as a bifunctional oxygen electrocatalyst *Dalton Trans.,* **2019**, *48,* 17258-17265.

[44] Sehlotho, N.; Nyokong, T. Electrocatalytic Oxidation of Thiocyanate, L-Cysteine and 2-Mercaptoethanol by Self-Assembled Monolayer of Cobalt Tetraethoxy Thiophene Phthalocyanine. *Electrochim. Acta* **2006**, *51* (21), 4463–4470.

[45] Salimi, A.; Mamkhezri, H.; Hallaj, R.; Soltanian, S. Electrochemical Detection of Trace Amount of arsenic (III) at Glassy Carbon Electrode Modified with Cobalt Oxide Nanoparticles. *Sensors Actuators, B Chem.* **2008**, *129* (1), 246–254.

[46] Caro, C. A.; Bedioui, F.; Zagal, J. H. Electrocatalytic Oxidation of Nitrite on a Vitreous Carbon Electrode Modified with Cobalt Phthalocyanine. *Electrochim. Acta* **2002**, *47* (9), 1489–1494.

[47] Maree, S.; Nyokong, T. Electrocatalytic Behavior of Substituted Cobalt Phthalocyanines towards the Oxidation of Cysteine. *J. Electroanal. Chem.* **2000**, *492* (2), 120–127.

[48] Zúñiga, C.; Tasca, F.; Calderon, S.; Farías, D.; Recio, F. J.; Zagal, J. H. Reactivity Indexes for the Electrocatalytic Oxidation of Hydrogen Peroxide Promoted by Several Ligand-Substituted and Unsubstituted Co Phthalocyanines Adsorbed on Graphite. *J. Electroanal. Chem.* **2016**, *765*, 22–29.

[49] Ralph G. P. Hard and Soft Acids and Bases *J. Am. Chem. Soc.* 1**963**, *85 (22)*, 3533-3539.

[50] Ralph G. P. The Principle of Maximum Hardness *Acc. Chem. Res.* **1993**, *26*, 250–255.

[51] Ralph G. P. Chemical Hardness, Wiley-VCH, Weinheim, **1997**.

# Chapter-4

## Geometrical Isomerism Directed Electrochemical Sensing

**Abstract**: In this Chapter, the independent role of isomerism of secondary sphere substituents over their nature in molecular electrocatalysis pertaining to electrochemical sensing is discussed. This study establishes that isomerism redefines the electronic structure at the catalytic reaction center via geometrical factors. UV–Vis spectroscopy and X-ray photoelectron spectroscopy suggest that a substituent's isomerism in molecular catalysts conjoins molecular planarity and catalytic activation through competing field effects and resonance effects. As a classical example, the influence of regioisomerism of the $-NO_2$ substituents for the electrocatalytic multi electron oxidation of Arsenic (III); a potentially important electrochemical pathway for water remediation and arsenic detection is demonstrated. The isomerism dependent oxidative activation of catalytic center leads to a nonprecious molecular catalyst capable for direct arsenic (III) oxidation with an experimental detection limit close to WHO guidelines. This isomerism induced activation of catalytic metal centre in molecular electrocatalysts opens up an unusual approach in analytical chemistry for developing various sensing platforms for challenging chemical and electrochemical reactions.

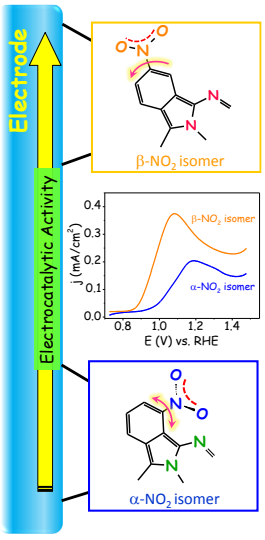


The work outlined in this chapter has been published in the following journal.

Alagar Raja K. et al., *Anal. Chem.* **2020**, *92, 6,* 4541-4547. Copyright American Chemical Society.

## 4.1. Introduction

Arsenic (III) is a toxic heavy element and a severe water contaminant in several parts of the world.[1–3] Since arsenic exposure can lead to chronic health complications like internal organ failure, cancer, atherosclerosis, etc., (Figure 4.1), the WHO guidelines restrict the permissible arsenic levels in drinking water to <10 ppb.[4–6] Arsenic exists in a variety of forms in drinking water. However, its trivalent arsenite and pentavalent arsenate are the most common forms in drinking water.[7–9] The former is generally perceived as the most toxic arsenic form in drinking water.[10] Therefore, its detection is of immense importance in the analytical field, and electrochemical methodologies are particularly attractive because of their capability for trace detection and field analysis.[11–14] It is known that, conventional electrochemical sensing of arsenic by a stripping method, however, suffers from serious interferences from other metallic ions such as Cu.[13,15–18] Researchers have developed various electrodes and sensing strategies to nullify the effect of interfering ions, and direct oxidation of arsenic (III) is found to be an efficient pathway in suppressing the response of interfering ions.[13,19–22] However, this direct oxidation of arsenic from As (III) to As (V) is often achieved over noble metal electrocatalysts,[23,24] such as gold, platinum and iridium based electrodes which were reported to result in better sensitivity for arsenic sensing in the potential range of 0.7–0.8 V (vs. SCE).[25] There have been lot of attempts to develop non-precious electrocatalytic platforms like $CoO_x$ nanoparticles, iron based catalysts, modified Hg electrodes, Prussian blue based screen printed electrodes, etc., for oxidizing arsenic (III) species.[26-28] However, their high overpotentials are close to the water decomposition potential which may also cause serious interferences from other metallic and organic species. Here, an approach based on the isomerism of substituents (Figure 4.2) in the secondary sphere of molecular electrocatalysts is presented for designing an active and a non-precious sensing platform for the direct oxidation of arsenic (III) with an experimental detection limit close to the WHO guidelines. The isomerism governed activation of the catalytic Co center leads to a non-precious sensing platform capable for multielectron As (III) oxidation with high activity, durability, and sensitivity. This work opens up an unusual approach in analytical chemistry for developing various sensing platforms for challenging chemical and electrochemical reactions.

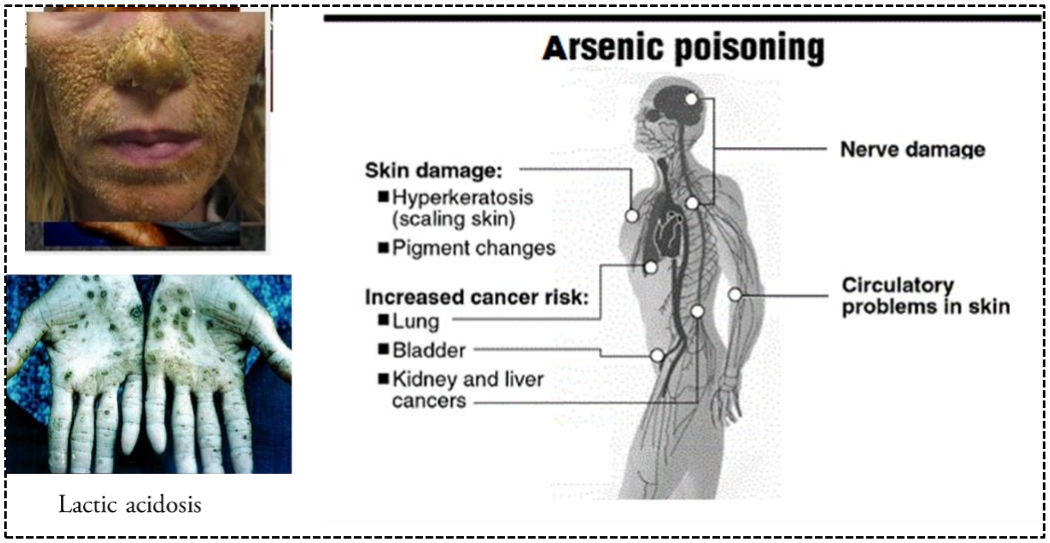


**Figure 4.1:** Effects of arsenic contact leading to chronic health complications. (http://www.sos-arsenic.net/english/environment/,https://sites.ualberta.ca/~xcle/arsenic.html)

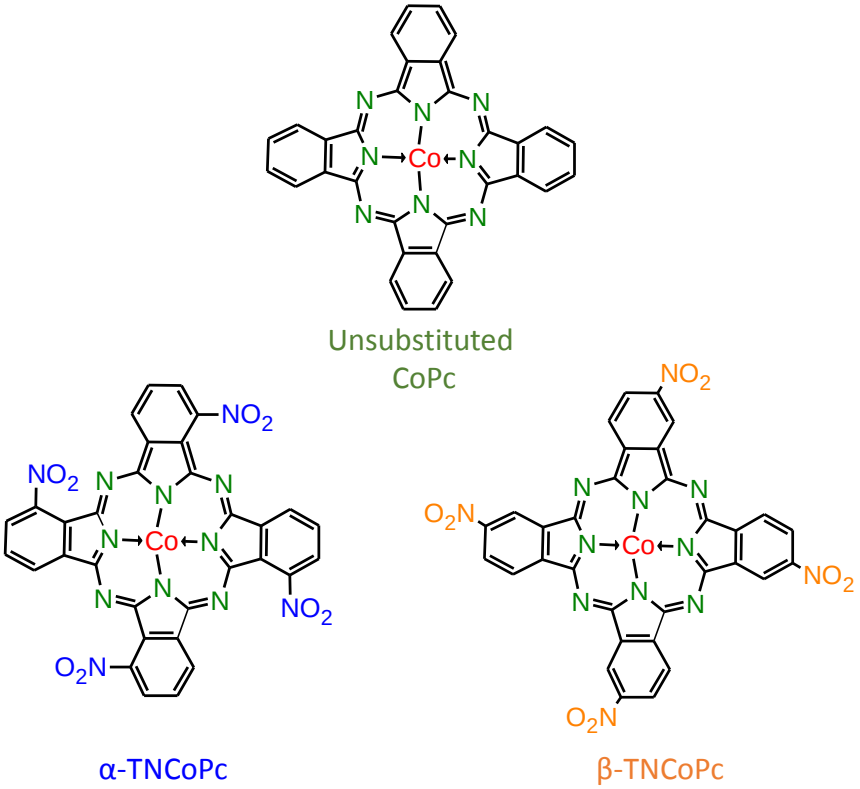


**Figure 4.2:** Molecular structure of unsubstituted CoPc, α-TNCoPc and β-TNCoPc isomers.

## 4.2. Results and discussion

As discussed in previous Chapter (Chapter 3), $N_4$ macrocycle based molecular catalysts have attracted considerable attention in electrochemical sensing due to their

tunability by secondary sphere substitution.[29-34] For faradaic electrochemical transformations, the metal centre is the active site whose activity can be controlled by the nature of the substituents (electron-donating/electron withdrawing). It is known that the nature of the substituent tunes the electron density at the active metal centre by activating the catalyst towards reduction/oxidation reactions.[35-45] Although, a lot of studies have been carried out to study the effect of the secondary sphere functionality on the catalytic center (as highlighted in the previous Chapters), to the best of our knowledge there have been no study that shines light on how the isomerism of these substituents affects the catalytic center and, consequently, its electrocatalytic activity. This is intriguing because the electronic structure of the catalytic center often can have a strong connection not only with the nature of substituents but also with their isomerism at the secondary sphere. This alterations in the electronic structure due to the isomerism of secondary sphere functionality was unambiguously proved in the Chapter 3 by various physicochemical techniques, wherein the role of isomerism of substituents in tuning various electrochemical oxidation reactions was discussed in detail.[46] To elaborate this further, particularly with respect to electrochemical sensing of substrates of analytical importance, unsubstituted cobalt phthalocyanine (CoPc) and geometrical isomers of tetranitro cobalt phthalocyanine (TNCoPc) were synthesized as per the literature[47-49] by substituting the $-NO_2$ group at α (α-TNCoPc) and β (β-TNCoPc) positions (please refer to the chapter 2, section 2.4.1, pages 46-47), as shown in Figure 4.2. These molecules were characterized with the help of various physico chemical techniques as discussed in Chapter 3. As discussed in Chapter 3 (Figure 3.2), matrix-assisted laser desorption ionization time-of-flight mass spectrometry (MALDI-TOF), UV-Visible spectroscopy, Fourier transform infrared (FTIR) spectroscopy and Raman spectroscopy of unsubstituted CoPc, and TNCoPc isomeric molecules confirm the formation of $-NO_2$ substituted molecules. Further, $^1H$ Nuclear magnetic resonance (NMR) spectra and 2D $^1H$ NMR (COSY) spectra of corresponding Zn phthalocyanines (α-TNZnPc and β-TNZnPc isomers) confirm the arrangements of protons around the aromatic ring of $N_4$ macrocycle and supports the formation of isomeric $-NO_2$ molecules as discussed in Chapter 3 (Figure 3.3).

### 4.2.1. Electrochemical analysis

As synthesized molecules were then anchored on carbon nanotube (CNT) electrodes (please refer to the synthesis, Chapter 2, section 2.4.4, pages 47-48, for more details) for fabricating the sensing platform (discussed in Chapter 3, pages 65-67, Figures 3.4-3.6). Carbon nanotubes were used because of their ability to facilitate the electron transfer.[50,51] These modified electrodes were then evaluated for their electrochemical activity toward direct arsenic (III) oxidation, a potentially important electrochemical pathway for water remediation and arsenic detection.[1–6] Linear sweep voltammetry data (Figure 4.3a) suggest that in terms of performance metrics, such as onset potential and driving force required to achieve a particular current density (Table 4.1), the β-TNCoPc isomer is superior to the corresponding α-TNCoPc isomer and unsubstituted CoPc. To evaluate their stability and durability, chronopotentiometric (potential vs. time) analysis were carried out, which confirms that β isomer is more durable and active compared to α isomer and unsubstituted CoPc, Figure 4.3b. Electrochemical activity towards oxidation has noticeably improved on substitution by the electron withdrawing $-NO_2$ group, comparative current-voltage, and current-time analyses of substituted molecular catalysts with unsubstituted CoPc; however, the independent role of isomerism over its chemical identity toward electrocatalysis is evident in the higher activity of β isomer compared to the corresponding α isomer (Figure 4.3a,b). As already demonstrated in Figure 4.3a,b and Table 4.1, the β isomer is more active towards direct As (III) oxidation compared to the α isomer. On these isomeric molecules (α and β) with As (III) as the substrate, linear plots of peak current vs. square root of scan rate evidenced a diffusion controlled behavior (Figures 4.4 and 4.5) at sufficiently positive potentials. This is further clear from the obtained slope of ~0.5 when log of (peak current density) is plotted against log (scan rate), Figure 4.4 and 4.5.

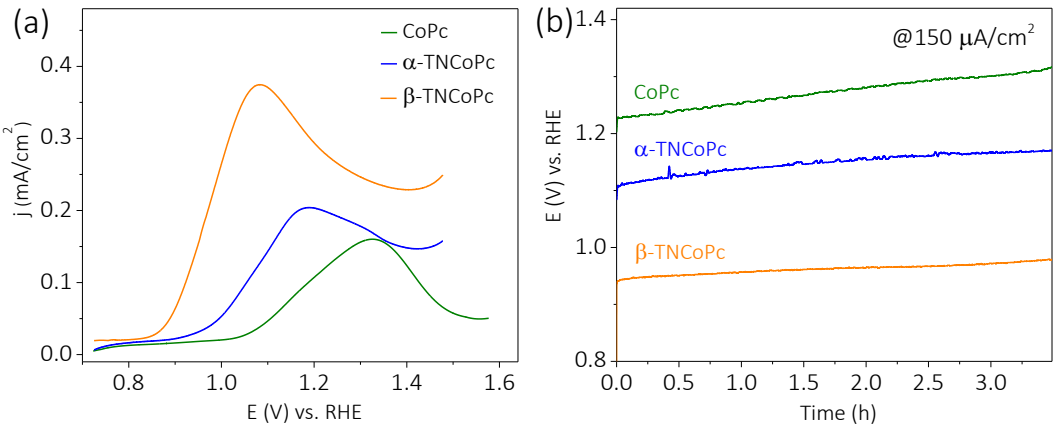

**Figure 4.3:** (a) Voltammograms recorded with unsubstituted CoPc and α and β-TNCoPc isomers at a scan rate of 10 mV/s and (b) chronopotentiometry traces on unsubstituted CoPc and α and β-TNCoPc isomers at a current density of 150 μA/cm² in the presence of 1 mM concentrations of arsenite (As (III)) in phosphate buffer of pH = 8.

**Table 4.1:** Electrochemical parameters extracted from Figure 4.3.

| Electrodes | Onset Potential (V) vs. RHE | Potential (V) @ 0.15 mA/cm² |
|---|---|---|
| CoPc | 1.05 | 1.30 |
| α-TNCoPc | 0.97 | 1.11 |
| β-TNCoPc | 0.85 | 0.96 |

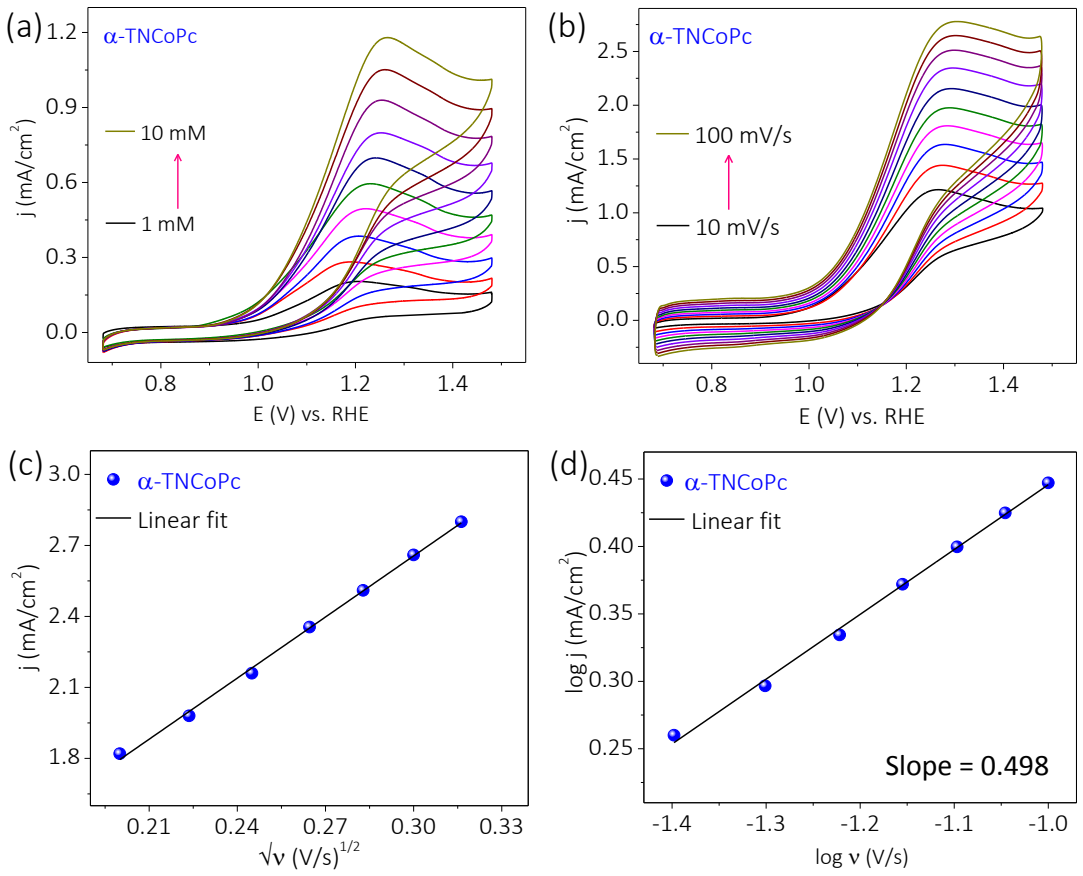


**Figure 4.4:** Cyclic voltammograms of α-TNCoPc isomer (a) as a function of concentration of arsenic (III) in phosphate buffer (pH = 8) at a scan rate of 10 mV/s and (b) as a function of scan rate with 10 mM As (III) in phosphate buffer (pH = 8). (c) Plot of peak current vs. square root of scan rate and (d) the plot of log of peak current vs. log of scan rate.

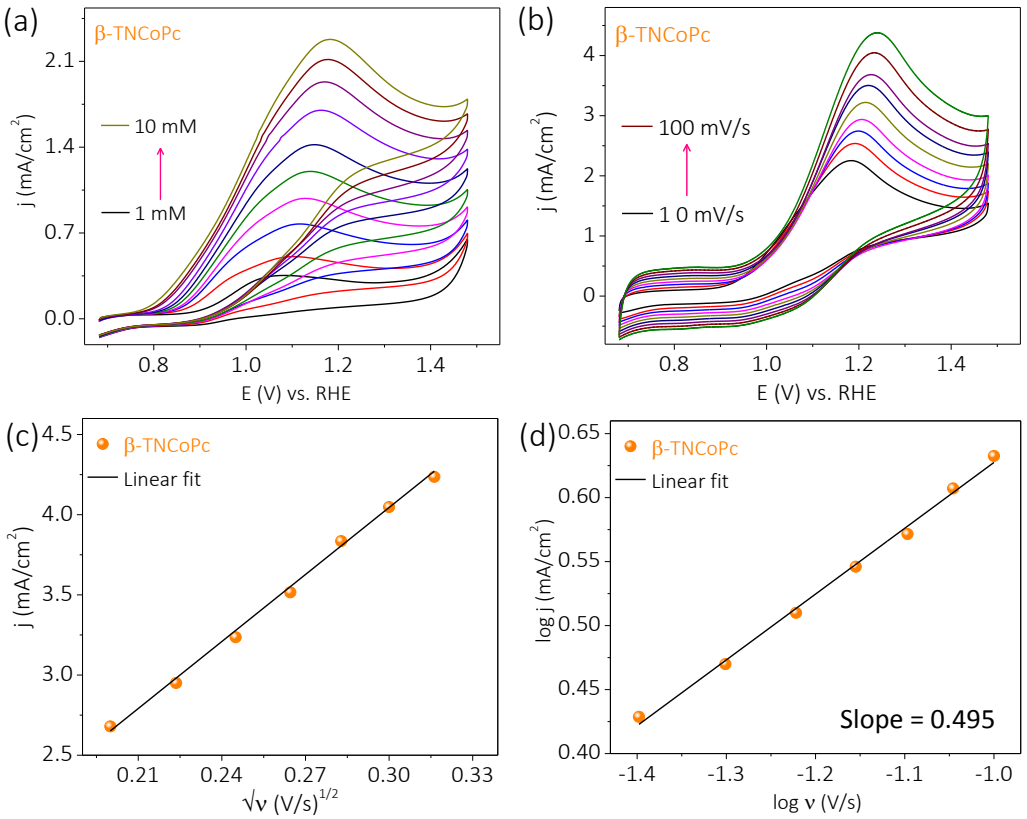


**Figure 4.5:** Cyclic voltammograms of β-TNCoPc isomer (a) as a function of concentration of arsenic (III) in phosphate buffer (pH = 8) at a scan rate of 10 mV/s and (b) as a function of scan rate with 10 mM As (III) in phosphate buffer (pH = 8). (c) Plot of peak current vs. square root of scan rate and (d) the plot of log of peak current vs. log of scan rate.

Nyquist plots (Figure 4.6a) further indicate that the charge transfer resistance ($R_{CT}$) for As (III) oxidation is significantly lowered on the β-TNCoPc isomer compared to the α-TNCoPc isomer, suggesting amplified electron transfer kinetics in the former (Table 4.2). In the equivalent electrical circuit used for the fitting (inset of Figure 4.6a), a series RC circuit combination was used. The parallel combination of $Q_1$ and $R_1$ in the first RC circuit (from the left) represents the geometrical capacitance of the catalyst and the resistance of the film layer, respectively.[52-54] In series with the first RC parallel circuit, the second RC composed of a constant phase element $Q_2$, a resistance $R_2$ ($R_{CT}$), and a Warburg impedance, $Z_W$, corresponding to interfacial capacitance, the charge transfer resistance, and mass transport component of active species to and from the electrode surface, respectively. It should be noted that bare CNT (the underlying support used for anchoring isomeric molecules) without TNCoPc molecules is not active toward As (III) oxidation, and mainly non-faradaic charging currents were observed in the cyclic voltammograms even in the presence of As (III), Figure 4.6b.

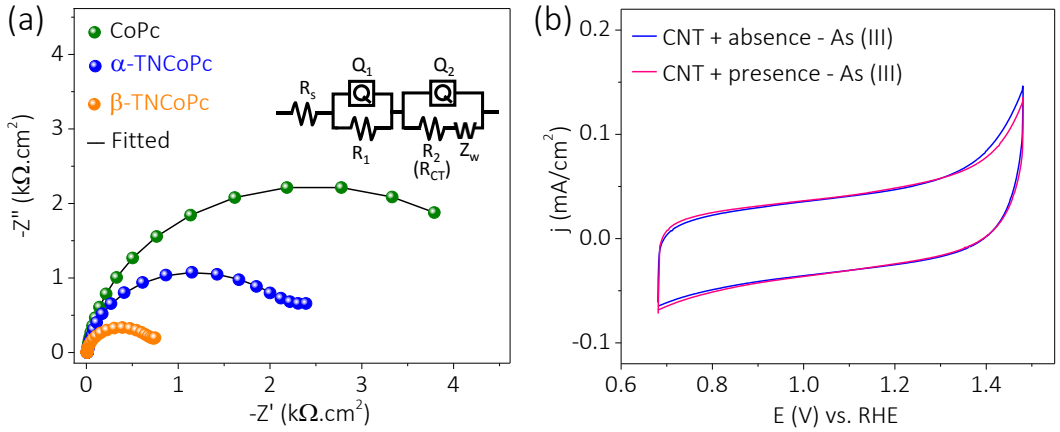


**Figure 4.6:** (a) Nyquist plots for unsubstituted CoPc and α and β-TNCoPc isomers at the open circuit voltage in pH = 8 phosphate buffer containing 10 mM arsenite. Impedance spectra were acquired in the frequency range 100 kHz to 10 mHz with an AC amplitude of 10 mV (peak to peak). Inset of Figure 4.6a shows the equivalent circuit used for the fitting. (b) Cyclic voltammograms of bare CNT electrode in the absence and the presence of 1 mM As (III) in pH = 8 phosphate buffer solution at a scan rate of 10 mV/s.

**Table 4.2:** Electrochemical parameters extracted from electrochemical impedance spectroscopy (Figure 4.6a).

| Electrodes | $R_{CT}$ (kΩ.cm²) |
|---|---|
| CoPc | 4.47 |
| α-TNCoPc | 2.13 |
| β-TNCoPc | 0.64 |

To prove beyond doubt that the electrochemical behavior of isomeric molecules toward arsenic oxidation are inherent to the molecules, the electrochemical oxidation of arsenic (III) to arsenic (V) was investigated out by forming a monolayer of molecular catalysts on a glassy carbon electrode (Figure 4.7a,b) and the trend was found out to be the same as in Figure 4.3a,b. The monolayers were characterized by a quartz crystal microbalance (QCM) technique (see in chapter 2, section 2.6.3, page 50), Figure 4.7 c,d. The surface coverage values obtained from QCM were in the order of $10^{-11}$ mol/cm² (insets of Figure 4.7c,d). As per the literature, this surface coverage value reflects a monolayer of molecular electrocatalysts on the electrode with nearly a flat orientation.[55,56] Their electrochemical behavior with respect to the isomerism of $-NO_2$ functionality toward arsenic (III) oxidation (Figure 4.7a,b)

confirm that the activity of the isomeric molecules are inherent to the molecules and isomerism of substituents makes an additional contribution to electrocatalysis over their nature.

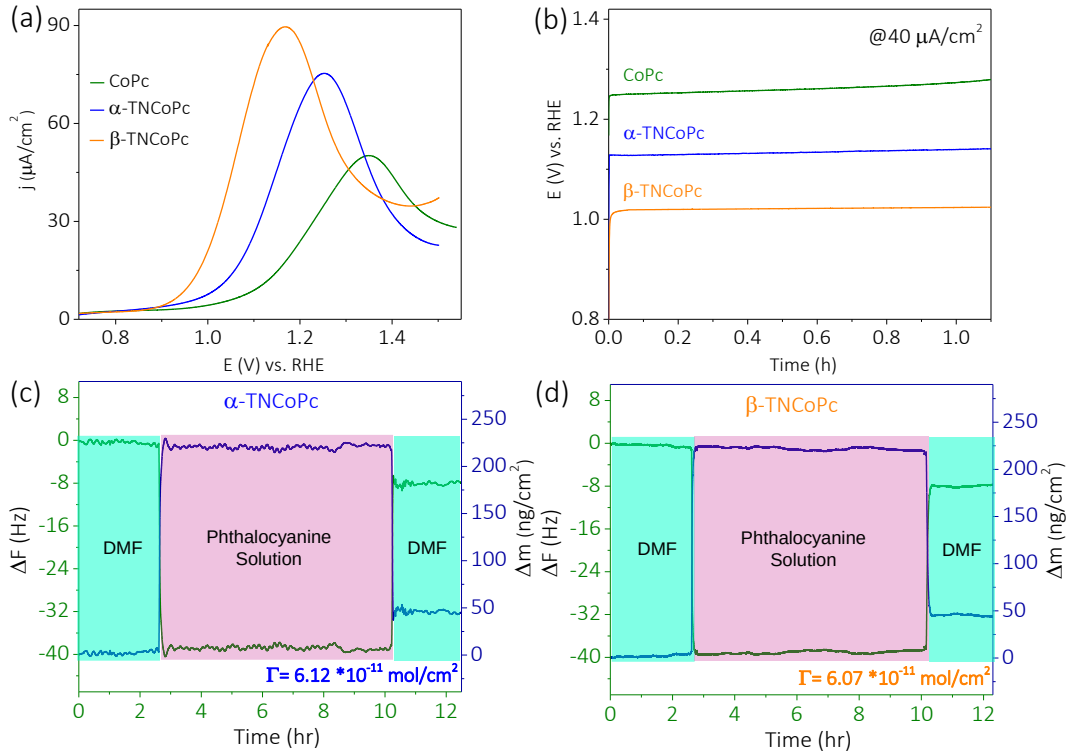


**Figure 4.7:** Electrochemical behavior of unsubstituted CoPc and α and β-TNCoPc isomers when they are adsorbed as monolayer on glassy carbon electrodes. (a) Voltammograms recorded at a scan rate of 10 mV/s and (b) chronopotentiometry traces at a current density of 40 μA/cm² in the presence of 1 mM concentrations of arsenite (As (III) in phosphate buffer of pH = 8. Quartz crystal microbalance (QCM) response during the adsorption of isomeric molecules from a 0.2 mM solution of (c) α-TNCoPc and (d) β-TNCoPc in dimethyl formamide (DMF). Green trace shows the frequency change during adsorption and the blue trance shows the mass change calculated using Saurbrey equation. Surface coverage (Γ) values of molecular catalysts extracted from QCM experiments are provided in respective images.

### 4.2.2. Investigation of number of electrons and catalytic rate constant ($k_{cat}$) for the direct oxidation of arsenic (III) to arsenic (V)

In order to understand the number of electrons transferred during As (III) oxidation with the isomeric molecules (α and β), As (III) oxidation was carried out under forced

convection technique using a rotating disk electrode (RDE), Figure 4.8 (Please refer to the Chapter-2, section 2.8, pages 51-52 for more details ). Based on RDE studies and the Levich plot, (Figure 4.8b,d) and by taking the diffusion coefficient of As (III) or $D_{As(III)}$ as 6.98 × $10^{-6}$ $cm^2/s$,[57] the number of electrons transferred is found to be close to 2 on both the isomeric molecules (α and β), Figure 4.8.

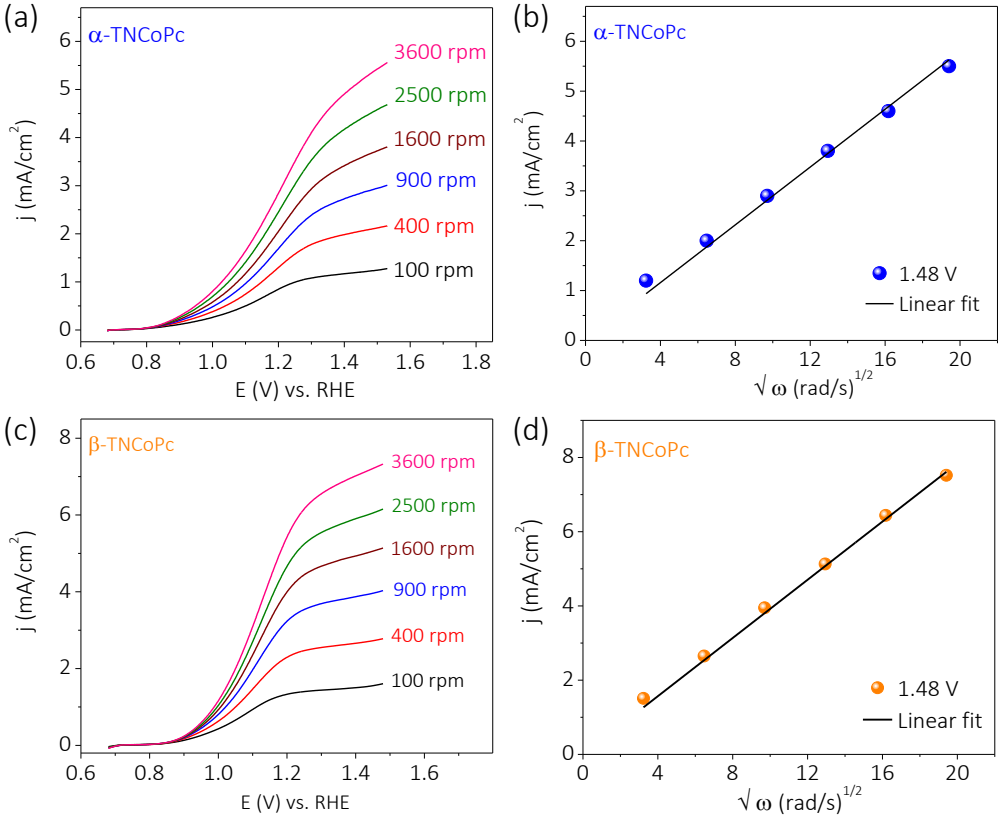


**Figure 4.8:** Rotating disk electrode (RDE) measurements acquired on (a) α-TNCoPc isomer and (b) corresponding Levich plot at 1.48 V vs. RHE. Rotating disk electrode (RDE) measurements acquired on (c) β-TNCoPc isomer and (d) corresponding Levich plot at 1.48 V vs. RHE.

The catalytic rate constant ($k_{cat}$) for As (III) oxidation reaction was calculated from the kinetic current ($i_{K.E}$) extracted from Koutecky–Levich plots, Figure 4.9 and Table 4.3 (Please refer to the Chapter-2, section 2.8 for more details, pages 51-52). The catalytic rate constant ($k_{cat}$ ($dm^3\,mol^{-1}s^{-1}$)) is related to $i_{K.E}$ as shown in eq 4.1.[25,26]

$$i_{K,E} = nFAk_{cat}C_{As(III)}\Gamma_{MPc} \ldots\ldots (4.1)$$

where $\Gamma_{MPc}$ is the surface coverage of redox active centres in $mol/cm^2$, which was estimated by integrating the area of Co (II) oxidation peak in the cyclic voltammograms. In

line with voltammetric and chronopotentiometric analyses, Figures 4.3a and b, the catalytic rate constant values of β isomer were ~3 times higher than those obtained for α isomer (Table 4.3). It is known that during the oxidation of As (III) to As (V) on cobalt based catalysts, electron transfer to As (III) is mediated by Co (III) species.[26] Taken together, on these isomeric TNCoPc molecules, the electrochemical oxidation of As (III) proceeds to As (V) via a two electron pathway mediated by Co (III), as given in eqs 4.2 and 4.3.

$$2Co\ (II) \rightarrow\ 2Co\ (III) + 2e^{-} \ldots..\ (4.2)$$

$$2Co\ (III) + As\ (III) \rightarrow\ 2Co\ (II) + As\ (V) \ldots..\ (4.3)$$

Therefore, the Co (II) center in the molecular catalyst gets electrochemically oxidized to Co (III), which in turn oxidizes As (III) to As (V) chemically. During this process, Co (II) will be chemically regenerated on the electrode surface following an EC mechanism.[25,26,57] However, it must be noted that, depending upon the complexity of the sensing reaction, the mechanistic pathways may change; however, the kinetics will always be higher in case of the β isomer compared to α isomer.

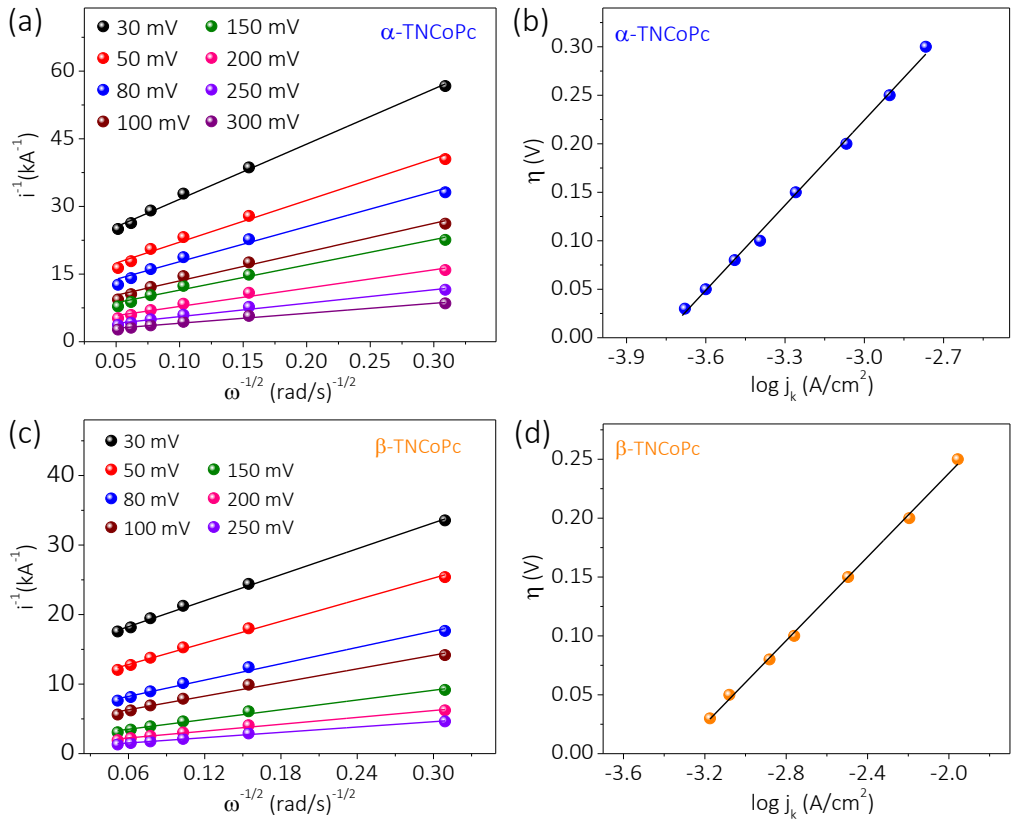


**Figure 4.9:** (a) Koutecky–Levich plots at different overpotentials for α-TNCoPc isomer and (b) corresponding plot of overpotential versus logarithm of kinetic current density. (c)

Koutecky–Levich plots at different overpotentials for β-TNCoPc isomer and (d) corresponding plot of overpotential versus logarithm of kinetic current density.

**Table 4.3:** Catalytic rate constant ($k_{cat}$) for α and β-TNCoPc isomers for the direct oxidation reaction of As (III) in pH = 8 phosphate buffer. Parameters are extracted from Figures 4.9b and 4.9d.

| Electrodes | Catalytic rate constant values ($k_{cat}$) ($dm^3\ mol^{-1}s^{-1}$) |
|---|---|
| **α-TNCoPc** | $6.42 \times 10^2$ |
| **β-TNCoPc** | $17.14 \times 10^2$ |

### 4.2.3. X-ray photoelectron spectroscopy study

It is well-known that, on unsubstituted CoPc during electrocatalytic oxidation of various species, the second step is rate-limiting (equation 4.3), which suggests that $Co^{3+}$ is the active species.[25,26,58] XPS analysis of unsubstituted CoPc and α and β isomers (Figure 4.10a) shows peaks corresponding to binding energies at ~780.21 eV ($Co^{2+}$ $2p_{3/2}$) and ~781.78 eV ($Co^{3+}$ $2p_{3/2}$), along with satellite features at ~789.31 eV, which matched well with the available literature.[59-61] The relative percentage of $Co^{2+}$ ($2p_{3/2}$) and $Co^{3+}$ ($2p_{3/2}$) species was clearly different with respect to the isomerism of the $-NO_2$ substituent. A higher $Co^{3+}/Co^{2+}$ ratio was found in favor of the β isomer compared to α isomer, and the $Co^{3+}/Co^{2+}$ ratio followed the order: β-TNCoPc > α-TNCoPc > CoPc (Figure 4.10b,c). The shifting of $Co2P_{3/2}$ to higher binding energies in the β isomer compared to the corresponding α isomer further suggests that there is a higher degree of partial positive charge at the catalytic metal center in the former compared to the latter (Figure 4.10b). The vanishing of the satellite feature at ~789.31 eV with relative decrease in $Co^{2+}$ species in the catalyst further supports this argument (Figure 4.10a).[61] As discussed earlier, $Co^{3+}$ is the active species during the electrochemical oxidation of As (III) (eqs 4.2 and 4.3), and XPS analysis reveals that isomerism of the substituent can enrich its contribution in the catalytic center. This higher contribution of partial positive charge at the catalytic metal center in the β isomer results in enhanced kinetics, as reflected by the catalytic rate constant values (Table 4.3).

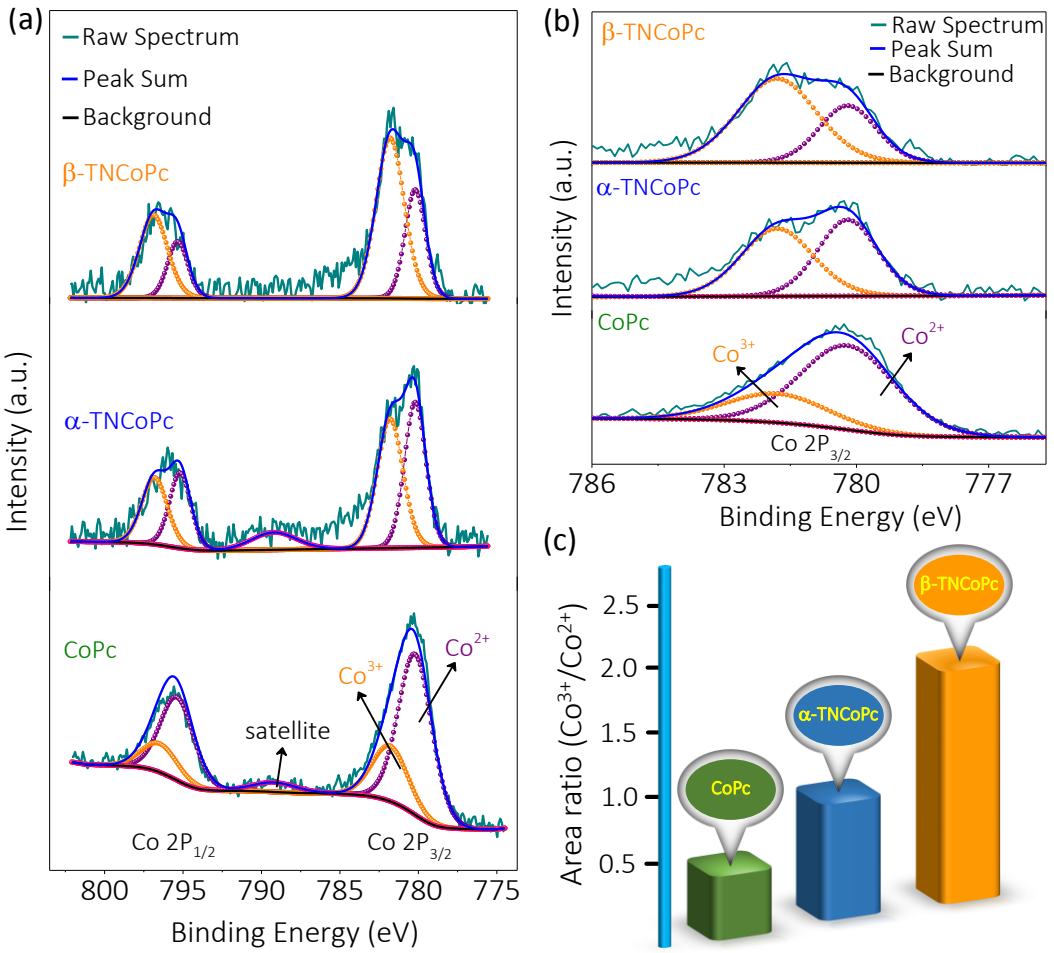


**Figure 4.10:** (a) X-ray photoelectron spectroscopy (XPS) of unsubstituted CoPc and α and β-TNCoPc isomers. (b) Enlarged view of $Co2P_{3/2}$ region and (c) the area ratio of $Co^{3+}/Co^{2+}$ peaks in molecular catalysts.

The possible reasons for this intriguing electrochemical behavior with respect to isomerism of substituents could be explained on the basis of the electron withdrawing effects associated with the $-NO_2$ group. As explained in the previous chapter (Chapter 3), there are two ways in which the $-NO_2$ group affects the electronic delocalization in the molecule viz. electron withdrawing inductive effect (–I) and the electron withdrawing resonance effect (–R). Since the inductive effect operates through the σ bond, its influence should not differ much in the two isomers. However, for the –R effect to operate in the molecule, the plane of the π electronic cloud of the $-NO_2$ group should be in plane with the π electronic cloud of the $N_4$ macrocycle. A closer look at the $-NO_2$ substituted macrocycle (Scheme 4.1) shows that the $-NO_2$ group in the α isomer is prone to experiencing repulsive interaction (field effect) between the O of $-NO_2$ and iminic N (Scheme 4.1), which may force the $-NO_2$ plane to be out of plane with respect to the macrocycle plane. This will result in the diminishing

of the –R effect between the $–NO_2$ group and $N_4$ macrocycle in the α isomer. Since the $–NO_2$ plane in the β isomer is farther away from the secondary macrocyclic N, the influence of field effect can be negligible and the $–NO_2$ substituent may prefer an in plane configuration with respect to the macrocycle plane due to the stabilization achieved from the conjugation of π electronic clouds. This conjugation place the β isomer under a dominant –R effect apart from the already existing –I effect (Scheme 4.1). This argument is supported by UV–vis spectroscopy (please refer to the Chapter 3, Figure 3.2d) where a noticeably broadened Q-band in the β isomer compared to the α isomer (please refer to the Chapter 3, Figure 3.2d) is indicative of higher degree of electronic delocalization in the former. Taken together, the metal center in the β isomer should possess a higher partial positive charge because of combined –I and –R effects, compared to α isomer where only the –I effect is dominant. The above explanation is in line with experimental results obtained from XPS and UV–vis spectroscopy (Chapter 3, Figure 3.2d and Figure 4.10). In essence, isomerism of substituents has an independent role in electrocatalysis over its nature, which can be exploited to design effective sensing platforms for various reactions.

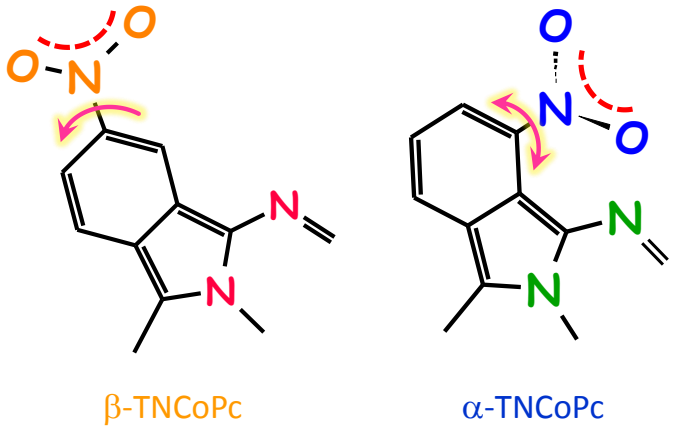


**Scheme 4.1:** Scheme showing the relative arrangement of $N_4$ macrocycle plane with respect to -$NO_2$ plane in α and β-TNCoPc isomers.

### 4.2.4. Analytical performance of the arsenic sensor

To further elaborate on the effectiveness of isomerism toward electrochemical sensing of As (III), the concentration, stability, and cycling tests were carried out with the highly active β-TNCoPc isomer. Chronoamperometry traces with the β isomer during successive addition of As (III) demonstrated a corresponding increase in the steady-state current with a

linear trend (Figure 4.11a,b). The analytical performance of the β isomer for As (III) detection suggests that the experimental detection limit was 0.07 µM or 9 ppb (9.0 µg $L^{-1}$) and sensitivity was 12 nA $ppb^{-1}$, Figure 4.11a,b and the performance metrics are close to the best electrodes reported in the literature, Table 4.4 (comparison of various chemically modified electrodes).[25,62-71] It should also be noted that the experimental detection limit calculated as per eq 4.4 [26,72-74] is close to the WHO guidelines of 10 ppb for arsenic in drinking water,[2,4–6] making the β isomer a suitable platform for arsenic detection. The slope of the calibration plot was found to be 12 nA $ppb^{-1}$ ($R^2$ = 0.99), Figure 4.11b. The detection limit by taking a signal to noise ratio (S/N) of 3 was found to be 2 ppb (Calculation 4.1), which is well below the WHO guidelines. Further, the cyclability the β-TNCoPc isomer and reproducibility of the sensor response toward direct As (III) oxidation were investigated by alternatively injecting the sensor compartment with 0 and 1 mM As (III) solution for ~8 h. The corresponding chronoamperometry response clearly suggests a reproducible sensor with high stability and durability (Figure 4.12a). Figure 4.12b further demonstrates that the FTIR spectral response of the β isomer electrode remain unchanged even after several hours of continuous cycling, indicating the stability of sensing architecture. Overall, the regioisomerism of electron withdrawing $-NO_2$ substituents on the macrocyclic phthalocyanine ligand provides a feasible pathway for designing a sensing platform with high activity, stability, and sensitivity toward arsenic detection.

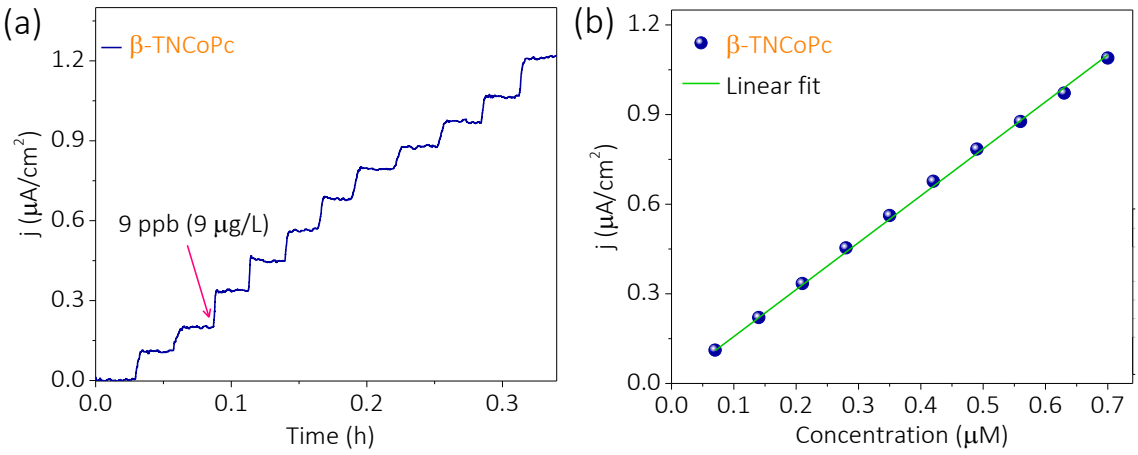


**Figure 4.11:** (a) Chronoamperometry traces (background subtracted currents are plotted) with β-TNCoPc isomer at 1.1 V vs. RHE during successive increment in the concentration of arsenite in phosphate buffer of pH = 8 and (b) the corresponding calibration plot.

Table 4.4: Performance metrics of chemically modified electrodes for As (III) detection.

| S. No. | Modified electrode | Methods / Techniques | Electrolytes | Linear range (mg $L^{-1}$) | Sensitivity (nA $ppb^{-1}$) | Detection limit (µg $L^{-1}$) |
|---|---|---|---|---|---|---|
| 1 | SPE/CNF-CHIT@$Au_{nano}$[25] | FIA-ECD | 0.1 M PBS (pH 7) | 0.1 – 100 | 218 | 11 |
| 2 | Silver electrode[62] | SWASV | 0.1 M $HNO_3$ | 0.15 – 1.5 | 35 | 45 |
| 3 | Au macroelectrode[63] | SWASV | 0.1 M $HNO_3$ | 0.15 – 1.5 | 16 | 14 |
| 4 | Meso Au-BDE[64] | ASV | 0.1 M $HNO_3$ | 0 – 0.8 | - | 30 |
| 5 | PolyPN$^{+}$–Pt@GCE[65] | ASV | 3 mM PBS (pH 8) | 7.5 – 43 | - | 170 |
| 6 | Au/GO/leucine@Nafion electrode[66] | CV | 0.1 M citrate (pH 5) | 5 – 50 | 6 | 500 |
| 7 | GCE/(PDDA–Au NPs)[67] | DPV | 0.1 M PBS (pH 8) | 1.4 – 8.2 | 10.6 (µA $ppb^{-1}$) | 34 |
| 8 | GCE/Fe(dmbpy)$_3^{2+}$–Nafion[68] | Amperometric i–t | 0.1 M $Na_2SO_4$ (pH 7) | 0.4 – 43.5 | - | 435 |
| 9 | GCE@AuNP–bentonite clay[69] | CV | 0.1 M PBS (pH 7) | 0.04 – 43.5 | 91 | 75 |
| 10 | SPE@AuNP[70] | ASV | 0.1 M HCl | 18 – 206 (µg $L^{-1}$) | 0.3 | 0.4 |
| 11 | BDE-iridium[71] | FIA | 0.1 M PBS (pH 4) | 7.5 – 750 (µg $L^{-1}$) | 248 | 2 |
| **12** | **β-TNCoPc*** | **Amperometric i–t** | **0.1 M PBS (pH 8)** | **9 – 90 (µg $L^{-1}$)** | **12** | **9** |

**Calculation 4.1:** All parameters are extracted from Figure 4.11b (calibration plot) and the detection limit was calculated by eq 4.4.[26,72-74]

Standard error = 2.69 * $10^{-9}$ A
Slope = 12 nA.$ppb^{-1}$
$R^2$ = 0.99
SD = 8.51 * $10^{-9}$ A

$$LOD = 3 \times \frac{SD}{slope} \quad \ldots\ldots(4.4)$$

LOD = 2 µg/L (2 *ppb*)

Where, LOD = Limit of detection
SD = Standard Deviation
Slope = Slope of calibration plot

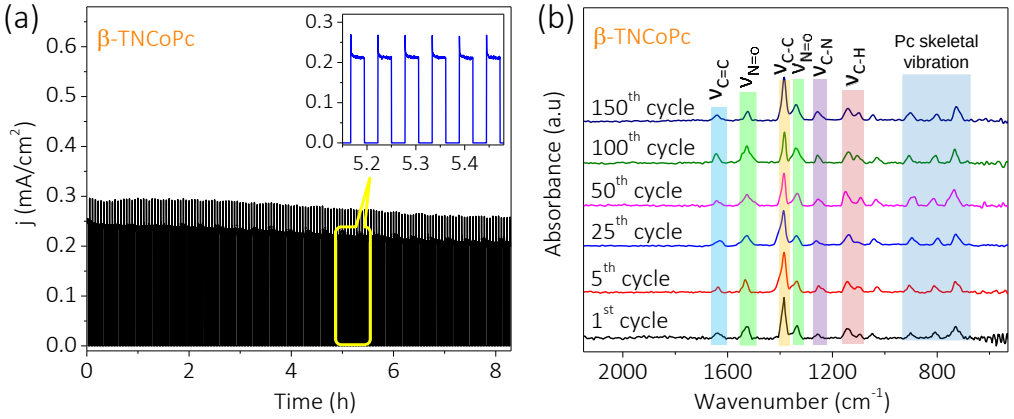


**Figure 4.12:** (a) Stability performance of β-TNCoPc isomer at 1.0 V vs. RHE when the sensing compartment is alternatively injected with 0 mM and 1 mM of arsenite in phosphate buffer of pH = 8 and (b) FTIR spectroscopy of β-TNCoPc isomer electrode with respect to cycle number.

## 4.3. Conclusions

It is demonstrated that isomerism of functionality in the secondary sphere of the molecular electrocatalyst independently contributes to electrocatalysis over its chemical identity. The study outlined in this chapter proves that the isomerism of the electron withdrawing $-NO_2$ group plays a primary role in dictating the catalytic activity of the central metal ion via competing field effects and resonance effects. Isomerism governed electrochemical activation of the catalytic center leads to a nonprecious arsenic sensor with a detection limit close to WHO guidelines, which in turn opens up a viable way for tuning the catalytic activity of molecular catalysts toward challenging electrochemical sensing reactions.

## 4.4. References

[1] Wasana, H. M. S.; Perera, G. D. R. K.; Gunawardena, P. D. S.; Fernando, P. S.; Bandara, J. WHO Water Quality Standards vs Synergic Effect(s) of Fluoride, Heavy Metals and Hardness in Drinking Water on Kidney Tissues. *Sci. Rep.* **2017**, *7*, 1–6.

[2] Argos, M.; Kalra, T.; Rathouz, P. J.; Chen, Y.; Pierce, B.; Parvez, F.; Islam, T.; Ahmed, A.; Rakibuz-zaman, M. Arsenic Exposure from Drinking Water , and All-Cause and Chronic-Disease Mortalities in Bangladesh ( HEALS ): *Lancet* **2010**, *376*, 252–258.

[3] Mandal, B. K.; Suzuki, K. T. Arsenic Round the World: A Review. *Talanta* **2002**, 58, 201–235.

[4] WHO, Geneva, **1993** (http://www.who.int/int-fs/en/fact210.html).

[5] World Health Organization (WHO). *Guidelines for Drinking Water Quality.* **1993**, *1*, 1–29.

[6] Gordon, B.; Callan, P.; Vickers, C. WHO Guidelines for Drinking-Water Quality. *WHO Chron.* **2008**, *38*, 564.

[7] Sarkar, A.; Paul, B. The global menace of arsenic and its conventional remediation-A critical review. *Chemosphere,* **2016**, *158*, 37–49.

[8] Zheng, L.; Liu, Z.; Yan, Z.; Yi, X.; Zhang, J.; Zhang, Y.; Zhu, Y. Deriving water quality criteria for trivalent and pentavalent arsenic. *Science of the Total Environment,* **2017**, *587–588*, 68–74.

[9] Villaescusa, I.; Bollinger, J.-C. Arsenic in drinking water: sources, occurrence and health effects (a review). *Reviews in Environmental Science and Bio/Technology,* **2008**, *7(4)*, 307–323.

[10] Mandal, S.; Sahu, M. K.; Patel, R. K. Adsorption Studies of Arsenic (III) Removal from Water by Zirconium Polyacrylamide Hybrid Material (ZrPACM-43). *Water Resour. Ind.* **2013**, *4*, 51–67.

[11] Cox, J. A.; Kulesza, P. J. Electrocatalytic Oxidation and Determination of Arsenic (III) on a Glassy Carbon Electrode Modified with a Thin Film of Mixed-Valent Ruthenium (III, II) Cyanide. *Anal. Chem.* **1984**, *56 (6)*, 1021–1025.

[12] Jena, B. K.; Raj, C. R. Gold Nanoelectrode Ensembles for the Simultaneous Electrochemical Detection of Ultratrace Arsenic, Mercury, and Copper. *Analytica Chimica Acta.* **2008**, *80*, 4836–4844.

[13] Mays, D. E.; Hussam, A. Voltammetric Methods for Determination and Speciation of Inorganic Arsenic in the Environment-A Review. *Anal. Chim. Acta* **2009**, *646* (1–2), 6–16.

[14] Ottakam Thotiyl, M. M.; Basit, H.; Sánchez, J. A.; Goyer, C.; Coche-Guerente, L.; Dumy, P.; Sampath, S.; Labbé, P.; Moutet, J. C. Multilayer Assemblies of Polyelectrolyte-Gold Nanoparticles for the Electrocatalytic Oxidation and Detection of arsenic(III). *J. Colloid Interface Sci.* **2012**, *383*, 130–139.

[15] Kopanica, M.; Novotny, L. Determination of Traces of Arsenic (III) by Anodic Stripping Voltammetry in Solutions, Natural Waters and Biological Material. *Anal. Chem. Acta* **1998**, *368*, 211–218.

[16] Idris, A. O.; Mafa, J. P.; Mabuba, N.; Arotiba, O. A. Dealing with Interference Challenge in the Electrochemical Detection of As (III) - A Complexometric Masking Approach. *Electrochem. commun.* **2016**, *64*, 18–20.

[17] Dai, X.; Compton, R. G. Detection of As (III) via Oxidation to As (V) Using Platinum Nanoparticle Modified Glassy Carbon Electrodes: Arsenic Detection without Interference from Copper. *Analyst* **2006**, *131*, 516.

[18] Dai, X.; Compton, R. G. Gold Nanoparticle Modified Electrodes Show a Reduced Interference by Cu (II ) in the Detection of As (III) Using Anodic Stripping Voltammetry. *Electroanalysis* **2005**, *2*, 1325–1330.

[19] Gupta, R.; Gamare, J. S.; Pandey, A. K.; Tyagi, D.; Kamat, J. V. Highly Sensitive Detection of Arsenite Based on Its Affinity toward Ruthenium Nanoparticles Decorated on Glassy Carbon Electrode. *Anal. Chem.* **2016**, 88, 2459–2465.

[20] Kempahanumakkagari, S.; Deep, A.; Kim, K.; Kailasa, S. K. Biosensors and Bioelectronics Nanomaterial-Based Electrochemical Sensors for Arsenic - A Review. *Biosens. Bioelectron.* **2017**, *95*, 106–116.

[21] Li, S.; Zhou, W.; Li, Y.; Jiang, M.; Guo, Z.; Liu, J.; Huang, X. Noble-Metal-Free $Co_{0.6}Fe_{2.4}O_4$ Nanocubes Self-Assembly Monolayer for Highly Sensitive Electrochemical Detection of As (III) Based on Surface Defects *Anal. Chem.* **2018**, 90, 1263–1272

[22] Luong, J. H. T.; Lam, E.; Male, K. B. Analytical Methods Arsenic in Drinking and Ground Waters. *Anal. Methods*, **2014**, 6, 6157–6169.

[23] Sanllorente-Méndez, S.; Domínguez-Renedo, O.; Arcos-Martínez, M. J. Determination of Arsenic (III) Using Platinum Nanoparticle-Modified Screen-Printed Carbon-Based Electrodes. *Electroanalysis* **2009**, *21*, 635–639.

[24] Williams, D. G.; Johnson, D. C. Pulsed Voltammetric Detection of arsenic (III) at Platinum Electrodes in Acidic Media. *Anal. Chem.* **1992**, *64*, 1785–1789.

[25] Nellaiappan, S.; Pillai, K. C.; Kumar, A. S. Flow-Injection Analysis Coupled with Electrochemical Detection of Poisonous Inorganic arsenic(III) Species Using a Gold

Nanoparticle/carbon Nanofiber/chitosan Chemically Modified Carbon Screen Printed Electrode in Neutral pH Solution. *Anal. Methods* **2018**, *10* (7), 799–808.

[26] Salimi, A.; Mamkhezri, H.; Hallaj, R.; Soltanian, S. Electrochemical Detection of Trace Amount of Arsenic (III) at Glassy Carbon Electrode Modified with Cobalt Oxide Nanoparticles. *Sensors Actuators, B Chem.* **2008**, *129*, 246–254.

[27] Hug, S. J.; Leupin, O.; Du, C.-. Iron-Catalyzed Oxidation of Arsenic (III) by Oxygen and by Hydrogen Peroxide : PH-Dependent Formation of Oxidants in the Fenton Reaction. *Environ. Sci. Technol.* **2003**, *37 (12)*, 2734–2742.

[28] Zen, J.; Chen, P.; Kumar, A. S. Flow Injection Analysis of an Ultratrace Amount of Arsenite Using a Prussian Blue-Modified Screen-Printed Electrode. *Anal. Chem.* **2003**, *75 (21)*, 6017–6022.

[29] Wang, J.; Huang, X.; Xi, S.; Lee, J.-M.; Wang, C.; Du, Y.; Wang, X. Linkage Effect in the Heterogenization of Cobalt Complexes by Doped Graphene for Electrocatalytic $CO_2$ Reduction. *Angew. Chemie Int. Ed.* 2019, 58 (38), 13532–13539.

[30] Li, R.; Zhang, X.; Zhu, P.; Ng, D. K. P.; Kobayashi, N.; Jiang, J. Electron-Donating or -Withdrawing Nature of Substituents Revealed by the Electrochemistry of Metal-Free Phthalocyanines. *Inorg. Chem.* **2006**, *45* (5), 2327–2334.

[31] Zagal, J. H.; Koper, M. T. M. Reactivity Descriptors for the Activity of Molecular MN4 Catalysts for the Oxygen Reduction Reaction. *Angew. Chemie - Int. Ed.* **2016**, *55* (47), 14510–14521.

[32] Silva, N.; Calderón, S.; Páez, M. A.; Oyarzún, M. P.; Koper, M. T. M.; Zagal, J. H. Probing the Fe N + /Fe (N −1)+ Redox Potential of Fe Phthalocyanines and Fe Porphyrins as a Reactivity Descriptor in the Electrochemical Oxidation of Cysteamine. *J. Electroanal. Chem.* **2018**, *819* (August 2017), 502–510.

[33] Rajić, N. Z.; Stojaković, D. R. Synthesis and Characterization of Some Nitro-Substituted Phthalocyanines of Nickel(II), Cobalt(II) and Copper(II). *J. Coord. Chem.* **2009**, *19* (4), 295–301.

[34] Raja, R.; Ratnasamy, P. Selective Oxidation of Phenols Using Copper Complexes Encapsulated in Zeolites. *Applied Catalysis A: General* **1996**, *143*, 145–158.

[35] Li, C.; Huang, T.; Huang, Z.; Sun, J.; Zong, C.; Yang, J.; Deng, W.; Dai, F. A Sulfonated Cobalt Phthalocyanine/carbon Nanotube Hybrid as a Bifunctional Oxygen Electrocatalyst. Dalt. Trans. 2019, 48 (46), 17258–17265.

[36] Morlanés, N.; Takanabe, K.; Rodionov, V. Simultaneous Reduction of CO2 and Splitting of H2O by a Single Immobilized Cobalt Phthalocyanine Electrocatalyst. *ACS Catal.* **2016**, *6* (5), 3092–3095.

[37] Mashazi, P. N.; Ozoemena, K. I.; Nyokong, T. Tetracarboxylic Acid Cobalt Phthalocyanine SAM on Gold: Potential Applications as Amperometric Sensor for $H_2O_2$ and Fabrication of Glucose Biosensor. *Electrochim. Acta* **2006**, *52* (1), 177–186.

[38] Mashazi, P.; Nyokong, T. Electrocatalytic Studies of Covalently Immobilized Metal Tetra-Amino Phthalocyanines onto Derivatized Screen-Printed Gold Electrodes. *Microchim. Acta* **2010**, *171* (3), 321–332.

[39] Wang, M.; Torbensen, K.; Salvatore, D.; Ren, S.; Joulié, D.; Dumoulin, F.; Mendoza, D.; Lassalle-Kaiser, B.; Işci, U.; Berlinguette, C. P.; Robert, M. $CO_2$ Electrochemical Catalytic Reduction with a Highly Active Cobalt Phthalocyanine. *Nat. Commun.* **2019**, *10*, 3602.

[40] Zhang, X.; Wu, Z.; Zhang, X.; Li, L.; Li, Y.; Xu, H.; Li, X.; Yu, X.; Zhang, Z.; Liang, Y.; Wang, H. Highly Selective and Active $CO_2$ Reduction Electrocatalysts Based on Cobalt Phthalocyanine/carbon Nanotube Hybrid Structures. *Nat. Commun.* **2017**, *8*, 14675.

[41] Acar, E. T.; Tabakoglu, T. A.; Atilla, D.; Yuksel, F.; Atun, G. Synthesis, Electrochemistry and Electrocatalytic Activity of Cobalt Phthalocyanine Complexes – Effects of Substituents for Oxygen Reduction Reaction. *Polyhedron* **2018**, *152*, 114–124.

[42] Özçeşmeci, İ.; Demir, A.; Akyüz, D.; Koca, A.; Gül, A. Electrocatalytic Hydrogen Evolution Reaction with a Supramolecular cobalt(II)phthalocyanine Carrying Four Cobaloxime Moieties. *Inorganica Chim. Acta* **2017**, *466*, 591–598.

[43] Cui, L.; Liu, Y.; He, X. Iron(II)Tetraaminophthalocyanine Functionalized Graphene: Synthesis, Characterization and Their Application in Direct Methanol Fuel Cell. *J. Electroanal. Chem.* **2014**, *727*, 91–98.

[44] Zúñiga, C.; Tasca, F.; Calderon, S.; Farías, D.; Recio, F. J.; Zagal, J. H. Reactivity Indexes for the Electrocatalytic Oxidation of Hydrogen Peroxide Promoted by Several Ligand-Substituted and Unsubstituted Co Phthalocyanines Adsorbed on Graphite. *J. Electroanal. Chem.* **2016**, *765*, 22–29.

[45] Guo, J.; Li, H.; He, H.; Chu, D.; Chen, R. CoPc and $CoPcF_{16}$ Modified Ag Nanoparticles as Novel Catalysts with Tunable Oxygen Reduction Activity in Alkaline Media. *J. Phys. Chem. C* **2011**, *115* (17), 8494–8502.

[46] Kottaichamy, A. R.; Begum, S.; Nazrulla, M. A.; Dargily, N. C.; Devendrachari, M. C.; Bhat, Z. M.; Thimmappa, R.; Makri Nimbegondi Kotresh, H.; Vinod, C. P.; Thotiyl, M. O. Unprecedented Isomerism – Activity Relation in Molecular Electrocatalysis. *J. Phys. Chem. Lett.* **2020**, *11*, 263–271.

[47] Al-Lami, A. K. A; Majeed, N. N.; Al-Mowali, A. H. Synthesis, Mesomorphic and Molar Conductivity Studies of Some Macrocyclic Phthalocyanine Palladium (II). *Chemistry and Materials Research.* **2013**, *3 (4)*, 59–68.

[48] Lukyanets, E. A.; Nemykin, V. N. The Key Role of Peripheral Substituents In The Chemistry of Phthalocyanines And Their Analogs. *J. Porphyr. Phthalocyanines* **2010**, *14 (1)*, 1–40.

[49] Kottaichamy, A. R.; Makri Nimbegondi Kotresh, H.; Devendrachari, M. C.; Thimmappa, R.; Paswan, B.; Tiwari, O.; Chanda, V.; Gaikwad, P.; Thotiyl, M. O. Effects of Electrochemical Tailoring of Monolayers On A Catalytic Redox Entity: An On-Off Phenomenon Regulated By The Surrounding Medium. *J. Phys. Chem. C* **2015**, *119 (51)*, 28276–28284.

[50] Cao, R.; Thapa, R.; Kim, H.; Xu, X.; Gyu Kim, M.; Li, Q.; Park, N.; Liu, M.; Cho, J. Promotion Of Oxygen Reduction By A Bio-Inspired Tethered Iron Phthalocyanine Carbon Nanotube-Based Catalyst. *Nat. Commun.* **2013**, *4*, 2076.

[51] B. D. Vogt, E. K. Lin, W. Wu, C. C. White Effect of Film Thickness on the Validity of the Sauerbrey Equation for Hydrated Polyelectrolyte Films. *J. Phys. Chem. B,* **2004**, *108*, 12685–12690.

[52] Huang, J.; Yang, Z.; Wang, S.; Feng, Z. Preparation and Stability Study of Potassium Ferrate (VI) Coated with Phthalocyanine for Alkaline Super-Iron Battery. *J. Solid State Electrochem.* **2015**, *19* (3), 723–730.

[53] Shobha Jeykumari, D. R.; Ramaprabhu, S.; Sriman Narayanan, S. A Thionine Functionalized Multiwalled Carbon Nanotube Modified Electrode for the Determination of Hydrogen Peroxide. *Carbon* **2007**, *45 (6)*, 1340–1353.

[54] Gupte, T.; Jana, S. K.; Mohanty, J. S.; Srikrishnarka, P.; Mukherjee, S.; Ahuja, T.; Sudhakar, C.; Thomas, T.; Pradeep, T. Highly Sensitive As3+ Detection Using Electrodeposited Nanostructured MnO X and Phase Evolution of the Active Material during Sensing. *ACS Appl. Mater. Interfaces* **2019**, *11 (31)*, 28154–28163.

[55] Somashekarappa, M. P.; Keshavayya, J.; Sampath, S. Self-Assembled Molecular Films of Tetraamino Metal (Co, Cu, Fe) Phthalocyanines on Gold and Silver. Electrochemical and Spectroscopic Characterization. *Pure Appl. Chem.* **2002**, *74 (9)*, 1609–1620.

[56] Makinde, Z. O.; Louzada, M.; Mashazi, P.; Nyokong, T.; Khene, S. Electrocatalytic Behaviour of Surface Confined Pentanethio Cobalt (II) Binuclear Phthalocyanines towards the Oxidation of 4-Chlorophenol. *Appl. Surf. Sci.* **2017**, *425*, 702–712.

[57] Sehlotho, N.; Nyokong, T. Electrocatalytic Oxidation of Thiocyanate, L-Cysteine and 2-Mercaptoethanol by Self-Assembled Monolayer of Cobalt Tetraethoxy Thiophene Phthalocyanine. *Electrochim. Acta* **2006**, *51 (21)*, 4463–4470.

[58] Zúñiga, C.; Tasca, F.; Calderon, S.; Farías, D.; Recio, F. J.; Zagal, J. H. Reactivity Indexes for the Electrocatalytic Oxidation of Hydrogen Peroxide Promoted by Several Ligand-Substituted and Unsubstituted Co Phthalocyanines Adsorbed on Graphite. *J. Electroanal. Chem.* **2016**, *765*, 22–29.

[59] Arechederra, R. L.; Artyushkova, K.; Atanassov, P.; Minteer, S. D. Growth of Phthalocyanine Doped and Undoped Nanotubes Using Mild Synthesis Conditions for Development of Novel Oxygen Reduction Catalysts. *ACS Appl. Mater. Interfaces* **2010**, *2 (11)*, 3295–3302.

[60] Venegas, R.; Recio, F. J.; Zuñiga, C.; Viera, M.; Oyarzún, M. P.; Silva, N.; Neira, K.; Marco, J. F.; Zagal, J. H.; Tasca, F. Comparison of the Catalytic Activity for $O_2$ Reduction of Fe and Co MN4 Adsorbed on Graphite Electrodes and on Carbon Nanotubes. *Phys. Chem. Chem. Phys.* **2017**, *19 (31)*, 20441–20450.

[61] Li, C.; Huang, T.; Huang, Z.; Sun, J.; Zong, C.; Yang, J.; Deng, W.; Dai, F. A sulfonated cobalt phthalocyanine/carbon nanotube hybrid as a bifunctional oxygen electrocatalyst. *Dalton Trans.,* **2019**, *48*, 17258-17265.

[62] Simm, A. O.; Banks, C. E.; Compton, R. G. The Electrochemical Detection of Arsenic (III) at a Silver Electrode. *Electroanalysis* **2005**, *3* (III), 1727–1733.

[63] Simm, A.; Banks, C.; Compton, R. Sonoelectroanalytical Detection of Ultra-Trace Arsenic. *Electroanalysis* **2005**, *17* (4), 335–342.

[64] Rassaei, L.; Sillanpää, M.; French, R. W.; Compton, R. G.; Markenc, F. Arsenite Determination in Phosphate Media at Electroaggregated Gold Nanoparticle Deposits. *Electroanalysis* **2008**, *20* (12), 1286–1292.

[65] Sánchez, J. A.; Rivas, B. L.; Pooley, S. A.; Basaez, L.; Pereira, E.; Pignot-Paintrand, I.; Bucher, C.; Royal, G.; Saint-Aman, E.; Moutet, J. C. Electrocatalytic Oxidation of As(III) to As(V) Using Noble Metal-Polymer Nanocomposites. *Electrochim. Acta* **2010**, *55* (17), 4876–4882.

[66] Kumar, S.; Bhanjana, G.; Dilbaghi, N.; Kumar, R.; Umar, A. Fabrication and Characterization of Highly Sensitive and Selective Arsenic Sensor Based on Ultra-Thin Graphene Oxide Nanosheets. *Sensors Actuators, B Chem.* **2016**, *227*, 29–34.

[67] Ottakam Thotiyl, M. M.; Basit, H.; Sánchez, J. A.; Goyer, C.; Coche-Guerente, L.; Dumy, P.; Sampath, S.; Labbé, P.; Moutet, J. C. Multilayer Assemblies of Polyelectrolyte-Gold Nanoparticles for the Electrocatalytic Oxidation and Detection of arsenic(III). *J. Colloid Interface Sci.* **2012**, *383* (1), 130–139.

[68] Azad, U. P.; Ganesan, V. Tris(4,4'-dimethyl-2,2'-bipyridine)iron(II)-Exchanged Nafion for Arsenite Determination in Water Samples. *ChemElectroChem* **2014**, *1* (2), 379–383.

[69] Rastogi, P. K.; Yadav, D. K.; Pandey, S.; Ganesan, V.; Sonkar, P. K.; Gupta, R. Synthesis and Characterization of Gold Nanoparticles Incorporated Bentonite Clay for Electrocatalytic Sensing of arsenic (III). *J. Chem. Sci.* **2016**, *128* (3), 349–356.

[70] Khairy, M.; Kampouris, D. K.; Kadara, R. O.; Banks, C. E. Gold Nanoparticle Modified Screen Printed Electrodes for the Trace Sensing of Arsenic (III) in the Presence of Copper(II). *Electroanalysis* **2010**, *22* (21), 2496–2501.

[71] Ivandini, T. A.; Sato, R.; Makide, Y.; Fujishima, A.; Einaga, Y. Electrochemical Detection of arsenic(III) Using Indium-Implanted Boron-Doped Diamond Electrodes. *Anal. Chem.* **2006**, *78* (18), 6291–6298.

[72] Shrivastava, A.; Gupta, V. Methods for the Determination of Limit of Detection and Limit of Quantitation of the Analytical Methods. *Chronicles Young Sci.* **2011**, *2 (1)*, 21.

[73] Fonollosa, J.; Vergara, A.; Huerta, R.; Marco, S. Estimation of the Limit of Detection Using Information Theory Measures. *Anal. Chim. Acta* **2014**, *810*, 1–9.

[74] Battu, S.; Itagi, M.; Bhat, Z. M.; Khaire, S.; Kottaichamy, A. R.; Sannegowda, L. K.; Thimmappa, R.; Thotiyl, M. O. Metal Coordination Polymer Framework Governed by Heat of Hydration for Noninvasive Differentiation of Alkali Metal Series. *Anal. Chem.* **2018**, *90*, 12917–12922.

# Chapter-5

## Isomerism-Activity Relation in Reductive Molecular Electrocatalysis

**Abstract**: Robust and durable molecular electrocatalysts based on earth abundant metals are essential for the interconversion of electrical energy and fuels to address the global mismatch between energy production and demand. In this context cobalt and iron based phthalocyanine complexes (CoPc and FePc) were extensively investigated as potential electrocatalysts for oxygen reduction reaction (ORR); the limiting cathodic half-cell reactions in air batteries and fuel cells. The state of the art approaches to improve the catalytic activity of these molecular catalysts primarily involves substitutions at the secondary sphere. In the context of ORR, a lot of focus has been devoted to understand the effect of the nature of secondary sphere functionality on the catalytic metal centre, however, much less is known about the role of the isomerism of the same functionality in tuning their electrocatalytic activity. We show in detail how the regioisomerism of electron-donating -$NH_2$ substituent at the $N_4$ macrocycle of metal phthalocyanines tunes the activity of the catalytic metal centre and influences the mechanistic pathways of ORR. Electrochemical and spectroscopic analyses and density functional theory calculations suggest that the attractive field effect existing via the intramolecular H bonding in the α-TACoPc isomeric molecule activates the central cobalt ion towards ORR by favoring a direct 4 electron pathway. On the other hand the absence of such non-covalent interactions in its β isomer counterpart (β-TACoPc) due to the relatively large spatial separation of H bonding groups, prompts ORR in a 2 electron pathway with the intermediacy of peroxide. Therefore, isomerism induced activation of molecular electrocatalysts induces selectivity in reductive electrocatalysis which in turn provides a new approach in the design of efficient non-precious electrocatalysts for energy conversion (4 electron process) and peroxide production (2 electron process). This study brings to light a factor that is often overlooked in the design of efficient non-precious molecular electrocatalysts i.e., the isomerism of the substituent at the secondary sphere can tune the catalytic activity of the central metal ion as well as the reaction mechanism.

**Declaration:** This is the original work and has not yet been published anywhere.

Alagar Raja et al., Isomerism-Activity Relation in Reductive Molecular Electrocatalysis (*Manuscript under preparation*).

## 5.1. Introduction

Electrocatalysis pertaining to the transformations of substrates such as $H_2$, $H^+$, $H_2O$, $O_2$, and $CO_2$ are central to renewable energy storage and conversion.[1-5] Among these, the electrochemical reduction of oxygen (ORR) is ubiquitous in many electrochemical energy systems including fuel cells[6-11] and metal-air batteries[12-16]. However, the sluggish kinetics involved in breaking the molecular oxygen bonds even on noble metal electrocatalysts make ORR equally a limiting half-cell reaction in electrochemical energy systems.[6-17] Though noble metals (like platinum, gold, silver etc.), metal oxides, mixed oxides such as spinels and perovskites have been widely investigated as electrocatalysts for ORR,[18-22] the benchmark ORR electrocatalyst have been based on platinum,[17, 20-22] however, issues associated with its availability and cost limit its practical viability in electrochemical power systems.[17, 22 ,23] This in turn demands the design and development of low-cost catalysts based on earth abundant metals which can catalyze ORR at lower overpotential in a pathway involving a direct four-electron transfer to molecular oxygen.[18, 23-27] In this context, molecular electrocatalysts such as metal phthalocyanines (MPcs) and metal porphyrins (MPs) have come to the frontier of energy research because of high degree of tunability of their electronic and geometric parameters.[28-32] Co and Fe based metal phthalocyanines have received special attention in ORR because of the corresponding central metal ion's high electrochemical activity.[22, 33-37] In these molecular electrocatalysts, it is well established that chemical identity of the secondary sphere functionality can promote the catalytic activity,[32, 38-42] by altering the electronic arrangement at the catalytic centre.[38-42] Equally, this electronic arrangement can also be a function of a substituent's isomerism and no previous research has made enough efforts to understand this isomerism-activity relation in reductive electrocatalysis. Therefore, the aim of this study is to resolve a distinction between the chemical identity of groups and their isomerism in reductive electrocatalysis such as ORR and fill the knowledge gap in the molecular structure-activity relation through an examination of isomerism induced electrocatalysis by amino substituted molecular electrocatalysts.

This exploratory investigation reveals that the isomerism of $-NH_2$ groups at the $N_4$ macrocycle of metal phthalocyanines (Figure 5.1a) can intensely tune the catalytic metal center with the α isomer highly favoring ORR compared to the corresponding β isomer. The interesting result is that the α-TACoPc isomer catalyzed ORR via a direct 4-electron pathway producing $H_2O$ compared to a 2 electron peroxide producing pathway catalyzed by the corresponding β-TACoPc isomer molecule. This study demonstrates that isomerism of secondary sphere functionality not only activates the catalytic metal centre but also the tunes the ORR mechanistic pathways. Therefore, isomerism induced activation of molecular electrocatalysts bring in selectivity in reductive electrocatalysis which in turn provides a new approach in the design of efficient non-precious electrocatalysts for energy conversion (4 electron process) and peroxide production (2 electron process).

## 5.2. Results and discussion

### 5.2.1. Characterization of α-TACoPc and β-TACoPc isomeric molecules

It is well-known that electron donating substituents like $-NH_2$ at the $N_4$ macrocycle of metal phthalocyanines can activate the catalytic central metal ion towards oxygen reduction reaction.[43-48] However, it still not known how these electron donating effects operate at the molecular level when the substituents position is altered at the secondary sphere of molecular catalysts. In order to investigate this, we have synthesized and characterized the regioisomers of tetra-amino cobalt phthalocyanines (TACoPc) with $-NH_2$ substitution at the α and β positions (Figure 5.1a) [48-50] (please refer to the synthesis, Chapter 2, section 2.4.2, page 47). Matrix assisted laser desorption/ionization-time of flight mass spectrometry (MALDI-TOF) shows the parent ion peak at m/z value of ~632 corresponding to the molecular masses of TACoPc, Figure 5.1b,c. Minor peaks at m/z values 273, 360, 437 and 566 indicate their fragment peaks. UV-Vis spectra of these molecules show Q band and B band in the range of 650-800 nm and 200-350 nm respectively which are characteristics of metal phthalocyanines, [51-53] Figure 5.1d. A small peak close to 450 nm is attributed to the charge transfer band.[51-53] A comparison between α-TACoPc (α isomer) and β-TACoPc (β isomer) isomeric molecules with respect to their UV-Vis spectra suggests a red-shifted Q band in the former. Q band has more ligand characteristics[54,55] and hence this

red shift indicates comparatively extensive delocalization of charge density in the α isomer compared to the β isomer.[56,57] FTIR spectra of isomeric molecules indicate C-N bond vibration at ~1114 $cm^{-1}$, aromatic ring vibrations at ~1635 $cm^{-1}$, phthalocyanine skeletal vibrations at ~1246 $cm^{-1}$, Figure 5.1e. The appearance of stretching vibrations in the range 3190-3450 $cm^{-1}$ is indicative of primary amine groups in the isomeric molecules.[58,59] Raman spectra (Figure 5.1f) reveal phthalocyanine signature peaks with C-H in plane deformation in the macrocyclic ring at ~1195 $cm^{-1}$ and macrocyclic stretching vibration at ~764 $cm^{-1}$.[55,56] Stretching vibration of the isoindole ring unit is observed at a Raman shift of ~1456 $cm^{-1}$ and C-N in plane stretching vibrations are observed at ~1404 $cm^{-1}$ and ~1678 $cm^{-1}$,[60,61] Figure 5.1f.

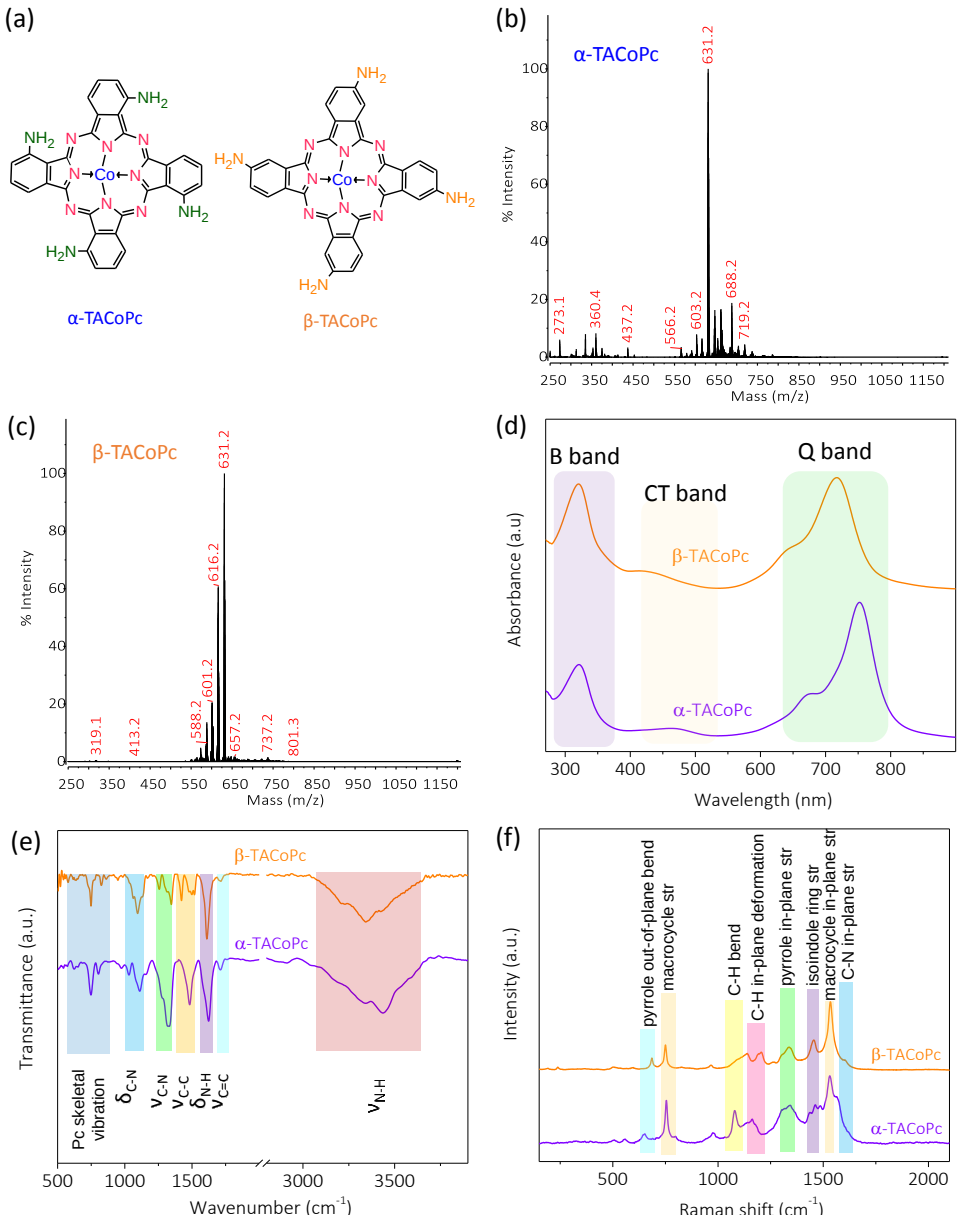

**Figure 5.1:** (a) Molecular structure of α-TACoPc and β-TACoPc isomeric molecules. Matrix-assisted laser desorption ionization time-of-flight mass spectrometry (MALDI-TOF) of (b) α-TACoPc isomer and (c) β-TACoPc isomer. (d) UV-Visible spectroscopy, (e) Fourier transform infra-red (FTIR) spectroscopy and (f) Raman spectroscopy of α-TACoPc and β-TACoPc isomeric molecules.

### 5.2.2. Electrochemical analysis

To investigate their isomerism-activity relation in ORR, the molecules were initially adsorbed as a monolayer on a glassy carbon electrode (GC) from dimethylformamide (DMF) solutions (See chapter 2, section 2.5 for more details, pages 48-49). Amatore parameter which indicates the quality of a monolayer is observed to be > 0.9 indicating the formation of relatively defect free monolayers on electrode surfaces, Figure 5.2 and Table 5.1, (Refer to chapter 2, section 2.6.2 for more details, pages 49-50).[62,63] Quartz crystal microbalance (QCM) studies during the electrode modification with CoPc, α-TACoPc and β-TACoPc molecules indicate almost equal changes in mass, Figure 5.3. The surface coverage values (using Saurbrey equation, please see chapter 2, section 2.6.3 section for more details, page 50)[64-66] extracted from QCM are ~4.71 × $10^{-11}$ mol/cm$^2$ and ~4.75 × $10^{-11}$ mol/cm$^2$, for α-TACoPc and β-TACoPc isomeric molecules respectively, Figure 5.3, and Table 5.2. These values are close to the theoretically expected value of 1.1 × $10^{-10}$ mol/cm$^2$ for a perfectly flat phthalocyanine monolayer on an electrode surface,[67-69] indicating the adsorption of isomeric molecules as a monolayer with nearly a flat orientation on the GC electrode surface.

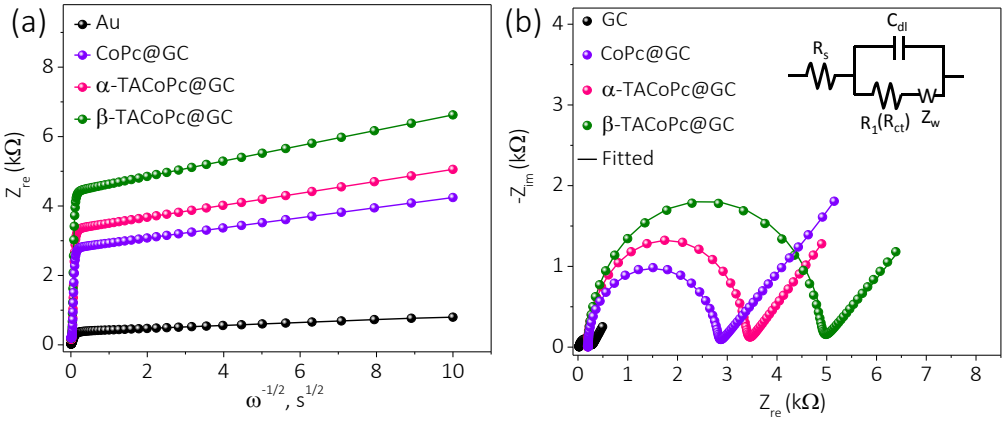


**Figure 5.2:** The Amatore's parameter for unsubstituted CoPc and α-TACoPc and β-TACoPc isomeric molecules when adsorbed as a monolayer on a GC electrode. Electrolyte is $N_2$ saturated 0.1 M phosphate buffer of pH = 7 containing 5 mM ferrocyanide/ferricyanide

redox couple. (a) The plot of real part of impedance ($Z_{re}$) vs. $1/(\omega)^{1/2}$ where ω is the angular frequency of AC in rad/s and (b) the complex plane impedance plot at the open circuit voltage acquired in the frequency range of 100 kHz to 5 mHz with an AC amplitude of 10 mV (peak to peak). The circuit used for fitting the Nyquist plot is shown in the inset of Figure 5.2b.

**Table 5.1:** Fractional surface coverage (θ) values of the modified GC electrodes from Amatore's model.

| Types of Electrodes | Monolayer Coverage (θ) | |
|---|---|---|
| | $^{*}\theta_{IS}{}^{R}$ | $^{*}\theta_{IS}{}^{P}$ |
| **CoPc@GC** | 0.92 ± 0.02 | 0.92 ± 0.02 |
| **α-TACoPc@GC** | 0.93 ± 0.02 | 0.94 ± 0.03 |
| **β-TACoPc@GC** | 0.96 ± 0.03 | 0.97 ± 0.01 |

$^{*}\theta_{IS}{}^{R}$ and $^{*}\theta_{IS}{}^{P}$ stand for coverage values estimated based on charge transfer resistance (Chapter 2, eq 2.2) and pinhole size (Chapter 2, eq 2.3) respectively.

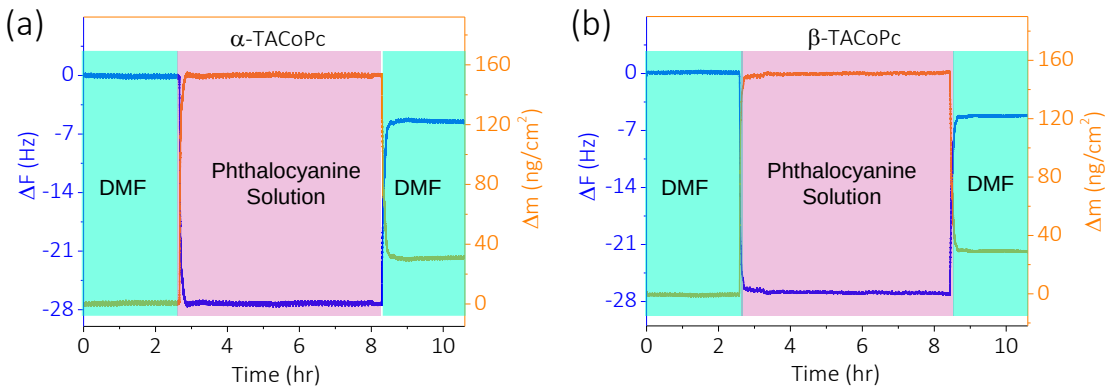


**Figure 5.3:** Quartz crystal microbalance (QCM) response during the adsorption of isomeric molecules (α-TACoPc and β-TACoPc) on carbon coated quartz resonator from 0.2 mM solution of (a) α-TACoPc and (b) β-TACoPc in dimethylformamide (DMF). The blue trace shows the frequency change during the adsorption and the orange trace shows the calculated mass change using the Saurbrey equation.

**Table 5.2:** Surface coverage (Γ) values of α-TACoPc and β-TACoPc isomeric molecules from Figure 5.3.

| Types of Electrodes | Surface Coverage (Γ) |
|---|---|
| **α-TACoPc@GC** | $4.71 \times 10^{-11}$ mol/cm$^2$ |
| **β-TACoPc@GC** | $4.75 \times 10^{-11}$ mol/cm$^2$ |

To explore the effect of the regioisomerism of unsubstituted and -$NH_2$ substituted cobalt phthalocyanines (CoPc) towards reductive ORR electrocatalysis, linear sweep voltammetry (LSV) and chronopotentiometry analyses were carried out with CoPc, α-TACoPc and β-TACoPc modified carbon electrodes, Figure 5.4. LSV and chronopotentiometric (potential vs. time) analysis suggest that the α-TACoPc isomer outperforms the corresponding β-TACoPc isomer in terms of onset potential and the potential required for achieving a particular current density with the unsubstituted CoPc demonstrating the least activity, Figure 5.4a,b and Table 5.3. The performance metrics of these catalysts, Table 5.3, demonstrate that α-TACoPc isomer molecule has dominant electrocatalytic activity towards ORR compared to its β counterpart and unsubstituted CoPc. These results suggest that the activity toward ORR is greatly influenced by the position of electron-donating –$NH_2$ group on the secondary sphere of CoPc which establishes an isomerism-activity relationship in reductive electrocatalysis.

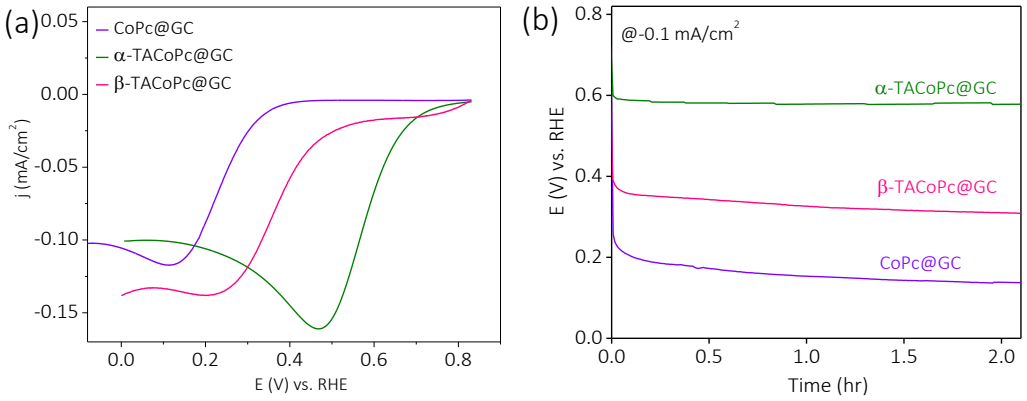


**Figure 5.4:** Linear sweep voltammograms (LSVs) at a scan rate of 20 mV/s in $O_2$ saturated 0.5 M $H_2SO_4$ with –$NH_2$ substituted isomeric molecules when they are incorporated as a monolayer on a glassy carbon electrode. (b) Chronopotentiometric traces at 0.1 mA/cm$^2$ in $O_2$ saturated 0.5 M $H_2SO_4$ with α and β-TACoPc isomeric molecules when they are adsorbed as a monolayer on a glassy carbon electrode.

**Table 5.3:** Electrochemical parameters extracted from Figure 5.4.

| Electrodes | Onset Potential (V) vs. RHE | Potential (V) @ -0.1 mA/cm$^2$ |
|---|---|---|
| **CoPc** | 0.36 | 0.18 |
| **α-TACoPc@GC** | 0.71 | 0.57 |
| **β-TACoPc@GC** | 0.52 | 0.35 |

### 5.2.3. Orientation versus isomerism

As explained above, the substitution with amino groups as well as its position at the secondary sphere of phthalocyanine ring have distinct effects on the course of electrocatalytic oxygen reduction reaction, wherein a higher electrocatalytic activation is experienced by the central metal ion when amino group resides at the α position compared to the β position. It has been reported in the literature that due to the differences in the position of $–NH_2$ group, on a Au electrode where this amino substituted molecules can self-assemble as a monolayer, the α-TACoPc molecule and the catalytic cobalt centre adopts nearly a flat orientation with respect to the anchoring substrate.[46,47,70] On the other hand, the β-TACoPc isomer adopts nearly a perpendicular orientation with respect to the anchoring Au electrode.[46,47,70] For aforementioned reasons, the disparity between their ORR activities are explained in the literature to be due to differences in their orientation with respect to the anchoring substrate.[46,47] In order to investigate whether electrocatalytic activity difference is a result of orientation or inherent property of the molecules, a series of experiments were carried out by controlling the orientation of molecules on gold electrodes. We first carried out the study with isomeric molecules adsorbed directly from dimethylformamide (DMF) solutions as a monolayer on Au electrodes (See chapter 2, section 2.5 for more details, pages 48-49). These modified electrodes demonstrate an Amatore parameter > 0.9 suggesting the formation of relatively defect free monolayer of molecules on the Au electrode surfaces, Figure 5.5 and Table 5.4 (refer to chapter 2, section 2.6.2 for more details, pages 49-50).[62-63] Quartz crystal microbalance (QCM) studies during the Au electrode modification with α-TACoPc and β-TACoPc isomeric molecules indicate a mass change due to adsorption of molecules, Figure 5.6 and the surface coverage values (using Saurbrey equation)[64-69] suggest that the coverage is in the range of $4.72 \times 10^{-11}$ mol/cm$^2$ and $1.34 \times 10^{-10}$ mol/cm$^2$ respectively for α-TACoPc and β-TACoPc isomeric molecules, Figure 5.6 and Table 5.5. Significant differences in the coverage values of isomeric molecules under the same experimental conditions seems to suggest a difference in their orientation with respect to the anchoring Au electrode. Theoretically expected value of coverage for a perfectly flat monolayer of phthalocyanine molecules is $1.1 \times 10^{-10}$ mol/cm$^2$.[67-70] The experimental coverage value for α-TACoPc isomer molecule is noticeably less than the theoretical value

indicating the adsorption of the molecule with nearly a flat orientation on the Au electrode, Scheme 5.1. On the other hand, the higher value of coverage than the theoretical value in the case of β-TACoPc isomer molecule signal the adsorption of the molecule with nearly a perpendicular orientation on the Au electrode, Scheme 5.1. Though the surface coverage falls in the range of monolayer coverage which is confirmed by Amatore's parameter (Table 5.1 and 5.2), the lower surface coverage observed with α-TACoPc isomer molecule compared to β-TACoPc counterpart prompted many groups to believe that they indeed adopt a different orientation,[46,47,70] and the disparities in their ORR electrocatalytic activities are derived from this orientation difference. In order to verify this, ORR studies were carried out with these modified electrodes in oxygen saturated solution, Figure 5.7. As expected, the LSVs, Figure 5.7a, and Figure 5.7b, suggest that the α-TACoPc isomer molecule anchored on gold substrates is highly active towards ORR in acidic medium compared to the β-TACoPc isomer molecule. It is to be noted that the bare gold electrode experiences an electrocatalytic shift on anchoring with α/β-TACoPc isomeric molecules, indicating these molecules are catalytic in nature towards ORR. Nevertheless as noted earlier, the higher activity of α-TACoPc isomer compared to β-TACoPc isomer molecule is attributed to their orientation difference with respect to anchoring Au electrode, Scheme 1. It is reported that the flat orientation of α-TACoPc brings the catalytic central metal ion closer to the Au substrate thereby facilitating the electron transfer to molecular oxygen and nearly a perpendicular orientation of β-TACoPc isomer molecule make this electron transfer less efficient. We do not question the possibility of orientation difference between these isomeric molecules contributing to their electrocatalytic disparity in the present architecture, but we disagree with the notion that orientation is the sole factor for their electrocatalytic activities due to following reasons.

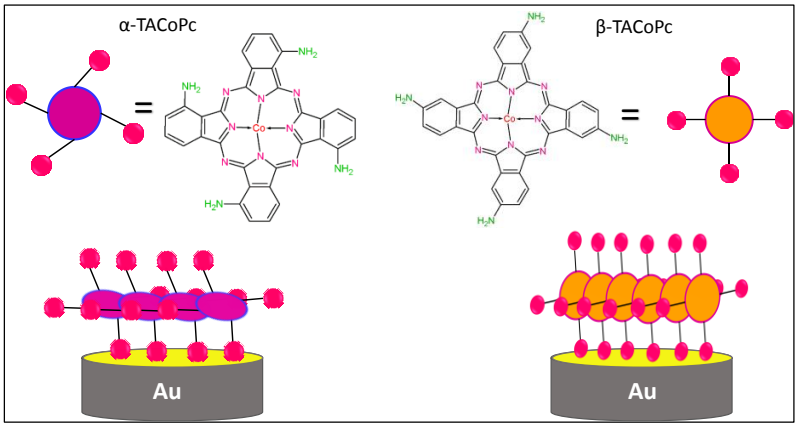

**Scheme 5.1:** Schematic representation of the orientation of α-TACoPc and β-TACoPc isomer molecules when a gold electrode is directly modified by these isomeric molecules.

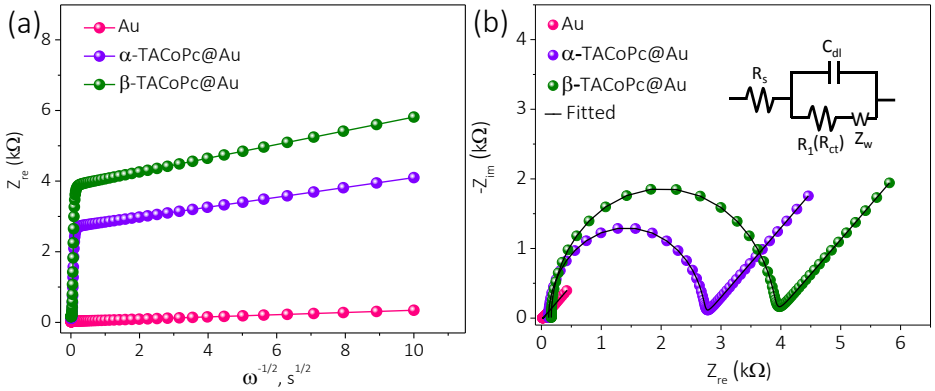


**Figure 5.5:** The Amatore's parameter for α-TACoPc and β-TACoPc isomeric molecules when they are adsorbed as a monolayer on a gold electrode. Electrolyte is $N_2$ saturated 0.1 M phosphate buffer of pH = 7 containing 5 mM ferrocyanide/ferricyanide redox couple. (a) The plot of real part of impedance ($Z_{re}$) vs. $1/(\omega)^{1/2}$ where ω is the angular frequency of AC in rad/s and (b) the complex plane impedance plot at the open circuit voltage acquired in the frequency range of 100 kHz to 5 mHz with an AC amplitude of 10 mV. The circuit used for fitting the Nyquist plot is shown in the inset of Figure 5.5b.

**Table 5.4:** Fractional surface coverage (θ) values of the modified gold electrodes from Amatore's model.

| Types of Electrodes | Monolayer Coverage (θ) | |
|---|---|---|
| | $^*\theta_{IS}{}^R$ | $^*\theta_{IS}{}^P$ |
| **α-TACoPc@Au** | 0.94 ± 0.01 | 0.95 ± 0.03 |
| **β-TACoPc@Au** | 0.97 ± 0.02 | 0.98 ± 0.01 |

$^*\theta_{IS}{}^R$ and $^*\theta_{IS}{}^P$ stand for coverage values estimated based on charge transfer resistance (Chapter 2, eq 2.2) and pinhole size (Chapter 2, eq 2.3) respectively.

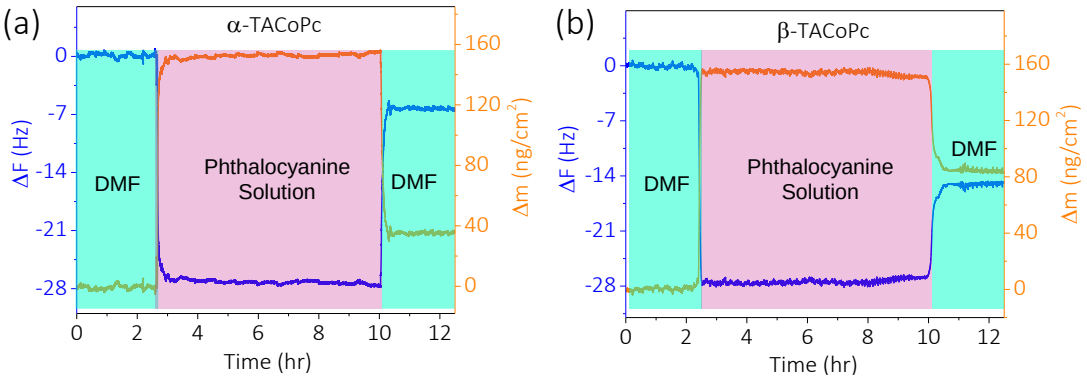


**Figure 5.6:** Quartz crystal microbalance (QCM) response during the adsorption of isomeric

molecules (α-TACoPc and β-TACoPc) on gold coated quartz resonator from 0.2 mM solution of (a) α-TACoPc and (b) β-TACoPc in dimethylformamide (DMF). The blue trace shows the frequency change during the adsorption and the orange trace shows the calculated mass change using the Saurbrey equation.

**Table 5.5:** Surface coverage (Γ) values of α-TACoPc and β-TACoPc isomeric molecules from Figure 5.6.

| Types of Electrodes | Surface Coverage (Γ) |
|---|---|
| α-TACoPc@Au | $4.72 \times 10^{-11}$ mol/cm$^2$ |
| β-TACoPc@Au | $1.34 \times 10^{-10}$ mol/cm$^2$ |

(a)

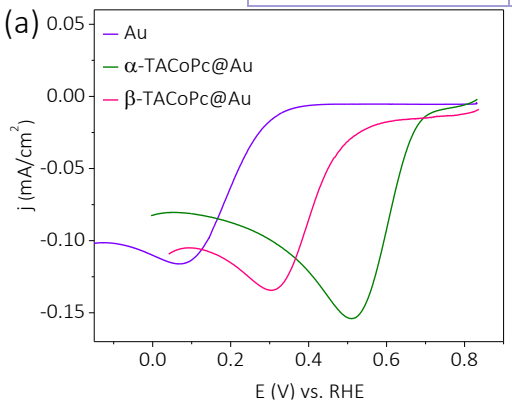


(b)

| Electrodes | Onset Potential (V) vs. RHE | Potential (V) @ -0.1 mA/cm² |
|---|---|---|
| Au | 0.33 | 0.14 |
| α-TACoPc@Au | 0.71 | 0.58 |
| β-TACoPc@Au | 0.54 | 0.38 |

**Figure 5.7:** (a) Linear sweep voltammograms at a scan rate of 20 mV/s in oxygen saturated 0.5 M $H_2SO_4$ with α-TACoPc, and β-TACoPc isomer molecules when they are adsorbed as a monolayer on a Au electrode and (b) electrochemical parameters extracted from Figure 5.7a.

Firstly, we controlled the orientation of the α-TACoPc and β-TACoPc isomeric molecules on a gold substrate using a mercapto pyridine (4-MP) interlayer, by exploiting the axial ligation capability of N on 4-MP (Scheme 5.2) to the catalytic Co center in isomeric molecules. This should orient either molecules on the Au substrate in the same flat configuration,[71-73] Scheme 5.2. These axially ligated isomeric molecules demonstrated an Amatore parameter > 0.9 suggesting that the formed monolayers are relatively defect free, Figure 5.8 and Table 5.6.[62,63] The quartz crystal microbalance (QCM) studies during the electrode modification of 4-MP modified Au coated quartz crystal with α-TACoPc and β-TACoPc isomeric molecules indicate that the mass changes, calculated using Saurbrey equation, corresponds to a monolayer surface coverage, Figure 5.9 and Table 5.7.[64-66]

The surface coverage values on axial ligation fall in the range of $4.63 \times 10^{-11}$ mol/cm$^2$ for α-TACoPc isomer and $4.68 \times 10^{-11}$ mol/cm$^2$ for β-TACoPc isomer, Table 5.7, which are lower than theoretical value of $1.1 \times 10^{-10}$ mol/cm$^2$ for a perfectly flat phthalocyanine monolayer on an electrode surface.[67-69] These clearly indicate that on axial ligation, the adsorption of isomeric molecules occurs as a monolayer with nearly a flat orientation on the electrode surface. With these isomeric molecules having almost similar orientation, LSVs for ORR still demonstrate a similar electrocatalytic disparity as with the Au electrodes having different orientation of isomeric molecules (direct modification, Scheme 5.1 and Figure 5.7) with a higher activity in favor of α-TACoPc isomer molecule compared to β-TACoPc isomer molecule, Figure 5.10a,b. If it is an orientation effect, it is rather intriguing and baffling to note the significantly different activity profiles of isomeric molecules when they adopt almost similar orientation on the electrode surface. Therefore, this study reveals, that the orientation effect cannot be taken as the responsible factor for the tuning of the catalytic metal center in α/β-TACoPc isomeric molecules during ORR.

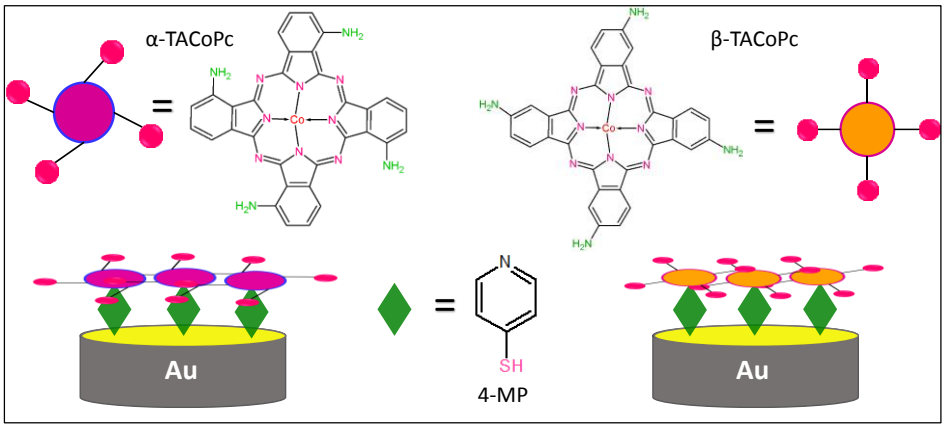


**Scheme 5.2:** Schematic representation of axial ligation of isomeric molecules on a Au electrode modified with 4-MP monolayer.

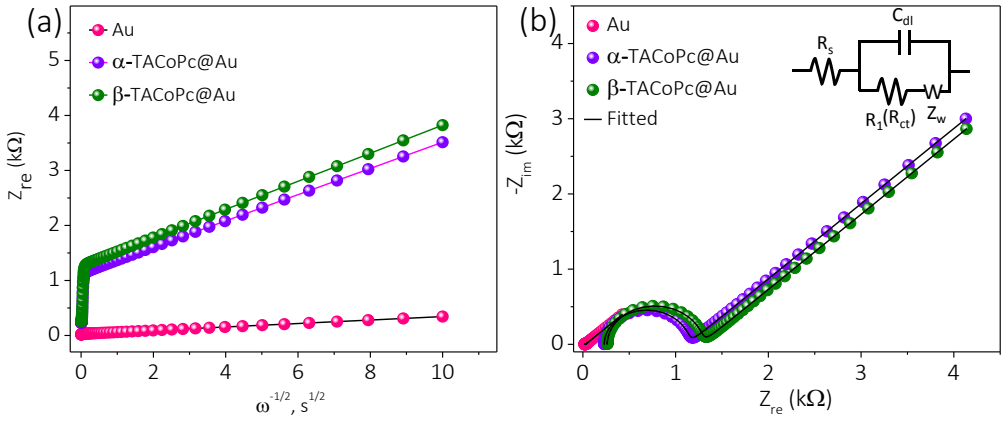

**Figure 5.8:** The Amatore's parameter for α-TACoPc and β-TACoPc isomeric molecules when adsorbed as a monolayer on a 4-MP interlayer modified gold electrode. Electrolyte is $N_2$ saturated 0.1 M phosphate buffer of pH = 7 containing 5 mM ferrocyanide/ferricyanide redox couple. (a) The plot of real part of impedance ($Z_{re}$) vs. $1/(\omega)^{1/2}$ where ω is the angular frequency of AC in rad/s and (b) the complex plane impedance plot at the open circuit voltage acquired in the frequency range of 100 kHz to 5 mHz with an AC amplitude of 10 mV. The circuit used for fitting the Nyquist plot is shown in the inset of Figure 5.8b.

**Table 5.6:** Fractional surface coverage (θ) values of the modified Au electrodes from Amatore's model.

| Types of Electrodes | Monolayer Coverage (θ) | |
|---|---|---|
| | $^*\theta_{IS}{}^R$ | $^*\theta_{IS}{}^P$ |
| α-TACoPc@Au | 0.92 ± 0.01 | 0.94 ± 0.03 |
| β-TACoPc@Au | 0.93 ± 0.02 | 0.95 ± 0.02 |

$^*\theta_{IS}{}^R$ and $^*\theta_{IS}{}^P$ stand for coverage values estimated based on charge transfer resistance (Chapter 2, eq 2.2) and pinhole size (Chapter 2, eq 2.3) respectively.

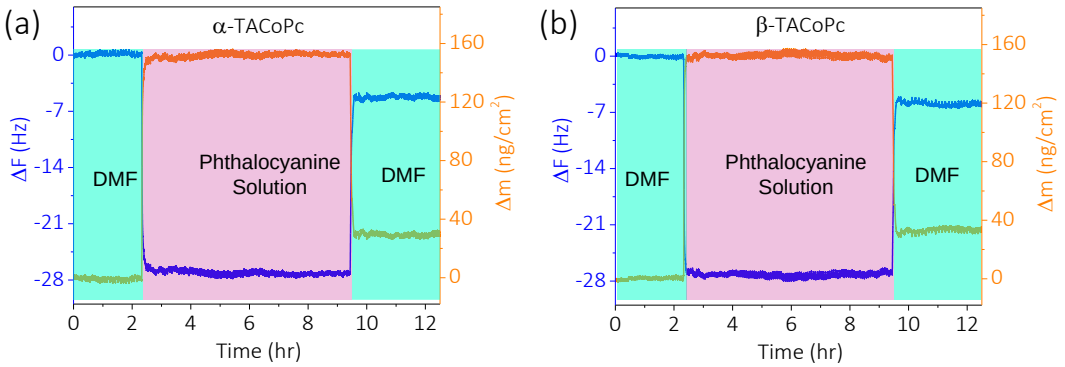


**Figure 5.9:** Quartz crystal microbalance (QCM) response during the adsorption of isomeric molecules (α-TACoPc and β-TACoPc) on a 4-MP interlayer modified gold coated quartz resonator from 0.2 mM solution of (a) α-TACoPc and (b) β-TACoPc in dimethylformamide (DMF). The blue trace shows the frequency change during the adsorption and the orange trace shows the calculated mass change using the Saurbrey equation.

**Table 5.7:** Surface coverage (Γ) values of α-TACoPc and β-TACoPc isomeric molecules from Figure 5.9.

| Types of Electrodes | Surface Coverage (Γ) |
|---|---|
| α-TACoPc@Au | $4.63 \times 10^{-11}$ mol/cm$^2$ |
| β-TACoPc@Au | $4.68 \times 10^{-11}$ mol/cm$^2$ |

(a)

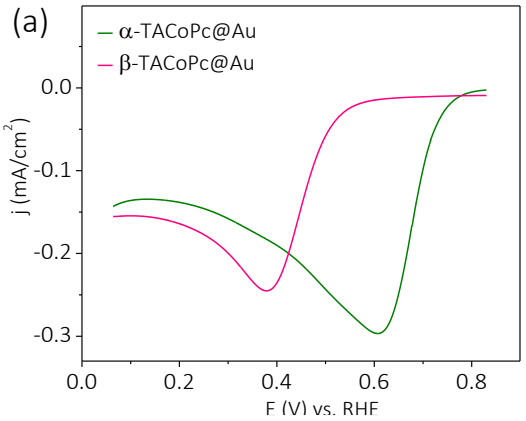


(b)

| Electrodes | Onset Potential (V) vs. RHE | Potential (V) @ -0.1 mA/cm$^2$ |
|---|---|---|
| α-TACoPc@Au | 0.77 | 0.68 |
| β-TACoPc@Au | 0.58 | 0.47 |

**Figure 5.10:** (a) LSVs at a scan rate of 20 mV/s in oxygen saturated 0.5 M $H_2SO_4$ with α-TACoPc and β-TACoPc isomeric molecules when they are adsorbed on a 4-MP interlayer modified gold electrode. (b) Electrochemical parameters extracted from Figure 5.10a.

From the foregoing discussion it is clear that the orientation effect is inaccurate for explaining the electrochemical activation of the catalytic metal center during regioisomerism of amino groups in CoPc molecules. In order to answer the obvious question as to why the isomerism of the –$NH_2$ group at the secondary sphere of the CoPc leads to an activation of the catalytic metal center, we would like to recall the discussion about α/β-TNCoPc in Chapter 3. In Chapter 3, we discussed in detail, how the repulsive field effect in the α-TNCoPc isomer between the O atom of –$NO_2$ group and the imine nitrogen of the phthalocyanine ring forces the –$NO_2$ group to cascade away from the conjugative plane of the $N_4$ macrocycle in their most stable conformation, (Refer Scheme 3.1 and associated discussion in Chapter 3 for more details). In similar lines, when the substitution is changed from -$NO_2$ to –$NH_2$ group at the α position on the phthalocyanine ring, an attractive field effect is expected because of the possible H bonding interaction between the –$NH_2$ group and the imine nitrogen of the phthalocyanine ring, (Scheme 5.3). This should lead to the presence of intramolecular hydrogen bonding in the α-TACoPc isomer. On the other hand, the relatively large spatial separation of H bonding groups in the β-TACoPc isomer should restrict the presence of any such attractive field effects in the molecule, Scheme 5.3. As shown below, this type of non-covalent interaction is responsible for tuning the activity of the

catalytic Co centre toward ORR in these isomeric molecules.

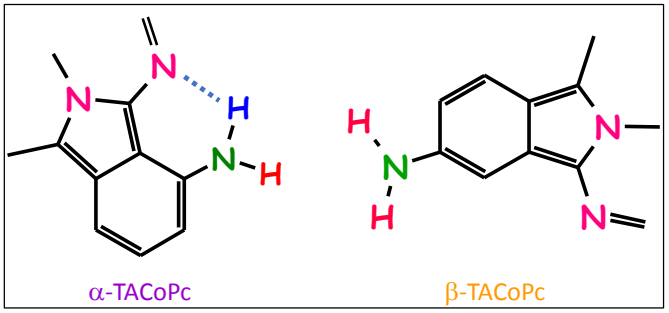


**Scheme 5.3:** Scheme showing intramolecular H bonding interactions in the α-TACoPc isomer involving imine nitrogen and amine protons. Scheme showing the absence of such hydrogen bonding interactions in β-TACoPc isomer due to the unfavourable positions of H bonding groups.

### 5.2.4. Nuclear magnetic resonance (NMR) spectroscopy investigations

To experimentally validate the hypothesis of hydrogen bonding, we have carried NMR analysis with isomeric amino substituted zinc phthalocyanines as corresponding cobalt phthalocyanines are paramagnetic in nature.[74,75] 1D (5.11a, b) and 2D proton NMR spectra (5.11c-f) of isomeric molecules reveal the existence of intramolecular hydrogen bonding interactions in the α isomer, Figure 5.11a, 5.11c and 5.11e. 1D NMR shows two distinctly chemical shifted amine protons in the case of α isomer (labelled as e and d in the inset of Figure 5.11a for α-TAZnPc) which could be exchanged on $D_2O$ addition confirming their origin to amine protons, Figure 5.11a. This suggests that chemical environments of amine protons are distinctly different in the α isomer which is possible if there is intramolecular hydrogen bonding interactions involving the primary amine group and imine nitrogen in the phthalocyanine ring as shown in the inset of Figure 5.11a. The corresponding COSY and NOESY 2D NMR further suggest that amine protons are in hydrogen bonding with imine nitrogen, Figure 5.11c and 5.11e.

1D NMR of the corresponding β isomer (Figure 5.11b) revealed only a broad amine proton signal (labelled as d in the inset of Figure 5.11b for β-TAZnPc) which disappeared on $D_2O$ addition, suggesting amine protons are not involved in intramolecular hydrogen bonding. The corresponding COSY and NOESY NMR further rule out these intramolecular hydrogen bonding interactions in the β isomer, Figure 5.11d and 5.11f, probably due to the

unfavourable position of H bonding groups. Temperature-dependent NMR suggest a lower chemical shift slope for the amine protons in the α isomer compared to a noticeably higher slope for the amine protons in the β isomer, Figure 5.12. It should be noted that this slope for the amine protons in the α-TACoPc isomer is in the order expected for intramolecularly H bonded protons as reported in the literature.[76-78] All these suggest that α isomer has intramolecular hydrogen bonding involving imine nitrogen and amine protons as shown in Scheme 5.3.

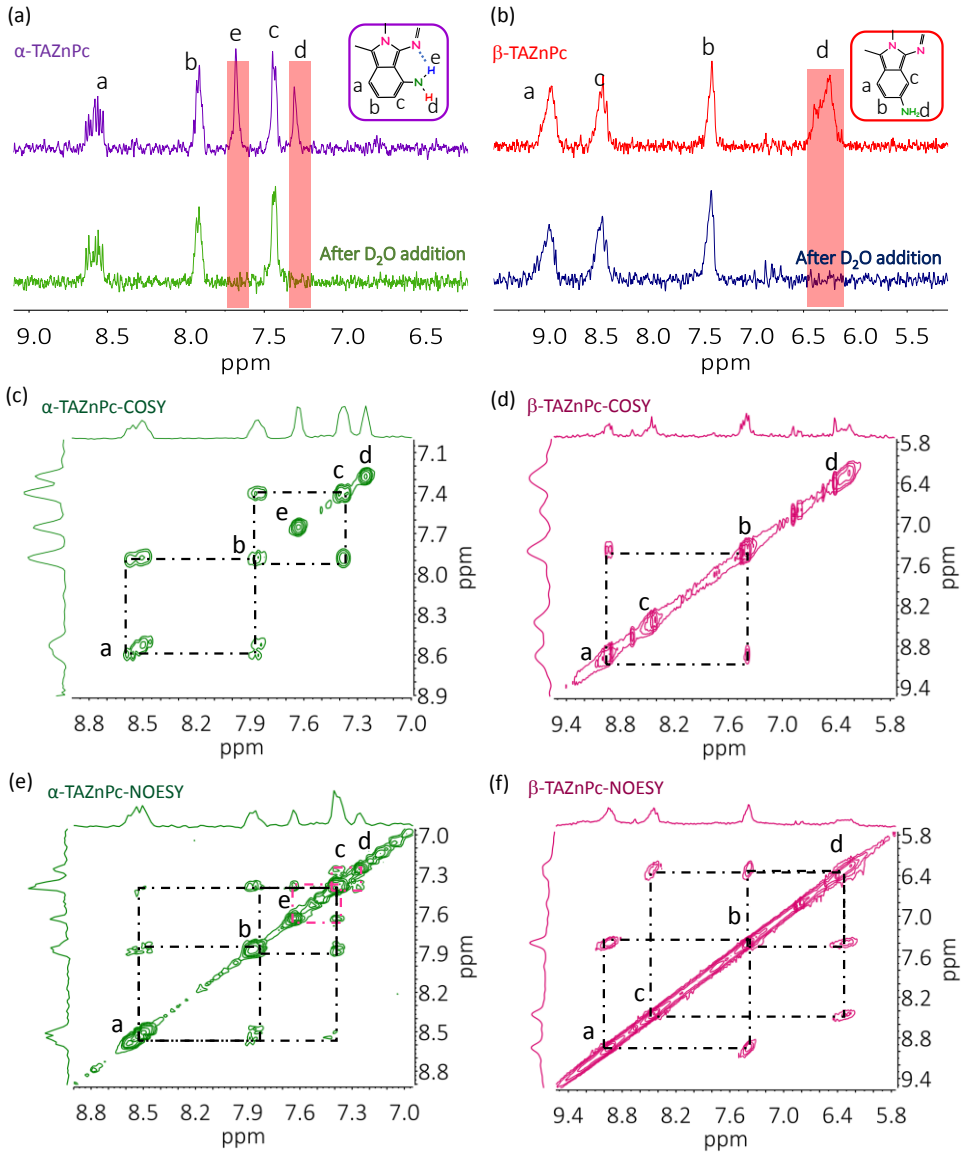


**Figure 5.11:** Nuclear magnetic resonance (NMR) spectra of α and β-TAZnPc isomeric molecules. (a and b) $^{1}$H NMR of α-TAZnPc and β-TAZnPc isomeric molecules before and after $D_2O$ addition. (c to f) 2D $^{1}$H NMR spectra (COSY and NOESY) of α-TAZnPc and β-TAZnPc isomeric molecules. COSY and NOESY spectra of α-TAZnPc (c and e) and β-TAZnPc (d and f) isomeric molecules.

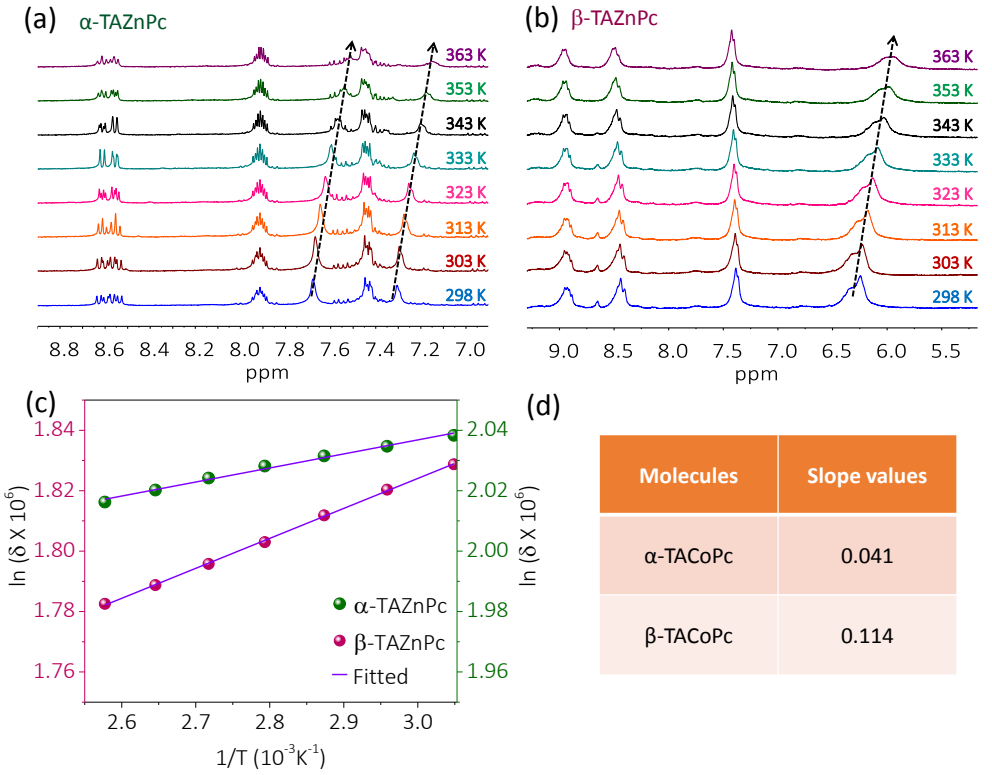


| Molecules | Slope values |
|---|---|
| α-TACoPc | 0.041 |
| β-TACoPc | 0.114 |

**Figure 5.12:** Temperature-dependent (25° to 90° C) $^{1}$H NMR spectra of (a) α-TNZnPc and (b) β-TNZnPc isomer molecules. (c) Plot of chemical shift vs. inverse of temperature (T) for the amine protons in isomeric α and β-TAZnPc molecules extracted from their respective temperature-dependent $^{1}$H NMR spectra (from Figures 5.12a and 5.12b) and (d) slope values extracted from Figure 5.12c.

In order to further understand the effect of this intermolecular hydrogen bonding on the catalytic metal centre, the catalytic systems were examined by X-ray photoelectron spectroscopy (XPS). XPS analysis of α and β-TACoPc isomers (Figure 5.13a) demonstrated two deconvoluted Co $2p_{3/2}$ peaks at binding energies of ~780.07 and ~781.83 eV corresponding to $Co^{2+}$ ($2p_{3/2}$) and $Co^{3+}$ ($2p_{3/2}$) species, respectively, along with a satellite feature at ~789.26 eV, which is a distinguishing feature of $Co^{2+}$.[79-81] The binding energy assignments are based on the available literature and on the clear peak broadening and asymmetry of the observed peaks in the $Co_{2p}$ region.[80,81] The relative contributions of $Co^{2+}$ ($2p_{3/2}$) and $Co^{3+}$ ($2p_{3/2}$) species in the isomeric molecules are found to be distinctly different with a higher $Co^{2+}/Co^{3+}$ ratio in favor of the α isomer (Figure 5.13a). Moreover, the higher contribution of $Co^{2+}$ in the α-TACoPc isomer is directly confirmed by the presence of satellite features at ~789.26 eV. Further, the $Co^{2+}/Co^{3+}$ area ratio (Figure 5.13b) followed the order α-TACoPc > β-TACoPc, which also matches very well by the presence of a satellite

feature at 789.26 eV, which more or less disappears when the relative composition of $Co^{2+}$ in the catalyst decreases below 50 %. It is to be noted that it is the partial positive charge density on the cobalt that is changing while going from α-TACoPc isomer to the β-TACoPc isomer. Taken together, XPS analysis suggests that regioisomerism of the $-NH_2$ group has a profound influence on the electron density experienced by the catalytic metal center which is higher in the α-TACoPc isomer compared to the β-TACoPc isomer. It is to be noted that in cobalt based phthalocyanine molecules, $Co^{2+}$ is the active intermediate during electrocatalytic ORR[22,34] as shown in eq 5.1 and 5.2, and its enrichment in the α-TACoPc isomer compared to β-TACoPc isomer explains the higher ORR activity of the former compared to the latter. It should be borne in mind that the exact fate of eq 5.1 and 5.2 depends heavily on the type of substrate as ORR is highly mechanistically complicated and cannot be described by a simple reaction scheme. Nevertheless, it can be concluded that the higher contribution of active catalytic species and the higher electron density experienc-

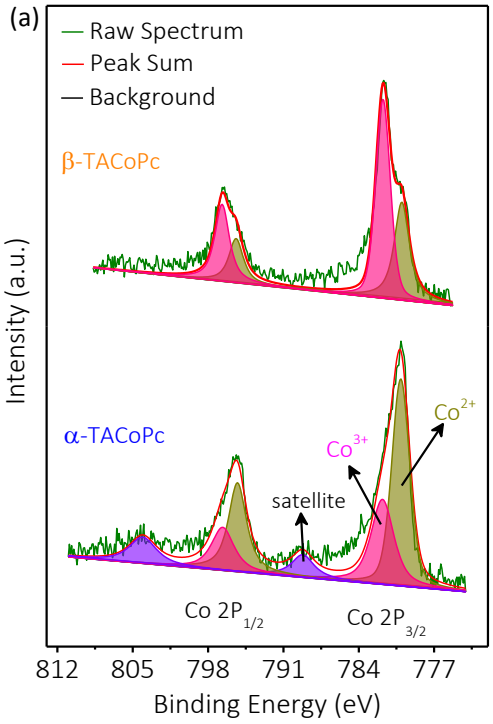


(b)

| Electrodes | Area | | Area ratio ($Co^{2+}$:$Co^{3+}$) |
|---|---|---|---|
| | $Co^{2+}$ | $Co^{3+}$ | |
| α-TACoPc | 16700 | 8400 | 1.98 |
| β-TACoPc | 6874 | 10924 | 0.63 |

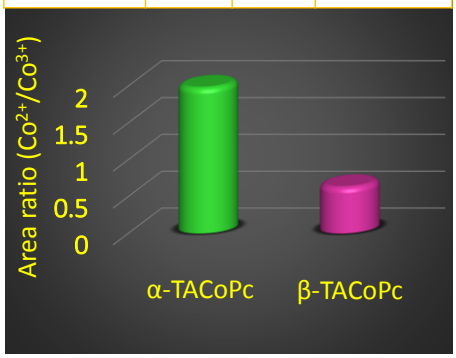


**Figure 5.13:** (a) X-ray photoelectron spectroscopy (XPS) of α and β-TACoPc isomers, (b) $Co^{2+}/Co^{3+}$ area ratio extracted from Co $2P_{3/2}$ region in Figure 5.13a.

-ed by the catalytic metal centre in α-TACoPc isomer molecule are responsible factors contributing to its distinctly different electrocatalytic ORR profile compared to β-TACoPc isomer molecule. This in turn undeniably reveals the existence of an isomerism-activity relation in reductive electrocatalysis.

$$Co(III) + e^- \rightleftharpoons Co(II) \ldots\ldots (5.1)$$

$$Co(II) + O_2 \rightleftharpoons Co(III)\text{-}O_2^- \text{ or } Co(II)\text{-}O_2 \ldots\ldots (5.2)$$

### 5.2.5. Mechanism of ORR on α/β-TACoPc isomeric molecules

The above discussion suggests that the isomerism of the substituents has a distinct effect on the electrocatalytic activities of TACoPcs towards the ORR. To elucidate it further, mechanistic studies were carried out for ORR on the isomeric molecules as it is considered important for efficient catalyst design. As reported in literature there are mainly two pathways for ORR, the first pathway is the direct 4 electron pathway, which involves the reduction of $O_2$ to $H_2O$, eq 5.3, and the second pathway is the indirect 2 electron pathway where the reduction of $O_2$ to $H_2O$ occurs with the intermediacy of $H_2O_2$, eqs 5.4 and 5.5.[22-27] The second pathway is an undesired pathway for electrochemical energy systems mainly because of the poisoning effect of $H_2O_2$ on the catalyst, however, it is the desired pathway in the electrochemical route to synthesize $H_2O_2$.[82-86]

**Direct pathway: (Acidic medium)**

$$O_2 + 4H^+ + 4e^- \rightarrow 2H_2O \ldots\ldots (5.3)$$

**Indirect pathway: (Acidic medium)**

$$O_2 + 2H^+ + 2e^- \rightarrow H_2O_2 \ldots\ldots (5.4)$$

$$H_2O_2 + 2H^+ + 2e^- \rightarrow 2H_2O \ldots\ldots (5.5)$$

In order to understand whether isomerism contributes to a change in their ORR mechanistic pathway, hydrodynamic voltammetry using rotating ring disk electrode (RRDE) were performed (See Chapter 2, section 2.9., pages 52-53 for more details) as shown in Figures 5.14a-5.14f. The number of electrons transferred and percentage of $H_2O_2$ produced during $O_2$ reduction on unsubstituted CoPc and isomeric α/β-TACoPc molecules were calculated using equations 5.6 and 5.7.[87-89] If there is intermediacy of $H_2O_2$, the number of electrons transferred should be close to 2 and the $H_2O_2$ percentage collected at the ring electrode should be relatively high. The present studies show that, number of electrons transferred on α-TACoPc isomer is close to 4, and the percentage of $H_2O_2$ is close to ~12.6 % suggesting that it primarily prefers a direct $4e^-$ pathway, Figure 5.14b, 5.14d-5.14f. In the

case of unsubstituted CoPc and β-TACoPc isomer molecule, the number of electrons transferred is close to 2 and the percentage of $H_2O_2$ falls in the range of 82-85 %, indicating the preference of the molecular catalysts to catalyze a $2e^-$ ORR pathway with the intermediacy of $H_2O_2$, Figure 5.14a, 5.14c-5.14f.

$$n = 4\left[I_d/\left(I_d + \left(\frac{I_r}{N}\right)\right)\right] \quad \ldots\ldots\ldots\ldots (5.6)$$

$$\% H_2O_2 = 200\left[\left(\frac{I_r}{N}\right)/\left(I_d + \left(\frac{I_r}{N}\right)\right)\right] \ldots\ldots\ldots (5.7)$$

where $I_d$ is the disc current, $I_r$ is the ring current and N is the collection efficiency of the Pt ring.

RRDE studies show that, the isomerism has not only a profound effect on the activity of these molecules but also has a direct effect on their mechanistic pathways. It is well-known in the literature that, the disparity in the mechanism is mainly governed by the orientation of reacting $O_2$ species with the catalytic center. Molecular oxygen can bind to catalytic metal centre either side-on or end-on configuration (Scheme 5.4) that in turn decides the overall ORR pathway.[22,35,90] Example, when there is a side-on orientation of the oxygen molecule at the catalytic metal centre, a direct 4 electron pathway will be favored with the formation of $H_2O$ as the final product. With an end-on orientation of the oxygen molecule at the catalytic metal center, on the other hand, a 2 electron pathway with intermediacy of $H_2O_2$ will be the possibility. To understand these possibilities we resorted to density functional theory (DFT) calculations with these isomeric molecules.

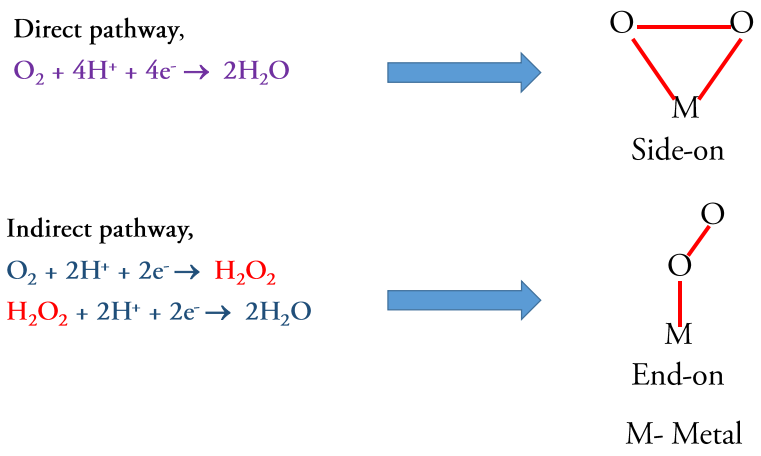


**Scheme 5.4:** Mechanistic pathways for oxygen reduction reaction.

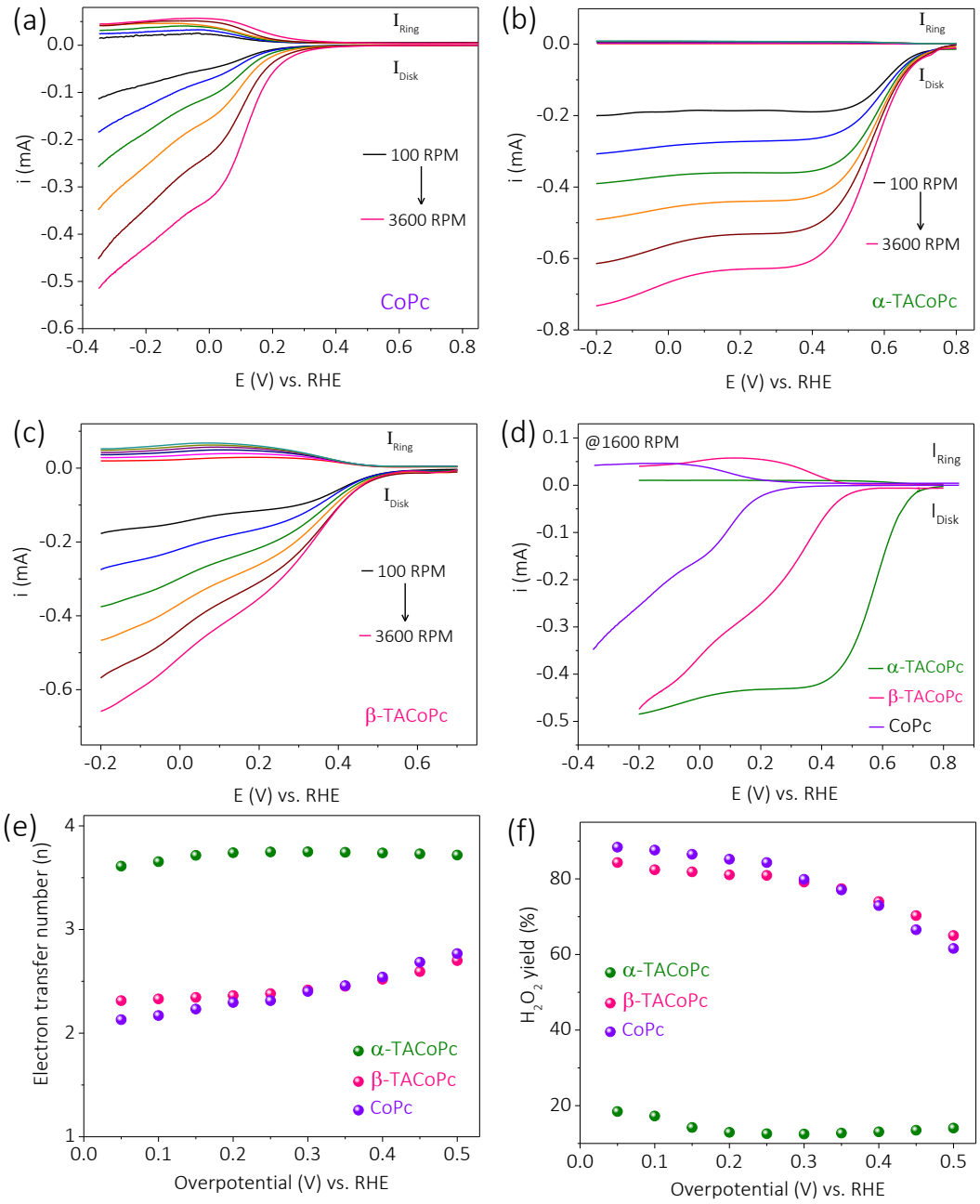


**Figure 5.14:** Rotating ring disk electrode (RRDE) studies on (a) unsubstituted CoPc, (b) α-TACoPc isomer and (c) β-TACoPc isomer when the disk is swept towards ORR potential (0.8 to -0.2 vs. RHE) and the ring is held at peroxide oxidation potential (1.0 V vs. RHE). (d) Comparative ORR study with unsubstituted CoPc, α-TACoPc isomer and β-TACoPc isomer in $O_2$ saturated 0.5 M $H_2SO_4$. Scan rate: 5 $mVs^{-1}$, electrode rotation rate: 1600 rpm. (e) Calculated values of apparent electron transfer number (n) and (f) the measured values of $H_2O_2$ % detected during the ORR pathway.

### 5.2.6. Density function theory (DFT) calculations

To gain more insight into the experimental results density function theory

calculations were carried out in the presence of protons. We have studied the interaction of the $O_2$ molecule with the Co metal center in both α/β-TACoPc isomeric molecules and calculated the various parameters which are important descriptors for the electrocatalytic ORR. We first optimized the structures in presence of $O_2$ to understand in which mode (side-on or end-on) $O_2$ binds to central metal ion. For both α and β-TACoPc isomeric molecules, most stable geometries were calculated along with the binding energies in end-on and side-on binding of the $O_2$ molecule, Figures 5.15-5.18. When molecular oxygen binds to catalytic Co centre in the side-on mode, DFT calculations predicts that it stabilizes the overall geometry of α-TACoPc by nearly 2.49 eV with an $O_2$ binding energy of -2.29 eV, (Figure, 5.15, 5.16, Table 5.8 and Table 5.9), compared to the end-on mode $O_2$ metal center interaction in the same molecule. On the other hand, end-on $O_2$ interaction with Co centre in the β-TACoPc has a binding energy of -2.92 eV, (Figure 5.17, 5.18, Table 5.8 and Table 5.9) and that in turn stabilized the overall geometry by nearly 1.62 eV relative to the side-on state $O_2$-metal centre interaction in the same molecule. As discussed in the previous section, the side-on interaction results in direct $4e^-$ ORR pathway whereas the end-on interaction leads to the dominance of a $2e^-$ pathway. Hence, DFT calculations predicts that α-TACoPc favours a direct $4e^-$ pathway by facilitating side-on molecular oxygen-metal centre interaction, whereas a $2e^-$ pathway is dominantly favoured via end-on molecular oxygen-metal centre interaction in the β-TACoPc isomer molecule.

In order to understand it further, IR stretching frequencies were calculated from DFT calculations for bound oxygen molecule. As can be seen from Table 5.9, the IR stretching frequency decreased significantly when $O_2$ binds to Co centre in α-TACoPc. This points to the feasibility for O-O bond breaking which is required for a direct $4e^-$ ORR pathway. Whereas, the IR stretching frequencies do not decrease significantly (Table 5.9) when $O_2$ molecule binds to Co centre in β-TACoPc and this may favor the formation of $H_2O_2$ over $H_2O$. This is further strengthened by O-O and Co-O bond lengths. The comparative parameters show that in case of the α-TACoPc isomer the O-O bond length increases from 1.200 Å to 1.302 Å on $O_2$ binding as compared to β-TACoPc isomer where the O-O bond length is only marginally increased to 1.214 Å on $O_2$ binding (Table 5.9). Similarly, the Co-O bond lengths of 2.131 Å and 2.014 Å for α-TACoPc isomer and β-TACoPc isomer

respectively suggest a strong binding of $O_2$ molecule with the central metal ion in latter compared to the former, Table 5.9. This may be due to the strong orbital interactions between the d-orbitals of Co and the p-orbitals of $O_2$ in the β-TACoPc isomer during end-on binding as compared to the weak interaction between the d-orbitals of Co and the π-orbitals of $O_2$ in the α-TACoPc isomer during the side-on binding. Further, the charge transfer values between the metal-$O_2$ intermediate (NBO values) for α-TACoPc isomer is -0.706 compared to -0.205 for β-TACoPc isomer suggesting facile charge transfer in the former compared to the latter. Thus the DFT descriptors like M-$O_2$ interactions, IR stretching frequencies, bond length and charge transfer analysis strengthen our claim about 4e- and 2e- ORR pathways respectively in α and β-TACoPc isomeric molecules. The possible reasons for the preference for side-on interaction of oxygen with metal centre in the α-TACoPc isomer molecule could be the higher electron density associated with Co metal centre as demonstrated by XPS, Figure 5.13. Taken together, electrochemical and spectroscopic analyses and DFT calculations reveal that the isomerism of amino functionalities in the secondary sphere of CoPc strongly influences mechanistic pathways of ORR via non covalent interactions and α-TACoPc isomer molecule dominantly catalyze a direct 4 electron ORR pathway compared to the 2 electron pathway catalyzed β-TACoPc isomer. This transforms α-TACoPc isomer molecule as a better electrocatalyst for driving the cathodic half-cell reaction in energy conversion devices such as air batteries and $H_2$-$O_2$ fuel cells.

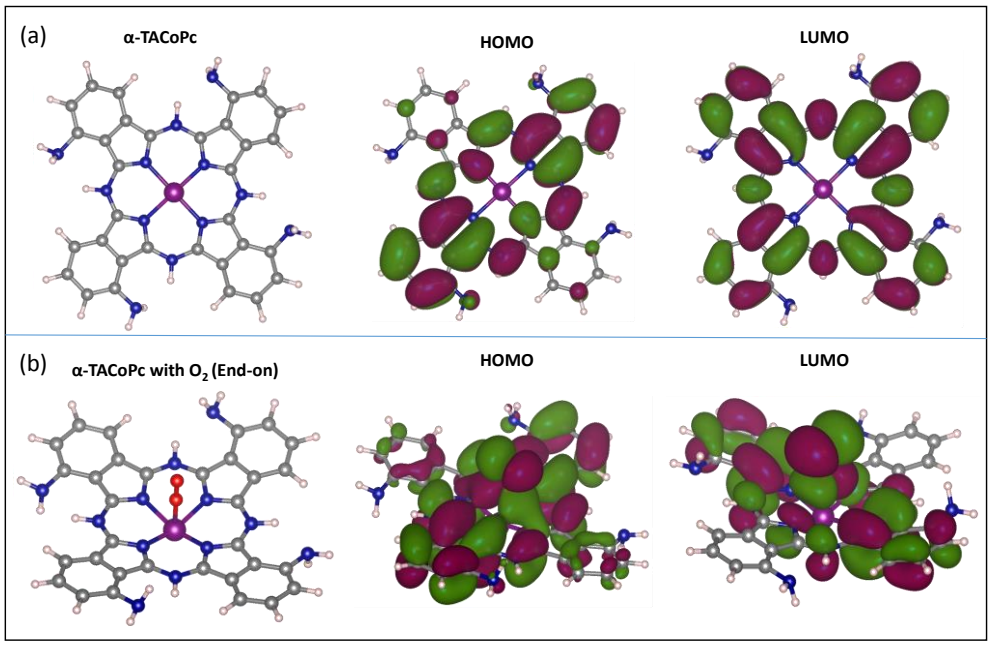

**Figure 5.15:** Stable geometry obtained from DFT calculations of α-TACoPc isomer in the absence (a) and the presence (b) of oxygen (end-on mode $O_2$ binding) along with the electronic properties of HOMO and LUMO. Wine red and green colors indicate the positive and negative lobes of the orbital surfaces.

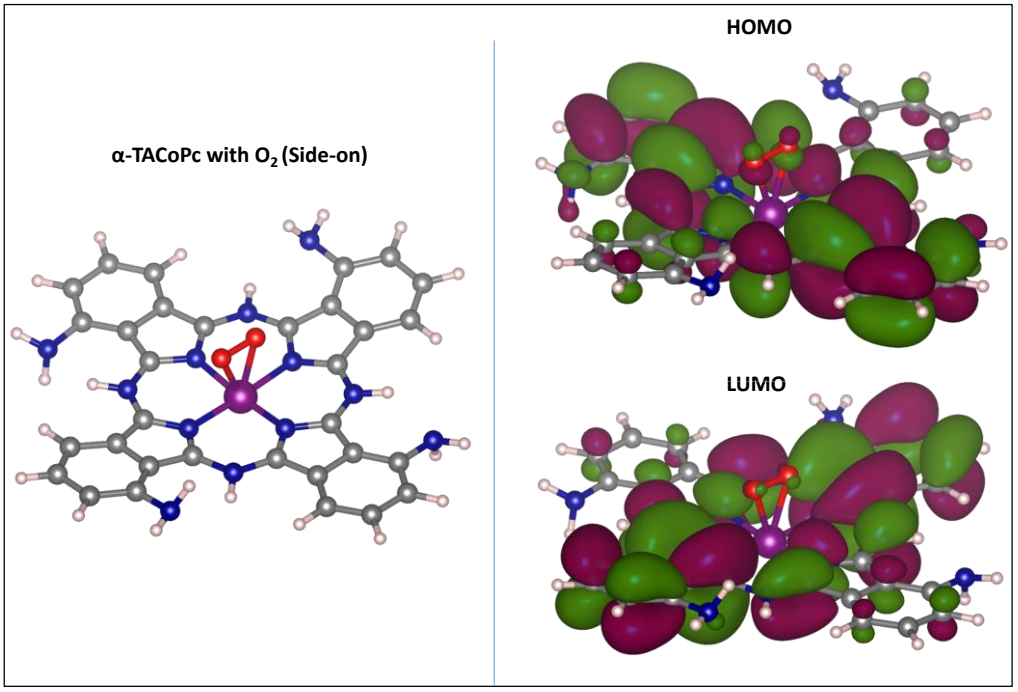


**Figure 5.16:** Stable geometry obtained from DFT calculations of α-TACoPc isomer when molecular oxygen binds to catalytic centre in the side-on mode along with the electronic properties of HOMO and LUMO. Wine red and green colors indicate the positive and negative lobes of the orbital surfaces.

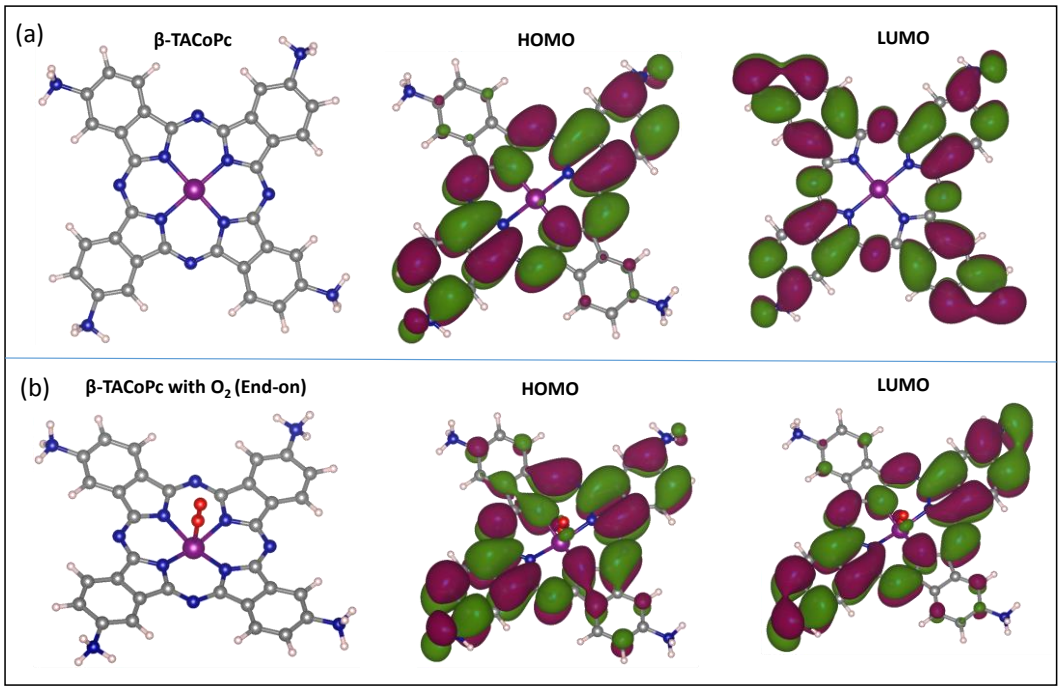

**Figure 5.17:** Stable geometry obtained from DFT calculations of β-TACoPc isomer in the absence (a) and the presence (b) of oxygen (end-on mode $O_2$ binding) along with the electronic properties of HOMO and LUMO. Wine red and green colors indicate the positive and negative lobes of the orbital surfaces.

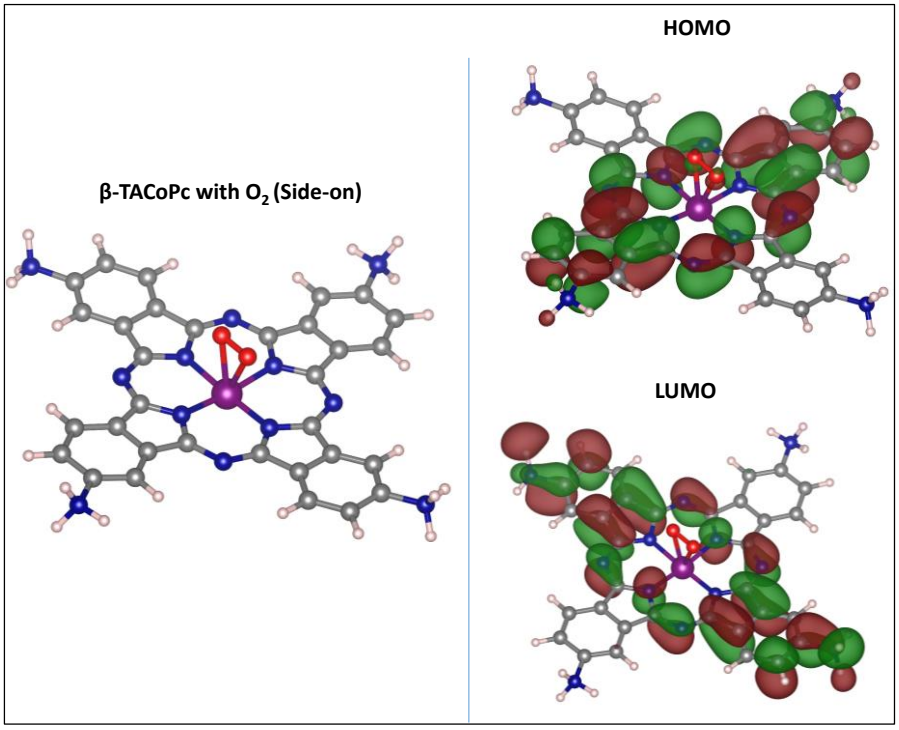


**Figure 5.18:** Stable geometry obtained from DFT calculations of β-TACoPc isomer when molecular oxygen binds to catalytic centre in the side-on mode along with the electronic properties of HOMO and LUMO. Wine red and green colors indicate the positive and negative lobes of the orbital surfaces.

**Table 5.8:** Relative energies for metal-$O_2$ interaction in isomeric α/β-TACoPc molecules from DFT calculations. The parameters are extracted from Figure 5.15-5.18.

| Isomeric Molecule | Relative energy for metal-$O_2$ interaction |
|---|---|
| α-TACoPc | α-TACoPc (End-on)<br>↕ 2.49 eV<br>α-TACoPc (Side-on) |
| β-TACoPc | β-TACoPc (Side-on)<br>↕ 1.62 eV<br>β-TACoPc (End-on) |

Table 5.9: The DFT descriptors from Figure 5.15-5.18.

| System | | | α-TACoPc | β-TACoPc |
|---|---|---|---|---|
| HOMO-LUMO Gap (eV) | | | 2.89 | 3.07 |
| Chemical Hardness, η (eV) | | | 1.44 | 1.53 |
| Chemical Softness, 1/η (eV) | | | 0.70 | 0.65 |
| Electronegativity, χ | | | 2.77 | 1.53 |
| Chemical Potential, μ | | | -2.77 | -1.53 |
| Global Electrophilicity Index, ω | | | 2.65 | 0.76 |
| Presence of $O_2$ | Bond Length (Å) | O-O | 1.302 | 1.214 |
| | | Co-O | 2.131 | 2.014 |
| | Charge Transfer | Mulliken | -0.525 | -0.182 |
| | | NBO | -0.706 | -0.205 |
| | IR stretching $cm^{-1}$ ($\nu_{O-O}$) | | 947.09 | 1713.55 |
| | Binding Energy (eV) ($M-O_2$) | | -2.290 | -2.922 |

### 5.2.7. $H_2$-$O_2$ fuel study

To exploit these peculiar structural characteristics for practical $H_2$-$O_2$ fuel cell applications we have made composites of these isomeric phthalocyanine molecules with carbon nanotubes (CNTs) via π–π interaction (please refer to chapter 2, section 2.4.4 for more details, pages 47-48).[91-93] α and β-TACoPcs anchored on the CNT (α-TACoPc@CNT and β-TACoPc@CNT) were characterized by FTIR and Raman spectroscopy (Figure 5.19). FTIR indicates the features of the CNT in the TACoPc@CNT catalytic system along with the corresponding phthalocyanine features (Figure 5.19a). Raman spectra show the presence of characteristic defect and graphitic bands in the CNT as well as the composite, (Figure 5.19b); however, the phthalocyanine features were almost masked (due to their low concentration) by the intense defect and graphitic bands of CNTs. Nevertheless, the $I_D/I_G$ (intensity of defect band/intensity of graphitic band) ratio in the CNT demonstrates a noticeable increase upon anchoring it with TACoPcs (Figure 5.19b), in line with the literature,[94-96] suggesting their successful incorporation. Scanning electron microscopy (SEM) with energy-dispersive X-ray spectroscopy (EDS), Figures 5.20, indicate the characteristic nanotubular morphology of the CNT along with the presence of Co, N,

and C (EDS pattern), further reinforcing the successful incorporation of TACoPcs on CNT platform. Taken together, all of the characterization techniques adopted evidence the presence of CNT and TACoPcs isomers as a part of the electrocatalytic architecture.

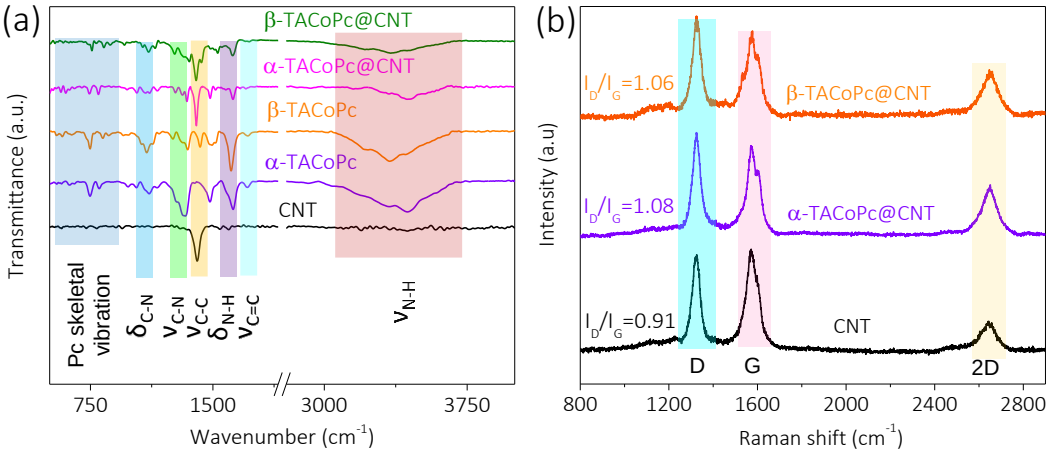


**Figure 5.19:** (a) FTIR spectroscopy and (b) Raman spectroscopy of α-TACoPc@CNT and β-TACoPc@CNT.

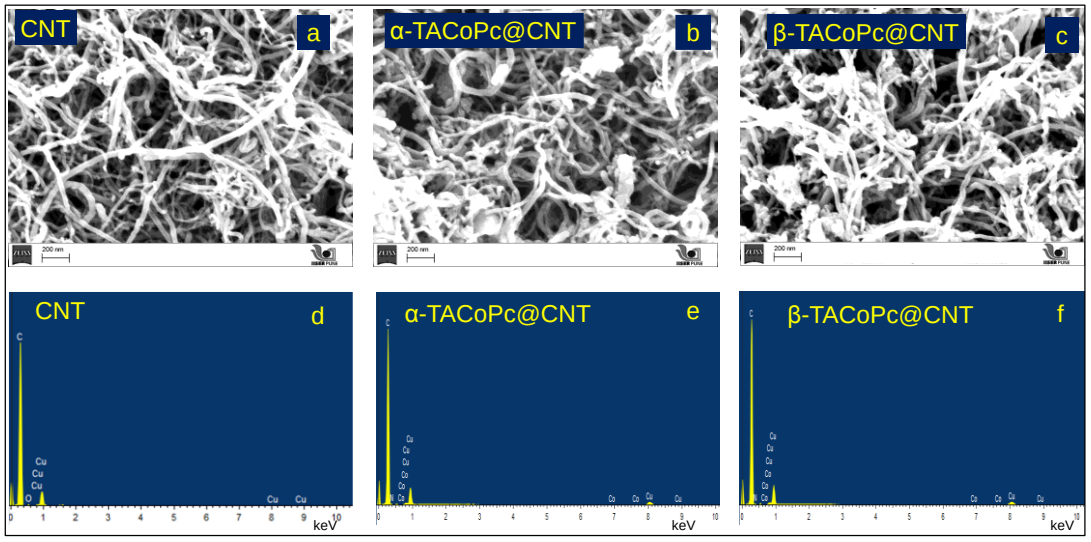


**Figure 5.20:** FESEM images and EDS pattern of (a, d) CNT, (b, e) α-TACoPc@CNT and (c, f) β-TACoPc@CNT. Cu signal in the EDS is derived from the Cu substrate.

After successful incorporation of molecules on CNT electrode, these composite electrode (TACoPc@CNT) were utilized as cathode electrocatalysts to catalyze the ORR in a low temperature $H_2$-$O_2$ fuel cell, Scheme 5.5. The membrane electrode assembly (MEA) fabrication with TACoPc@CNT as cathode electrocatalysts (1 mg/cm$^2$) is explained in detail in Chapter 2 (Refer section 2.10., pages 53-54 for more details). Pt/C (0.5 mg/cm$^2$) was utilized as the anode catalyst for driving the hydrogen oxidation reaction. The performance analysis was carried out by polarization techniques which suggest that the performance

metrics of $H_2$-$O_2$ fuel cell based on α-TACoPc isomer cathode catalyst is significantly higher compared to the corresponding β-TACoPc isomer, Figure 5.21a. The peak power density is nearly twice in case of α-TACoPc-based fuel cell compared to the β-TACoPc based fuel cell. The long-term durability tests at a constant current of 100 mA/cm$^2$ further suggest higher performance and durability of α-TACoPc-based fuel cell, Figure 5.21b. Since the overall fuel cell architecture remains the same except the cathode electrocatalysts, this higher performance of α-TACoPc isomer based fuel cell compared to the corresponding β-TACoPc isomer based fuel cell attests the capability of the α-TACoPc isomer molecule to catalyze the direct 4 electron ORR pathway during energy conversion.

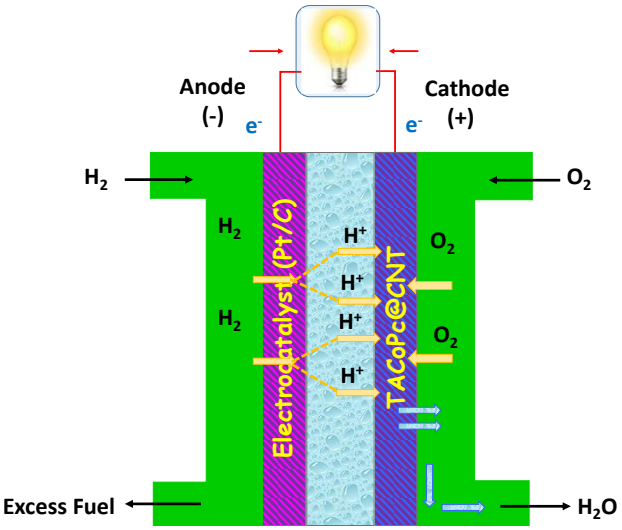


**Scheme 5.5:** Schematic representation of $H_2$-$O_2$ fuel cell with TACoPc@CNT as cathode electrocatalysts to drive the ORR pathway.

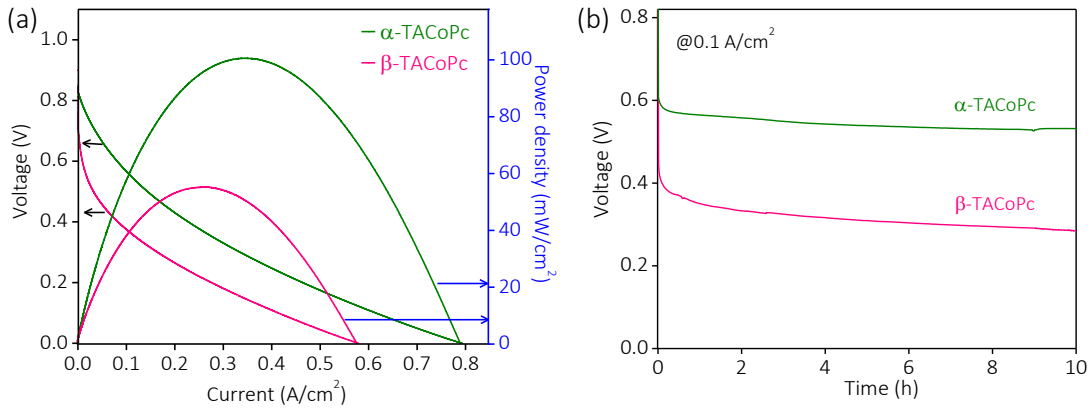


**Figure 5.21:** (a) Polarization of α-TACoPc@CNT and β-TACoPc@CNT based $H_2$-$O_2$ fuel cell and (b) their long term stability at 0.1 A/cm$^2$ current density. The anode Pt/C loading was 0.5 mg/cm$^2$ and the cathode TACoPc@CNT loading was 1 mg/cm$^2$. Fuel cell experiments were carried out at 25° C with a $H_2$-$O_2$ flow rate of 100 mL/min.

## 5.3. Conclusions

An isomerism-activity relation is uncovered in reductive electrocatalysis with respect to ORR wherein the isomerism of electron donating $-NH_2$ functionality strongly influenced the activity of central metal ion and tuned the mechanistic pathways of ORR. It is established that the disparity in electrocatalysis between isomeric α/β-TACoPc molecules is not an orientation effect; a notion previously attributed to the higher catalytic activity of α isomer over its β counterpart, but an effect due to intramolecular H-bonding in the former that in turn enhances the electron density at the catalytic Co center. Electrochemical and spectroscopic analyses and DFT calculations reveal that the isomerism of amino functionalities in the secondary sphere of CoPc influences the kinetics as well as the mechanistic pathways of oxygen reduction reaction. This investigation reveals that isomerism induced activation of catalytic metal centre can be exploited to instigate selectivity in reductive electrocatalysis which in turn provides an alternative approach in the design of efficient non-precious electrocatalysts for energy conversion (4 electron process) and peroxide production (2 electron process).

## 5.4. References

[1] She, Z. W.; Kibsgaard, J.; Dickens, C. F.; Chorkendorff, I.; Nørskov, J. K.; Jaramillo, T. F. Combining Theory and Experiment in Electrocatalysis: Insights into Materials Design. *Science* **2017**, *355*, 6321.

[2] Dubois, D. L. Development of Molecular Electrocatalysts for Energy Storage. *Inorg. Chem.* **2014**, *53* (8), 3935–3960.

[3] Cook, T. R.; Dogutan, D. K.; Reece, S. Y.; Surendranath, Y.; Teets, T. S.; Nocera, D. G. Solar Energy Supply and Storage for the Legacy and Nonlegacy Worlds. *Chem. Rev.* **2010**, *110* (11), 6474–6502.

[4] Lopez, N.; Graham, D. J.; McGuire, R.; Alliger, G. E.; Shao-Horn, Y.; Cummins, C. C.; Nocera, D. G. Reversible Reduction of Oxygen to Peroxide Facilitated by Molecular Recognition. *Science* **2012**, *335* (6067), 450–453.

[5] Kanan, M. W.; Nocera, D. G. In Situ Formation of an Oxygen-Evolving Catalyst in Neutral Water Containing Phosphate and $Co^{2+}$. *Science* **2008**, *321* (5892), 1072–1075.

[6] Bidault, F.; Brett, D. J. L.; Middleton, P. H.; Brandon, N. P. Review of Gas Diffusion Cathodes for Alkaline Fuel Cells. *J. Power Sources* **2009**, *187* (1), 39–48.

[7] Park, J. S.; Park, S. H.; Yim, S. D.; Yoon, Y. G.; Lee, W. Y.; Kim, C. S. Performance of Solid Alkaline Fuel Cells Employing Anion-Exchange Membranes. *J. Power Sources* **2008**, *178* (2), 620–626.

[8] Asazawa, K.; Yamada, K.; Tanaka, H.; Oka, A.; Taniguchi, M.; Kobayashi, T. A Platinum-Free Zero-Carbon-Emission Easy Fuelling Direct Hydrazine Fuel Cell for Vehicles. *Angew. Chemie* **2007**, *119* (42), 8170–8173.

[9] Kuttiyiel, K. A.; Sasaki, K.; Choi, Y.; Su, D.; Liu, P.; Adzic, R. R. Bimetallic IrNi Core Platinum Monolayer Shell Electrocatalysts for the Oxygen Reduction Reaction. *Energy Environ. Sci.* **2012**, *5* (1), 5297–5304.

[10] Xu, H.; Fu, Q.; Yao, Y.; Bao, X. Highly Active Pt-Fe Bicomponent Catalysts for CO Oxidation in the Presence and Absence of $H_2$. *Energy Environ. Sci.* **2012**, *5* (4), 6313–6320.

[11] Oezaslan, M.; Hasché, F.; Strasser, P. $PtCu_3$, PtCu and $Pt_3Cu$ Alloy Nanoparticle Electrocatalysts for Oxygen Reduction Reaction in Alkaline and Acidic Media. *J. Electrochem. Soc.* **2012**, *159* (4), B444–B454.

[12] Park, H. W.; Lee, D. U.; Nazar, L. F.; Chen, Z. Oxygen Reduction Reaction Using $MnO_2$ Nanotubes/Nitrogen-Doped Exfoliated Graphene Hybrid Catalyst for Li-$O_2$ Battery Applications . *J. Electrochem. Soc.* **2013**, *160* (2), A344–A350.

[13] Lee, D. U.; Park, H. W.; Higgins, D.; Nazar, L.; Chen, Z. Highly Active Graphene Nanosheets Prepared via Extremely Rapid Heating as Efficient Zinc-Air Battery Electrode Material. *J. Electrochem. Soc.* **2013**, *160* (9), F910–F915.

[14] Zhang, H.; Zhong, X.; Shaw, J. C.; Liu, L.; Huang, Y.; Duan, X. Very High Energy Density Silicide-Air Primary Batteries. *Energy Environ. Sci.* **2013**, *6* (9), 2621–2625.

[15] Shui, J. L.; Okasinski, J. S.; Kenesei, P.; Dobbs, H. A.; Zhao, D.; Almer, J. D.; Liu, D. J. Reversibility of Anodic Lithium in Rechargeable Lithium-Oxygen Batteries. *Nat. Commun.* **2013**, *4*, 1–7.

[16] Chen, Z.; Higgins, D.; Chen, Z.; Lee, D. U. Activated and Nitrogen-Doped Exfoliated Graphene as Air Electrodes for Metal-Air Battery Applications. *J. Mater. Chem. A* **2013**, *1* (7), 2639–2645.

[17] Dai, L.; Xue, Y.; Qu, L.; Choi, H. J.; Baek, J. B. Metal-Free Catalysts for Oxygen Reduction Reaction. *Chem. Rev.* **2015**, *115* (11), 4823–4892.

[18] Liu, Q.; Jin, J.T.; Zhang, J.Y. NiCo2S4@Graphene as a Bifunctional Electrocatalyst for Oxygen Reduction and Evolution Reactions. *ACS Appl. Mater. Interfaces* **2013**, *5* (11), 5002–5008.

[19] Zhao, A.; Masa, J.; Xia, W.; Maljusch, A.; Willinger, M. G.; Clavel, G.; Xie, K.; Schlögl, R.; Schuhmann, W.; Muhler, M. Spinel Mn-Co Oxide in N-Doped Carbon Nanotubes as a Bifunctional Electrocatalyst Synthesized by Oxidative Cutting. *J. Am. Chem. Soc.* **2014**, *136* (21), 7551–7554.

[20] Lübke, M.; Sumboja, A.; McCafferty, L.; Armer, C. F.; Handoko, A. D.; Du, Y.; McColl, K.; Cora, F.; Brett, D.; Liu, Z.; Darr, J. A. Transition-Metal-Doped α-$MnO_2$ Nanorods as Bifunctional Catalysts for Efficient Oxygen Reduction and Evolution Reactions. *ChemistrySelect* **2018**, *3* (9), 2613–2622.

[21] Yang, Z.; Yao, Z.; Li, G.; Fang, G.Y.; Nie, H.G.; Liu, Z.; Zhou, X.M.; Chen, X.A.; Huang, S.M. Sulfur-Doped Graphene as an Efficient Metal-Free Cathode Catalyst for Oxygen Reduction. *ACS Nano* **2012**, *6* (1), 205–211.

[22] Zagal, J.H.; Bedioui, F.; Dodelet, J. P. *$N_4$-macrocyclic metal complexes.* Springer, New York. **2006**. pp - 45-93.

[23] Zhong, H.; Campos-Roldán, C. A.; Zhao, Y.; Zhang, S.; Feng, Y.; Alonso-Vante, N. Recent Advances of Cobalt-Based Electrocatalysts for Oxygen Electrode Reactions and Hydrogen Evolution Reaction. *Catalysts* **2018**, *8* (11), 559.

[24] Lim, B.; Jiang, M.; Camargo, P. H. C.; Cho, E. C.; Tao, J.; Lu, X.; Zhu, Y.; Xia, Y. Pd-Pt Bimetallic Nanodendrites with High Activity for Oxygen Reduction. *Science* **2009**, *324* (5932), 1302–1305.

[25] Shao, M.; Chang, Q.; Dodelet, J. P.; Chenitz, R. Recent Advances in Electrocatalysts for Oxygen Reduction Reaction. *Chem. Rev.* **2016**, *116* (6), 3594–3657.

[26] Xia, Z.; An, L.; Chen, P.; Xia, D. Non-Pt Nanostructured Catalysts for Oxygen Reduction Reaction: Synthesis, Catalytic Activity and Its Key Factors. *Adv. Energy Mater.* **2016**, *6* (17), 1600458.

[27] Huang, Z. F.; Wang, J.; Peng, Y.; Jung, C. Y.; Fisher, A.; Wang, X. Design of Efficient Bifunctional Oxygen Reduction/Evolution Electrocatalyst: Recent Advances and Perspectives. *Adv. Energy Mater.* **2017**, *7* (23), 1700544.

[28] Wan, X.; Liu, X.; Li, Y.; Yu, R.; Zheng, L.; Yan, W.; Wang, H.; Xu, M.; Shui, J. Fe–N–C Electrocatalyst with Dense Active Sites and Efficient Mass Transport for High-Performance Proton Exchange Membrane Fuel Cells. *Nat. Catal.* **2019**, *2* (3), 259–268.

[29] Sorokin, A. B. Phthalocyanine Metal Complexes in Catalysis BT - Chemical Reviews. *Chem. Rev.* **2013**, *113* (10), 8152–8191.

[30] Sobbi, A. K.; Wöhrie, D.; Schlettwein, D. Photochemical Stability of Various Porphyrins in Solution and as Thin Film Electrodes. *J. Chem. Soc. Perkin Trans. 2* **1993**, 3, 481–488.

[31] Rigsby, M. L.; Wasylenko, D. J.; Pegis, M. L.; Mayer, J. M. Medium Effects Are as Important as Catalyst Design for Selectivity in Electrocatalytic Oxygen Reduction by Iron-Porphyrin Complexes. *J. Am. Chem. Soc.* **2015**, *137* (13), 4296–4299.

[32] Bottari, G.; de la Torre, G.; Guldi, D. M.; Torres, T. Covalent and Noncovalent Phthalocyanine–Carbon Nanostructure Systems: Synthesis, Photoinduced Electron Transfer, and Application to Molecular Photovoltaics. *Chem. Rev.* **2010**, *110* (11), 6768–6816.

[33] Zagal J.H. *Macrocycles, In Handbook of Fuel Cells Fundamentals, Technology and Applications*, John Wiley & Sons, Ltd.: Chichester, **2003**, *Vol. 2, Part 5*, 544.

[34] Zagal, J. H. Metallophthalocyanines as Catalysts in Electrochemical Reactions. *Coord. Chem. Rev.* **1992**, *119* (C), 89–136.

[35] Masa, J.; Ozoemena, K.; Schuhmann, W.; Zagal, J. H. Oxygen Reduction Reaction Using $N_4$-Metallomacrocyclic Catalysts: Fundamentals on Rational Catalyst Design. *J. Porphyr. Phthalocyanines* **2012**, *16* (7–8), 761–784.

[36] Jiang, Y.; Lu, Y.; Lv, X.; Han, D.; Zhang, Q.; Niu, L.; Chen, W. Enhanced Catalytic Performance of Pt-Free Iron Phthalocyanine by Graphene Support for Efficient Oxygen Reduction Reaction. *ACS Catal.* **2013**, *3* (6), 1263–1271.

[37] Cao, R.; Thapa, R.; Kim, H.; Xu, X.; Kim, M. G.; Li, Q.; Park, N.; Liu, M.; Cho, J. Promotion of Oxygen Reduction by a Bio-Inspired Tethered Iron Phthalocyanine Carbon Nanotube-Based Catalyst. *Nat. Commun.* **2013**, *4*, 2076.

[38] Wang, J.; Huang, X.; Xi, S.; Lee, J.; Wang, C.; Du, Y.; Wang, X. Linkage Effect in the Heterogenization of Cobalt Complexes by Doped Graphene for Electrocatalytic $CO_2$ Reduction . *Angew. Chemie* **2019**, *131* (38), 13666–13673.

[39] Li, R.; Zhang, X.; Zhu, P.; Ng, D. K. P.; Kobayashi, N.; Jiang, J. Electron-Donating or -Withdrawing Nature of Substituents Revealed by the Electrochemistry of Metal-Free Phthalocyanines. *Inorg. Chem.* **2006**, *45* (5), 2327–2334.

[40] Zagal, J. H.; Koper, M. T. M. Reactivity Descriptors for the Activity of Molecular $MN_4$ Catalysts for the Oxygen Reduction Reaction. *Angew. Chemie - Int. Ed.* **2016**, *55* (47), 14510–14521.

[41] Silva, N.; Calderón, S.; Páez, M. A.; Oyarzún, M. P.; Koper, M. T. M.; Zagal, J. H. Probing the $Fe^{n+}/Fe^{(n-1)+}$ Redox Potential of Fe Phthalocyanines and Fe Porphyrins as a Reactivity Descriptor in the Electrochemical Oxidation of Cysteamine. *J. Electroanal. Chem.* **2018**, *819*, 502–510.

[42] Raja, R.; Ratnasamy, P. Selective Oxidation of Phenols Using Copper Complexes Encapsulated in Zeolites. *Appl. Catal. A Gen.* **1996**, *143* (1), 145–158.

[43] Park, J. S.; Chang, D. W. Iron Phthalocyanine/Graphene Composites as Promising Electrocatalysts for the Oxygen Reduction Reaction. *Energies* **2020**, *13*(16), 4073.

[44] Tse, Y. H.; Janda, P.; Lam, H.; Zhang, J.; Pietro, W. J.; Lever, A. B. P. Monomeric and Polymeric Tetra-Aminophthalocyanatocobalt(II) Modified Electrodes: Electrocatalytic Reduction of Oxygen. *J. Porphyr. Phthalocyanines* **1997**, *1* (1), 3–16.

[45] Pavez, J.; Páez, M.; Ringuedé, A.; Bedioui, F.; Zagal, J. H. Effect of Film Thickness on the Electro-Reduction of Molecular Oxygen on Electropolymerized Cobalt Tetra-Aminophthalocyanine Films. *J. Solid State Electrochem.* **2005**, *9* (1), 21–29.

[46] Somashekarappa, M. P.; Sampath, S. Orientation Dependent Electrocatalysis Using Self-Assembled Molecular Films. *Chem. Commun.* **2002**, *2* (12), 1262–1263.

[47] Sivanesan, A.; Abraham John, S. Amino Group Position Dependent Orientation of Self-Assembled Monomolecular Films of Tetraaminophthalocyanatocobalt (II) on Au Surfaces. *Langmuir* **2008**, *24* (5), 2186–2190.

[48] Kottaichamy, A. R.; Makri Nimbegondi Kotresh, H.; Devendrachari, M. C.; Thimmappa, R.; Paswan, B.; Tiwari, O.; Chanda, V.; Gaikwad, P.; Thotiyl, M. O. Effects of Electrochemical Tailoring of Monolayers on a Catalytic Redox Entity: An ON-OFF Phenomenon Regulated by the Surrounding Medium. *J. Phys. Chem. C* **2015**, *119* (51), 28276–28284.

[49] Alzeer, J.; Roth, P. J. C.; Luedtke, N. W. An Efficient Two-Step Synthesis of Metal-Free Phthalocyanines Using a Zn(II) Template. *Chem. Commun.* **2009**, (15), 1970–1971.

[50] Al-lami, A. K. A.; Majeed, N. N.; Al-mowali, A. H. Synthesis , Mesomorphic and Molar Conductivity Studies of Some Macrocyclic Phthalocyanine Palladium (II). *Chemistry and Materials Research.* **2013**, *3* (4), 59–68.

[51] Trollund, E.; Ardiles, P.; Aguirre, M. J.; Biaggio, S. R.; Rocha-Filho, R. C. Spectroelectrochemical and Electrical Characterization of Poly(Cobalt - Tetraaminophthalocyanine)-Modified Electrodes: Electrocatalytic Oxidation of Hydrazine. *Polyhedron* **2000**, *19* (22–23), 2303–2312.

[52] Cidlina, A.; Novakova, V.; Miletin, M.; Zimcik, P. Peripheral Substitution as a Tool for Tuning Electron-Accepting Properties of Phthalocyanine Analogs in Intramolecular Charge Transfer. *Dalt. Trans.* **2015**, *44* (15), 6961–6971.

[53] Yarasir, M. N.; Kandaz, M.; Güney, O.; Salih, B. Synthesis and Photophysical Properties of Metallophthalocyanines Substituted with a Benzofuran Based Fluoroprobe. *Spectrochim. Acta - Part A Mol. Biomol. Spectrosc.* **2012**, *93*, 379–383.

[54] Panwar, V.; Kumar, P.; Ray, S. S.; Jain, S. L. Organic Inorganic Hybrid Cobalt Phthalocyanine/Polyaniline as Efficient Catalyst for Aerobic Oxidation of Alcohols in Liquid Phase. *Tetrahedron Lett.* **2015**, *56* (25), 3948–3953.

[55] Kobayashi, N.; Miwa, H.; Nemykin, V. N. Adjacent versus Opposite Type Di-Aromatic Ring-Fused Phthalocyanine Derivatives: Synthesis, Spectroscopy, Electrochemistry, and Molecular Orbital Calculations. *J. Am. Chem. Soc.* **2002**, *124* (27), 8007–8020.

[56] Ogunsipe, A.; Nyokong, T. Effects of Substituents and Solvents on the Photochemical Properties of Zinc Phthalocyanine Complexes and Their Protonated Derivatives. *J. Mol. Struct.* **2004**, *689* (1–2), 89–97.

[57] Moinuddin Khan, M. H.; Venugopala Reddy, K. R.; Keshavayya, J.; Fasiulla; Raghavendra, S. Synthesis, Characterizations and Biological Studies of Symmetrically Substituted 2, 9, 16, 23-Tetra-Hydroxyphenylimino Phthalocyanine Complexes. *Green Chem. Lett. Rev.* **2009**, *2* (2), 77–85.

[58] Mugadza, T.; Nyokong, T. Synthesis, Characterization and the Electrocatalytic Behaviour of Nickel (II) Tetraamino-Phthalocyanine Chemically Linked to Single Walled Carbon Nanotubes. *Electrochim. Acta* **2010**, *55* (20), 6049–6057.

[59] Mugadza, T.; Nyokong, T. Synthesis and Characterization of Electrocatalytic Conjugates of Tetraamino Cobalt (II) Phthalocyanine and Single Wall Carbon Nanotubes. *Electrochim. Acta* **2009**, *54* (26), 6347–6353.

[60] Madhuri, K. P.; John, N. S. Solution Processable Transition Metal Phthalocyanine Nanofibres. *ChemistrySelect* **2019**, *4* (24), 7292–7299.

[61] Georgescu, R.; Boscornea, C.; Calinescu, I.; State, R. Raman, IR and UV-Vis Spectroscopic Investigations of Some Substituted Phthalocyanines. *Rev. Chim.* **2015**, *66* (10), 1554–1557.

[62] Amatore, C.; Oleinick, A. I.; Svir, I. Diffusion from within a Spherical Body with Partially Blocked Surface: Diffusion through a Constant Surface Area. *ChemPhysChem* **2010**, *11* (1), 149–158.

[63] Janek, R. P.; Fawcett, W. R.; Ulman, A. Impedance Spectroscopy of Self-Assembled Monolayers on Au(111): Sodium Ferrocyanide Charge Transfer at Modified Electrodes. *Langmuir* **1998**, *14* (11), 3011–3018.

[64] Fleming, B. D.; Praporski, S.; Bond, A. M.; Martin, L. L. Electrochemical Quartz Crystal Microbalance Study of Azurin Adsorption onto an Alkanethiol Self-Assembled Monolayer on Gold. *Langmuir* **2008**, *24* (1), 323–327.

[65] Viana, A. S.; Kalaji, M.; Abrantes, L. M. Electrochemical Quartz Crystal Microbalance Study of Self-Assembled Monolayers and Multilayers of Ferrocenylthiol Derivatives on Gold. *Langmuir* **2003**, *19* (22), 9542–9544.

[66] Nakano, K.; Yoshitake, T.; Yamashita, Y.; Bowden, E. F. Cytochrome c Self-Assembly on Alkanethiol Monolayer Electrodes as Characterized by AFM, IR, QCM, and Direct Electrochemistry. *Langmuir* **2007**, *23* (11), 6270–6275.

[67] Makinde, Z. O.; Louzada, M.; Mashazi, P.; Nyokong, T.; Khene, S. Electrocatalytic Behaviour of Surface Confined Pentanethio Cobalt (II) Binuclear Phthalocyanines towards the Oxidation of 4-Chlorophenol. *Appl. Surf. Sci.* **2017**, *425*, 702–712.

[68] Kottaichamy, A. R.; Begum, S.; Devendrachari, M. C.; Bhat, Z. M.; Thimmappa, R.; Nimbegondi Kotresh, H. M.; Vinod, C. P.; Thotiyl, M. O. Geometrical Isomerism Directed Electrochemical Sensing. *Anal. Chem.* **2020**, *92* (6), 4541–4547.

[69] Kottaichamy, A. R.; Begum, S.; Nazrulla, M. A.; Dargily, N. C.; Devendrachari, M. C.; Manzoor Bhat, Z.; Thimmappa, R.; Makri Nimbegondi Kotresh, H.; Vinod, C. P.; Thotiyl, M. O. Unprecedented Isomerism-Activity Relation in Molecular Electrocatalysis. *J. Phys. Chem. Lett.* **2020**, *11* (1), 263–271.

[70] Lokesh, K. S.; De Keersmaecker, M.; Adriaens, A. Self-Assembled Films of Porphyrins with Amine Groups at Different Positions: Influence of Their Orientation on the Corrosion Inhibition and the Electrocatalytic Activity. *Molecules* **2012**, *17* (7), 7824–7842.

[71] Mashazi, P. N.; Ozoemena, K. I.; Nyokong, T. Tetracarboxylic Acid Cobalt Phthalocyanine SAM on Gold: Potential Applications as Amperometric Sensor for $H_2O_2$ and Fabrication of Glucose Biosensor. *Electrochim. Acta* **2006**, *52* (1), 177–186.

[72] Nyokong, T.; Bedioui, F. Self-Assembled Monolayers and Electropolymerized Thin Films of Phthalocyanines as Molecular Materials for Electroanalysis. *J. Porphyr. Phthalocyanines* **2006**, *10* (9–10), 1101–1115.

[73] Silva, J. F.; Pavez, J.; Silva, C. P.; Zagal, J. H. Electrocatalytic Actvity of Modified Gold Electrodes Based on Self-Assembled Monolayers of 4-Mercaptopyridine and 4-Aminothiophenol on Au(111) Surfaces Chemically Functionalized with Substituted and Unsubstituted Iron Phthalocyanines. *Electrochim. Acta* **2013**, *114*, 7–13.

[74] Cong, F. Di; Ning, B.; Du, X. G.; Ma, C. Y.; Yu, H. F.; Chen, B. Facile Synthesis, Characterization and Property Comparisons of Tetraaminometallo phthalocyanines with and without Intramolecular Hydrogen Bonds. *Dye. Pigment.* **2005**, *66* (2), 149–154.

[75] Zhang, X. F.; Li, X.; Niu, L.; Sun, L.; Liu, L. Charge Transfer Photophysics of Tetra(α-Amino) Zinc Phthalocyanine. *J. Fluoresc.* **2009**, *19* (6), 947–954.

[76] Froimowicz, P.; Zhang, K.; Ishida, H. Intramolecular Hydrogen Bonding in Benzoxazines: When Structural Design Becomes Functional. *Chem. - A Eur. J.* **2016**, *22* (8), 2691–2707.

[77] Che, P.; Lu, F.; Nie, X.; Huang, Y.; Yang, Y.; Wang, F.; Xu, J. Hydrogen Bond Distinction and Activation upon Catalytic Etherification of Hydroxyl Compounds. *Chem. Commun.* **2015**, *51* (6), 1077–1080.

[78] Luo, Y.; Ma, H.; Sun, Y.; Che, P.; Nie, X.; Wang, T.; Xu, J. Understanding and Measurement for the Binding Energy of Hydrogen Bonds of Biomass-Derived Hydroxyl Compounds. *J. Phys. Chem. A* **2018**, *122* (3), 843–848.

[79] Arechederra, R. L.; Artyushkova, K.; Atanassov, P.; Minteer, S. D. Growth of Phthalocyanine Doped and Undoped Nanotubes Using Mild Synthesis Conditions for Development of Novel Oxygen Reduction Catalysts. *ACS Appl. Mater. Interfaces* **2010**, *2* (11), 3295–3302.

[80] Gu, W.; Hu, L.; Hong, W.; Jia, X.; Li, J.; Wang, E. Noble-Metal-Free $Co_3S_4$-S/G Porous Hybrids as an Efficient Electrocatalyst for Oxygen Reduction Reaction. *Chem. Sci.* **2016**, *7* (7), 4167–4173.

[81] Venegas, R.; Recio, F. J.; Zuñiga, C.; Viera, M.; Oyarzún, M. P.; Silva, N.; Neira, K.; Marco, J. F.; Zagal, J. H.; Tasca, F. Comparison of the Catalytic Activity for O2 Reduction of Fe and Co $MN_4$ Adsorbed on Graphite Electrodes and on Carbon Nanotubes. *Phys. Chem. Chem. Phys.* **2017**, *19* (31), 20441–20450.

[82] Siahrostami, S.; Verdaguer-Casadevall, A.; Karamad, M.; Deiana, D.; Malacrida, P.; Wickman, B.; Escudero-Escribano, M.; Paoli, E. A.; Frydendal, R.; Hansen, T. W.; Chorkendorff, I.; Stephens, I. E. L.; Rossmeisl, J. Enabling Direct $H_2O_2$ Production through Rational Electrocatalyst Design. *Nat. Mater.* **2013**, *12* (12), 1137–1143.

[83] Jiang, K.; Back, S.; Akey, A. J.; Xia, C.; Hu, Y.; Liang, W.; Schaak, D.; Stavitski, E.; Nørskov, J. K.; Siahrostami, S.; Wang, H. Highly Selective Oxygen Reduction to Hydrogen Peroxide on Transition Metal Single Atom Coordination. *Nat. Commun.* **2019**, *10*, 3997.

[84] Jung, E.; Shin, H.; Lee, B. H.; Efremov, V.; Lee, S.; Lee, H. S.; Kim, J.; Hooch Antink, W.; Park, S.; Lee, K. S.; Cho, S. P.; Yoo, J. S.; Sung, Y. E.; Hyeon, T. Atomic-Level Tuning of Co–N–C Catalyst for High-Performance Electrochemical $H_2O_2$ Production. *Nat. Mater.* **2020**, *19* (4), 436–442.

[85] Verdaguer-casadevall, A.; Deiana, D.; Karamad, M.; Siahrostami, S.; Hansen, T. W.; Rossmeisl, J.; Chorkendorff, I.; Erfyl, I.; Stephens, L. Trends in the Electrochemical Synthesis of $H_2O_2$. *Nano Lett.* **2014**, *14* (3), 1603–1608.

[86] Sudhakara, S. M.; Bhat, Z. M.; Devendrachari, M. C.; Kottaichamy, A. R.; Itagi, M.; Thimmappa, R.; Khan, F.; Kotresh, H. M. N.; Thotiyl, M. O. A Zinc-Quinone Battery for Paired Hydrogen Peroxide Electrosynthesis. *J. Colloid Interface Sci.* **2020**, *559*, 324–330.

[87] Zhou, R.; Zheng, Y.; Jaroniec, M.; Qiao, S. Z. Determination of the Electron Transfer Number for the Oxygen Reduction Reaction: From Theory to Experiment. *ACS Catal.* **2016**, *6* (7), 4720–4728.

[88] Devendrachari, M. C.; Basappa, C.; Thimmappa, R.; Bhat, Z. M.; Kotresh, H. M. N.; Kottaichamy, A. R.; Varhade, S.; Khaire, S.; Reddy, K. R. V.; Thotiyl, M. O. An All Solid-State Zinc–Air Battery with a Corrosion-Resistant Air Electrode. *ChemElectroChem* **2018**, *5* (14), 1817–1821.

[89] Murata, T.; Kotsuki, K.; Murayama, H.; Tsuji, R.; Morita, Y. Metal-Free Electrocatalysts for Oxygen Reduction Reaction Based on Trioxotriangulene. *Commun. Chem.* **2019**, *2*, 46.

[90] He, H.; Lei, Y.; Xiao, C.; Chu, D.; Chen, R.; Wang, G. Molecular and Electronic Structures of Transition-Metal Macrocyclic Complexes as Related to Catalyzing Oxygen Reduction Reactions: A Density Functional Theory Study. *J. Phys. Chem. C* **2012**, *116* (30), 16038–16046.

[91] Le, Z.; Liu, F.; Nie, P.; Li, X.; Liu, X.; Bian, Z.; Chen, G.; Wu, H. Bin; Lu, Y. Pseudocapacitive Sodium Storage in Mesoporous Single-Crystal-like $TiO_2$-Graphene Nanocomposite Enables High-Performance Sodium-Ion Capacitors. *ACS Nano* **2017**, *11* (3), 2952–2960.

[92] Dou, Q.; Liu, L.; Yang, B.; Lang, J.; Yan, X. Silica-Grafted Ionic Liquids for Revealing the Respective Charging Behaviors of Cations and Anions in Supercapacitors. *Nat. Commun.* **2017**, *8*, 2188.

[93] Merlet, C.; Rotenberg, B.; Madden, P. A.; Taberna, P. L.; Simon, P.; Gogotsi, Y.; Salanne, M. On the Molecular Origin of Supercapacitance in Nanoporous Carbon Electrodes. *Nat. Mater.* **2012**, *11* (4), 306–310.

[94] Zhu, J.; Li, Y.; Chen, Y.; Wang, J.; Zhang, B.; Zhang, J.; Blau, W. J. Graphene Oxide Covalently Functionalized with Zinc Phthalocyanine for Broadband Optical Limiting. *Carbon N. Y.* **2011**, *49* (6), 1900–1905.

[95] Zhang, X.; Wu, Z.; Zhang, X.; Li, L.; Li, Y.; Xu, H.; Li, X.; Yu, X.; Zhang, Z.; Liang, Y.; Wang, H. Highly Selective and Active $CO_2$ Reduction Electrocatalysts Based on Cobalt Phthalocyanine/Carbon Nanotube Hybrid Structures. *Nat. Commun.* **2017**, *8*, 14675.

[96] Shrestha, M.; Amatya, I.; Wang, K.; Zheng, B.; Gu, Z.; Fan, Q. H. Electrophoretic Deposition of Activated Carbon YP-50 with Ethyl Cellulose Binders for Supercapacitor Electrodes. *J. Energy Storage* **2017**, *13*, 206–210.

# Chapter 6

## Non-covalent Interaction Regulated Molecular Charge Storage

**Abstract**: Since the energy density of supercapacitors scales-up linearly with surface-confined charge density, the pursuit towards high energy and high-power supercapacitors are conventionally accomplished in solid systems by maximizing their surface-to-volume ratio. With regard to molecular systems, despite a few reports on improving their surface charge density by secondary-sphere functionalization, a lack of in-depth understanding exists in defining what controls their structure-charge storage relationship. An unusual molecular structure-charge storage relation is uncovered; where solvent dependent non-covalent interactions in the molecule strongly interconnected their charge storage with the nature as well as the isomerism of the secondary sphere functionality. Electrochemical, spectroscopic and theoretical investigations demonstrate that isomerism of amino functionality triggered attractive field effect via intramolecular hydrogen-bonding which in turn suppressed the extent of protonation and consequently the electrochemical capacity of the molecule. When attractive field effect is inhibited in the molecule by spatially separating the H-bonding groups via geometrical isomerism, electrochemical capacity is significantly enhanced. Interestingly, repulsive field effect in isomeric nitro molecules leads only to a geometric rotation of the $-NO_2$ functionality which did not contribute to a disparity in their charge storage. Unveiling the subtle role of non-covalent interactions in conjoining the molecular charge storage with the nature as well as isomerism of the functionality opens up an alternative dimension in the design of molecular supercapacitors to target their energy density without compromising the power capability.

**Declaration:** The work outlined in this chapter has not yet been published anywhere.

Alagar Raja et al., Non-covalent Interaction Directed Molecular Charge Storage, (*Manuscript under preparation*).

## 6.1. Introduction

Charge storage which is primarily surface-confined in supercapacitors as opposed to the bulk in batteries is directly responsible for the former's well-known energy deficiency and latter's limited power capability.[1-8] Since there exists a linear correlation between energy density of supercapacitors and their surface charge storage capability, next generation supercapacitors with high energy density are conventionally targeted in solid systems mainly by maximizing their surface to volume ratio.[9-14] With regard to molecular systems such as metal phthalocyanines and porphyrines, a few demonstrations exist on improving their charge storage capability by secondary sphere functionalization and by anchoring the molecular systems directly on various carbon derived substrates.[15-26] For example, Chidembo et al., reported that nature of the functionality in the secondary sphere of metal phthalocyanine (MPc) complexes can tune their supercapacitive charge storage and impressive performance was demonstrated with the composites of amino functionalized MPc with multi-walled carbon nanotubes (MWCNTs).[15,16] Composites of cobalt based phthalocyanines with MWCNTs and nickel based phthalocyanines with graphene based electrodes were recently reported to demonstrate superior charge storage capability.[17,18] Ultrahigh specific capacitance was demonstrated with an electrode architecture prepared by covalently and homogenously functionalized graphene with iron tetraaminophthalocyanine.[19] The superior performance was attributed to facile charge and ionic transport due to the structural and functional synergy of the covalently bound components, giving rise to a zwitter ionic surface with extensive π–π stacking. Recently, outstanding cycling stability and a high areal capacitance were observed with copper phthalocyanine based 2D metal organic framework nano sheets.[20] In similar lines, researchers have explored the charge storage in substituted metallophthalocyanine complexes and in their composites which undeniably signal their potential to excel as electrodes for supercapacitive charge storage.[21-26] Though, the foregoing discussion especially the work of Chidembo et al.,[15] highlights that the nature of the functionality in the secondary sphere of MPcs provides an extra handle to control their supercapacitive performance, a deeper knowledge gap exists in comprehending what defines a molecule's structure-charge storage relation. We show that nature of the functionality together with its isomerism in the secondary sphere of MPcs via attractive and repulsive non-covalent interactions leads to

unusual events in molecular charge storage. This non-covalent interactions leading to unprecedented molecular charge storage are strongly solvent dependent which in turn uncover a unique structure-charge storage relation in molecular supercapacitors. This study establishes that non-covalent interactions play subtle but decisive roles in deciding a molecule's electrochemical capacity which in turn should be promptly considered when new molecules are designed for charge storage applications. It is to be noted that the structure-charge storage relation uncovered in this chapter opens up a new dimension to target the energy density of molecular supercapacitors without compromising their power capability.

## 6.2. Results and discussion

### 6.2.1. Characterization of α-TAMPc and β-TAMPc (M- Co, Ni, Cu and Zn)

In the context of molecular charge storage, so far, the role of non-covalent interactions is not yet investigated and understood which brings up a critical knowledge gap in comprehending their structure-charge storage relation. In order to bridge this knowledge gap and to further deepen our understanding on what defines a molecule's structure-charge storage relation, in the present work non-covalent interactions were activated/deactivated in molecular systems via functionality's geometrical isomerism in the secondary sphere of the molecule. The structure of the molecular scaffolds used in this investigation is shown in Figure 6.1. They are denoted as α and β tetra amino-substituted metal (metal ions can be based on Co, Zn, Ni, Cu, Fe etc.) phthalocyanines (denoted as α-TAMPc and β-TAMPc where M = Co, Zn, Ni, Cu, Fe etc.). These two molecules differ only with respect to the position of the secondary sphere substituent and hence they are isomeric molecules or more precisely regioisomers, Figure 6.1. They were synthesized and characterized as per the litera-

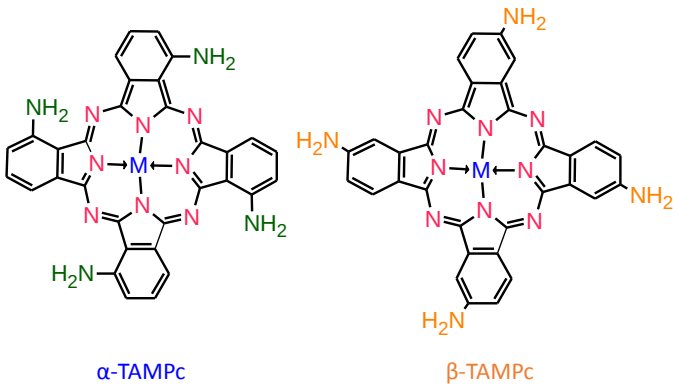


**Figure 6.1:** Molecular structure of α-TACoPc and β-TACoPc isomeric molecules where M stands for Co, Ni, Cu, Fe and Zn ions.

-ature (please refer to the synthesis, Chapter 2, section 2.4.2, page 47).[27,28] These molecules were characterized with the help of various physico chemical techniques as discussed in previous Chapter 5, Figures 5.1. As discussed in Chapter 5 (Figure 5.1), matrix-assisted laser desorption ionization time-of-flight mass spectrometry (MALDI-TOF), UV-Visible spectroscopy, Fourier transform infrared (FTIR) spectroscopy and Raman spectroscopy of isomeric TACoPc molecules confirm the formation of -$NH_2$ substituted molecules. Similarly, amino substituted metal phthalocyanines of Ni, Cu and Zn were synthesized and characterized as per the literature (please refer to synthesis, Chapter 2, section 2.4.3, page 47).[27,28] The MALDI-TOF data show the parent ion peak for α-TANiPc/β-TANiPc at m/z value of ~629, α-TACuPc/β-TACuPc at m/z value of ~634 and α-TAZnPc/β-TAZnPc at m/z value of ~636. These correspond to their respective molecular masses. Minor peaks at various m/z values indicate their fragment peaks, Figure 6.2.

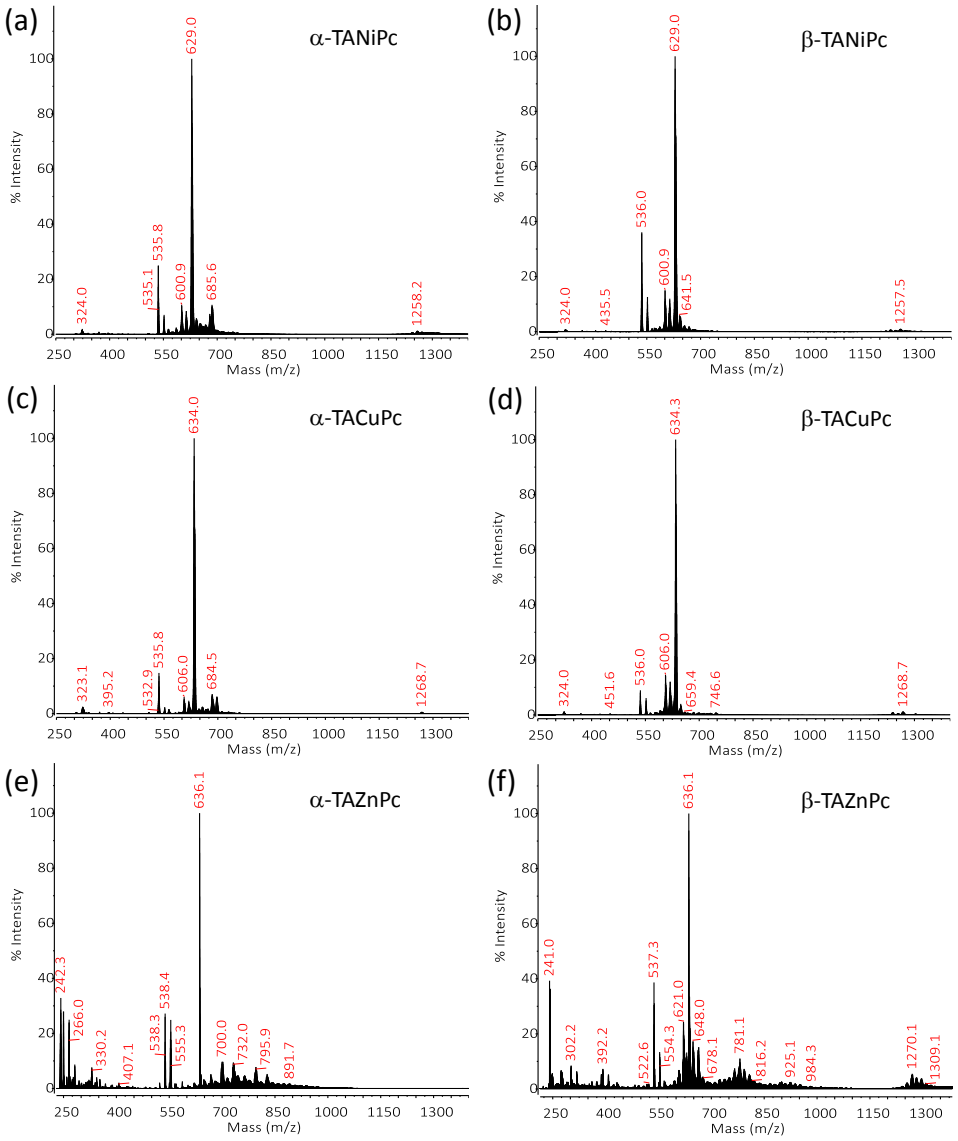

**Figure 6.2:** MALDI-TOF of α and β-TAMPc isomeric molecules (where M = Ni, Cu and Zn). (a, b) α-TANiPc and β-TANiPc isomeric molecules, (c, d) α-TACuPc and β-TACuPc isomeric molecules and (e, f) α-TAZnPc and β-TAZnPc isomeric molecules.

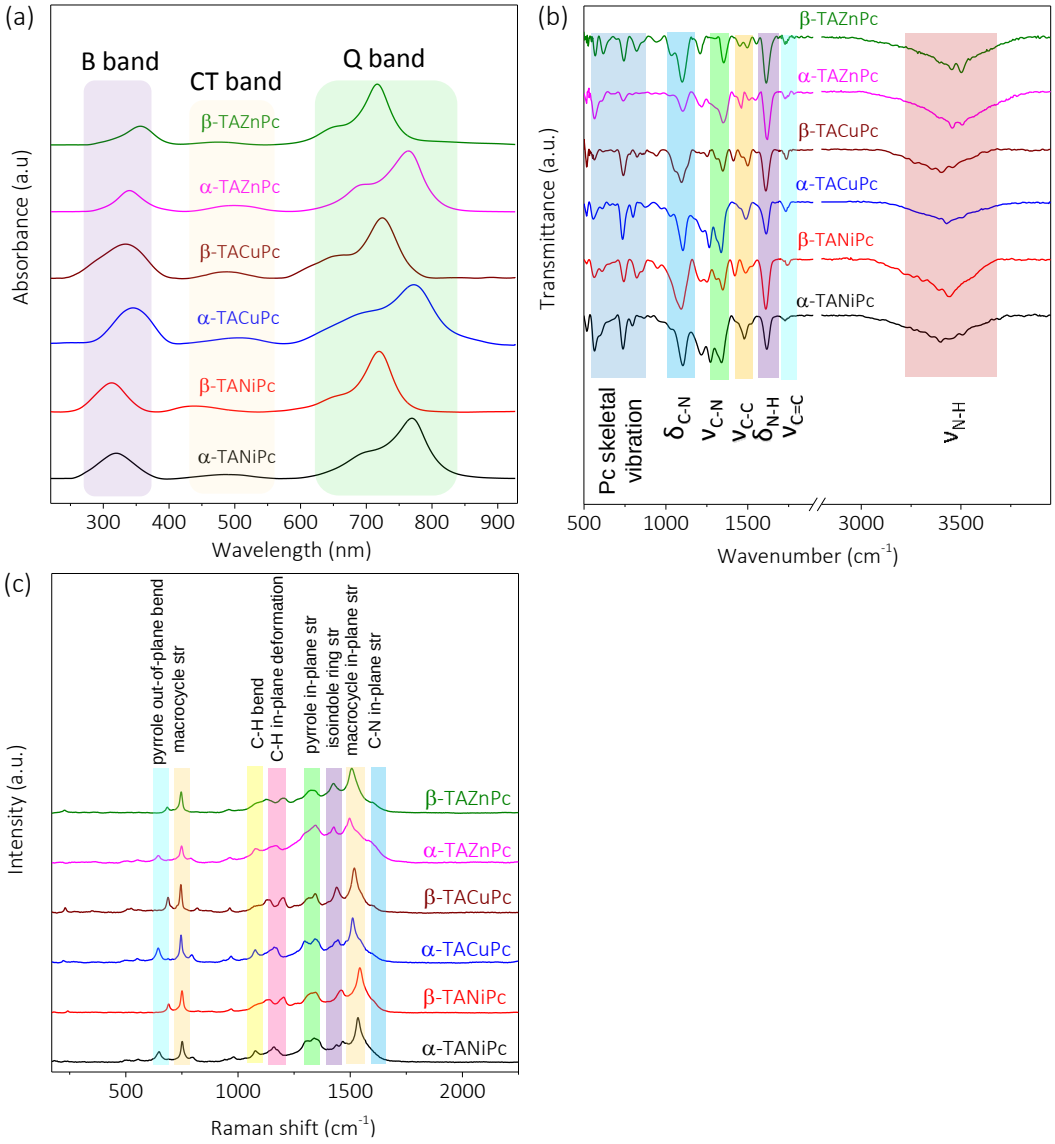


**Figure 6.3:** (a) UV-visible spectroscopy, (b) FT-IR spectroscopy and (c) Raman spectroscopy of α-TAMPc and β-TAMPc isomers (where M= Ni, Cu and Zn).

The UV-vis spectra of TAMPc isomers (where M= Ni, Cu and Zn) show Q band, B band and CT band corresponding to phthalocyanines, Figure 6.3a. The appearance of phthalocyanine skeletal vibrations in the range 525-945 $cm^{-1}$, C-N bond vibration at 1000-1165 $cm^{-1}$, pyrrole ring vibrations at 1215-1245 $cm^{-1}$, aromatic ring vibrations at 1620-1640 $cm^{-1}$ and the appearance of primary amine stretching vibrations close to 3140-3490 $cm^{-1}$ signal the formation of phthalocyanine molecules, Figure 6.3b. Raman spectra show phthalocyanine signature peaks where the 740-765 $cm^{-1}$ peak represents the macrocyclic

stretching vibration and 1190-1215 $cm^{-1}$ represents the C-H in plane deformation in the macrocyclic ring. The Raman shift at 1423-1465 $cm^{-1}$ corresponds to the stretching vibration of the isoindole ring unit, 1395-1410 $cm^{-1}$ and 1645-1680 $cm^{-1}$ represents the C-N in plane stretching vibrations. All these indicate the successful formation of molecular complexes, Figure 6.3c. The obvious difference in their spectral behavior is attributed to the influence of the central metal cation (Ni, Cu, Zn).

### 6.2.2. Electrochemical analysis

To investigate their electrochemical properties, the molecules were adsorbed as a monolayer on a glassy carbon electrode (GC) from dimethylformamide (DMF) solutions (See chapter 2, section 2.5 for more details, pages 48-49). Amatore parameter which indicates the quality of a monolayer is observed to be > 0.9 indicating the formation of relatively defect free monolayers on electrode surfaces, Figure 6.4 and Table 6.1, (Refer to chapter 2, section 2.6.2 for more details, pages 49-50).[40,41] Quartz crystal microbalance (QCM) studies during the electrode modification with α-TACoPc and β-TACoPc isomeric molecules indicate almost equal changes in mass, Figure 6.5. The surface coverage values (using Saurbrey equation, please see chapter 2, section 2.6.3 for more details, page 50)[42-44] are $4.67 \times 10^{-11}$ mol/$cm^2$ and $4.73 \times 10^{-11}$ mol/$cm^2$, for α-TACoPc and β-TACoPc isomeric molecules respectively, Figure 6.5, and Table 6.2. Since the experimental values of coverage are less than the theoretically expected value of $1.1 \times 10^{-10}$ mol/$cm^2$ for a perfectly flat phthalocyanine monolayer on an electrode surface,[45-47] it is reasonable to argue that both the isomeric molecules adsorb on the electrode surface as monolayer with nearly flat orientation. Cyclic voltammograms of GC electrodes modified with α-TACoPc and β-TACoPc isomeric molecules in 0.5 M $H_2SO_4$ solution demonstrate distinct redox features corresponding to central cobalt ions and phthalocyanine (Pc) ring, Figure 6.6a. The redox peaks at lower and higher positive potentials are assigned in the literature to cobalt ions and Pc ring respectively.[48-51] The striking feature which is distinctly evident in the voltammograms of α and β isomeric molecules are their electrochemical capacity which is dominant in the β isomer compared to the α isomer, Figure 6.6a. It should be noted that these distinct differences in their electrochemical capacities are observed for electrode surfaces modified with a monolayer of isomeric TACoPc molecules (as demonstrated above with

respect to Amatore's parameter and QCM, Figure 6.4 and Figure 6.5), signalling its origin to the intrinsic nature of the molecules. When the central metal ion in TACoPc is changed to Cu, Ni and Zn, all of them have maintained this striking contrast in their electrochemical characteristics with a dominant electrochemical capacity contribution in the β isomer over the corresponding α isomer, Figure 6.6b-d. Interestingly, even the TAZnPc molecule with a non-electrochemically active central metal ion, revealed a distinctly higher electrochemical capacity contribution in the β isomer compared to the α isomer suggesting its origin mainly to ligand characteristics. It should be noted that a redox wave is observed at lower positive potentials even with TAZnPc molecule with non-electrochemically active central metal ion, Figure 6.6d. It is reported in the literature that the redox wave observed in MPcs at lower potentials has some contribution from imine like groups within the phthalocyanine structure[15] as shown in equation 6.1 and we attribute this to the lower potential redox wave in TAZnPc.

$$R_2C{=}NR + 2e^- + 2H^+ \rightleftharpoons R_2CH\text{-}NHR \ldots\ldots (6.1)$$

Nevertheless, when the $-NH_2$ group in the secondary sphere of the phthalocyanine ligand is replaced by $-NO_2$ group, the disparity in isomeric molecule's electrochemical capacity disappeared, Figure 6.7. These reflect that the disparity in the charge storage capability of these isomeric molecules is largely independent of the central metal ion but is interlinked strongly not only with the nature but also with the isomerism of their secondary sphere functionality. It is to be noted that in the domain of molecular charge storage, the role of isomerism is often ignored, however the results outlined here reveal that it undeniably deserves consideration if the maximum potential of the molecule has to be exploited for charge storage applications.

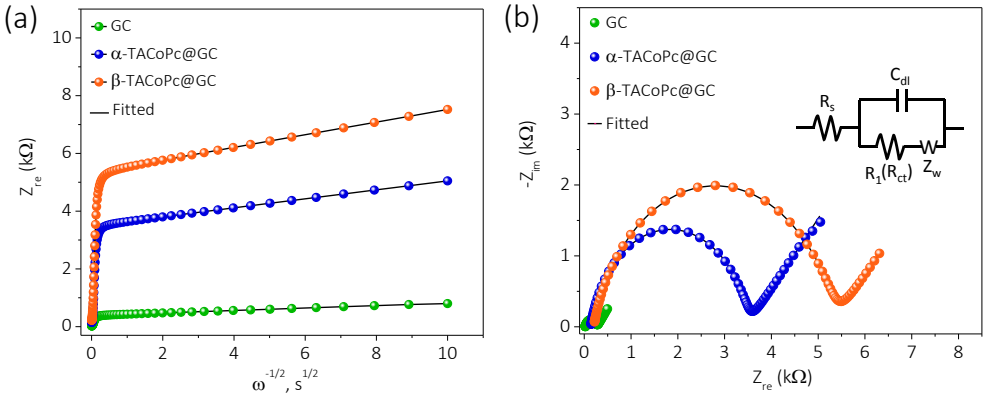

**Figure 6.4:** The Amatore's parameter for α-TACoPc and β-TACoPc isomeric molecules when adsorbed as a monolayer on a GC electrode. Electrolyte is $N_2$ saturated 0.1 M phosphate buffer (pH - 7) containing 5 mM ferrocyanide/ferricyanide redox couple. (a) The plot of real part of impedance ($Z_{re}$) vs. $1/(\omega)^{1/2}$ where ω is the angular frequency of AC in units of rad/s and (b) the complex plane impedance plot at the open circuit voltage acquired in the frequency range of 100 kHz to 5 mHz. The AC amplitude was 10 mV (peak to peak). The circuit used for fitting the Nyquist plot is shown in the inset of Figure 6.4b.

**Table 6.1:** Fractional surface coverage (θ) values of the modified GC electrode obtained using Amatore's model.

| Types of Electrodes | Monolayer Coverage (θ) | |
|---|---|---|
| | $^*\theta_{IS}{}^R$ | $^*\theta_{IS}{}^P$ |
| **α-TACoPc@GC** | 0.93 ± 0.02 | 0.94 ± 0.02 |
| **β-TACoPc@GC** | 0.96 ± 0.02 | 0.97 ± 0.01 |

$^*\theta_{IS}{}^R$ and $^*\theta_{IS}{}^P$ stand for fractional coverage values estimated based on charge transfer resistance (Chapter 2, eq 2.2) and pinhole size (Chapter 2, eq 2.3) respectively.

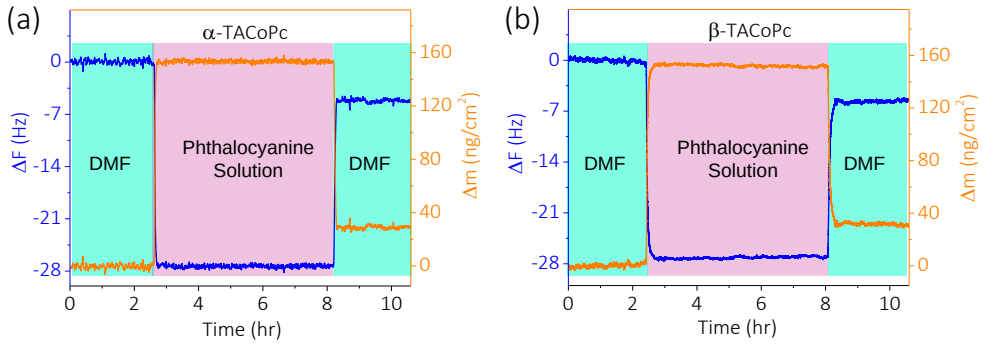


**Figure 6.5:** Quartz crystal microbalance (QCM) response during the adsorption of isomeric molecules (α-TACoPc and β-TACoPc) on a carbon coated quartz resonator from 0.2 mM solutions of (a) α-TACoPc and (b) β-TACoPc in dimethylformamide (DMF). The blue trace shows the frequency change during the adsorption and the orange trace shows the calculated mass change using the Saurbrey equation.

**Table 6.2:** Surface coverage (Γ) values of α-TACoPc and β-TACoPc isomeric molecules extracted from Figure 6.5.

| Types of Electrodes | Surface Coverage (Γ) |
|---|---|
| **α-TACoPc@GC** | $4.67 \times 10^{-11}$ mol/cm$^2$ |
| **β-TACoPc@GC** | $4.73 \times 10^{-11}$ mol/cm$^2$ |

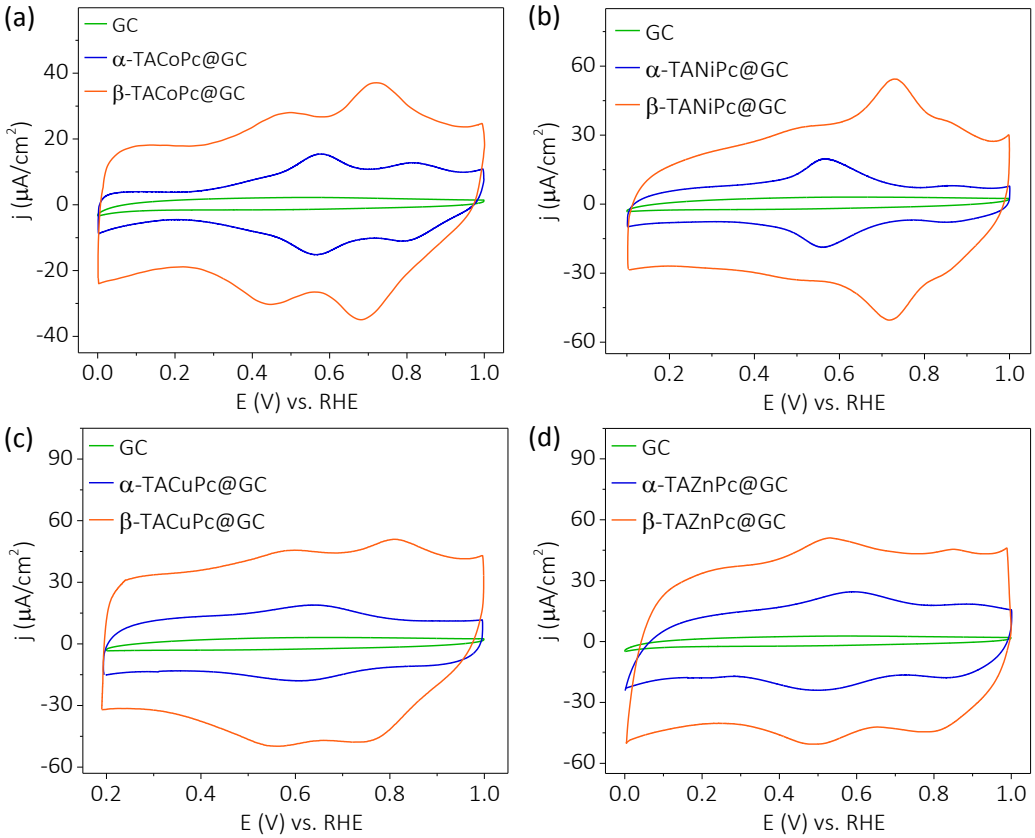


**Figure 6.6:** Cyclic voltammograms (CVs) of isomeric molecules when incorporated as a monolayer on a glassy carbon electrode at a scan rate of 20 mV/s in $N_2$ saturated 0.5 M $H_2SO_4$. CVs of (a) α-TACoPc and β-TACoPc isomeric molecules, (b) α-TANiPc and β-TANiPc isomeric molecules (c) α-TACuPc and β-TACuPc isomeric molecules and (d) α-TAZnPc and β-TAZnPc isomeric molecules.

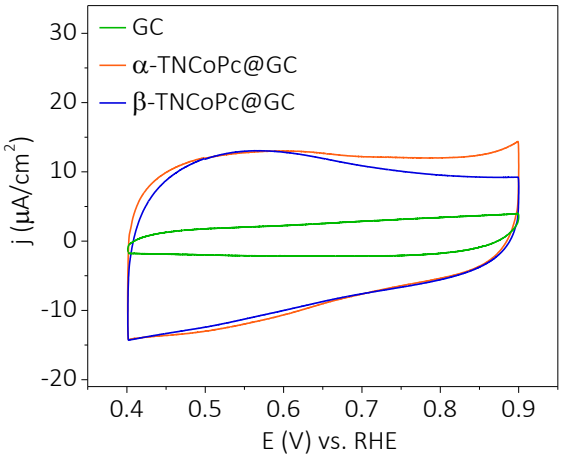


**Figure 6.7:** Cyclic voltammograms at a scan rate of 20 mV/s for α-TNCoPc and β-TNCoPc isomeric molecules (adsorbed as a monolayer on a glassy carbon electrode) in $N_2$ saturated 0.5 M $H_2SO_4$ solutions.

### 6.2.3. Density functional theory (DFT) calculation

The fact that electrochemical capacity is independent of the central metal ion but is correlated strongly to the nature as well as isomerism of the secondary sphere functionality (Figure 6.6 and Figure 6.7), prompted us to attribute this to non-covalent interactions governed by functionality's nature and isomerism. In order to strengthen this claim, we resorted initially to density functional theory (DFT) calculations of α and β isomers of amino substituted cobalt phthalocyanines (TACoPcs), Figure 6.8 (The details can be found in Chapter 2, section 2.7, pages 50-51). The stabilized structures reveal that the pristine α-TACoPc possesses intramolecular hydrogen bonding between the secondary sphere $–NH_2$ group and imine N at the meso-position of the Pc ring with the former as the H bond donor and the latter as the H bond acceptor, Figure 6.8a. This H bonding has a characteristic distance of 2.225 Å with N-H---N bond angle of 129.75°, Table 6.3. Hence, this intramolecular hydrogen bond is moderate in strength and mostly electrostatic in nature.[52-54] Besides, the pristine α isomer lies 0.87 eV (relative energy difference) lower on potential energy surface than the corresponding β isomer, indicating this type of H bonding stabilizes the former, Figure 6.8a and 6.8b, and Table 6.3. However, DFT calculations reveal that such intramolecular hydrogen bonding is absent in the pristine β isomer molecule perhaps due to lack of interaction between the H bonding groups given their relatively large spatial separation. In essence, DFT calculations suggest that isomerism of $–NH_2$ functionality in the secondary sphere triggers non-covalent interactions in the α isomer which is absent in the corresponding β isomer due to the large spatial separations of H bonding groups, Figure 6.8a and 6.8b. Interesting observations related to structural geometry was evident when DFT calculations were performed in the presence of protons (Figure 6.8c,d and Figure 6.9a) which is considered important as charge storage investigations were carried out in proton containing media (Figure 6.6). β isomer showed quite stable structures when molecule to proton ratio was 1:4 as well as 1:8 suggesting that both imine N as well as amine nitrogen can be protonated, Figure 6.8d and Figure 6.9a. However, α isomer which showed a stable structure when molecule to proton ratio was 1:4, became highly unstable at 1:8 molecule to proton ratio, suggesting the protonation of eight N atoms as in the case of β isomer is highly unfavourable, Figure 6.8c and Figure 6.9a. DFT calculations also reveal that intramolecular H bonding in the pristine α isomer grew stronger with 1:4 molecule to proton ratio, Figure 6.8a, 6.8c, Figure 6.9 and Table 6.3. The relative energy diagram, Figure 6.9b, shows that

the proton shuttles from amine nitrogen to imine nitrogen in the most stable structure of the α isomer which in turn stabilizes the structure by nearly 6 eV. This could explain the preferential protonation of imine N compared to amine N, with the consequence of the former being the hydrogen bond donor and the latter being H bond acceptor. DFT calculation shows that this stability attained by the α isomer via H bonding will be lost on further protonation with 1:8 molecule to proton ratio due to structural deformation, Figure 6.9a and Table 6.3. Therefore, DFT calculations indicate that the presence of intramolecular H bonding in the α isomer restricts the extent of protonation of N atoms and the absence of it in the β isomer allows the majority of its N atoms to be protonated. This has important consequences in their ability to store charge as shown below.

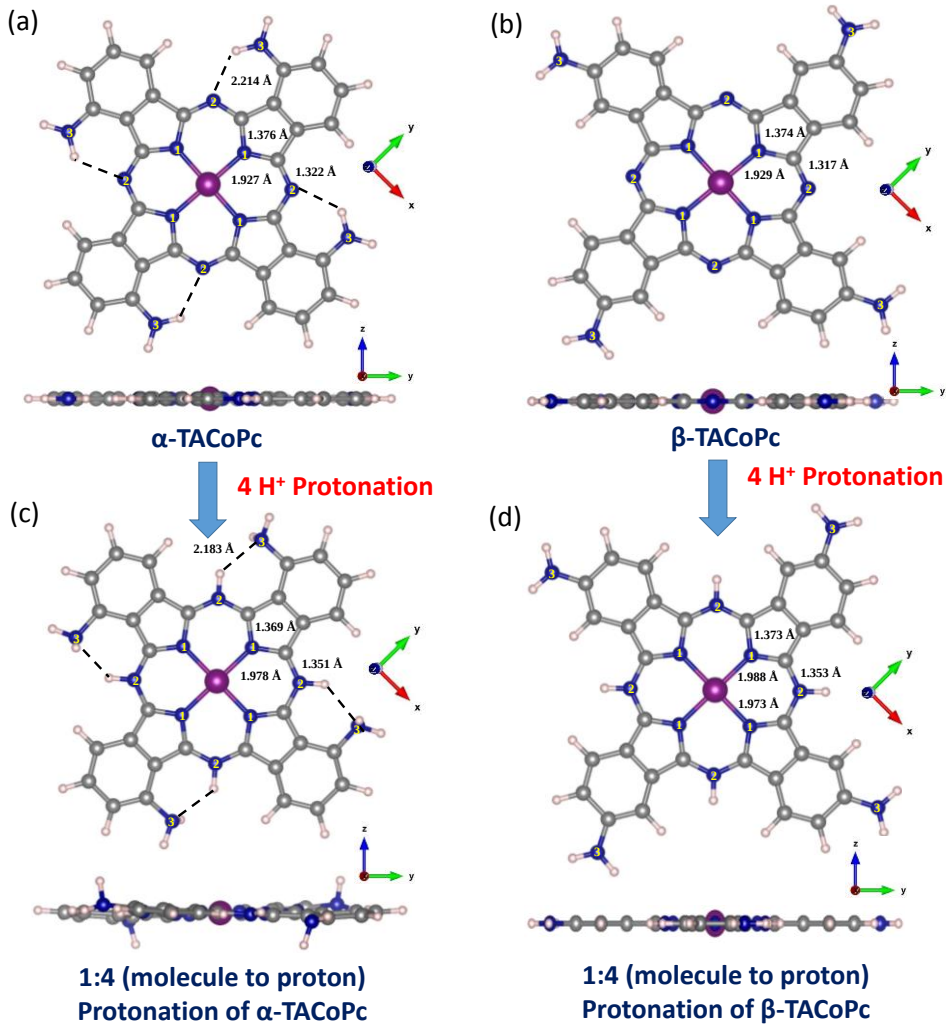


**Figure 6.8:** Stable geometry of pristine (a) α-TACoPc and (b) β-TACoPc isomers. Stable geometry of four protonated (c) α-TACoPc and (d) β-TACoPc isomers. Nitrogen atoms are labeled in their stable geometry in Figure 6.8: N1: pyrrole nitrogen atoms; N2: iminic nitrogen atoms; and N3: nitrogen atom of $NH_2$ groups.

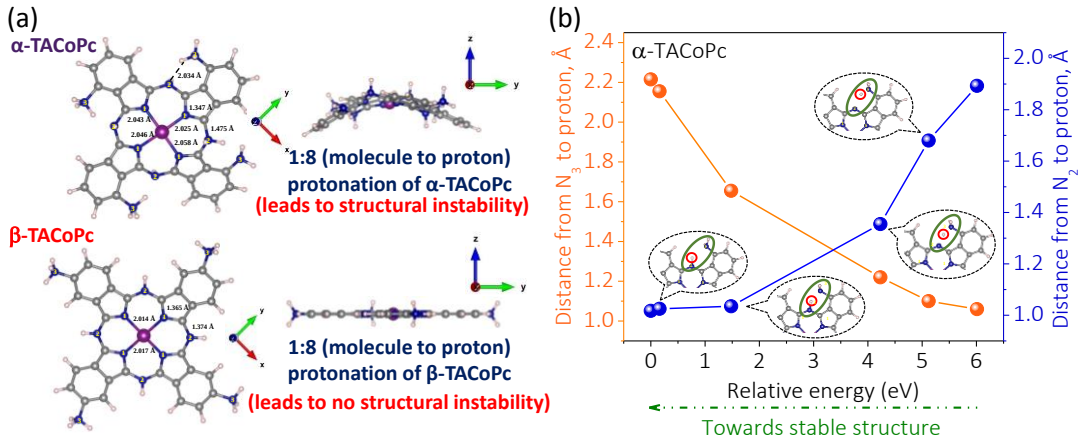


**Figure 6.9:** (a) Stable geometry of eight protonated form of α-TACoPc and β-TACoPc isomers. (b) The correlation plot of N/H distance between in iminic-nitrogen atom (N2 in Figure 6.8a) and amine-nitrogen atom (N3 in Figure 6.8a) vs. relative energy for α-TACoPc molecule.

**Table 6.3:** Comparative parameters from DFT calculations (Figures 6.8 and 6.9).

| System | | Parameters | | Relative energy difference between alpha and beta isomers |
|---|---|---|---|---|
| | | Hydrogen bond distance (N-H---N ) | Bond angle (N-H---N) (degrees) | |
| Pristine | α-TACoPc | 2.214 Å | 129.75° | β-TACoPc ⇕ 0. 87 eV α-TACoPc |
| | β-TACoPc | - | - | |
| 1:4 (molecule to proton) protonation | α-TACoPc | 2.183 Å | 132.40° | β-TACoPc (1:4) protonation ⇕ 2.68 eV α-TACoPc (1:4) protonation |
| | β-TACoPc | - | - | |

### 6.2.4. Nuclear magnetic resonance (NMR) spectroscopy and X-ray photoelectron spectroscopy (XPS) investigations

To experimentally validate the theoretical predictions, NMR and X-ray photoelectron spectroscopic (XPS) investigations were carried out. NMR analysis were carried out with corresponding zinc phthalocyanines as cobalt phthalocyanines are paramagnetic in nature.[55,56] 1D and 2D proton NMR spectra of isomeric molecules reveal the existence of intramolecular hydrogen bonding interactions in the α isomer, Figure 6.10a, 6.10c and 6.10e. 1D NMR shows two distinctly chemical shifted amine protons in the case

of α isomer (labelled as e and d in the inset of Figure 6.10a for α-TAZnPc) which could be exchanged on $D_2O$ addition confirming their origin to amine protons, Figure 6.10a. This suggests that chemical environments of amine protons are distinctly different in the α isomer which is possible if there is intramolecular hydrogen bonding interactions involving the primary amine group and imine nitrogen in the Pc ring as shown in the inset of Figure 6.10a. The corresponding COSY and NOESY 2D NMR suggest that amine protons are in hydrogen bonding with imine nitrogen, Figure 6.10c and 6.10e.

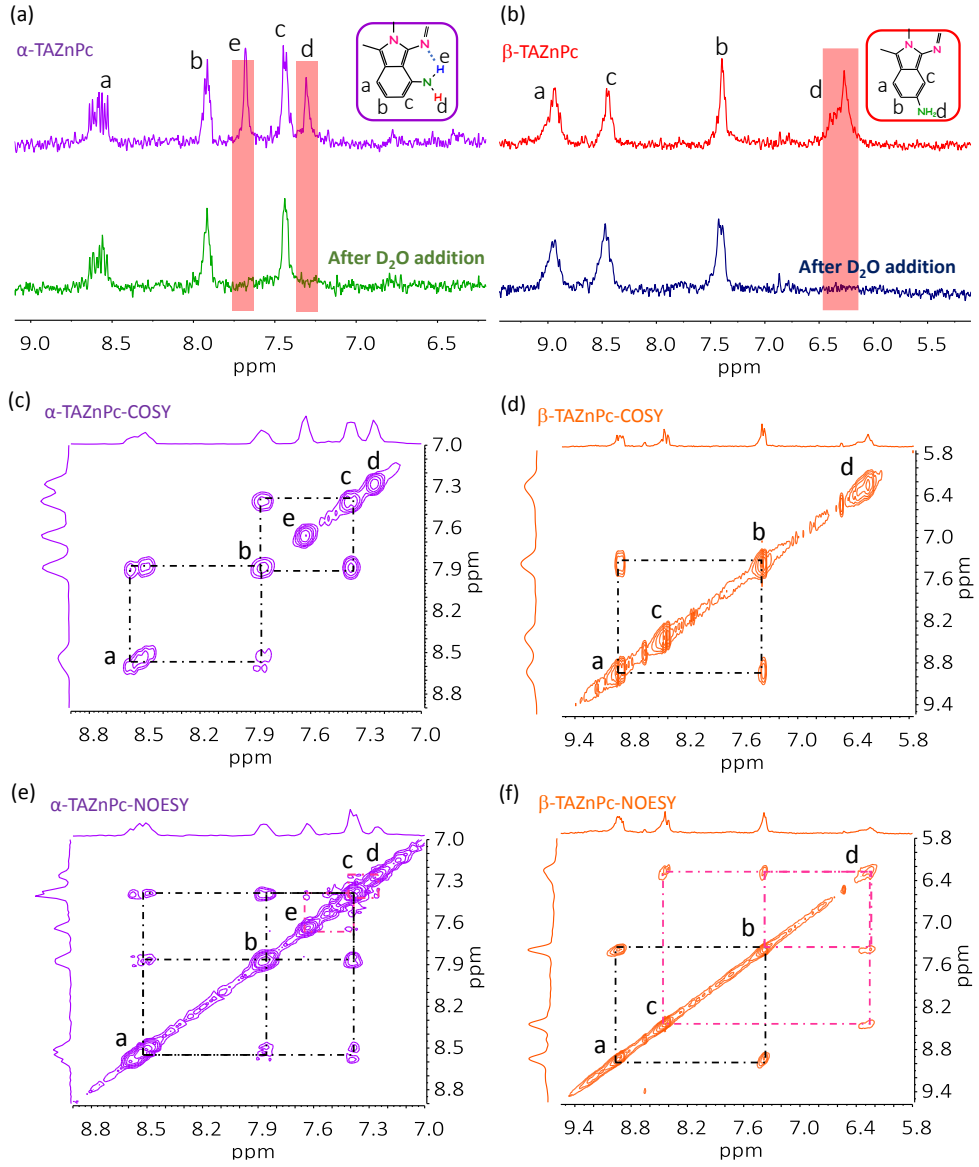


**Figure 6.10:** Nuclear magnetic resonance (NMR) spectra of α and β-TAZnPc isomeric molecules. (a and b) $^1H$ NMR of α-TAZnPc and β-TAZnPc isomeric molecules before and after $D_2O$ addition. (c to f) 2D $^1H$ NMR spectra (COSY and NOESY) of α-TAZnPc and β-TAZnPc isomeric molecules. COSY and NOESY spectra of (c and e) α-TAZnPc and (d and f) β-TAZnPc.

1D NMR of the corresponding β isomer revealed only a broad amine proton signal (labelled as d in the inset of Figure 6.10b for β-TAZnPc) which disappeared on $D_2O$ addition, suggesting amine protons are not involved in intramolecular hydrogen bonding, Figure 6.10b. The corresponding COSY and NOESY NMR further rule out these intramolecular hydrogen bonding interactions in the β isomer, Figure 6.10d and 6.10f, probably due to their unfavourable position. Temperature-dependent NMR suggest a lower chemical shift slope for the amine protons in the α isomer compared to a noticeably higher slope for the amine protons in the β isomer, Figure 6.11. It should be noted that this slope for the amine protons in the α isomer is in the order expected for intramolecularly H bonded protons as reported in the literature.[57-59] All these support theoretical predictions by DFT and suggest that α isomer has intramolecular hydrogen bonding involving imine nitrogen and amine protons as shown in Scheme 6.1.

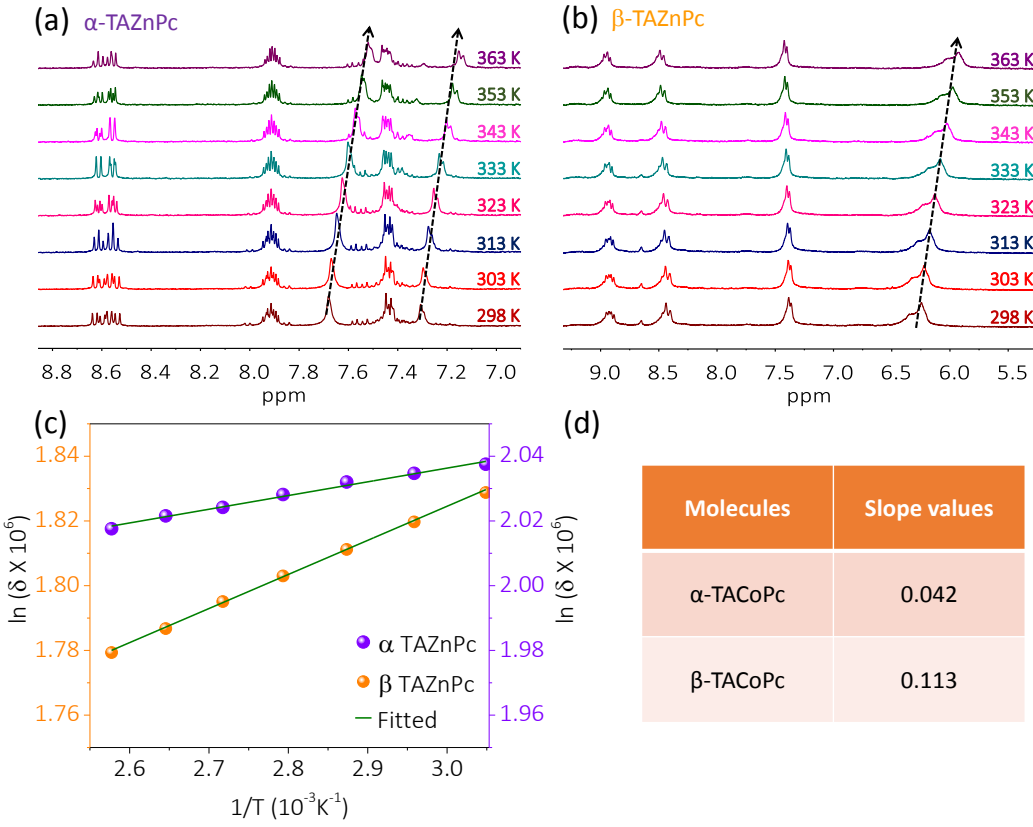


**Figure 6.11:** Temperature-dependent (25° to 90° C) $^1$H NMR spectra of (a) α-TNZnPc and (b) β-TNZnPc. (c) Plot of chemical shift vs. inverse of temperature (T) for the amine protons in isomeric α and β-TAZnPc molecules extracted from their respective temperature-dependent $^1$H NMR spectra (from Figures 6.10a and 6.10b) and (d) slope values extracted from Figure 6.11c.

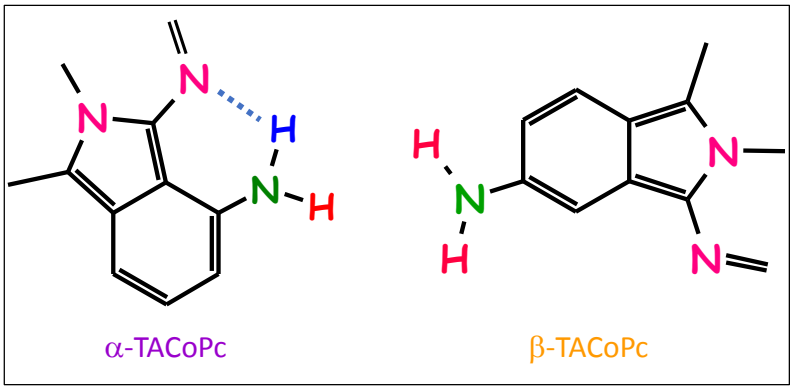


**Scheme 6.1:** Scheme showing intramolecular H bonding interactions in α-TACoPc isomer involving imine nitrogen and amine protons. Scheme showing the absence of such hydrogen bonding interactions in β-TACoPc isomer due to the unfavourable positions of H bonding groups.

As we noted earlier based on DFT predictions, the presence of intramolecular hydrogen bonding in the α isomer make the nitrogen atoms less available for protonation (in acidic media) compared to the nitrogen atoms in the β isomer. This claim is strengthened by N1S XPS analysis, Figure 6.12a-d. The XPS spectra of α isomer/β isomer reveal three peaks in N1S regime corresponding to $N_1$ (Co-N), $N_2$ (C=N, imine), and $N_3$ (C-$NH_2$, amine) as marked in the Figure 6.12 with the binding energies in order $N_1 < N_2 < N_3$.[60-62] The nitrogen atoms especially $N_2$ and $N_3$ of pristine α isomer demonstrated a noticeable shift towards higher binding energy (Figure 6.12a, 6.12d and Table 6.4) compared to that of β isomer. This relatively larger shift of N1S binding energy (BE) towards higher values is a clear indication of the loss of electron density on nitrogen species in the pristine α isomer which in turn can be attributed to intramolecular H-bonding interaction involving amine protons and imine N in the Pc ring as explained earlier. Further, the N1S XPS spectra of both the isomers exhibited an upshift in their binding energies on acid treatment than the pristine isomers and this upshift is much more pronounced in the β isomer compared to the α isomer (Figure 6.12b and 6.12c and Table 6.4). This corroborates the fact that extent of protonation is significantly higher in the β isomer compared to the α isomer which further strengthens our insight based on DFT that the intramolecular H bonding should make the protonation of N atoms in the α isomer more difficult compared to the β isomer. Therefore, the β isomer should possess a higher surface charge and consequently a higher electrochemical capacity in proton containing media.

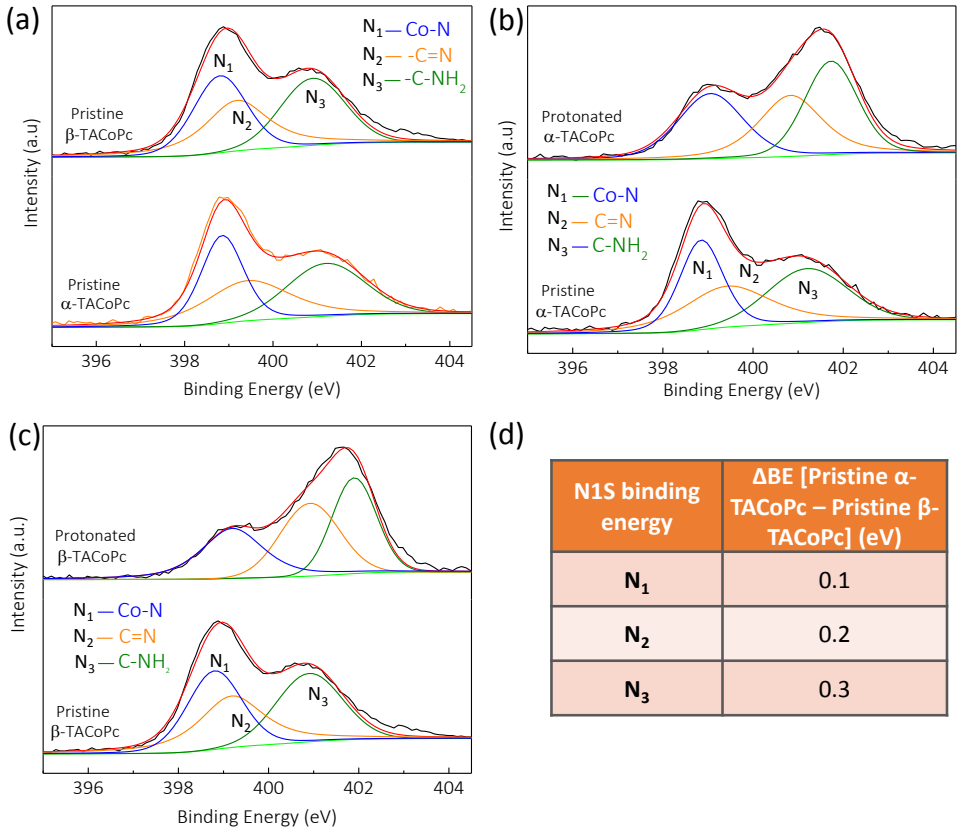


| N1S binding energy | ΔBE [Pristine α-TACoPc – Pristine β-TACoPc] (eV) |
|---|---|
| $N_1$ | 0.1 |
| $N_2$ | 0.2 |
| $N_3$ | 0.3 |

**Figure 6.12:** N1S XPS spectra of (a) pristine α-TACoPc and β-TACoPc isomeric molecules, (b) pristine and protonated forms of α-TACoPc molecule and (c) pristine and protonated forms of β-TACoPc molecule. (d) Difference between the N1S binding energy values (ΔBE) of pristine α-TACoPc and β-TACoPc isomeric molecules from Figure 6.12a.

**Table 6.4:** N1S binding energy values for α-TACoPc and β-TACoPc isomeric molecules (extracted from Figure 6.12). $N_1$ (Co-N), $N_2$ (C=N, imine), and $N_3$ ($C-NH_2$, amine).

| Molecules | α-TACoPc | | | β-TACoPc | | |
|---|---|---|---|---|---|---|
| | $N_1$ | $N_2$ | $N_3$ | $N_1$ | $N_2$ | $N_3$ |
| Pristine (eV) | 398.9 | 399.4 | 401.2 | 398.8 | 399.2 | 400.9 |
| Protonated (eV) | 399.1 | 400.8 | 401.7 | 399.2 | 400.9 | 401.9 |
| ΔBE [Protonated - Pristine] (eV) | 0.2 | 1.4 | 0.5 | 0.4 | 1.7 | 1.0 |
| ΔBE [Pristine α-TACoPc – Pristine β-TACoPc] (eV) | $N_1$ | | $N_2$ | | $N_3$ | |
| | 0.1 | | 0.2 | | 0.3 | |

### 6.2.5. Investigation of surface charge

Investigation of surface charge with outer-sphere redox complexes such as negatively

charged ferricyanide and positively charged $[Ru(NH_3)_6]^{3+}$ (Figure 6.13a-d) suggests that in acidic medium β isomer can electrostatically attract negatively charged ferricyanide and block to some extent positively charged $[Ru(NH_3)_6]^{3+}$ compared to the α isomer, Figure 6.13a and 6.13c. This signals that in acidic medium β isomer acquires more positive charge density compared to the α isomer which is in fact a direct consequence of intramolecular hydrogen bonding in the latter (as explained above). When intramolecular hydrogen bonding is blocked by replacing the amino groups by nitro groups in the secondary sphere, the outer-sphere redox probe responses are almost the same, Figure 6.13b and 6.13d, pointing to similar molecular charge densities and consequently, similar electrochemical capacities in these isomeric molecules, Figure 6.7. This is supported by DFT calculations of isomeric nitro molecules (α and β-TNCoPc) which did not reveal a disparity in their extent of protonation, Figure 6.14. Finally, when isomeric TACoPc molecules are investigated for their charge storage contribution in electrolytes containing $OH^-$ instead of $H^+$, their electrochemical capacities are found to be almost similar, Figure 6.15a. In line with this, the redox responses of isomeric TACoPc molecules towards outer sphere redox species in alkaline medium did not show an obvious difference (Figure 6.15b), indicating that the non-covalent interactions leading to a disparity in isomeric molecule's charge storage is solvent dependent.

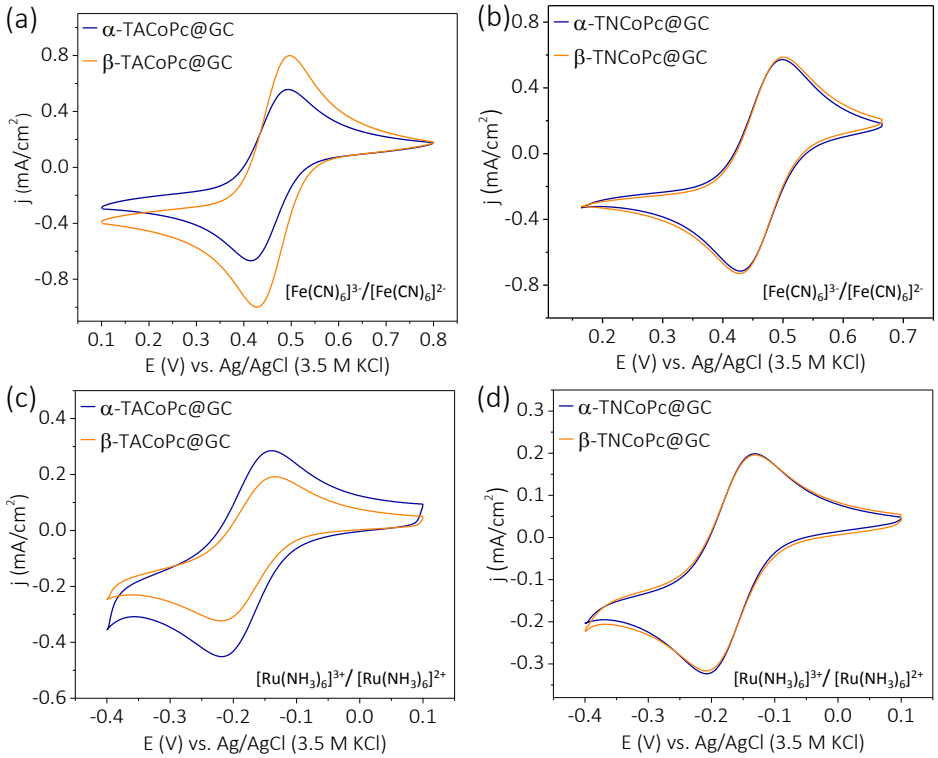


**Figure 6.13:** Cyclic voltammograms with the isomeric molecules for the redox reactions of

5 mM ferricyanide (a and b) and 2 mM hexamine ruthenium (c and d) at a scan rate of 20 mV/s in in $N_2$ saturated 0.5 M $H_2SO_4$. (a and c) for α-TACoPc, and β-TACoPc and (b and d) for α-TNCoPc and β-TNCoPc modified glassy carbon electrodes.

Taken together, DFT predictions in association with electrochemistry, NMR and XPS analyses strongly suggest that the nature of the substituent along with their geometrical isomerism govern the charge storage in substituted phthalocyanines via non-covalent interactions, however the consequence is solvent dependent. Their charge-discharge characteristics are further investigated by cyclic voltammetry and galvanostatic charge-discharge measurements, Figure 6.16 and 6.17. The data reveal that the areal capacitances are more than 2 times higher in the case of β isomer compared to the α isomer when they are adsorbed as a monolayer on a glassy carbon electrode surface.

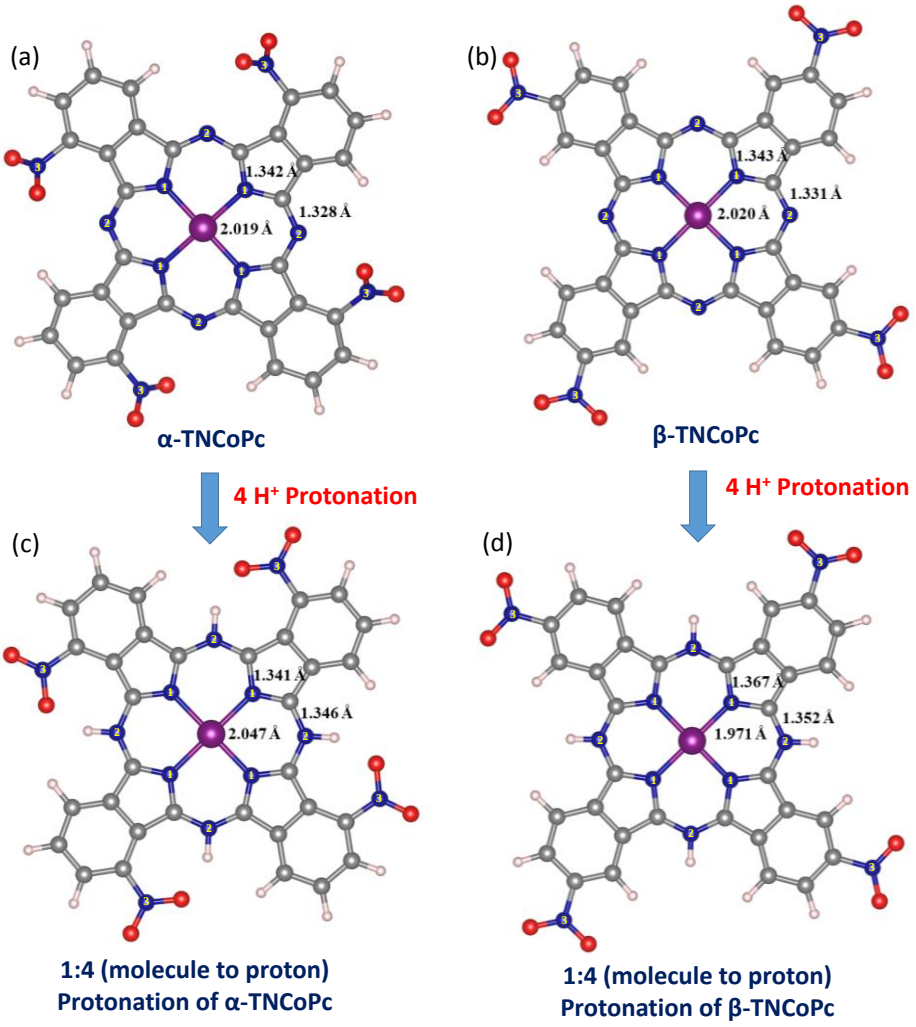


**Figure 6.14:** Stable geometry of pristine (a) α-TNCoPc and (b) β-TNCoPc isomers. Stable geometry of protonated (c) α-TNCoPc and (d) β-TNCoPc isomers with molecule to proton ratio of 1:4. (Nitrogen atoms are labeled in their stable geometry in Figure 6.14: N1: pyrrole

nitrogen atoms; N2: iminic nitrogen atoms; and N3: nitrogen atom of $NO_2$ groups.

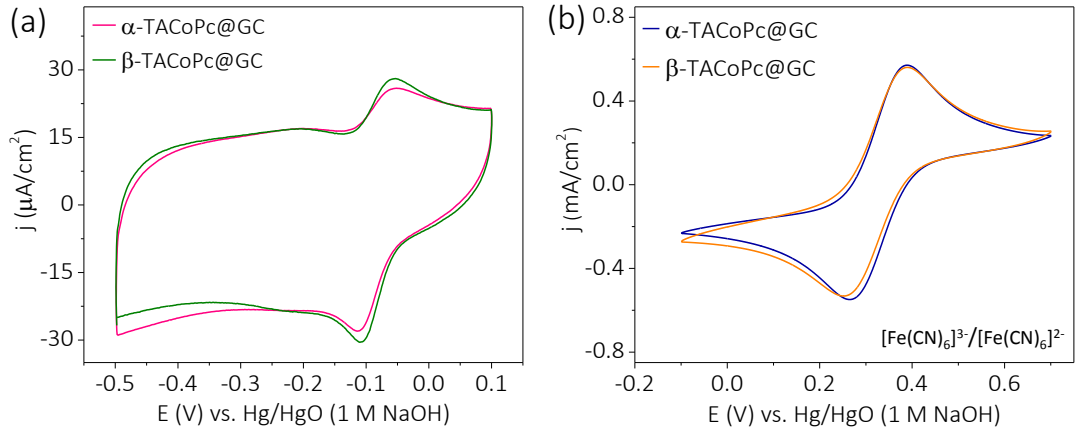


**Figure 6.15:** (a) Cyclic voltammograms for α-TACoPc and β-TACoPc isomeric molecules adsorbed as a monolayer on a glassy carbon electrode at a scan rate of 20 mV/s in $N_2$ saturated 0.5 M NaOH and (b) cyclic voltammograms for the redox reaction of 5 mM ferricyanide at a scan rate of 20 mV/s in $N_2$ saturated 0.5 M NaOH with α-TACoPc and β-TACoPc modified glassy carbon electrodes.

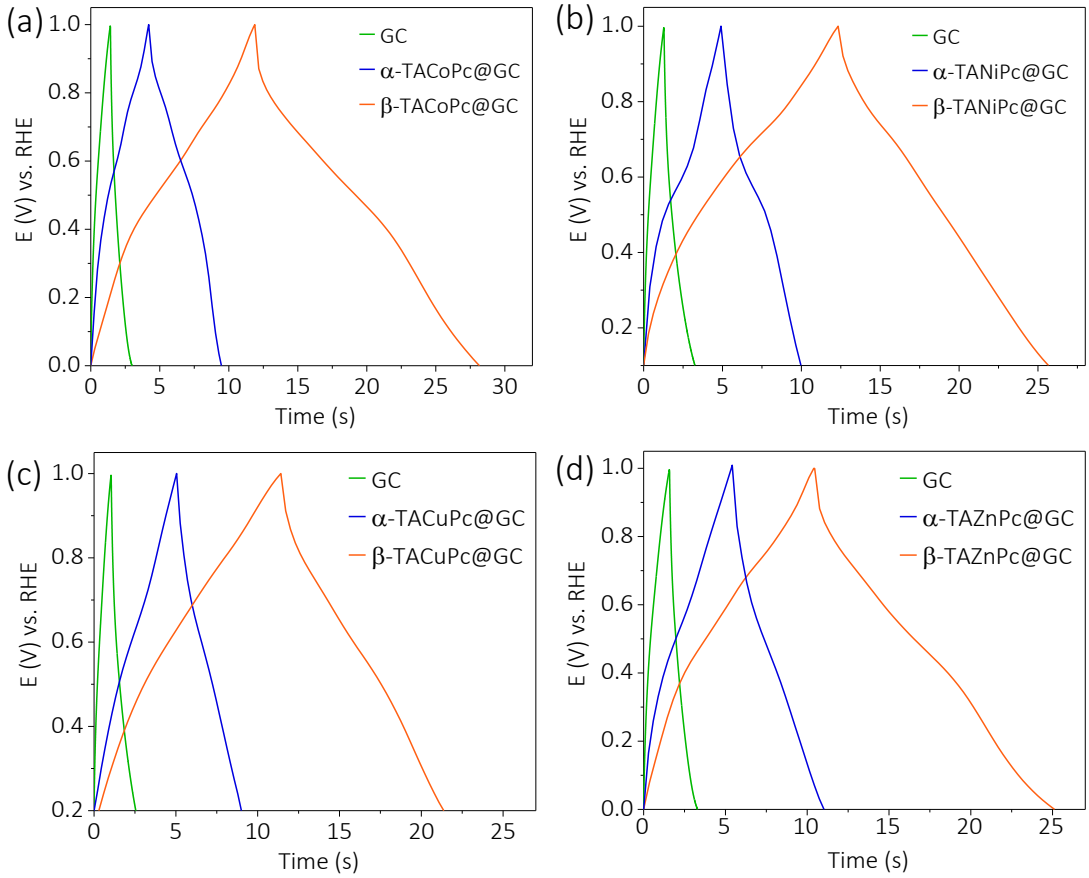


**Figure 6.16:** Galvanostatic charge-discharge at a rate of 0.1 mA/cm² in $N_2$ saturated 0.5 M $H_2SO_4$ for (a) α-TACoPc and β-TACoPc, (b) α-TANiPc and β-TANiPc, (c) α-TACuPc and β-TACuPc and (d) α-TAZnPc and β-TAZnPc isomeric molecules when they are

adsorbed as a monolayer on glassy carbon electrodes in $N_2$ saturated solutions.

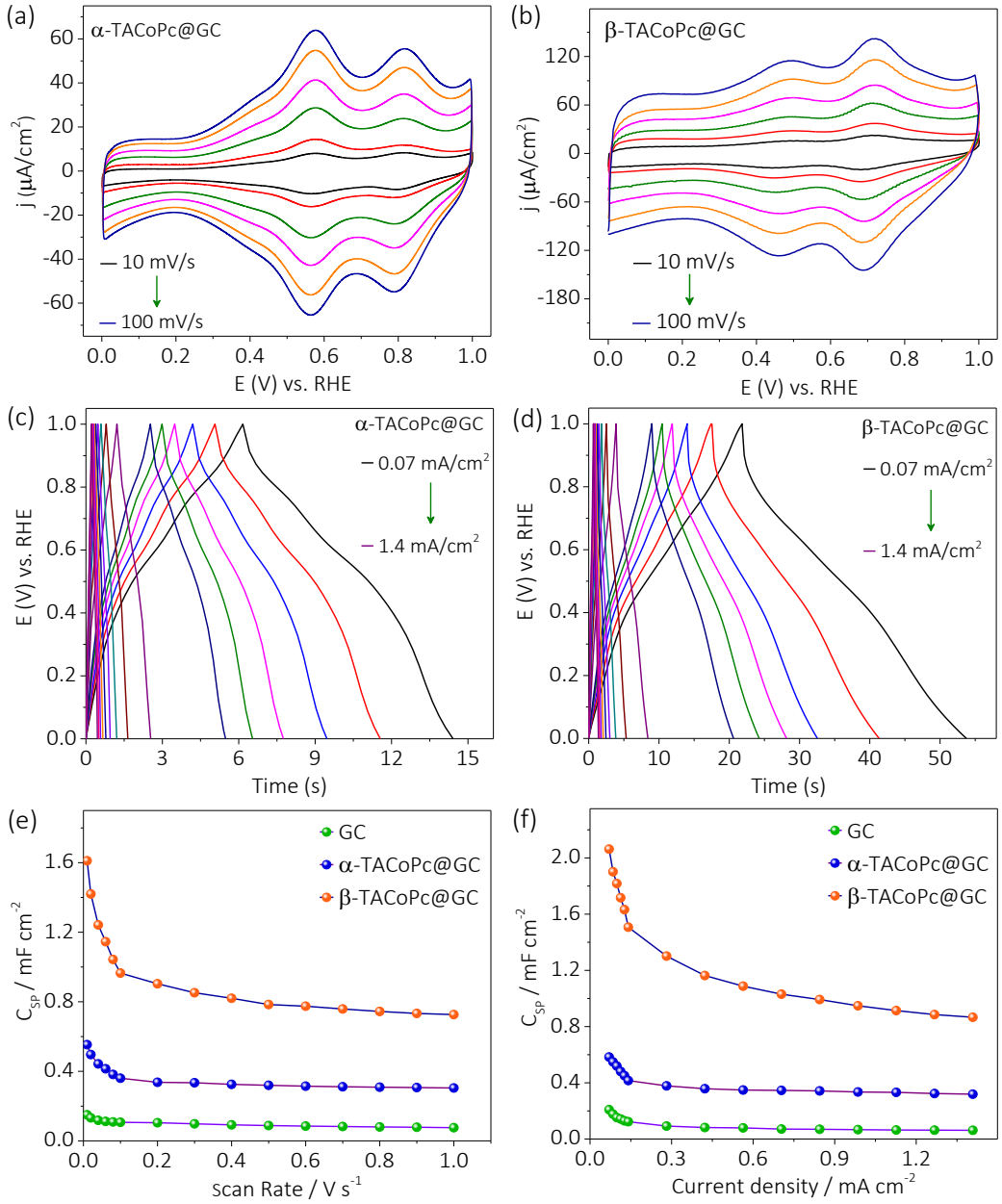


**Figure 6.17:** Rate profiles for α-TACoPc and β-TACoPc isomeric molecules when they are adsorbed as a monolayer on glassy carbon electrode surface. Cyclic voltammetry (a, b), galvanostatic charge-discharge (c, d) and rate profiles (e, f). Specific capacitance ($F/cm^2$) values are calculated based on the geometric area of the electrode.

### 6.2.6. Charge storage in composite electrodes

To exploit these peculiar structural characteristics for practical charge storage applications we have made composites of these isomeric phthalocyanine molecules with porous carbon material (YP-50F) (please refer to Chapter, section 2.4.5 for more details, page

48).[63-65] The presence of phthalocyanine molecules on YP-50F surface is proved by FTIR, Raman spectroscopy and FESEM, Figure 6.18 and 6.19. Briefly, FTIR indicates the features of TACoPc in TACoPc@YP-50F along with corresponding YP-50 features, Figure 6.18a. Raman spectra, show the presence of characteristic defect and graphitic bands in YP-50F as well as in the composite, Figure 6.18b, however, the phthalocyanine features are almost masked by the intense YP-50F bands. Nevertheless, the $I_D/I_G$ (intensity of defect band/intensity of graphitic band) ratio in YP-50F demonstrates a noticeable increase on anchoring it with the isomers of TACoPcs, suggesting their successful incorporation.[66-68] Scanning electron microscopy (SEM) with energy dispersive X-ray spectroscopy (EDS), Figure 6.19, indicate characteristic spherical morphology of YP-50F and the EDS spectra demonstrate the presence of Co, N and C, further reinforcing the successful incorporation of TACoPc's in the composite. All these evidence the presence of YP-50F and TACoPcs isomers as a part of the electrode architecture. Such modified electrodes demonstrated similar characteristics as monolayer electrodes with a dominant electrochemical capacity in β-TACoPc@YP-50F compared to α-TACoPc@YP-50F, Figure 6.20. The gravimetric capacitance of β-TACoPc@YP-50F is found to be ~730 F/g (please refer to chapter 2, section 2.11, pages 54 for more details) which is more than twice compared to α-TACoPc@YP-50F (~360 F/g). Rate capability by cyclic voltammetry and galvanostatic charge-discharge measurements, further reinforce the superior charge storage in β-TACoPc@YP-50F compared to α-TACoPc@YP-50F, Figure 6.21.

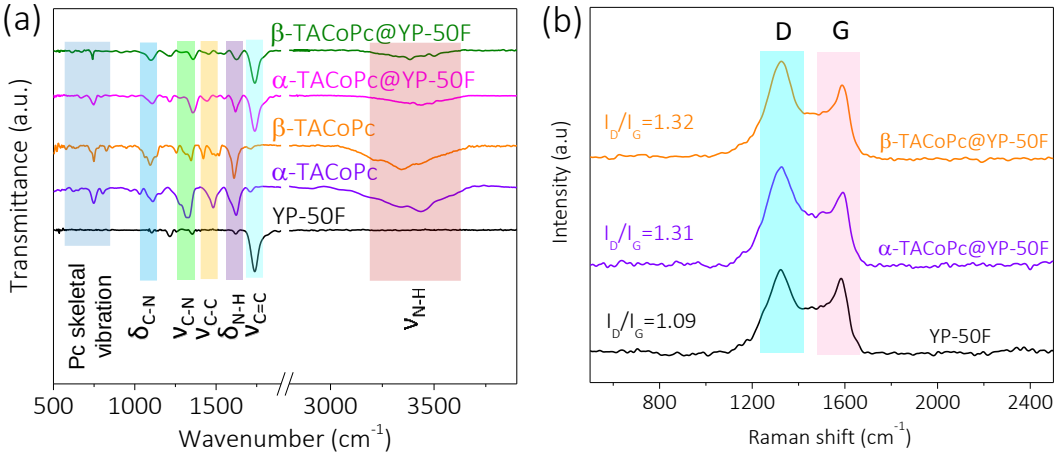


**Figure 6.18:** (a) FTIR spectroscopy and (b) Raman spectroscopy of α-TACoPc@YP-50F and β-TACoPc@YP-50F.

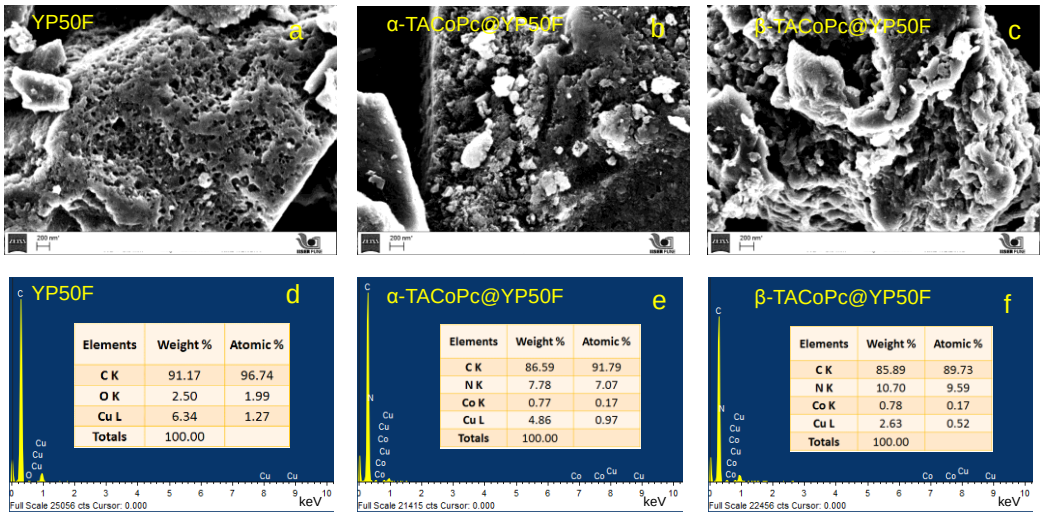


**Figure 6.19:** FESEM images and EDS pattern of (a, d) YP-50F, (b, e) α-TACoPc@YP-50F and (c, f) β-TACoPc@YP-50F. (Cu signal in the EDS is derived from the Cu substrate).

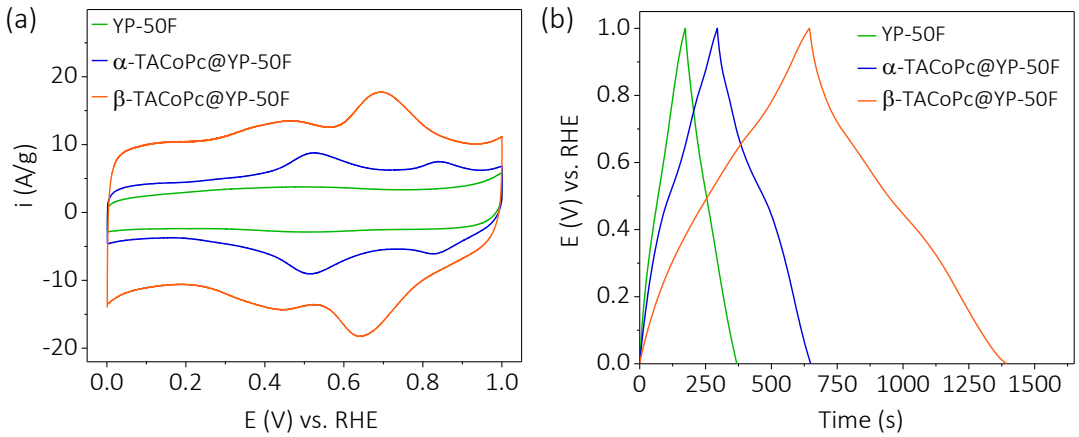


**Figure 6.20:** Charge-discharge characteristics of YP-50F, α-TACoPc@YP-50F and β-TACoPc@YP-50F. (a) Cyclic voltammetry and (b) galvanostatic charge-discharge.

To obtain further insights into the capacitive behavior of the α and β isomers, a comparative electrochemical impedance spectroscopy (EIS) experiments were carried out for the YP50F, α-TACoPc@YP-50F and β-TACoPc@YP-50F electrodes, Figure 6.22a-d. As shown in the inset of Figure 6.22a, the impedimetric behaviour of the best electrode (β-TACoPc@YP-50F) could be fitted with an electrical equivalent circuit, comprising the solution resistance ($R_s$ = 2.61 Ω), a double-layer capacitance ($C_{dl}$ = 78.12 nF), an electron-transfer resistance ($R_{ct1}$ = 9.80 Ω and $R_{ct2}$ = 88.08 Ω), and a constant-phase elements ($CPE_1$ = 8.08 mF with $n_1$= 0.95 and $CPE_2$ = 61.81 mF with $n_2$ = 0.68). The Bode plot (phase angle (degree) vs. log of frequency), Figure 6.22b, indicate that resistive to capacitive switching takes place at a higher frequency for β-TACoPc@YP-50F compared to α-TACoPc@YP-50F which is indicative of better supercapacitor characteristics of the former than the latter. The

characteristic frequency known as "knee" or "onset" frequency ($f_o$) which reflects the power capability of a supercapacitor, was extracted from the frequency corresponding to the maximum of imaginary part of the capacitance (C") in the C" *versus* frequency plot. C" signifies the energy loss associated with a capacitor and in the C" *versus* frequency plot, the maximum of C" is defined as the frontier between a pure capacitive and a pure resistive behavior, Figure 6.22c,d.[15,69,70] $f_o$ decreases in the order β-TACoPc@YP-50F (32 Hz) >> α-TACoPc@YP-50F (9 Hz) >> YP50F (3 Hz). The knee frequency is also the maximum frequency at which the total energy of the supercapacitor can be discharged with an efficiency greater than 50%.[69,70]

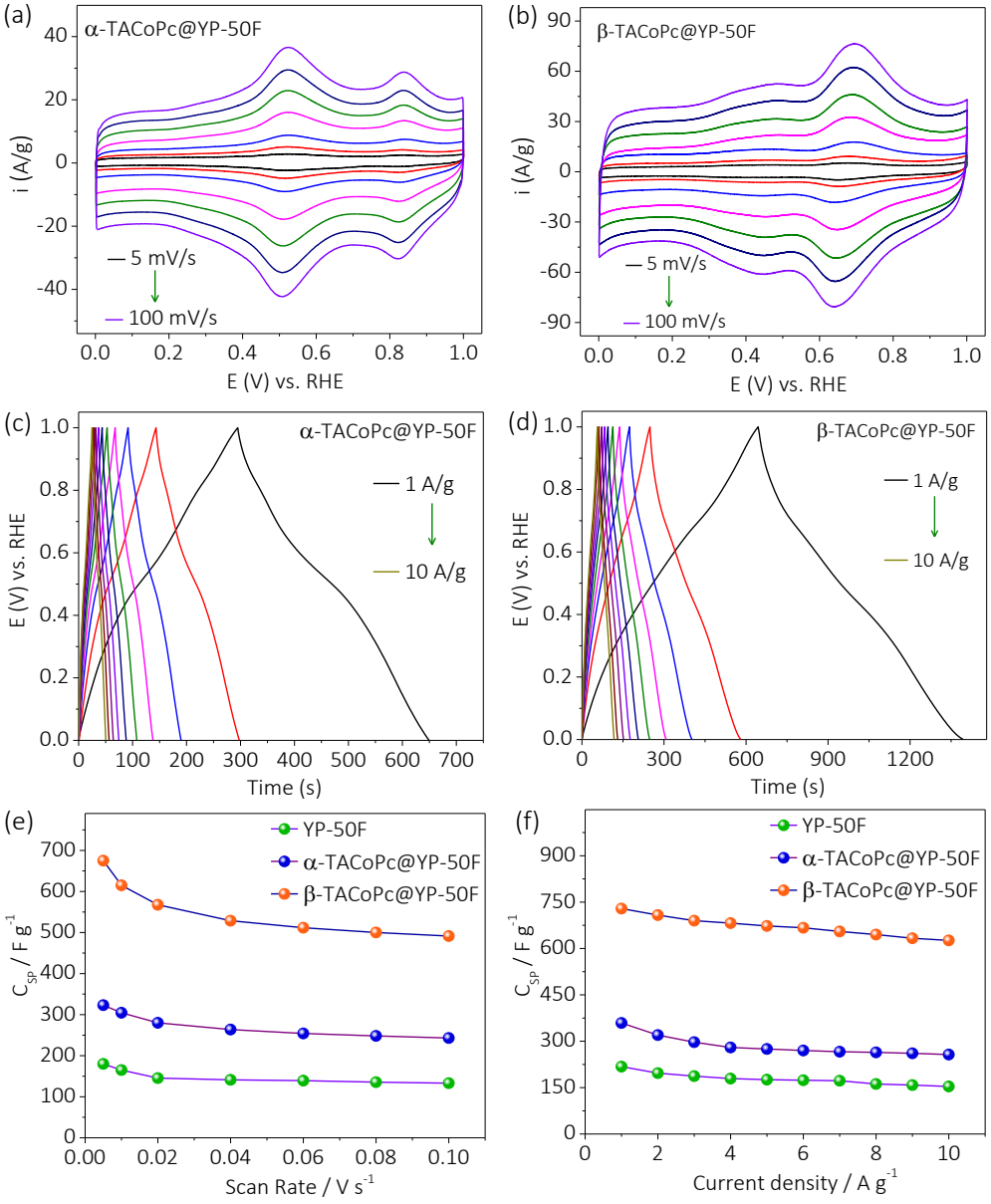


**Figure 6.21:** Charge-discharge characteristics of α-TACoPc@YP-50F and β-TACoPc@YP-50F. (a, b) Cyclic voltammetry, (c, d) galvanostatic charge-discharge profiles, (e) rate profiles

from cyclic voltammetry and (f) rate profiles from galvanostatic charge-discharge.

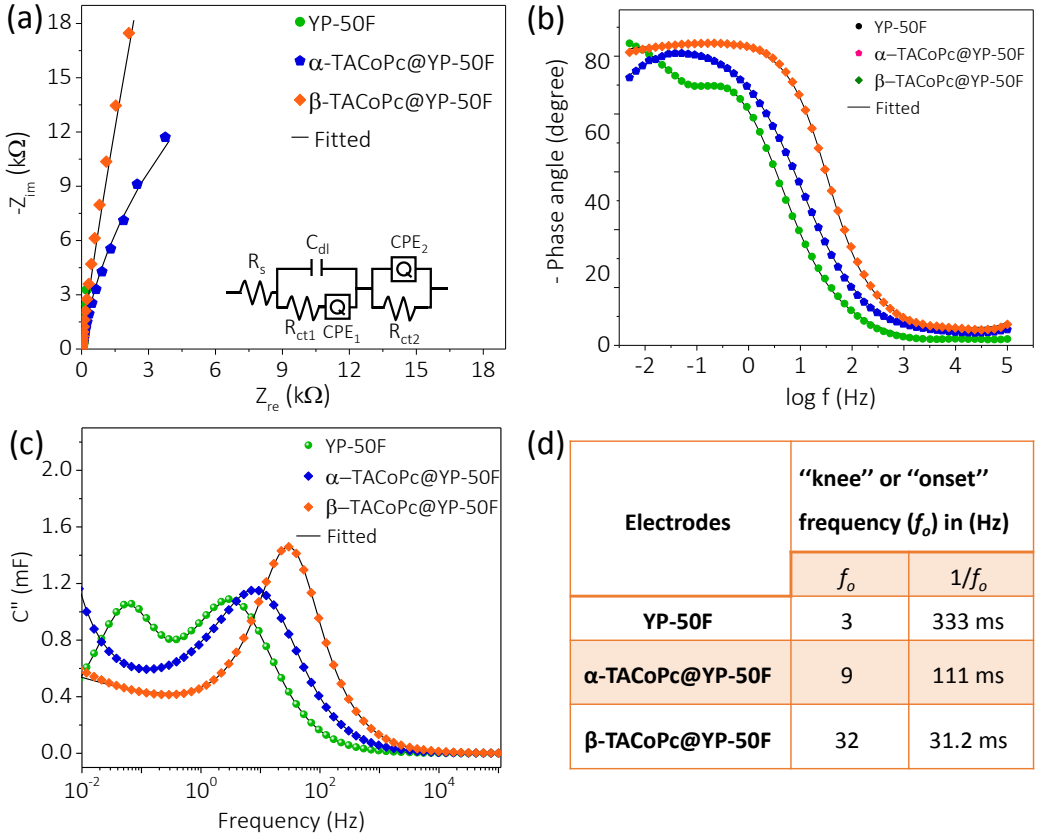


| Electrodes | "knee" or "onset" frequency ($f_o$) in (Hz) | |
|---|---|---|
| | $f_o$ | $1/f_o$ |
| YP-50F | 3 | 333 ms |
| α-TACoPc@YP-50F | 9 | 111 ms |
| β-TACoPc@YP-50F | 32 | 31.2 ms |

**Figure 6.22:** Comparative impedance spectroscopy of YP-50F, α-TACoPc@YP-50F and β-TACoPc@YP-50F electrodes. (a) Nyquist plots at 0 V vs. OCV. Inset: electrical equivalent circuit used in the fitting of the experimental EIS data. (b) Bode plots (phase angle vs. log of frequency), and (c) plot of the imaginary part of capacitance (C") vs. frequency, acquired in the frequency range of 100 kHz and 5 mHz. The amplitude of AC was 10 mV (peak to peak). (d) Knee frequency and relaxation time of YP-50F and its composite electrodes with α-TACoPc and β-TACoPc isomers extracted from Figure 6.22c.

Accordingly, the higher $f_o$ value of the β-TACoPc@YP-50F confirms its higher power capability compared to the α-TACoPc@YP-50F and YP-50F, which is consistent with the comparative CV and charge-discharge data shown in Figure 6.20 and 6.21. The characteristic time constant ($\tau_0=1/f_o$) (also known as the relaxation time) reflects the minimum time required to discharge the capacitor fully [71-73] was also calculated. The shorter $\tau_0$ of the β-isomer compared to α-isomer, Figure 6.22d, suggests a faster response of the former compared to the latter. The self-discharge rate and leakage current were measured (please refer to chapter 2, section 2.12 for more details, pages 55-56) and it suggest a remarkably lowered self-discharge rate and leak currents in the β isomer compared to the α isomer, Figure

6.23a and Table 6.5. The Ragone plot, Figure 6.23b and Table 6.6, indicate that isomerism of amine functionality profoundly influences the charge storage and it improves the energy density of the molecule without compromising the power capability. The stability of the β-TACoPc@YP-50F electrode was examined by continuous cycling at current density 5.6 mA $cm^{-2}$ (10 A/g), Figure 6.23c. Charge-discharge profiles are reasonably stable even after 6000 cycles, indicating that the electrode can be charged and discharged continuously without significant loss in capacitance, Figure 6.23c. Further, the FTIR spectra of β-TACoPc@YP-50F electrode demonstrate that the electrode is durable even after extended cycling for 6000 cycles, Figure 6.23d.

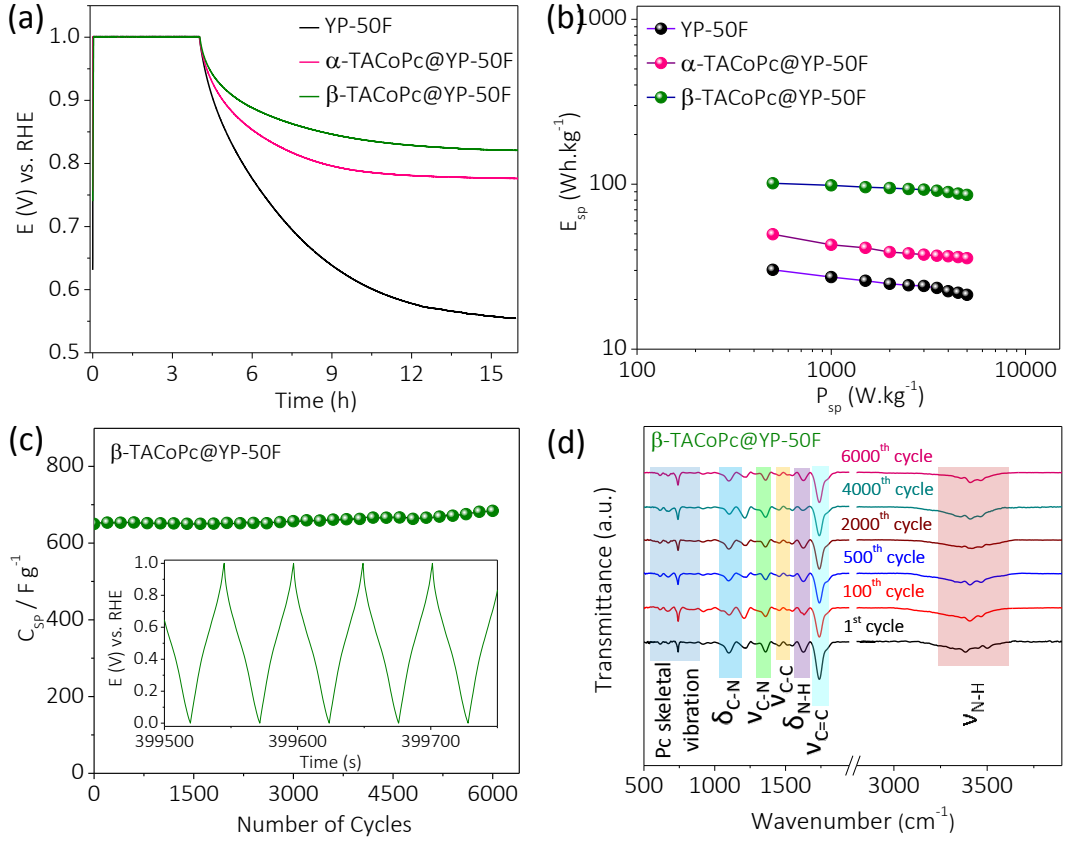


**Figure 6.23:** Comparative electrochemical studies of YP-50F, α-TACoPc@YP-50F and β-TACoPc@YP-50F electrodes. (a) Self-discharge profile and (b) Ragone plot. (c) Variation of specific capacitance with the number of cycles at 5.6 mA/$cm^2$ (10 A/g). Inset is a portion of the charge-discharge curves obtained during the 5$^{th}$ day of repetitive cycling. Supporting electrolyte is $N_2$ saturated 0.5 M $H_2SO_4$. (d) FTIR spectroscopy of β-TACoPc@YP-50F electrodes during extended cycling.

**Table 6.5:** Specific capacitances measured by galvanostatic discharge method at a rate of 1 A/g. Self-discharge currents and leak currents are determined for YP-50F and its composites

with α-TACoPc and β-TACoPc. (Values are extracted from Figure 6.23a).

| Electrode Materials | YP-50F | α-TACoPc@YP-50F | β-TACoPc@YP-50F |
|---|---|---|---|
| Open circuit voltage (OCV) vs. RHE | 0.63 | 0.75 | 0.74 |
| Specific capacitance ($F \cdot g^{-1}$) | 218 | 359 | 729 |
| Self-discharge current (μA) | $30*10^{-3}$ | $23*10^{-3}$ | $19*10^{-3}$ |
| Leakage current ($mA \cdot F^{-1} \cdot V^{-1}$) | $177*10^{-3}$ | $124*10^{-3}$ | $79*10^{-3}$ |

**Table 6.6:** Supercapacitive properties of YP-50F and its composites with α-TACoPc and β-TACoPc determined using the galvanostatic discharge method at a rate of 1 A/g (mass loading per electrode area = ~0.56 mg $cm^{-2}$).

| Electrodes | Specific Capacitance / F $g^{-1}$ | Specific Capacitance / mF $cm^{-2}$ | Specific Power / W $kg^{-1}$ | Specific Energy / W h $kg^{-1}$ |
|---|---|---|---|---|
| YP-50F | 218 | 30 | 500 | 30 |
| α-TACoPc@YP-50F | 359 | 51 | 500 | 50 |
| β-TACoPc@YP-50F | 729 | 103 | 500 | 102 |

(Specific capacitance (mF $cm^{-2}$) values are calculated per geometric area of the electrode).

## 6.3. Conclusions

The work outlined in this chapter demonstrates isomerism dependent charge storage in amino substituted phthalocyanine molecules with the β isomer demonstrating dominant electrochemical capacity over the α isomer. A range of physicochemical characterization point to attractive field effect via intramolecular hydrogen bonding for the suppressed electrochemical capacity in the α isomer that in turn delocalizes the charge density in the Pc ring. When attractive field effect is inhibited by spatially separating the H-bonding groups

via geometrical isomerism, electrochemical capacity is significantly enhanced. Interestingly, repulsive field effect in the isomeric nitro molecules leads only to a geometric rotation of the $–NO_2$ functionality which did not contribute to a disparity in their charge storage. Unveiling the subtle role of non-covalent interactions in conjoining the molecular charge storage with nature as well as isomerism of the functionality opens up an alternative pathway in the design of molecular supercapacitors to target their energy density without compromising the power capability.

## 6.4. References


[1] Noori, A.; El-Kady, M. F.; Rahmanifar, M. S.; Kaner, R. B.; Mousavi, M. F. Towards Establishing Standard Performance Metrics for Batteries, Supercapacitors and beyond. *Chem. Soc. Rev.* **2019**, *48* (5), 1272–1341.

[2] Cong, G.; Wang, W.; Lai, N. C.; Liang, Z.; Lu, Y. C. A High-Rate and Long-Life Organic–oxygen Battery. *Nat. Mater.* **2019**, *18* (4), 390–396.

[3] Dubal, D. P.; Chodankar, N. R.; Kim, D. H.; Gomez-Romero, P. Towards Flexible Solid-State Supercapacitors for Smart and Wearable Electronics. *Chem. Soc. Rev.* **2018**, *47* (6), 2065–2129.

[4] Mourad, E.; Coustan, L.; Lannelongue, P.; Zigah, D.; Mehdi, A.; Vioux, A.; Freunberger, S. A.; Favier, F.; Fontaine, O. Biredox Ionic Liquids with Solid-like Redox Density in the Liquid State for High-Energy Supercapacitors. *Nat. Mater.* **2017**, *16* (4), 446–454.

[5] Schafzahl, L.; Mahne, N.; Schafzahl, B.; Wilkening, M.; Slugovc, C.; Borisov, S. M.; Freunberger, S. A. Singlet Oxygen during Cycling of the Aprotic Sodium–$O_2$ Battery. *Angew. Chemie - Int. Ed.* **2017**, *56* (49), 15728–15732.

[6] Sathiya, M.; Prakash, A. S.; Ramesha, K.; Tarascon, J. M.; Shukla, A. K. $V_2O_5$-Anchored Carbon Nanotubes for Enhanced Electrochemical Energy Storage. *J. Am. Chem. Soc.* **2011**, *133* (40), 16291–16299.

[7] Chmiola, J.; Yushin, G.; Gogotsi, Y.; Portet, C.; Simon, P.; Taberna, P. L. Anomalous Increase in Carbon at Pore Sizes Less than 1 Nanometer. *Science (80).* **2006**, *313* (5794), 1760–1763.

[8] Hassoun, J.; Lee, K. S.; Sun, Y. K.; Scrosati, B. An Advanced Lithium Ion Battery Based on High Performance Electrode Materials. *J. Am. Chem. Soc.* **2011**, *133* (9), 3139–3143.

[9] Miroshnikov, M.; Divya, K. P.; Babu, G.; Meiyazhagan, A.; Reddy Arava, L. M.; Ajayan, P. M.; John, G. Power from Nature: Designing Green Battery Materials from Electroactive Quinone Derivatives and Organic Polymers. *J. Mater. Chem. A* **2016**, *4* (32), 12370–12386.

[10] Ke, Q.; Wang, J. Graphene-Based Materials for Supercapacitor Electrodes – A Review. *J. Mater.* **2016**, *2* (1), 37–54.

[11] Cavaliere, S.; Subianto, S.; Savych, I.; Jones, D. J.; Rozière, J. Electrospinning: Designed Architectures for Energy Conversion and Storage Devices. *Energy Environ. Sci.* **2011**, *4* (12), 4761–4785.

[12] Wang, F.; Wu, X.; Yuan, X.; Liu, Z.; Zhang, Y.; Fu, L.; Zhu, Y.; Zhou, Q.; Wu, Y.; Huang, W. Latest Advances in Supercapacitors: From New Electrode Materials to Novel Device Designs. *Chem. Soc. Rev.* **2017**, *46* (22), 6816–6854.

[13] Zhao, X.; Sánchez, B. M.; Dobson, P. J.; Grant, P. S. The Role of Nanomaterials in Redox-Based Supercapacitors for next Generation Energy Storage Devices. *Nanoscale* **2011**, *3* (3), 839–855.

[14] Wu, Z.; Li, L.; Yan, J. M.; Zhang, X. B. Materials Design and System Construction for Conventional and New-Concept Supercapacitors. *Adv. Sci.* **2017**, *4* (6). 1600382.

[15] Chidembo, A. T.; Ozoemena, K. I.; Agboola, B. O.; Gupta, V.; Wildgoose, G. G.; Compton, R. G. Nickel(ii) Tetra-Aminophthalocyanine Modified MWCNTs as Potential Nanocomposite Materials for the Development of Supercapacitors. *Energy Environ. Sci.* **2010**, *3* (2), 228–236.

[16] Chidembo, A. T.; Ozoemena, K. I. Electrochemical Capacitive Behaviour of Multiwalled Carbon Nanotubes Modified with Electropolymeric Films of Nickel Tetraaminophthalocyanine. *Electroanalysis* **2010**, *22* (21), 2529–2535.

[17] Makgopa, K.; Ejikeme, P. M.; Ozoemena, K. I. Graphene Oxide-Modified Nickel (II) Tetra-Aminophthalocyanine Nanocomposites for High-Power Symmetric Pseudocapacitor. *Electrochim. Acta* **2016**, *212*, 876–882.

[18] Xu, Z.; Li, Z.; Holt, C. M. B.; Tan, X.; Wang, H.; Amirkhiz, B. S.; Stephenson, T.; Mitlin, D. Electrochemical Supercapacitor Electrodes from Sponge-like Graphene Nanoarchitectures with Ultrahigh Power Density. *J. Phys. Chem. Lett.* **2012**, *3* (20), 2928–2933.

[19] Bakandritsos, A.; Chronopoulos, D. D.; Jakubec, P.; Pykal, M.; Čépe, K.; Steriotis, T.; Kalytchuk, S.; Petr, M.; Zbořil, R.; Otyepka, M. High-Performance Supercapacitors Based on a Zwitterionic Network of Covalently Functionalized Graphene with Iron Tetraaminophthalocyanine. *Adv. Funct. Mater.* **2018**, *28* (29), 1–9.

[20] Wang, M.; Shi, H.; Zhang, P.; Liao, Z.; Wang, M.; Zhong, H.; Schwotzer, F.; Nia, A. S.; Zschech, E.; Zhou, S.; Kaskel, S.; Dong, R.; Feng, X. Phthalocyanine-Based 2D Conjugated Metal-Organic Framework Nanosheets for High-Performance Micro-Supercapacitors. *Adv. Funct. Mater.* **2020**, 2002664 (1-7).

[21] Agboola, B. O.; Ozoemena, K. I. Synergistic Enhancement of Supercapacitance upon Integration of Nickel (II) Octa [(3,5-Biscarboxylate)-Phenoxy] Phthalocyanine with SWCNT Phenylamine. *J. Power Sources* **2010**, *195 (12)*, 3841–3848.

[22] Mu, J.; Shao, C.; Guo, Z.; Zhang, M.; Zhang, Z.; Zhang, P.; Chen, B.; Liu, Y. Solvothermal Synthesis and Electrochemical Properties of 3D Flower-like Iron Phthalocyanine Hierarchical Nanostructure. *Nanoscale* **2011**, *3 (12)*, 5126–5131.

[23] Madhuri, K. P.; John, N. S. Supercapacitor Application of Nickel Phthalocyanine Nanofibres and Its Composite with Reduced Graphene Oxide. *Appl. Surf. Sci.* **2018**, *449*, 528–536.

[24] Lu, Y.; Zheng, Q.; Wu, J.; Yu, Y. Enhanced Electrochemical Charge Storage Performance by Doping of Copper Phthalocyanine-3,4′,4″,4‴-Tetrasulfonic Acid Tetrasodium Salt into Polypyrrole/multi-Walled Carbon Nanotubes 3D-Nanostructured Electrodes. *Electrochim. Acta* **2018**, *265*, 594–600.

[25] Ramachandran, R.; Hu, Q.; Wang, F.; Xu, Z. X. Synthesis of N-CuMe 2 Pc Nanorods/Graphene Oxide Nanocomposite for Symmetric Supercapacitor Electrode with Excellent Cyclic Stability. *Electrochim. Acta* **2019**, *298*, 770–777.

[26] Taşaltln, N.; Taşaltln, C.; Aydln, H.; Şahintürk, U.; Gürek, A. G. Hexylsulfanyl-Substituted CoPc and GO-CoPc on Ni Foam as Electroactive Material for Supercapacitors. *J. Porphyr. Phthalocyanines* **2019**, *23 (11–12)*, 1616–1621.

[27] Alzeer, J.; Roth, P. J. C.; Luedtke, N. W. An Efficient Two-Step Synthesis of Metal-Free Phthalocyanines Using a Zn (II) Template. *Chem. Commun.* **2009**, No. 15, 1970.

[28] Al-lami, A. K.; Majeed, N. N.; Al-mowali, A. H. Synthesis, Mesomorphic and Molar Conductivity Studies of Some Macrocyclic Phthalocyanine Palladium (II). *Chemistry and Materials Research*. **2013**, *3* (4), 59–68.

[29] Trollund, E.; Ardiles, P. Spectroelectrochemical and Electrical Characterization of Poly (Cobalt Tetraminophthalocyanine)-Modified Electrodes : Electrocatalytic Oxidation of Hydrazine. *Polyhedron* **2000**, *19*, 2303–2312.

[30] Cidlina, A.; Novakova, V.; Miletin, M.; Zimcik, P. Peripheral Substitution as a Tool for Tuning Electron-Accepting Properties of Phthalocyanine Analogs in Intramolecular Charge Transfer. *Dalton Trans.* **2015**, *44*, 6961–6971.

[31] Yarasir, M. N.; Kandaz, M.; Güney, O.; Salih, B. Synthesis and Photophysical Properties of Metallophthalocyanines Substituted with a Benzofuran Based Fluoroprobe. *Spectrochim. Acta - Part A Mol. Biomol. Spectrosc.* **2012**, *93*, 379–383.

[32] Panwar, V.; Kumar, P.; Ray, S. S.; Jain, S. L. Organic Inorganic Hybrid Cobalt Phthalocyanine / Polyaniline as Efficient Catalyst for Aerobic Oxidation of Alcohols in Liquid Phase. *Tetrahedron Lett.* **2015**, *56* (25), 3948–3953.

[33] Kobayashi, N.; Miwa, H.; Nemykin, V. N. Adjacent versus Opposite Type Di-Aromatic Ring-Fused Phthalocyanine Derivatives: Synthesis, Spectroscopy, Electrochemistry, and Molecular Orbital Calculations. *J. Am. Chem. Soc.* **2002**, *124* (27), 8007–8020.

[34] Ogunsipe, A.; Nyokong, T. Effects of Substituents and Solvents on the Photochemical Properties of Zinc Phthalocyanine Complexes and Their Protonated Derivatives. *J. Mol. Struct.* **2004**, *689* (1-2), 89–97.

[35] Moinuddin Khan, M. H.; Venugopala Reddy, K. R.; Keshavayya, J.; Fasiulla; Raghavendra, S. Synthesis, Characterizations and Biological Studies of Symmetrically Substituted 2, 9, 16, 23-Tetra-Hydroxyphenylimino Phthalocyanine Complexes. *Green Chem. Lett. Rev.* **2009**, *2* (2), 77–85.

[36] Mugadza, T.; Nyokong, T. Synthesis, Characterization and the Electrocatalytic Behaviour of Nickel (II) Tetraamino-Phthalocyanine Chemically Linked to Single Walled Carbon Nanotubes. *Electrochim. Acta* **2010**, *55* (20), 6049–6057.

[37] Mugadza, T.; Nyokong, T. Synthesis and Characterization of Electrocatalytic Conjugates of Tetraamino Cobalt (II) Phthalocyanine and Single Wall Carbon Nanotubes. *Electrochim. Acta* **2009**, *54* (26), 6347–6353.

[38] Madhuri, K. P.; John, N. S. Solution Processable Transition Metal Phthalocyanine Nanofibres. *ChemistrySelect* **2019**, *4* (24), 7292–7299.

[39] Georgescu, R.; Boscornea, C.; Calinescu, I.; State, R. Raman, IR and UV-Vis Spectroscopic Investigations of Some Substituted Phthalocyanines *Rev. Chim.* **2016**, *10,* 1554-1557

[40] Amatore, C.; Oleinick, A. I.; Svir, I. Diffusion from within a Spherical Body with Partially Blocked Surface: Diffusion through a Constant Surface Area. *ChemPhysChem* **2010**, *11* (1), 149–158.

[41] Janek, R. P.; Fawcett, W. R.; Ulman, A. Impedance Spectroscopy of Self-Assembled Monolayers on Au (111): Sodium Ferrocyanide Charge Transfer at Modified Electrodes. *Langmuir* **1998**, *14* (111), 3011–3018.

[42] Fleming, B. D.; Praporski, S.; Bond, A. M.; Martin, L. L. Electrochemical Quartz Crystal Microbalance Study of Azurin Adsorption onto an Alkanethiol Self-Assembled Monolayer on Gold. *Langmuir* **2008**, *24* (1), 323–327.

[43] Viana, A. S.; Kalaji, M.; Abrantes, L. M. Electrochemical Quartz Crystal Microbalance Study of Self-Assembled Monolayers and Multilayers of Ferrocenylthiol Derivatives on Gold. *Langmuir* **2003**, *19* (22), 9542–9544.

[44] Nakano, K.; Yoshitake, T.; Yamashita, Y.; Bowden, E. F. Cytochrome c Self-Assembly on Alkanethiol Monolayer Electrodes as Characterized by AFM, IR, QCM, and Direct Electrochemistry. *Langmuir* **2007**, *23* (11), 6270–6275.

[45] Makinde, Z. O.; Louzada, M.; Mashazi, P.; Nyokong, T.; Khene, S. Electrocatalytic Behaviour of Surface Confined Pentanethio Cobalt (II) Binuclear Phthalocyanines towards the Oxidation of 4- Chlorophenol. *Appl. Surf. Sci.* **2017,** 425**,** 702-712.

[46] Kottaichamy, A. R.; Begum, S.; Devendrachari, M. C.; Bhat, Z. M.; Thimmappa, R.; Nimbegondi Kotresh, H. M.; Vinod, C. P.; Thotiyl, M. O. Geometrical Isomerism Directed Electrochemical Sensing. *Anal. Chem.* **2020**, *92* (6), 4541–4547.

[47] Kottaichamy, A. R.; Begum, S.; Nazrulla, M. A.; Dargily, N. C.; Devendrachari, M. C.; Manzoor Bhat, Z.; Thimmappa, R.; Makri Nimbegondi Kotresh, H.; Vinod, C. P.; Thotiyl, M. O. Unprecedented Isomerism-Activity Relation in Molecular Electrocatalysis. *J. Phys. Chem. Lett.* **2020**, *11* (1), 263–271.

[48] Nyoni, S.; Nyokong, T. Electrocatalytic Behahiour of Cobalt Tetraamino-Phthalocyanine in the Presence of a Composite of Reduced Graphene Nanosheets and of Multi-Walled Carbon Nanotubes. *Electrochim. Acta* **2014**, *136*, 240–249.

[49] Obirai, J.; Nyokong, T. Synthesis, Spectral and Electrochemical Characterization of Mercaptopyrimidine-Substituted Cobalt, Manganese and Zn (II) Phthalocyanine Complexes. *Electrochim. Acta* **2005**, *50* (16-17), 3296–3304.

[50] Obirai, J.; Nyokong, T. Synthesis, Electrochemical and Electrocatalytic Behaviour of Thiophene-Appended Cobalt, Manganese and Zinc Phthalocyanine Complexes. *Electrochim. Acta* **2005**, *50* (27), 5427–5434.

[51] Sehlotho, N.; Nyokong, T. Electrocatalytic Oxidation of Thiocyanate, L-Cysteine and 2-Mercaptoethanol by Self-Assembled Monolayer of Cobalt Tetraethoxy Thiophene Phthalocyanine. *Electrochim. Acta* **2006**, *51* (21), 4463–4470.

[52] G. A. Jeffrey, An Introduction to Hydrogen Bonding, *Oxford University Press, Oxford,* **1997**.

[53] Thomas, S. The Hydrogen Bond in the Solid State. *Angew. Chemie Int. Ed.* **2002**, *41* (1), 48–76.

[54] S. Scheiner, Hydrogen Bonding. A Theoretical Perspective, *Oxford University Press, Oxford,* **1997**.

[55] Cong, F.; Ning, B.; Du, X.; Ma, C.; Yu, H.; Chen, B. Facile Synthesis, Characterization and Property Comparisons of Tetraaminometallo phthalocyanines with and without Intramolecular Hydrogen Bonds. *Dye. Pigment.* **2005**, *66*, 1–6.

[56] Zhang, X. F.; Li, X.; Niu, L.; Sun, L.; Liu, L. Charge Transfer Photophysics of Tetra(α-Amino) Zinc Phthalocyanine. *J. Fluoresc.* **2009**, *19* (6), 947–954.

[57] Froimowicz, P.; Zhang, K.; Ishida, H. Intramolecular Hydrogen Bonding in Benzoxazines: When Structural Design Becomes Functional. *Chem. - A Eur. J.* **2016**, *22* (8), 2691–2707.

[58] Che, P.; Lu, F.; Nie, X.; Huang, Y.; Yang, Y.; Wang, F.; Xu, J. Hydrogen Bond Distinction and Activation upon Catalytic Etherification of Hydroxyl Compounds. *Chem. Commun.* **2015**, *51* (6), 1077–1080.

[59] Luo, Y.; Ma, H.; Sun, Y.; Che, P.; Nie, X.; Wang, T.; Xu, J. Understanding and Measurement for the Binding Energy of Hydrogen Bonds of Biomass-Derived Hydroxyl Compounds. *J. Phys. Chem. A* **2018**, *122* (3), 843–848.

[60] Aristov, V. Y.; Molodtsova, O. V.; Maslyuk, V. V.; Vyalikh, D. V.; Bredow, T.; Mertig, I.; Preobrajenski, A. B.; Knupfer, M. Electronic Properties of Potassium-Doped FePc. *Org. Electron.* **2010**, *11* (8), 1461–1468.

[61] Mthethwa, T.; Antunes, E.; Nyokong, T. Photophysical Properties of a New Water Soluble Tetra Thiamine Substituted Zinc Phthalocyanine Conjugated to Gold Nanorods of Different Aspect Ratios. *Dalt. Trans.* **2014**, *43* (22), 8230–8240.

[62] Haidu, F.; Gordan, O. D.; Zahn, D. R. T.; Smykalla, L.; Hietschold, M.; Senkovskiy, B. V.; Mahns, B.; Knupfer, M. Electronic Structure of Manganese Phthalocyanine Modified via Potassium Intercalation: A Comprehensive Experimental Study. *arXiv:1702.03575 [physics.chem-ph]* **2017**.

[63] Le, Z.; Liu, F.; Nie, P.; Li, X.; Liu, X.; Bian, Z.; Chen, G.; Wu, H. Bin; Lu, Y. Pseudocapacitive Sodium Storage in Mesoporous Single-Crystal-like TiO2-Graphene Nanocomposite Enables High-Performance Sodium-Ion Capacitors. *ACS Nano* **2017**, *11* (3), 2952–2960.

[64] Dou, Q.; Liu, L.; Yang, B.; Lang, J.; Yan, X. Silica-Grafted Ionic Liquids for Revealing the Respective Charging Behaviors of Cations and Anions in Supercapacitors. *Nat. Commun.* **2017**, *8* (1).

[65] Merlet, C.; Rotenberg, B.; Madden, P. A.; Taberna, P. L.; Simon, P.; Gogotsi, Y.; Salanne, M. On the Molecular Origin of Supercapacitance in Nanoporous Carbon Electrodes. *Nat. Mater.* **2012**, *11* (4), 306–310.

[66] Zhu, J.; Li, Y.; Chen, Y.; Wang, J.; Zhang, B.; Zhang, J.; Blau, W. J. Graphene Oxide Covalently Functionalized with Zinc Phthalocyanine for Broadband Optical Limiting. *Carbon N. Y.* **2011**, *49 (6)*, 1900–1905.

[67] Zhang, X.; Wu, Z.; Zhang, X.; Li, L.; Li, Y.; Xu, H.; Li, X.; Yu, X.; Zhang, Z.; Liang, Y.; Wang, H. Highly Selective and Active CO2 Reduction Electrocatalysts Based on Cobalt Phthalocyanine/carbon Nanotube Hybrid Structures. *Nat. Commun.* **2017**, *8*, 14675.

[68] Shrestha, M.; Amatya, I.; Wang, K.; Zheng, B.; Gu, Z.; Fan, Q. H. Electrophoretic Deposition of Activated Carbon YP-50 with Ethyl Cellulose Binders for Supercapacitor Electrodes. *J. Energy Storage* **2017**, *13*, 206–210.

[69] Purkait, T.; Singh, G.; Kumar, D.; Singh, M.; Dey, R. S. High-Performance Flexible Supercapacitors Based on Electrochemically Tailored Three-Dimensional Reduced Graphene Oxide Networks. *Sci. Rep.* **2018**, *8* (1), 1–13.

[70] Sheng, K.; Sun, Y.; Li, C.; Yuan, W.; Shi, G. Ultrahigh-Rate Supercapacitors Based on Eletrochemically Reduced Graphene Oxide for Ac Line-Filtering. *Sci. Rep.* **2012**, *2*, 3–7.

[71] Yang, K.; Cho, K.; Kim, S. Effect of Carbon Black Addition on Thermal Stability and Capacitive Performances of Supercapacitors. *Sci. Rep.* **2018**, *8* (1), 1–7.

[72] Taberna, P. L.; Simon, P.; Fauvarque, J. F. Electrochemical Characteristics and Impedance Spectroscopy Studies of Carbon-Carbon Supercapacitors. *J. Electrochem. Soc.* **2003**, *150* (3), A292.

[73] Yoo, Y.; Kim, M. S.; Kim, J. K.; Kim, Y. S.; Kim, W. Fast-Response Supercapacitors with Graphitic Ordered Mesoporous Carbons and Carbon Nanotubes for AC Line Filtering. *J. Mater. Chem. A* **2016**, *4* (14), 5062–5068.

# Chapter 7

## Conclusions

In essence the work outlined in this thesis uncovers an isomerism-catalytic activity relation and an isomerism-charge storage relation in molecular systems. Specifically, while the nature of the substituent plays a central part in tuning the electrocatalysis and charge storage, its isomerism-induced contribution undeniably offers a unique pathway for utilizing the maximum potential of the molecule for challenging electrochemical transformations and charge storage applications. Further, the structure-activity relations of molecules will be incomplete if one neglects this isomerism induced contribution because as demonstrated they are too significant to be neglected. It is to be noted that the effect cannot be generalized across the spectrochemical series as this relation is substituent specific. This indeed demands insightful studies about each substituent at a molecular level to understand their substituent specific isomerism–catalytic activity/charge storage relation. This is mainly because, often non-covalent interactions interconnects the electrochemical properties of the molecule with the nature of the functionality as well as its isomerism, and such interactions are often substituent specific which offers a plethora of opportunities for researchers working in the domain of molecular electrocatalysis and molecular charge storage. The uncovering of isomerism-activity relation in $N_4$-macrocyclic molecules is expected to fill the inadequacies and knowledge gap in their structure-activity relations which will immensely contribute to the development of next generation electrodes for energy conversion, electrocatalysis, bio-sensing, and energy storage.

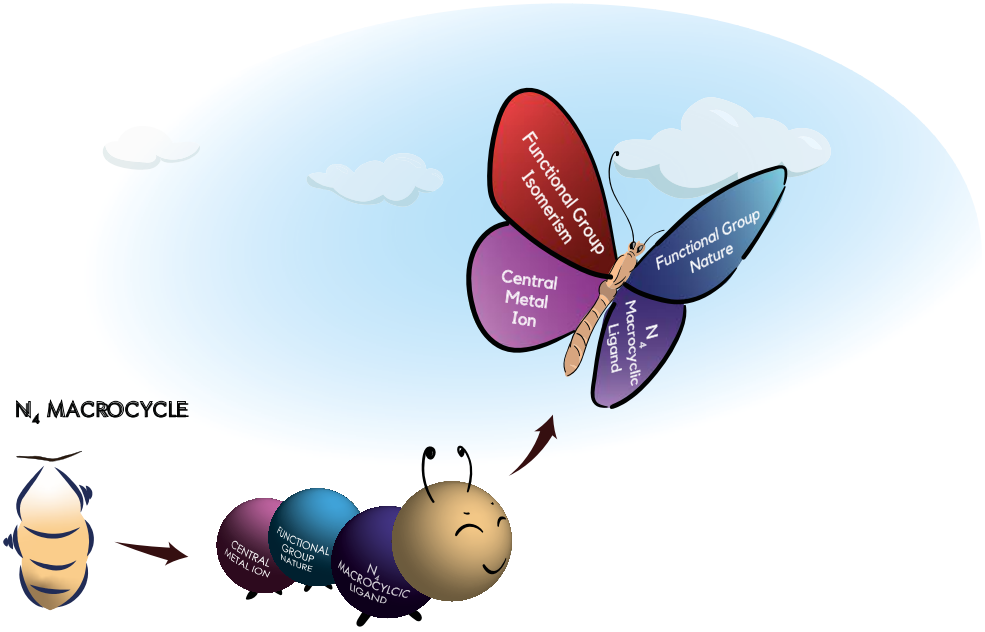


A bird's eye view of isomerism-activity relation in molecular electrocatalysis and molecular charge storage.

# List of Publications


[1] Unprecedented Isomerism–Activity Relation in Molecular Electrocatalysis. **Alagar Raja K.;** Shabbah B.; Mohammed Azeezulla N.; Neethu C. D.; Mruthyunjayachari C. D.; Zahid M. Bhat; Ravikumar T.; Harish M. N. K.; Vinod C.P. and Musthafa O. T. *J. Phys. Chem. Lett.* **2020**, *11*, 263–271.

[2] Geometrical Isomerism Directed Electrochemical Sensing **Alagar Raja K.;** Shabbah B.; Mruthyunjayachari C. D.; Zahid M. Bhat; Ravikumar T.; Harish M. N. K.; Vinod C.P. and Musthafa O. T. *Anal. Chem.* **2020**, *92, 6,* 4541-4547.

[3] Effects of electrochemical tailoring of monolayers on a catalytic redox entity: An ON–OFF phenomenon regulated by the surrounding medium. **Alagar Raja K.;** Kotresh, H. M. N.; Devendrachari, M. C.; Thimmappa, R.; Paswan, B.; Tiwari, O.; Chanda, V.; Gaikwad, P.; Thotiyl, M. O. *Journal of Physical Chemistry C* **2015**, *119*, 28276-28284.

[4] Isomerism-Activity Relation in Molecular Electrocatalysis: A Perspective Sanchayita M.[†]; **Alagar Raja K.[†];** Manzoor Bhat, Z.; Neethu C. D.; Thotiyl, M. O. *Electroanalysis* **2020**, *32 (11)*, 2387-2392.

[5] An Electrochemical Neutralization Cell for Spontaneous Water Desalination Manzoor Bhat, Z.; Deepraj P.; Shane A.; Thimmappa, R.; **Alagar Raja K.;** Neethu C. D.; Devendrachari, M. C. Musthafa O. T. *Joule* **2020**, *4*, 1–13.

[6] A Rechargeable Hydrogen Battery. Neethu C. D., Thimmappa, R.; Manzoor Bhat, Z.; Devendrachari, M. C.; **Alagar Raja K.;** Gautam M.; Shafi, S. P. and Thotiyl, M. O. *The Journal of Physical Chemistry Letters* **2018**, 9 (10), 2492–2497.

[7] Fuel exhaling fuel cell. Manzoor Bhat, Z.; Thimmappa, R.; Devendrachari, M. C.; **Alagar Raja K.;** Shafi, S. P.; Varhade, S.; Gautam, M. and Thotiyl, M. O. *The Journal of Physical Chemistry Letters* **2018**, *9*, 388-392.

[8] A direct alcohol fuel cell driven by an outer sphere positive electrode. Manzoor Bhat, Z.; Thimmappa, R.; Devendrachari, M. C.; Shafi, S. P.; Aralekallu, S.; **Alagar Raja K.;** Gautam, M. and Thotiyl, M. O. *The Journal of Physical Chemistry Letters* **2017**, *8*, 3523-3529.

[9] Metal Coordination Polymer Framework Governed by Heat of Hydration for Noninvasive Differentiation of Alkali Metal Series. Battu S.; Itagi M.; Manzoor Bhat,

Z.; Khiare, S.; **Alagar Raja K.;** Lokesh K. S.; Thimmappa, R. and Thotiyl, M. O. *Analytical Chemistry* 2018, *90 (21)*, 12917–12922.

[10] A zinc-quinone Battery for Paired Hydrogen Peroxide Electrosynthesis. Sudhakara, S.M.; Zahid M. Bhat; Mruthyunjayachari C. D.; **Alagar Raja K.;** Mahesh Itagi; Ravikumar T.; Khan, F.; Harish M. N. K. and Musthafa O. T. *Journal of Colloid and Interface Science* **2020**, *559, 324–330.*

[11] Hydrogen Fuel Exhaling Zn-Ferricyanide Redox Flow Battery. Thamaraichelvan, M.; Manzoor Bhat, Z.; Thimmappa, R.; Devendrachari, M. C.; **Alagar Raja K.;** Venkata Narayanan N. S. and Musthafa O. T. *ACS Sustainable Chem. Eng.,* **2019**, *7, 19,* 16241–16246.

[12] Hexaaminobenzene Derived Two-Dimensional Polymer Supercapacitor with High Specific Capacitance and Energy Density Vivek C. W.; **Alagar Raja K.;** Aakash D. N.; Kayaramkodath C. R.; Mohammed A. N.; Musthafa O. T.; Sukumaran S. Babu *ACS Appl. Energy Mater.* **2020**, *3(7),* 6352–6359.

[13] Proton-Conducting Graphene Membrane Electrode Assembly for High Performance Hydrogen Fuel Cells. Thimmappa, R.; Gautam M.; Devendrachari, M. C.; **Alagar Raja K.;** Manzoor Bhat, Z.; Ahmed Umar and Musthafa O. T. *ACS Sustainable Chem. Eng.,* **2019**, *7*, 14189–14194.

[14] A Zinc Battery Driven by an Electro-organic Reactor Cathode. Itagi M.; Battu S.; Devendrachari, M. C.; Manzoor Bhat, Z.; **Alagar Raja K.;** Pandit D.; Gautam M.; Thimmappa, R.; Lokesh K. S. and Thotiyl, M. O. *ACS Sustainable Chem. Eng.,* **2018**, *6 (11),* 15007–15014.

[15] A Rechargeable Aqueous Sodium Ion Battery. Thimmappa, R.; Gautam M.; Aralekallu, S.; Devendrachari, M. C.; **Alagar Raja K.;** Manzoor Bhat, Z. and Musthafa O. T. *ChemElectroChem* **2019**, *6*, 1371–1375.

[16] An Electrochemical Wind Velocity Sensor. Khiare, S.; Gaikwad, P.; Devendrachari, M. C.; **Alagar Raja K.;** Manzoor Bhat, Z.; Varhade, S.; Shafi, S. P.; Thimmappa, R. and Thotiyl, M. O. *Analytical Chemistry* **2018**, 90 (7), 4501–4506.

[17] A pH dependent high voltage aqueous supercapacitor with dual electrolytes. Sur S.; **Alagar Raja K.;** Manzoor Bhat, Z.; Devendrachari, M. C.; Thimmappa and R.; Thotiyl, M. O. *Chemical Physics Letters*, **2018**, *712,* 160–164.

[18] A Hybrid Hydrazine Redox Flow Battery with a Reversible Electron Acceptor. Swapnil V., Manzoor Bhat, Z.; Devendrachari, M. C.; **Alagar Raja K.;** Gautam M.; Shafi, S. P.; Kalegowda Y. and Thotiyl, M. O. *Phys. Chem. Chem. Phys.*, **2018**, 20, 21724.

[19] A Vitamin C Fuel Cell with a Non-Bonded Cathodic Interface. Devendrachari, M. C.; Thimmappa, R.; Manzoor Bhat, Z.; Shafi, S. P.; Harish M. N. K., **Alagar Raja K.;** Kallam R. V. Reddy and Thotiyl, M. O. *Sustainable Energy Fuels*, **2018**, 2, 1813.

[20] An Inherent Heat Driven Fuel Exhaling Hydrazine Fuel Cell. Swapnil V., Manzoor Bhat, Z.; Devendrachari, M. C.; **Alagar Raja K.;** Khiare, S.; Shafi, S. P. and Thotiyl, M. O. *Chemical Physics Letters,* **2018**, 706, 553–557.

[21] An All Solid-State Zinc–Air Battery with a Corrosion-Resistant Air Electrode. Devendrachari, M. C.; Chidananda B., Zahid M. Bhat, Kotresh, H. M.; **Alagar Raja K.;** Swapnil V., Khiare, S.; Kallam R. V. Reddy and Thotiyl, M. O. *ChemElectroChem* **2018**, 5, 1–6.

[22] An interface-controlled redox switch for wastewater remediation. Khaire, S.; Gaikwad, P.; Aralekallu, S.; Manzoor Bhat, Z.; **Alagar Raja K.;** Devendrachari, M. C.; Thimmappa, R.; Shafi, S. P.; Gautam, M. and Thotiyl, M. O. *ChemElectroChem* **2018,** 5, 362 – 366.

[23] A redox-active electrochemical decoder. Gaikwad, P.; Misal, M.; Khiare, S.; Raafik, A.; Aralekallu, S.; Varhade, S.; Manzoor Bhat, Z.; **Alagar Raja K.;** Devendrachari, M. C.; Gautam, M. and Thotiyl, M. O. *Advanced Materials Technologies* **2018**, 3*(4),* 1700337.

[24] Proton exchange membrane fuel cell with a Pt-free cathode and a freely diffusing electron acceptor. Thimmappa, R.; **Alagar Raja K.;** Devendrachari, M. C.; Aralekallu, S.; Shafi, S. P.; Gautam, M.; Kotresh, H. M. N. and Thotiyl, M. O. *ChemElectroChem* **2017**, *4*, 283-286.

[25] 2.6 V Aqueous Battery with a Freely Diffusing Electron Acceptor. Thimmappa, R.; Devendrachari, M. C. ; **Alagar Raja K.;** Aralekallu, S.; Gautam, M.; Shafi, S. P.; Bhat, Z. M. and Thotiyl, M. O. *Journal of Physical Chemistry C* **2017**, *121*, 3707-3713.

[26] Redox active binary logic gate circuit for homeland security. Gaikwad, P.; Kadlag, K.; Nambiar, M.; Devendrachari, M. C.; Aralekallu, S.; **Alagar Raja K.;** Manzoor Bhat, Z.; Thimmappa, R.; Shafi, S. P. and Thotiyl, M. O. *Analytical Chemistry* **2017**, *89*, 7893-7899.

[27] A single chamber direct methanol fuel cell. Thimmappa, R.; Aralekallu, S.; Devendrachari, M. C.; **Alagar Raja K.;** Manzoor Bhat, Z.; Shafi, S. P.; Lokesh, K. S. and Thotiyl, M. O. *Advanced Materials Interfaces* **2017**, *4*, 1700321.

[28] Anisotropic amplification of proton transport in proton exchange membrane fuel cells. Thimmappa, R.; Fawaz, M.; Devendrachari, M. C.; Gautam, M.; **Alagar Raja K.;** Shafi, S. P. and Thotiyl, M. O. *Chemical Physics Letters* **2017**, *679*, 1-5.

[29] Polarity governed selective amplification of through plane proton shuttling in proton exchange membrane fuel cells. Gautam, M.; Devendrachari, M. C.; Thimmappa, R.; **Alagar Raja K.;** Shafi, S. P.; Gaikwad, P.; Kotresh, H. M. N. and Thotiyl, M. O. *Physical Chemistry Chemical Physics* **2017**, *19*, 7751-7759.

[30] Tuning the Interfacial Chemistry of Redox-Active Polymer for Bifunctional Probing. Aralekallu, S.; Thimmappa, R.; Gaikwad, P.; Devendrachari, M. C.; **Alagar Raja K.;** Shafi, S. P.; Lokesh, K. S.; Sánchez, J. and Thotiyl, M. O. *ChemElectroChem* **2017**, *4*, 692-700.

[31] Stereochemistry-dependent proton conduction in proton exchange membrane fuel cells. Thimmappa, R.; Devendrachari, M. C.; **Alagar Raja K.;** Tiwari, O.; Gaikwad, P.; Paswan, B. and Thotiyl, M. O. *Langmuir* **2016**, *32*, 359-365.

[32] Galvanic cell type sensor for soil moisture analysis. Gaikwad, P.; Devendrachari, M. C.; Thimmappa, R.; Paswan, B.; **Alagar Raja K.;** Kotresh, H. M. N. and Thotiyl, M. O. *Analytical Chemistry* **2015**, *87*, 7439-7445.

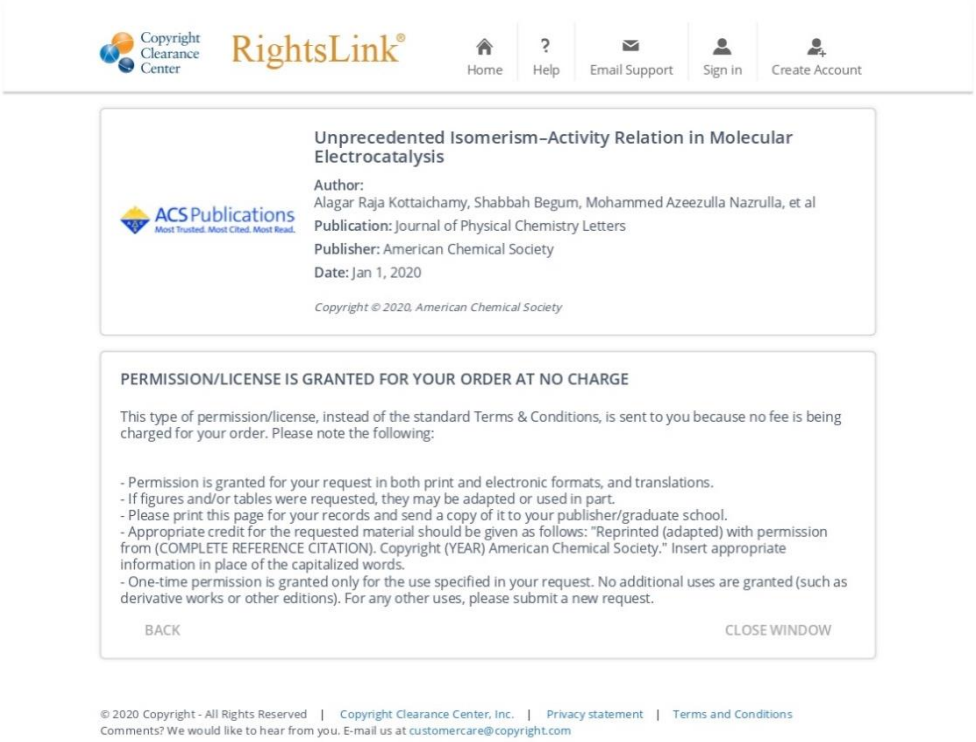

Copyright Clearance Center RightsLink®

Home | Help | Email Support | Sign in | Create Account

ACS Publications
Most Trusted. Most Cited. Most Read.

**Unprecedented Isomerism–Activity Relation in Molecular Electrocatalysis**

**Author:**
Alagar Raja Kottaichamy, Shabbah Begum, Mohammed Azeezulla Nazrulla, et al

**Publication:** Journal of Physical Chemistry Letters

**Publisher:** American Chemical Society

**Date:** Jan 1, 2020

*Copyright © 2020, American Chemical Society*

**PERMISSION/LICENSE IS GRANTED FOR YOUR ORDER AT NO CHARGE**

This type of permission/license, instead of the standard Terms & Conditions, is sent to you because no fee is being charged for your order. Please note the following:

- Permission is granted for your request in both print and electronic formats, and translations.
- If figures and/or tables were requested, they may be adapted or used in part.
- Please print this page for your records and send a copy of it to your publisher/graduate school.
- Appropriate credit for the requested material should be given as follows: "Reprinted (adapted) with permission from (COMPLETE REFERENCE CITATION). Copyright (YEAR) American Chemical Society." Insert appropriate information in place of the capitalized words.
- One-time permission is granted only for the use specified in your request. No additional uses are granted (such as derivative works or other editions). For any other uses, please submit a new request.

BACK CLOSE WINDOW

© 2020 Copyright - All Rights Reserved | Copyright Clearance Center, Inc. | Privacy statement | Terms and Conditions
Comments? We would like to hear from you. E-mail us at customercare@copyright.com

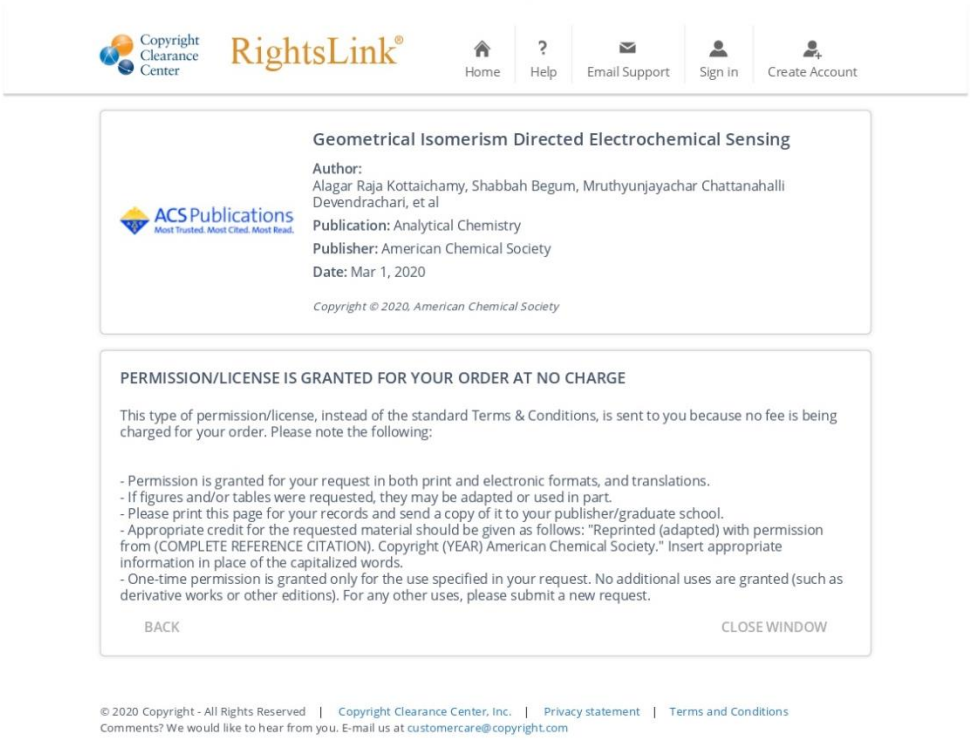

Copyright Clearance Center RightsLink®

Home | Help | Email Support | Sign in | Create Account

**Geometrical Isomerism Directed Electrochemical Sensing**

**Author:**
Alagar Raja Kottaichamy, Shabbah Begum, Mruthyunjayachar Chattanahalli Devendrachari, et al

ACS Publications
Most Trusted. Most Cited. Most Read.

**Publication:** Analytical Chemistry

**Publisher:** American Chemical Society

**Date:** Mar 1, 2020

*Copyright © 2020, American Chemical Society*

**PERMISSION/LICENSE IS GRANTED FOR YOUR ORDER AT NO CHARGE**

This type of permission/license, instead of the standard Terms & Conditions, is sent to you because no fee is being charged for your order. Please note the following:

- Permission is granted for your request in both print and electronic formats, and translations.
- If figures and/or tables were requested, they may be adapted or used in part.
- Please print this page for your records and send a copy of it to your publisher/graduate school.
- Appropriate credit for the requested material should be given as follows: "Reprinted (adapted) with permission from (COMPLETE REFERENCE CITATION). Copyright (YEAR) American Chemical Society." Insert appropriate information in place of the capitalized words.
- One-time permission is granted only for the use specified in your request. No additional uses are granted (such as derivative works or other editions). For any other uses, please submit a new request.

BACK CLOSE WINDOW

© 2020 Copyright - All Rights Reserved | Copyright Clearance Center, Inc. | Privacy statement | Terms and Conditions
Comments? We would like to hear from you. E-mail us at customercare@copyright.com